Università degli Studi di Bologna

FACOLTÀ DI SCIENZE MATEMATICHE, FISICHE E NATURALI

Dipartimento di Astronomia

The High Energy LLarge Area Survey: PROBING THE MULTIWAVELENGTH PROPERTIES OF THE SOURCES MAKING THE HARD X–RAY BACKGROUND

Tesi di Dottorato

di:

CRISTIAN VIGNALI

Tutore: **Prof. GIORGIO PALUMBO**

Correlatore: **Dott. ANDREA COMASTRI**

DOTTORATO DI RICERCA IN ASTRONOMIA

XII CICLO [1997–2000]

The High Energy Large Area Survey (HELLAS): *probing the multiwavelength properties of the sources making the hard X-ray Background*

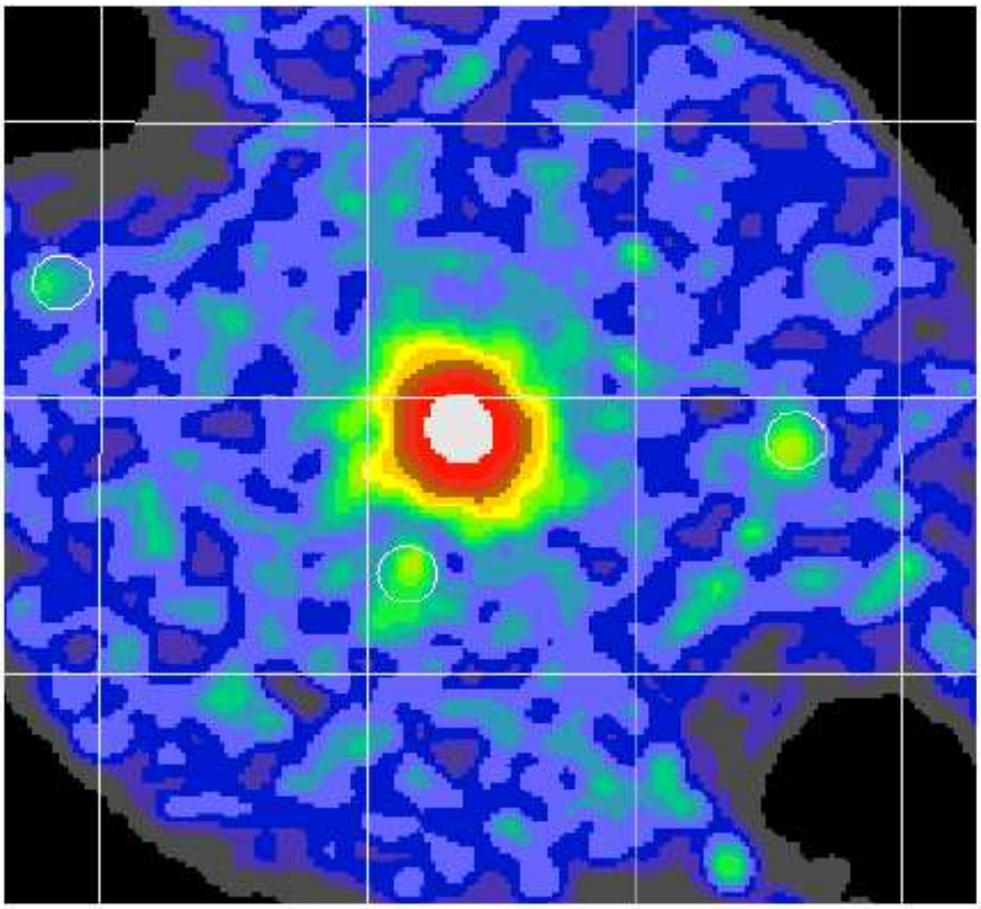

Cristian Vignali
Dipartimento di Astronomia
Universita` degli Studi di Bologna

Supervisor: Prof. Giorgio Palumbo
Co-supervisor: Dr. Andrea Comastri

Contents

Preface **1**

Introduction **5**

X–ray surveys 6

The "ancient view" from non-imaging hard X–ray detectors . 6

Soft X–ray imaging instruments 7

The "modern" perspective with hard X–ray imaging detectors . . . 8

The *ASCA* contribution to the knowledge of the XRB 8

The *BeppoSAX* view on the hard X–ray background 9

A new era in hard X–ray surveys: *Chandra* and *XMM-Newton* results 10

[1] BeppoSAX payload: the MECS instrument **13**

1.1 Introduction 13

1.2 The satellite and the scientific instruments 13

1.3 The MECS detectors 15

1.3.1 The mirror unit 15

1.3.2 The detector unit 16

1.4 MECS performances 18

1.4.1 The gain 18

1.4.2 Channel-to-energy conversion 18

1.4.3 Energy resolution 18

1.4.4 Point spread function 19
1.4.5 Effective area 19
1.5 Instrumental background 21

[2] The HELLAS: source detection and technical related issues. The 5–10 keV LogN-LogS **23**
2.1 Introduction: scientific purposes 23
2.2 The HELLAS 24
2.2.1 Source detection 27
2.2.2 Count rate to flux conversion 30
2.2.3 Sky coverage 32
2.3 Parameters uncertainties 35
2.3.1 Flux and sky coverage uncertainties 35
2.3.2 Source confusion 35
2.3.3 Spurious sources 36
2.4 Position accuracy: causes and corrections 37
2.5 The integral LogN–LogS 40
2.6 The XRB model 42
2.7 The HELLAS LogN-LogS compared with model predictions . 44

[3] BeppoSAX spectral analysis **49**
3.1 Introduction 49
3.2 X–ray spectral analysis 49
3.3 The HELLAS average spectral properties compared with model predictions 57

[4] Studying the soft X–ray properties of the HELLAS sources with ROSAT **65**
4.1 Introduction 65
4.2 The *ROSAT* satellite: a brief introduction 66

4.3 The cross correlation 67
4.4 *ROSAT* fields 67
4.4.1 *ROSAT* source detection 67
4.4.2 *ROSAT* data analysis 68
4.4.3 HELLAS sources detected by *ROSAT* 70
4.4.4 HELLAS sources undetected by *ROSAT* 72
4.5 *ROSAT* results 74
4.5.1 Absorption 74
4.5.2 Soft X–ray components 77
4.6 Comparison with the *ROSAT* Deep Survey sample 78
4.7 Discussion and conclusions 83

[5] HELLAS sources in ASCA fields **93**
5.1 Introduction 93
5.2 The HELLAS sources in archival *ASCA* data 94
5.3 *ASCA* data reduction 96
5.4 Spectral analysis and results 98
5.4.1 The radio-loud objects 99
5.4.2 The clusters 105
5.4.3 The radio-quiet objects 106
5.5 Follow-up observations 117
5.6 Conclusions 122

[6] Optical and near-infrared properties of the HELLAS sources **125**
6.1 Introduction 125
6.2 Spectroscopic runs 126
6.2.1 Spectroscopic identifications and results 126
6.3 Photometric runs 133
6.3.1 Optical and Near-Infrared data reduction 134

6.4 Probing the nature of the Optical+NIR continuum in a subsample of HELLAS sources 137
6.5 SAXJ 1353.9+1820 (HELLAS 228): a red quasar 144
6.5.1 Optical and NIR photometry 145
6.5.2 X–ray absorption 146
6.5.3 The nature of SAXJ 1353.9+1820 147
6.6 Optical properties of the HELLAS sample Comparison with hard X–ray properties 150
6.7 The role of small galaxy groups 153
6.8 The "restricted" HELLAS sample: choosing a magnitude limit 154
6.9 The contribution of the HELLAS sources to the sub-mm background 157

[7] Radio observations of the HELLAS sources 159
7.1 Introduction 159
7.2 Radio follow-up observations and data reduction 159
7.2.1 Data reduction 160
7.2.2 Regions for the source extraction 160
7.3 Cross-correlation with NVSS and FIRST 161
7.4 The HELLAS sources at radio wavelengths 161
7.5 Comparison with other X–ray samples 170

[8] Conclusions 173

Bibliography 179

Related publications 193

Acknowledgments 199

List of Figures

1.1 *BeppoSAX* scientific payload accomodation 14
1.2 Nominal energy coverage of the *BeppoSAX* instruments. . . . 15
1.3 Schematic view of the MECS instrument 16
1.4 Geometry of the strongback 17
1.5 The individual effective areas of the three MECS units as function of energy 20
1.6 The MECS effective area as function of energy for different off-axis angles 21
1.7 The MECS vignetting correction as function of off-axis angle for the three MECS units and for three energies 22
2.1 Encircled energy function for *BeppoSAX* MECS and *ASCA* GIS instruments 25
2.2 Effective areas of *BeppoSAX* MECS and LECS instruments vs. SIS and GIS detectors on board *ASCA* 26
2.3 The distribution of the net exposure times in the 142 HELLAS fields 28
2.4 The distribution of the HELLAS sources in detector coordinates 30
2.5 MECS count rate as a function of the off-axis angle 32
2.6 The HELLAS sky coverage for three different assumptions of the source spectral slope 33
2.7 The flux distribution of the HELLAS sources in the 5–10 keV band 34

2.8 The deviations in RA and DEC between MECS positions and catalog positions for a sample of about one hundred AGNs . 39
2.9 The HELLAS 5–10 keV LogN–LogS 40
2.10 The model absorption distribution compared with the observed $N_{\rm H}$ distribution for a sample of nearby Seyfert 2 galaxies 43
2.11 The HELLAS 5–10 keV integral LogN-LogS 45
2.12 A compilation of the 2–10 keV logN-logS from different surveys 46
2.13 The relative fraction of unobscured and obscured sources as a function of the 0.5–2 keV, 2–10 keV and 5–10 keV flux . . . 47
3.1 The softness ratio as a function of the 5–10 keV flux 51
3.2 The hardness ratio HR1 vs. HR2 for the HELLAS sources . . 53
3.3 The *BeppoSAX* softness ratio as a function of redshift 55
3.4 The softness ratio as a function of the redshift for the Type 1 objects computed through the method of the running mean . 56
3.5 The model predicted fraction of relatively unobscured and highly obscured AGNs as a function of the 5–10 keV flux . . 57
4.1 Distribution of the distances between *BeppoSAX* and *ROSAT* source positions 69
4.2 Flux distribution of the HELLAS sources with a soft X–ray counterpart with respect to the whole sample 70
4.3 Distribution of the distances between *ROSAT* and optical positions for the HELLAS sources 71
4.4 Distribution of the off-axis angles for the HELLAS sources detected by *ROSAT* with respect to the total. 72
4.5 Exposure times distribution for the HELLAS sources detected by *ROSAT* with respect to the total 73
4.6 *BeppoSAX* 5–10 keV flux against *ROSAT* 0.5–2 keV flux . . . 74

4.7 *BeppoSAX* 5–10 keV to *ROSAT* 0.5–2 keV flux ratios as a function of redshift 76
4.8 5–10 keV to 0.5–2 keV flux ratios for the HELLAS and the *ASCA* LSS broad-line objects 77
4.9 Redshift distribution of the HELLAS and the RDS sources . 79
4.10 0.5–2 keV luminosity vs. redshift for the HELLAS sources . . 80
4.11 0.5–2 keV luminosity vs. redshift for the RDS sources 81
4.12 *ROSAT* HR1 vs. HR2 for the HELLAS sources 82
4.13 *ROSAT* HR1 vs. HR2 for the Lockman Hole sources 83
4.14 *ROSAT* HR1 as a function of Galactic column density 84
4.15 Distribution of the sources (detected and undetected) as a function of Galactic absorption 84
4.16 *ROSAT* HR1 distribution for the HELLAS and the RDS sources 85
4.17 *ROSAT* HR2 as a function of Galactic column density 85
4.18 *ROSAT* HR2 distribution for the HELLAS and the RDS sources 86
4.19 HR2 vs. redshift for the HELLAS sources 87
4.20 HR2 vs. redshift for the Lockman Hole objects 88
4.21 HR2 vs. *BeppoSAX* softness ratio for the HELLAS sources . 89
5.1 Distribution of the off-axis angles of the HELLAS sources detected by *ASCA* with respect to the total in *ASCA* field of view 95
5.2 Distribution of the exposure times of the HELLAS sources detected by *ASCA* with respect to the total 96
5.3 Distribution of the softness ratios of the HELLAS sources detected by *ASCA* with respect to the total 97
5.4 Power-law fit to the *ASCA* GIS data of the HELLAS source #72 (BL Lac at z=0.308) and residuals 101
5.5 Power-law fit to the *ASCA* GIS2 data of the HELLAS source #73 (RLQ, z=1.537) and residuals 102

5.6 Power-law fit to the *ASCA* GIS data of the HELLAS source #387 (RLQ, z=1.46) and residuals 102
5.7 Power law + thermal fit to the *ASCA* SIS+GIS data of the HELLAS source #84 (the radio-galaxy IC 4296, z=0.013) and residuals 104
5.8 Thermal fit to the *ASCA* SIS+GIS data of the HELLAS source #392 (cluster, z=0.216) and residuals 106
5.9 Power-law fit to the *ASCA* GIS data of the HELLAS source #167 (Type 1 at z=0.300) and residuals 107
5.10 Power-law fit to the *ASCA* GIS2 data of the HELLAS source #176 (Type 1 at z=0.804) and residuals 107
5.11 Power-law fit to the *ASCA* GIS data of the HELLAS source #390 (Type 1 at z=0.089) and residuals 108
5.12 Power-law fit to the *ASCA* GIS data of the HELLAS source #394 (Type 1 at z=0.312) and residuals 109
5.13 *ASCA* GIS data of the HELLAS source #264 (Type 1.9, z=0.176) fitted with a simple power-law model and residuals. 110
5.14 Power-law fit to the *ASCA* GIS spectrum of the HELLAS source #319 (Type 1.8, z=0.205) and residuals 111
5.15 *ASCA* GIS2 spectrum of the HELLAS source #254 fitted with a single power-law model and relative residuals 113
5.16 Single power-law fit to the *ASCA* GIS spectrum of the HELLAS source #256 and residuals 114
5.17 Thermal fit to the *ASCA* GIS spectrum of the HELLAS source #393 and relative residuals 115
5.18 *ASCA* GIS2+GIS3 spectrum of the HELLAS source #296 fitted with a simple power-law model and relative residuals . 116
5.19 SAXJ 1519.5+6535 (HELLAS #375) best-fit spectrum with residuals 117

5.20 *ASCA* hard X–ray intensity levels regarding SAXJ 1519.5+6535 overlaid on the POSS image 118
5.21 *ASCA* SIS+GIS spectrum SAXJ 1353.9+1820 and relative data/model ratio 120
5.22 *ASCA* confidence contours in the Γ – $N_{\rm H_{int}}$ space parameters for the source SAXJ 1353.9+1820 120
5.23 *ASCA* GIS spectrum of SAXJ 1353.9+1820, serendipitously observed in the field of view of the spectroscopic binary HD 121370 122
5.24 *BeppoSAX* vs. *ASCA* softness ratio for the "bright" HELLAS sample 124
6.1 The offset distribution between the X–ray and the optical positions for all the identified HELLAS sources 131
6.2 The offset distribution between the X–ray and the optical positions as a function of the off-axis angles in *BeppoSAX* . . 132
6.3 The offset distribution between the X–ray and the optical positions as a function of the 5–10 keV flux 133
6.4 The 5–10 keV flux distribution of the HELLAS identified sources with respect to the full sample 134
6.5 The redshift distribution of the HELLAS sources 135
6.6 The 5–10 keV luminosity of the HELLAS sources as a function of their redshift 136
6.7 B−R plotted against B−K_S for a subsample of 15 HELLAS sources (blue-continuum QSOs, red-continuum QSOs, Type 1.8-2 AGNs and emission-line galaxies) 140
6.8 Comparison between photometric measurements and observed optical spectral shapes with the best-fit models for three representative objects 143
6.9 The optical spectrum of the red quasar SAXJ 1353.9+1820 . 144

6.10 The optical surface brightness profiles of SAXJ 1353.9+1820 fitted with a de Vaucouleurs $r^{1/4}$ law 146
6.11 SAXJ 1353.9+1820 photometric (optical + NIR) points fitted with a synthetic model of an evolved early-type galaxy plus the contribution of a moderately absorbed quasar 148
6.12 Comparison of SAXJ 1353.9+1820 colors with those of the extended objects which populate the Marano field in the B magnitude range 19–22. 149
6.13 The B−R distribution for the HELLAS sources identified as Type 1 AGNs, Type 1.8–2 AGNs, red quasars and emission-line galaxies 151
6.14 The *BeppoSAX* softness ratio vs. the optical B−R color . . . 152
6.15 The X–ray-to-optical ratio vs. the 5–10 keV flux for the HELLAS identified sources 153
6.16 The flux distribution of the subsample of 115 sources with respect to the original HELLAS sample and that of the 63 spectroscopically identified sources 156
7.1 Distribution of the distances between radio and X–ray (*BeppoSAX*) position 162
7.2 The radio contours for the HELLAS source 321 obtained at the *VLA* (6 cm) 167
7.3 Radio fluxes (at 6 cm) against 5–10 keV flux 168
7.4 The radio-to-optical $\alpha_{\rm RO}$ vs. the optical-to-X–ray $\alpha_{\rm OX}$ index 169

List of Tables

2.1 *BeppoSAX* MECS PSF for different off-axis angles 25
3.1 The list of the **147** HELLAS sources and their X–ray parameters 59
4.1 The HELLAS sources detected by *ROSAT* 90
5.1 *ASCA* spectral results obtained for the highest signal-to-noise ratio HELLAS sources 100
5.2 *ASCA* SIS+GIS spectral fits to SAXJ 1353.9+1820 in the 0.9–10 keV energy range 119
6.1 Optically identified HELLAS sources 127
6.2 Summary of spectroscopic identifications 130
6.3 Optical and NIR magnitudes obtained through follow-up observations 138
6.4 Optical magnitudes obtained at the 1.5-m Mexican telescope at S. Pedro Martir and with EFOSC2 acquisition images at ESO 3.6-m 139
7.1 Properties of the radio counterparts of the HELLAS sources . 164
7.2 Summary of the results concerning radio/X–ray associations from previous X–ray surveys and the present one 170

I was walking along a path with two friends
the sun was setting
I felt a breath of melancholy
Suddenly the sky turned blood-red
I stopped and lent against the railing, deathly tired
looking out across the flaming clouds that hung
like blood and sword over the deep blue fjord and town
My friends walked on
I stood there trembling with anxiety
and felt a great, infinite scream pass through nature.
E. M. - 1893

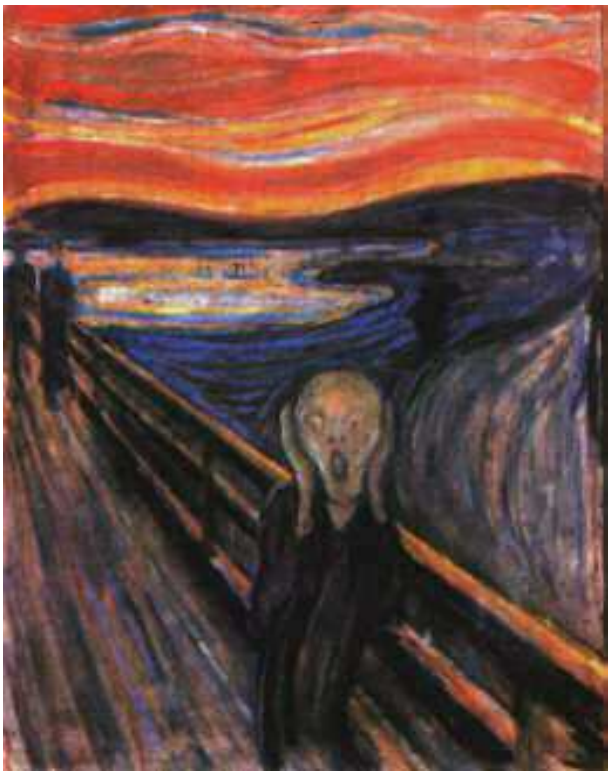

Preface

The intensity and the spectral shape of the X–ray background (XRB) are well matched by the summed emission from active galactic nuclei (AGNs) with a broad range of luminosities and absorbing column densities (Setti & Woltjer 1989; Madau, Ghisellini & Fabian 1994; Comastri et al. 1995). As a consequence, about 80 % of the accretion power in the Universe is obscured (Fabian et al. 1998; Fabian & Iwasawa 1999; Hasinger et al. 2000). However, the recent optical identification breakthrough of *Chandra* sources have demonstrated that part of the newly discovered XRB sources may be quite different from established classes of AGNs. These sources may be the unobserved phase associated with the major growth of massive black holes, whereas classical quasars and Seyfert galaxies represent a later, transient phase of accretion into the black hole with lower efficiency (Fabian 1999). These AGNs are expected to be strongly obscured, the possible high-z counterparts of nearby ultra-luminous infrared galaxies (ULIRGs), most of which are Compton-thick (i.e. characterized by column densities higher than 10^{24} cm^{-2}). Whatever is the nature of these sources, they would hardly populate the optical and the soft X–ray surveys, which are strongly biased against highly absorbed objects, thus implying that a sizeable fraction of the accreting power in the Universe has been lost so far. An example is given by NGC 6240, which is optically classified as a starburst galaxy, whereas the emission is clearly AGN-powered in the X–rays (Vignati et al. 1999).

Therefore, hard X–ray surveys represent the most efficient way to find a considerable number of hard, presumably absorbed sources, to estimate their contribution to the hard XRB and, finally, to trace the accretion history of the Universe (i.e. the history of the light ultimately produced by gravity).

The **H**igh **E**nergy **LL**arge **A**rea **S**urvey (HELLAS), carried out with *BeppoSAX* in the 5–10 keV energy range (the hardest band accessible with imaging instruments), has been designed to study the nature of the hard

X–ray source population. The sample consists of 147 sources detected down to a flux limit of about 5×10^{-14} erg cm^{-2} s^{-1}, where $\sim$ 20–30 % of the XRB is resolved.

In order to investigate the nature and the physics of the hard X–ray source populations, a multi-wavelength approach has been adopted in the course of the survey.

This hard X–ray survey can be considered fully complementary to the present pencil-beam surveys carried out with *Chandra*, since a different portion of the redshift-luminosity plane is sampled, over a larger area of sky. At the bright X–ray fluxes reached by *BeppoSAX* it is possible to get useful information about the X–ray spectra of the hard X–ray selected sources (such as the X–ray continuum slope, the presence of soft X–ray components and emission-line features), to obtain high-quality optical spectroscopy and, given the large area of sky surveyed, to find a sizeable sample of "rare" objects, such as Type 2 quasars (with narrow optical lines) and red quasars. The physics of the sources can be investigated by comparing their properties at different wavelengths.

The PhD thesis is structured as follows: after a brief review of the results obtained by past X–ray surveys, with particular emphasis on those carried out in hard energy ranges, the *BeppoSAX* MECS properties (effective area, vignetting, point spread function) will be discussed in chapter 1, while chapter 2 introduces to the survey (source detection, sky coverage, source confusion and possible biases, position accuracy and the 5–10 keV LogN-LogS). Chapter 3 describes the hard X–ray properties of the HELLAS sources through the hardness ratio technique based on *BeppoSAX* counts, while the soft X–ray properties are extensively discussed in chapter 4, along with a comparison with a soft X–ray selected sample extracted from the Lockman Hole. Chapter 5 deals with the spectral analysis of *ASCA* data carried out on a subsample of relatively bright HELLAS sources. The X–ray properties of some still unidentified, but intriguing sources will be presented as well. Chapter 6 is based on the optical and near-infrared properties of the HELLAS sources, and on a detailed study of their host galaxies through a multicolor approach. An exhaustive discussion of the spectroscopic properties of the HELLAS sources is not presented in this thesis, but in a forthcoming paper by La Franca and collaborators (in preparation). The same applies to the radio data, whose preliminary results are shown in chapter 7 (but a more exhaustive discussion will be presented by Ciliegi et al., in preparation).

In the concluding chapter the broad-band properties of the hard X–ray selected sources from $BeppoSAX$ and $ASCA$ will be summarized, and a brief comparison with the more recent $Chandra$ and $XMM\text{-}Newton$ results will be presented as well.

Introduction

Since the discovery of cosmic X–ray Background (hereafter XRB) in early sixties (Giacconi et al. 1962), a great deal of effort has been made to understand its origin (for a review, see Fabian & Barcons 1992; Comastri 2000). Although the XRB emission extends over a wide energy range in more than 5 decades from X–rays to γ–rays, the majority of its energy density is emitted in the hard X–rays, peaking at about 20–30 keV.

The XRB characteristics are very different below and above 2 keV. Indeed, in the soft X–rays strong anisotropy has been observed (Tanaka & Bleeker 1977). Most of the XRB in the 0.1–0.5 keV band is of galactic origin and probably due to a local bubble with a temperature of about 10^6 K. In the 0.5–0.9 passband (M band) a large fraction of the XRB is due to thermal emission from hot ($T \sim 2.2 \times 10^6$ K) gas in our Galaxy (Hasinger 1992; Wang & McCray 1993). On the other hand, above 2 keV the XRB is highly uniform except for an excess component along the Galactic plane (Koyama 1989). The uniform component has an extra-galactic origin and will be extensively discussed in this thesis.

Although the spectrum of the XRB from a few keV to tens of keV resembles that of a hot plasma emitting at about 40 keV (Marshall et al. 1980; Rothschild et al. 1983), this hypothesis has been discarded since the hot gas should give rise to evident high-frequency distortions in the cosmic microwave background (CMB) through inverse-Compton scattering, which have not been observed by COBE (Mather et al. 1990, 1994), the contribution of hot ($T \gtrsim 10^8$ K) gas to the XRB being less than 0.01 % (Wright et al. 1994). As a consequence, the only viable alternative is that the XRB is due to the superposition of discrete sources.

While *ROSAT* resolved about 70–80 % of the XRB in the 0.5–2 keV energy range into individual discrete sources (Hasinger et al. 1993;

Hasinger et al. 1998; Schmidt et al. 1998), most of which being broad-line Active Galactic Nuclei (hereafter AGNs) at $< z > \sim 1.5$ (Shanks et al. 1991; Boyle et al. 1994; McHardy et al. 1998; Lehmann et al. 2000), in the hard band, where the bulk of the energy density resides, the nature of the sources of the XRB remains less obvious. The most serious problem with the discrete-source origin for the XRB is the so-called "spectral paradox", i.e. a discrepancy between the XRB spectrum ($\Gamma \simeq 1.4$–1.5, Gendreau et al. 1995; Chen, Fabian & Gendreau 1997; Vecchi et al. 1999) and that of the bright AGNs ($\Gamma \simeq 1.7$–1.9, Turner & Pounds 1989; Nandra & Pounds 1994; Nandra et al. 1997) in the hard X–ray domain. This finding has been theoretically solved by assuming that the XRB is due to to a mixture of absorbed and unabsorbed objects (Setti & Woltjer 1989). Following this indication, the contribution of different classes of sources to the hard XRB has been evaluated through population-synthesis models (e.g. Madau, Ghisellini & Fabian 1994; Comastri et al. 1995). In the last few years, both *ASCA* and *BeppoSAX* surveys (Ueda et al. 1999a; Della Ceca et al. 1999; Fiore et al. 1999, 2000a, 2001) have revealed that obscured AGNs are indeed the main contributors to the hard XRB, whose flat slope is ascribed to the superposition of X–ray obscured sources over a large redshift range.

Recent *Chandra* observations have confirmed that AGNs do significantly contribute to the XRB (Mushotzky et al. 2000; Giacconi et al. 2001; Fiore et al. 2000b; Brandt et al. 2000a; Barger et al. 2001), but at very low X–ray fluxes both a significant number of apparently normal galaxies and objects with a very faint (or absent) optical counterpart do emerge.

X–ray surveys

The "ancient view" from non-imaging hard X–ray detectors

Before the advent of *ASCA* and *BeppoSAX*, hard X–ray surveys were performed with non-imaging detectors and thus reaching only relatively bright fluxes ($\sim 10^{-11}$ erg cm^{-2} s^{-1}).

Using the *HEAO-1* A2 data, Piccinotti et al. (1982) found 85 X–ray objects with limiting sensitivity of about 3×10^{-11} erg cm^{-2} s^{-1} in 8.2 sr of sky. The optical identification breakdown is as follows: 32

clusters of galaxies, 30 Seyfert galaxies, 1 radio-loud quasar (3C 273), 4 BL Lac objects and 1 starburst galaxy (M 82). Subsequently, the *Ginga* slow scan data in a limited area of the North ecliptic pole region (the *Ginga* unbiased survey) allowed to carry out a survey covering 383 deg^2 at a limiting 2–10 keV flux of 8×10^{-12} erg cm^{-2} s^{-1} (Kondo 1990). The extrapolation to brighter fluxes did match well the source density obtained by *HEAO-1* (Piccinotti et al. 1982) assuming an Euclidean LogN-LogS.

Surveys performed with non-imaging instruments are usually limited by source confusion: even though the detected photon count exceeds that of the local background, it is hard to determine whether the observed count come from a single source or more. In these cases, a fluctuation analysis is carried out. It consists to constrain the LogN-LogS by analyzing the fluctuation of the faint source number in the detector field-of-view. This can be applied also for sources fainter than the detection limit, because the background level of the detector fluctuates according to the fluctuation of the source number. Through the fluctuation analysis of *HEAO-1* A2 (Shafer 1983) and *Ginga* data (Hayashida 1990; Butcher et al. 1997), about 30 % of the 2–10 keV XRB could be explained. Moreover, by evaluating the X–ray spectral slope of the fluctuation component, a value $\Gamma \simeq 1.8$ (2–10 keV) was obtained (Hayashida, Inoue & Kii 1992), which is considerably steeper than the corresponding value of the XRB spectrum in the same energy range, thus confirming the "spectral paradox".

Soft X–ray imaging instruments

The *Einstein* observatory was the first experiment carrying out a grazing incidence X–ray telescope in orbit, thus making viable the observation of the soft X–ray sky (below 3 keV) with good spatial resolution. The *Einstein* Deep Sensitivity Survey (DS), at a limiting X–ray flux of 2.6×10^{-14} erg cm^{-2} s^{-1} ($\sim$ 0.3–3.5 keV energy range) allowed Giacconi and collaborators (1979) to resolve 26$\pm$11 % of the XRB. The *Einstein* deep survey data have been complemented at brighter fluxes (5×10^{-14} erg cm^{-2} s^{-1}) by the Medium Sensitivity Survey (MSS, Gioia et al. 1984), and its follow-up campaign (EMSS, Gioia et al. 1990; Stocke et al. 1991; Maccacaro et al. 1991), finding that AGNs contribution to the XRB is dominant (about 40 % at 2 keV) with respect to the other extra-galactic objects (clusters and normal

galaxies).

The higher performance capabilities of the *ROSAT* satellite (better angular resolution and a larger collecting area than *Einstein*) allowed a deeper investigation of the soft XRB. The *ROSAT* Deep Survey (RDS) in the Lockman Hole (Hasinger et al. 1998), at a limiting 0.5–2 keV flux of about 10^{-15} erg cm^{-2} s^{-1}, was able to resolve about 70–80 % of the 0.5–2 keV XRB into discrete sources (Schmidt et al. 1998; Lehmann et al. 2000). 40 out of the 50 spectroscopically identified sources (above an X–ray flux of 5.5×10^{-15} erg cm^{-2} s^{-1}) are AGNs (most of which with broad optical lines). Interesting enough, there is evidence of a flattening of the average slope of the constituents of the soft XRB as the flux decreases (Hasinger et al. 1993; Vikhlinin et al. 1995; Almaini et al. 1996).

The "modern" perspective with hard X–ray imaging detectors

The *ASCA* contribution to the knowledge of the XRB

The imaging capabilities of the *ASCA* satellite made possible to observe faint sources with a flux limit of a few 10^{-14} erg cm^{-2} s^{-1} in the 2–10 keV energy band, and therefore to resolve a larger fraction ($\sim$ 20–30 %) of the hard XRB. Several surveys have been carried out with *ASCA*. The Large Sky Survey (LSS), consisting of 76 pointing observations covering about 7 deg^2 of sky near the north Galactic pole (Ueda et al. 1998; Ueda et al. 1999a), down to a flux limit of about 10^{-13} erg cm^{-2} s^{-1} (2–10 keV) and resolving $\sim 23\pm3$ % of the XRB. 33 X–ray sources have been identified: most are AGNs (25 broad-line and 5 narrow-line), while among the remaining objects 2 clusters and 1 star are found. The average photon index of the hard X–ray sources detected by the LSS is $\Gamma = 1.49\pm0.10$, consistent with that of the XRB in this energy range and suggesting that the contribution of sources with hard X–ray spectra becomes significant at flux of the order of 10^{-13} erg cm^{-2} s^{-1} (Ueda et al. 1999a). This result is fully confirmed by the *ASCA* Medium-Sensitivity Survey (AMSS, or GIS project, Takahashi et al. 1998; Ueda et al. 1999b): from the serendipitous fields covering 106 deg^2, 714 sources have been detected, 323 of which in the 2–10 keV band, down to an X–ray flux of 7×10^{-14} erg cm^{-2} s^{-1}. A similar

survey has been carried out on 87 *ASCA* GIS2 images by Della Ceca and collaborators (1999), down to a 2–10 keV flux of the order of 10^{-13} erg cm^{-2} s^{-1}, and confirming the hardening of the X–ray spectra towards fainter X–ray fluxes ($<\Gamma> = 1.36\pm0.14$ for the "faint" sample, i.e. $F_{2-10\ keV} \lesssim 4 \times 10^{-13}$ erg cm^{-2} s^{-1}, whereas $<\Gamma> = 1.87\pm0.08$ for the "bright" sample). A different approach has been followed by Ogasaka et al. (1998), who used deep (from a hundred to several hundreds of ks) *ASCA* observations (the SA 57 field, the Lockman Hole, the Lynx field), reaching a flux limit of 4×10^{-14} erg cm^{-2} s^{-1}. The source counts are consistent with the Euclidean extrapolation of the shallower *ASCA* surveys.

The *ASCA* surveys have revealed a population of hard (very hard in some cases, Akiyama et al. 1998; Sakano et al. 1998; Akiyama et al. 2000; Della Ceca et al. 2000a) sources which strongly contribute to the hard XRB. The average spectral index of these sources is significantly harder and closer to the one of the XRB than that obtained by previous X–ray measurements with no-imaging instruments and at brighter flux limits.

The *BeppoSAX* view of the hard X–ray background

The spectral hardening towards faint X–ray fluxes has been found also by the *BeppoSAX* 2–10 keV survey carried out on high-Galactic latitude MECS fields (Giommi, Perri & Fiore 2000). The hardening has been preferentially ascribed to an increasing percentage of absorbed sources at faint fluxes than to a gradual flattening of the spectral slope. At the flux limit of the survey ($\sim 5 \times 10^{-14}$ erg cm^{-2} s^{-1}) about 25 % of the XRB is resolved into discrete sources. The complementary fluctuation analysis (Perri & Giommi 2000) has allowed to derive a LogN-LogS still close to the Euclidean one and well matching that obtained recently by *Chandra* (Mushotzky et al. 2000). At the flux limit reached by the fluctuation analysis ($\sim 1.5 \times 10^{-14}$ erg cm^{-2} s^{-1}) about 40–50 % of the XRB is resolved, depending on its normalization (Vecchi et al. 1999).

The hard 5–10 keV energy range has been explored by the HELLAS, performed on the same *BeppoSAX* fields. This PhD thesis deals with this hard X–ray selected survey, therefore it will be extensively described in the following chapters, and the results will be compared to the AGNs synthesis model for the XRB (e.g. Comastri et al. 1995).

A new era in hard X–ray surveys: *Chandra* and *XMM-Newton* results

Recently, the *Chandra* X–ray observatory (Weisskopf, O'Dell & Van Speybroeck 1996) has resolved the bulk of the 2–7 keV hard X–ray background into point sources (Mushotzky et al. 2000; Brandt et al. 2000a; Giacconi et al. 2001). The principal aim of hard X–ray surveys is to test the AGNs synthesis models for the XRB and to understand the physics and the evolution of the XRB constituents. Mushotzky et al. (2000) surveyed the SSA 13 field (with an exposure of $\sim$ 100 ks), finding 22 sources in the 2–10 keV band down to a flux limit of 3.2×10^{-15} erg cm^{-2} s^{-1}. Roughly a third of the sources were broad-line (Type 1) AGNs, another third were identified with apparently normal galaxies (see also Fiore et al. 2000b) and the final third had an extremely faint or no optical counterpart (i.e. I >> 23 mag.). These objects have been detected in the near-infrared band (Crawford et al. 2001), showing the presence of featureless spectra and suggesting the possible existence of heavily obscured AGNs, whose colors are consistent with reddened elliptical galaxies at redshifts of the order of 1–2.

The presence of apparently normal galaxies among the *Chandra* sources has been confirmed by the 130 ks observation of the *Chandra* Deep Field South (Giacconi et al. 2001), with a 2–10 keV flux limit of 2×10^{-15} erg cm^{-2} s^{-1}.

Chandra sources follow the trend already suggested by *ASCA*, i.e. the increasing hardness towards faint fluxes ($<\Gamma> = 1.70 \pm 0.06$ for the "bright" subsample, while $<\Gamma> = 1.35 \pm 0.10$ for the "faint" one). However, only a small fraction (about 9 %) of the sources are detected in the hard band and not in the soft band. This is due to the combined effect of *Chandra* effective area, peaking in the soft X–rays, and possibly to the presence, even in highly obscured AGNs, of soft X–ray emission, likely produced by partial covering of the nuclear emission, scattered components, or circum-nuclear starbursts associated with AGNs. Similar results have been obtained by both *ASCA* (Della Ceca et al. 1999), *BeppoSAX* surveys (Giommi et al. 2000; see also chapter 4), and recently by *XMM-Newton* observation of the Lockman Hole (Hasinger et al. 2001).

Chandra results have demonstrated that the newly discovered XRB sources are both AGNs, as expected, and apparently normal galaxies. Fabian (1999) has argued that these sources represent the hitherto

unobserved phase associated with the major growth of massive black hole, whereas quasars and Seyfert galaxies represent a later, transient phase (at $z < 2.5$) during which the black hole acquires little additional mass accreting at about 10 % of the Eddington limit (Wilman, Fabian & Nulsen 2000). In this model, the X–ray absorption can be explained by the presence of cold, dusty clouds surrounding the newly forming galactic bulges around massive black holes.

Preliminary *XMM-Newton* (Jansen et al. 2001) results obtained with a 100 ks observation of the Lockman Hole (Hasinger et al. 2001), reaching a flux limit of 1.4×10^{-15} erg cm^{-2} s^{-1} and discovering 112 sources in the 2–10 keV energy range (with off-axis angles less than 10 arcmin), suggest that a significant fraction (about 40 %) of the sources are characterized by hard, probably intrinsically absorbed X–ray spectra, and their hardness is also evident in the soft X–rays.

BeppoSAX payload: the MECS instrument

1.1 Introduction

The X–ray astronomy Satellite *SAX* is a joint project of the Italian Space Agency (ASI) and the Netherlands Agency for Aerospace Programs (NIVR). After launch (on April 30 1996) it was renamed *BeppoSAX* in honor of Giuseppe (Beppo) Occhialini. The payload is characterized by a very wide spectral coverage, spanning from 0.1 keV up to 300 keV (Boella et al. 1997a), and comprises four Narrow Field Instruments (NFI, the Low Energy Concentrator Spectrometer LECS, the Medium Energy Concentrator Spectrometer MECS, the High Pressure Gas Scintillation Proportional Counter HPGSPC, and the Phoswich Detection System PDS), all pointing towards the same direction, and two Wide Field Cameras (WFC), pointing to diametrically opposite directions perpendicular to the NFI common axis.

1.2 The satellite and the scientific instruments

The configuration of the scientific payload and the energy bands covered by the different instruments are showed in Fig. 1.1 and Fig. 1.2, respectively. The broad band capability (which represents the fundamental achievement of *BeppoSAX*) is provided by a set of instruments co-aligned with the Z axis of the satellite, the Narrow Field Instruments:

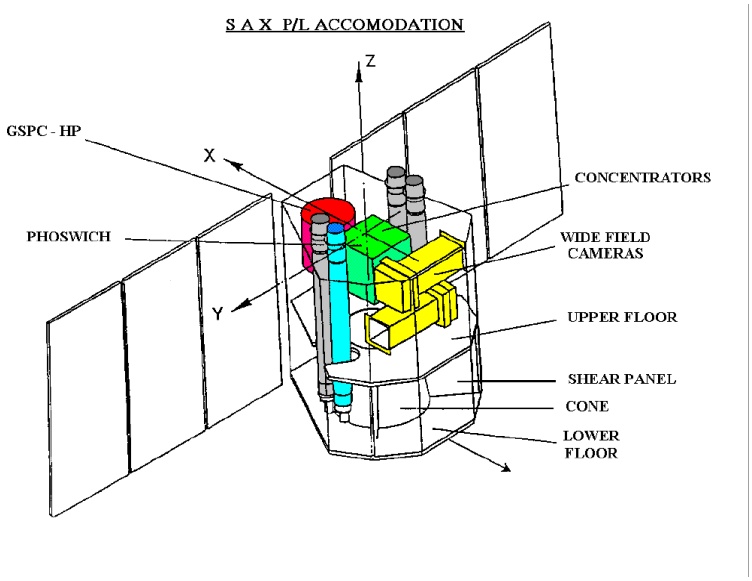

Figure 1.1: *BeppoSAX* scientific payload accomodation.

• **MECS**: Medium Energy Concentrator Spectrometers: a medium energy (1.3–10 keV) set of three identical grazing incidence telescopes with a double cone geometry (Citterio et al. 1986; Conti et al. 1994), with position sensitive proportional counters in their focal planes (Boella et al. 1997b). The main characteristics of the MECS instruments will be widely discussed in the following sections, since the HELLAS has been performed through these detectors.

• **LECS**: Low Energy Concentrator Spectrometers: a low energy (0.1–10 keV) instrument, identical to the three MECS units, but characterized by a thin window position sensitive proportional counter in its focal plane (Parmar et al. 1997).

• **HPGSPC**: a collimated High Pressure Gas Scintillation Proportional Counter, covering the 4–120 keV energy range (Manzo et al. 1997).

• **PDS**: a collimated Phoswich Detector System, with a spectral coverage ranging from 15 to 300 keV (Frontera et al. 19997, and references therein).

Perpendicular to the axis of the NFI and pointed in perpendicular directions there are two coded mask proportional counters (Wide Field

Cameras, WFC, Jager et al. 1997), which cover the 2–30 keV energy range and provide a large field of view (20° × 20° FWHM each).

Moreover, the four lateral active shields of the PDS instrument are used as monitor of the Gamma–ray bursts (GRB) in the range 60–600 keV.

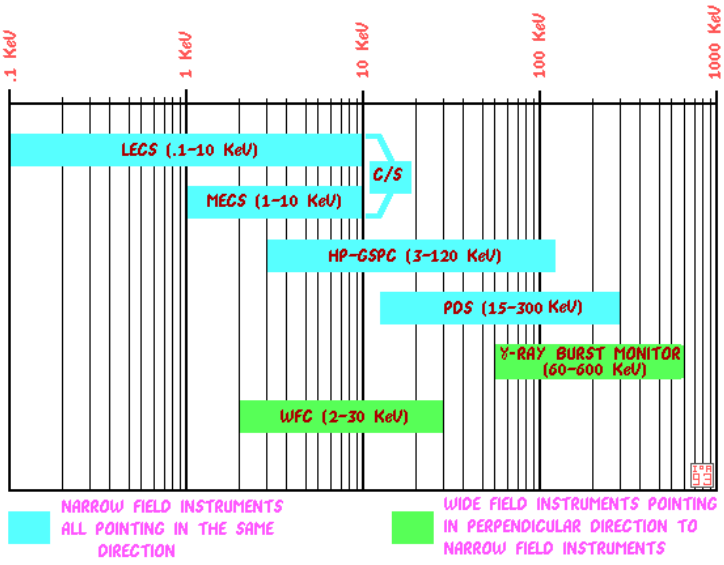

Figure 1.2: Nominal energy coverage of the *BeppoSAX* instruments.

1.3 The MECS detectors

1.3.1 The mirror unit

The MECS consists of three units, each composed of a grazing incidence Mirror Unit (MU), and of a position sensitive gas scintillation proportional counter located at the focal plane. Each MU is composed of 30 nested coaxial and confocal mirrors having a double cone geometry (one paraboloid and one hyperboloid surfaces) resembling the Wolter I configuration (Citterio et al. 1986), with diameters ranging from 68 to 162 mm, a total length of 300 mm, thickness from 0.2 to 0.4 mm and focal length of 1850 mm. The MU design was optimized in such a way to have the best response curve at about 6 keV.

1.3.2 The detector unit

The focal plane detectors are proportional counters filled with Xenon and working in the range 1.3–10 keV with an energy resolution of about 8% at 5.9 keV and a position resolution of about 1 arcmin on-axis at the same energy. The gas cell is a cylindrical ceramic body closed, at the top, by a 50 μm thick entrance Beryllium window and, at the bottom, by an UV exit window, as shown in Fig. 1.3.

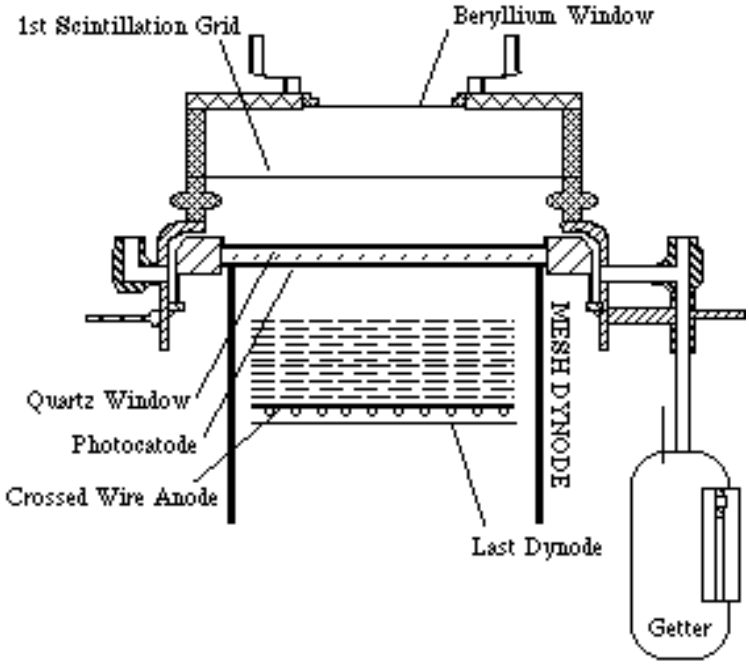

Figure 1.3: Schematic view of the MECS instrument: the gas cell and the position sensitive gas scintillation proportional counter.

The entrance window is externally supported by a Beryllium strongback structure 0.55 mm thick, composed of a ring (10 mm inner diameter, 1 mm width) connected to the borders of the window by four ribs, as shown in Fig. 1.4. The strongback partly prevents the soft X–ray photons from being detecting, thus partially hiding the X–ray sources at low energies.

An X–ray photon, absorbed in the gas cell, creates a cloud of

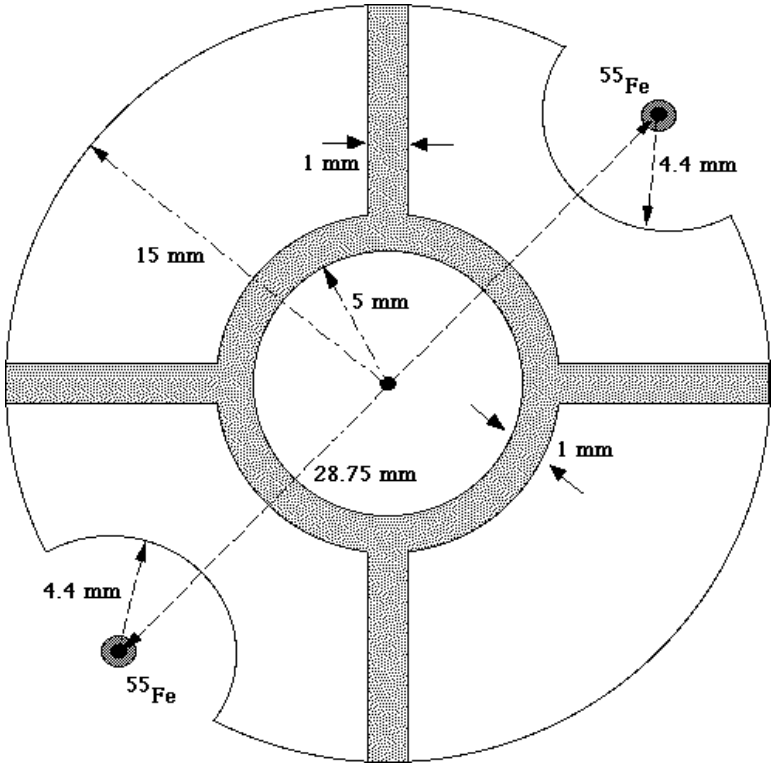

Figure 1.4: Geometry of the strongback, which delimits the sensitive part at the center of the field of view.

electrons. A uniform electrical field across the drift cell moves the cloud to the scintillation region (characterized by a higher electrical field), where UV photons are produced through the interaction of the accelerated photons with the Xenon ions. The amplitude of the UV signal, which is detected by a photo-multiplier (with a quantum efficiency of the order of 20%), is proportional to the energy of the primary X–ray photon. Spurious events may be rejected by applying a selection on the duration of the signal (the so-called burst length).

Two ^{55}Fe collimated calibration sources (nuclear line at 5.95 keV) are located near the edge of the Beryllium window, in diametrically opposed positions. These sources are used to monitor the detector gain, but are excluded from the accumulation process by rejecting two nearby regions of 3 mm radius. Moreover, a passive ion shield is placed in front of the detector.

1.4 MECS performances

1.4.1 The gain

The gain has a very weak dependence on the variations of temperature (1 °C causes a difference of 1.5% in the gain). A dependence of the gain on the position is also present in all the three units. A photon falling at the edge of the detector will be revealed in a different PHA channel than a photon falling close to the center. This effect can be corrected by deriving a gain map for each data acquisition. The gain normalized to the detector center is a very weak function of the energy and is practically unaffected by time variations of the absolute gain.

1.4.2 Channel-to-energy conversion

The main feature in the channel-to-energy conversion (i.e. in the detector gain) is the discontinuity at 4.78 keV corresponding to the Xenon L-edge. This is caused by a decrease in the photon-electron conversion efficiency of the gas at the Xe L-edge (Dos Santos, Conde & Bento 1993). This effect has been found also in previous X–ray satellites, such as *EXOSAT* (White 1985), *Tenma* and Spacelab gas scintillation proportional counters.

1.4.3 Energy resolution

The theoretical limit for the energy resolution of a gas scintillation proportional counter is

$$\frac{\Delta E}{E} = 235 \times \sqrt{F/N}$$

where F is the Fano factor (~ 0.2 for Xenon) and N the number of primary electrons produced by the incident X–ray photon. Given the mean energy required for an electron-ion production in the Xenon gas (about 22 eV), the theoretical limit of the energy resolution is $\sim 6.5\%$ at 6 keV (Ramsey, Austin & Decher 1994). The nominal energy resolution of the MECS is about 8% and reveals no dependence on the position in the central region of the detector gas cell.

1.4.4 Point spread function

The Point Spread Function (PSF) of the MECS is the convolution of the MU PSF and the detector PSF. The precision achieved in the X–ray event localization in the detector is essentially determined by the number of electrons which are liberated by the interaction of the photon with the Xe gas. Therefore the detector PSF is expected to be a Gaussian G(r) with $\sigma \propto E^{-1/2}$, whereas the PSF of the mirror is well described by a generalized Lorentzian L(r). The final PSF (the one which will be taken into account in the following source detection procedure) comes from the convolution of the two.
The probability that a photon of energy E coming from an on-axis source is revealed at a distance within r and r+dr is given by:

$$2\ \pi\ \mathrm{r}\ \mathrm{PSF}_{\mathrm{MECS}}(\mathrm{E,r})\ \mathrm{dr}$$

By imposing that the integral of the PSF over the entire plane be equal to unity, i.e.

$$2\ \pi\ \int_0^\infty \mathrm{PSF(r)}\ \mathrm{r}\ \mathrm{dr} = 1$$

the number of the independent parameters of the Gaussian and Lorentzian functions is reduced to 4, whose dependence on energy can be reproduced through simple algebraic functions.

1.4.5 Effective area

The total MECS effective area, $A_e(E,\theta)$, comes from the MU effective area (A_{MU}), reduced by the plasma protection grid (T_{f1}), the plasma/UV filters (T_{f2}), the Be window (T_w), and the detector efficiency (P_a). A further reduction can derive from the burst length threshold (BLs). The final expression is therefore the following:

$$A_e(E,\theta) = A_{MU,\infty}(E,\theta) \times T_{f1} \times T_{f2}(E) \times T_w(E) \times P_a(E) \times BLs(E).$$

Figure 1.5 and 1.6 show the effective area of the three MECS units and the global effective area as function of energy for different off-axis angles, respectively.

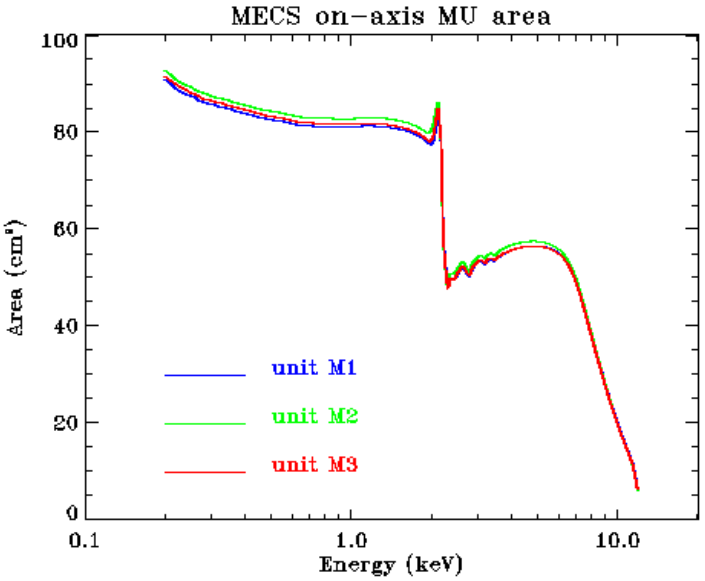

Figure 1.5: The individual effective areas of the three MECS units as function of energy.

The previous equation can be written in a different way:

$$A(E,\theta) = A(E,0) \times V(E,\theta)$$

where A(E,0) is the on-axis effective area and V(E,θ) is the vignetting function, which represents the reduction of the off-axis collecting area due to the shadowing of the inner shells by the outer ones. The vignetting is a steep function of the energy (Fig. 1.7), because the inner mirrors are those reflecting the highest energy photons. Therefore, the reduction in collecting area is higher at higher energies. The vignetting function has been calibrated using on-ground and in-flight data (Cusumano & Mineo 1998). The empirical law for the MECS vignetting function is

$$V(E,\theta) = \frac{1}{a+V_1(E)\times\theta^{V_2(E)}}$$

where $V_1(E)$ and $V_2(E)$ are energy-dependent coefficients.

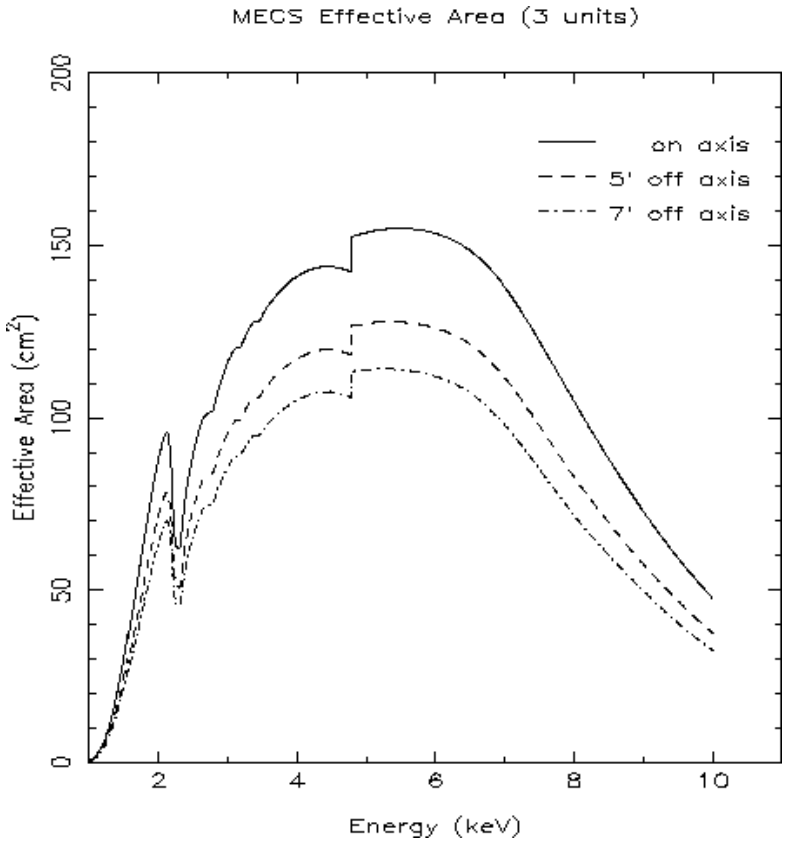

Figure 1.6: The MECS effective area as function of energy for different off-axis angles.

1.5 Instrumental background

In this section, there will be a brief description concerning the instrumental background, whose knowledge is of fundamental importance in the source detection process.

Environmental charged particles, interacting with the gas in the detector cell, lose their energy producing electron clouds, whose dimension is generally bigger than the one generated by the X–ray photons of the same energy, due to the longer path the particles cover before being stopped. A useful way to discriminate genuine photons from charged induced particles is the Burst Length, which is proportional to the cloud dimension.

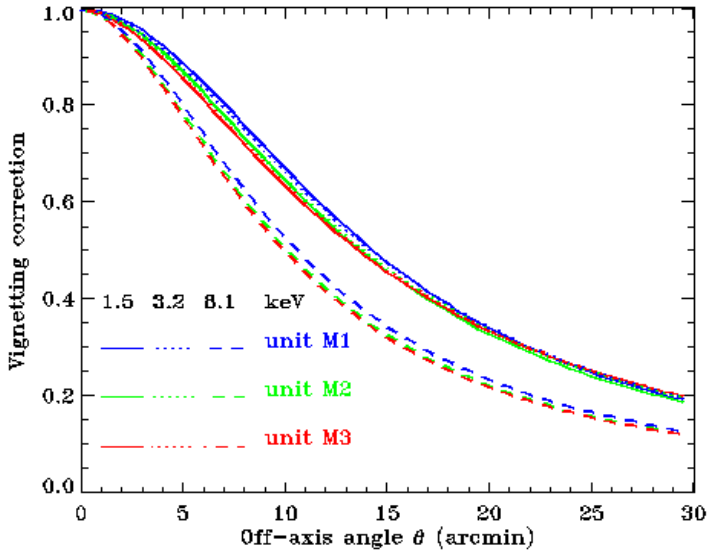

Figure 1.7: The MECS vignetting correction as a function of off-axis angle for the three MECS units, and for three energies (1.5, 3.2 and 8.1 keV).

The instrumental background is constituted by a number of different components (Chiappetti et al. 1998):
(a) the noise of the photo-multiplier, which is different in each MECS unit, but is present only for channels below 25;
(b) a continuum appearing as a plateau at energies below 4 keV, and another at a higher level at energies greater than 4.5 keV;
(c) an instrumental feature appearing as a line-like between 4 and 4.5 keV;
(d) a line feature peaked around the calibration source (^{55}Fe) energy (5.9 keV), spatially modulated and broader than the energy resolution;
(e) some weak line features below 4 keV, maybe due to the Sun albedo or to the atmospheric fluorescence (the Ar line).

A tentative modeling of the instrumental components of the background has been developed by Chiappetti et al. (1998). However, all the above described features have been taken into account in the source detection, by selecting that set of satellite parameters capable of minimizing their effect on the X–ray data.

The HELLAS:
source detection and technical related issues.
The 5–10 keV LogN–LogS

2.1 Introduction: scientific purposes

The study of hard X–ray sources should allow to provide reliable constraints on both the unified schemes and the AGNs synthesis models for the XRB. According to these models, a large fraction of the 2–100 keV XRB energy density is due to the integrated contributions of AGNs characterized by a broad distribution of luminosities and column densities (Setti & Woltjer 1989; Matt & Fabian 1994; Comastri et al. 1995 [C95]; Madau, Ghisellini & Fabian 1995; Wilman & Fabian 1999). The population of obscured objects strongly emerges in the hard X–ray regime, since the soft X–rays are highly suppressed by photoelectric absorption.

In this regard, hard X–ray observations are extremely efficient in tracing the emission due to accretion processes, like the ones working in active galactic nuclei. Moreover, the hard X–ray selection is less affected by strong biases than other wavelengths. As a matter of fact, soft X–ray selection is strongly biased towards unabsorbed (or mildly obscured) objects (a column density of the order of 10^{22} cm^{-2} reduces the nuclear emission below 2 keV by a factor of 100, while it has a negligible effect at energies higher than 4—5 keV). Optical and UV selection is biased against objects with even modest extinction or an intrinsically "red" spectrum (see e.g. Vignali et al. 2000a; Maiolino

et al. 2000). Therefore, in order to study the space density and evolutionary properties of the sources responsible for the HXRB, the **HELLAS** (**H**igh **E**nergy **LL**arge **A**rea **S**urvey) survey was carried out in the 5–10 keV band, taking full advantage of the large field of view and relatively high sensitivity and spatial resolution of the *BeppoSAX* MECS (Boella et al. 1997a,b). Moreover, this band is closest to the maximum of the XRB energy density reachable with existing X–ray imaging instruments. Even though *Chandra* and *XMM-Newton* go much deeper than *BeppoSAX* at low energies, in the 5–10 keV band the MECS collecting area is comparable to that of *Chandra* ACIS. Furthermore, the MECS field of view (about 25 arcmin radius) is about a factor 7 larger than that of *Chandra* ACIS-I (one chip) and about a factor 3 larger than that of the *XMM-Newton* EPIC PN. The large field of view of *BeppoSAX* MECS allows to cover a portion of sky considerably larger that the one which will be surveyed by *Chandra* and *XMM-Newton* in the next few years, at the expense of a lower sensitivity. The principal scientific goal of the HELLAS is therefore the study of the nature of the hard X–ray sources populations along with their evolutionary and spectral properties at relatively bright fluxes but over a large area of the sky. *Chandra* and *XMM-Newton* follow-up observations of these sources should be able to provide a detailed analysis of the source physics (through the X–ray spectral properties, such as the spectral slope, the absorbing column density and the iron Kα emission line parameters), thus fully unveiling the nature of the sources responsible for a fraction of the XRB. It will be also possible, for the first time, a statistical approach to the study of the distribution and evolution of the obscuring gas in a hard X–ray selected sample. In this regard, *BeppoSAX* HELLAS can be considered fully complementary to the deeper, pencil-beam *Chandra* and *XMM-Newton* surveys.

2.2 The HELLAS

The HELLAS has been performed in the 4.5–10 keV energy range for several reasons:

• this is the band closest to the maximum of the XRB energy density (at 5–10 keV it is about 3 times higher than at 1 keV) which was reachable with imaging X–ray satellites.

OFF-AXIS ANGLE	POWER RADIUS
$< 7'$	$1.'2$
$7' < R_{\rm off} < 18.'8$	$1.'65$
$18.'8 < R_{\rm off} < 24.'5$	$2.'2$

Table 2.1: *BeppoSAX* MECS PSF for different off-axis angles.

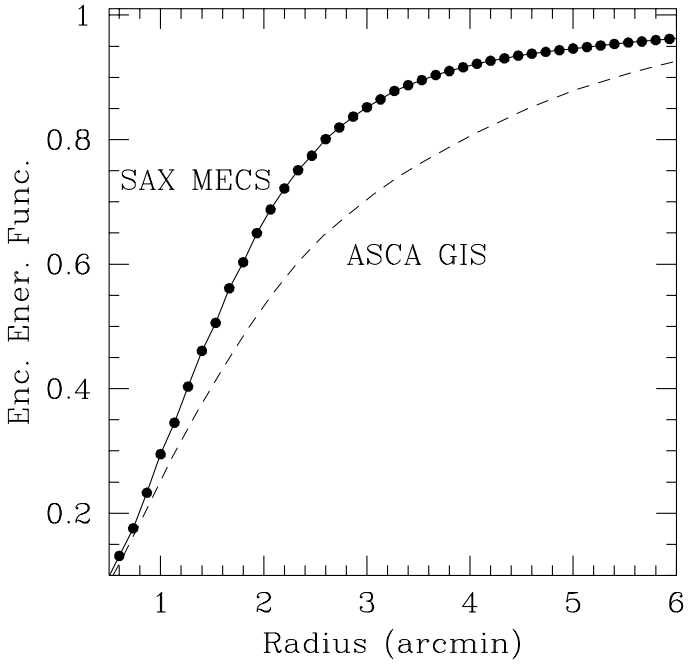

Figure 2.1: Encircled energy function for *BeppoSAX* MECS and *ASCA* GIS instruments.

• The BeppoSAX MECS (Boella et al. 1997b) point spread function (PSF, see chapter 1 and Table 2.1) greatly improves with energy: in the hard 4.5–10 keV energy range it is a factor ~ 2 sharper than in the softer 1.5–4.5 band, thus providing a 95 % error radius of about 1 arcmin (see Ricci, Fiore & Giommi 1998; Fiore et al. 2000a). This results in a

faster optical identification of the sources with respect to *ASCA* surveys (Della Ceca et al. 1999; Akiyama et al. 2000). For comparison, Fig. 2.1 shows the PSF of *ASCA* gas scintillation spectrometers (GIS) and that of *BeppoSAX* MECS in the full band covered by the two satellites: it appears evident that MECS performances are higher than those of GIS on board *ASCA*.

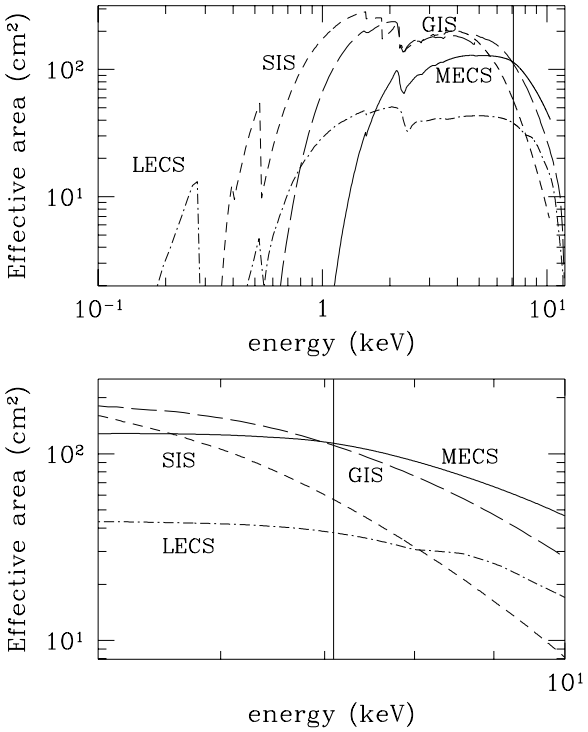

Figure 2.2: Effective areas of *BeppoSAX* MECS and LECS instruments vs. SIS and GIS detectors on board *ASCA*. The lower panel displays the difference in the effective area which becomes evident at energies higher than 7 keV.

• MECS provides a good sensitivity up to 10 keV (about 100 cm^{-2} and 50 cm^{-2} at 7 and 10 keV, respectively), larger than *ASCA* GIS (see Fig. 2.2).

• As previously described, *BeppoSAX* MECS field of view (about 0.7

square degrees/pointing) allows a good coverage of the X–ray sky.

• The on-axis MECS background (internal, see chapter 1, plus 70% cosmic XRB) is $\sim 4.3 \times 10^{-3}$ counts s^{-1} $arcmin^{-2}$ (3 MECS units) in the 4.5–10 keV band, whereas it is 3.0×10^{-3} counts s^{-1} $arcmin^{-2}$ in the softer 1.3–4.5 keV energy range. As a consequence, using only the higher energy band reduces the total background by about 40 %, thus the probability of detecting faint, probably highly-obscured or hard X–ray sources is enhanced.

About 85 square degrees of sky have been surveyed in the 4.5–10 keV energy range using 142 independent *BeppoSAX* MECS high Galactic latitude ($|b| > 20°$) fields. Fields have been selected among public data (as March 1999) and among the data belonging to the group I collaborate with. When multiple observations of the same field were available, they have been merged in order to increase the sensitivity. Fields centered on bright extended sources and bright Galactic sources have been discarded, as well as those fields close to the Magellanic Clouds and M 33.

The distribution of the exposure times is showed in Fig. 2.3. Most of the fields have exposures between 30 and 100 ks, and twenty fields have an exposure longer than 80 ks.

2.2.1 Source detection

A robust detection algorithm (described below) has been used in MECS1 + MECS2 + MECS3 co-added images (or MECS1 + MECS2 images after the loss of MECS1 on May 7th 1997). The detection was run in the images accumulated between channels 97 and 213, i.e. in the 4.5–10 keV band. The choice of including the Xenon L edges in the detection range is due to the absence of linearity in the channel-energy relationship across the edge. The analysis was performed on cleaned and linearized event MECS event files available in the *BeppoSAX* Science Data Center (SDC) on-line archive, by applying standard screening criteria (Fiore, Guainazzi & Grandi 1999), due to the low and stable MECS background.

The detection algorithm is a variation of the DETECT routine included in the XIMAGE software package (Giommi et al. 1991). The detection method is as follows:

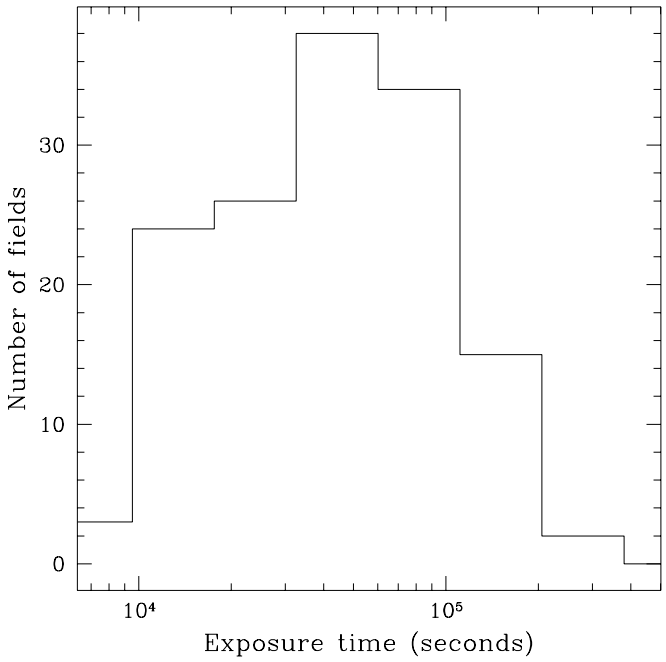

Figure 2.3: The distribution of the net exposure times in the 142 HELLAS fields.

the X–ray image is first convolved with a wavelet function, in order to smooth the image and increase the contrast.

Then a standard slide-cell detection method is run on the smoothed image, to locate the count excesses above the local background.

In order to interactively check and verify the results obtained in the detection procedure, the algorithm has been run several times with different choices of both the slide-cell size (ranging from 48 to 120 arcsec) and the width of the wavelet function (24-120 arcsec), with the aim of **(a)** taking into account the variation of the MECS PSF with the off-axis angle, **(b)** avoiding source confusion (when possible) and **(c)** detecting efficiently extended sources (such as clusters and some

Seyfert galaxies).

The detection procedure was performed independently by F. Fiore and myself, by varying the above discussed parameters and by checking step by step the results. In particular, extreme attention was paid to the sources detected near the so-called MECS "calibration sources" (described in chapter 1). Their effect is such to enhance the 5.5–6.5 keV background in the nearby regions. For these sources the detection algorithm was run also by excluding the channel interval 125–135. Nevertheless, the number of sources detected near the calibration sources regions, even after the exclusion of these channels, was undoubtedly too high to belong to a random distribution across the MECS field of view. Therefore a more sophisticated check was applied to the data, in order to correct the count rates obtained for some of the dubious sources. It consists in calculating the ratio between the 4.5–10 keV and the 5.8–6.3 keV (i.e. channels 125–135) count rates for some of the sources in the MECS field of view, from the center (target) to those in the outer detector. A conservative threshold of 2 was then applied to this ratio in order to exclude presumably spurious sources, while the remaining dubious sources have been corrected by re-normalizing their 4.5–10 keV count rates to the average 4.5–10 keV/5.8–6.3 keV ratio of the sources analyzed in the same field of view. The distribution of the HELLAS sources in the MECS focal plane is showed in Fig. 2.4. There appears no evident concentration of sources in the outer regions of the detector.

The final net counts have been estimated by the original unsmoothed image, in order to preserve Poissonian statistics. The background is evaluated using ten source-free boxes nearby the source region and is rescaled to the source position to take into account for any spatial variation of the MECS background (as described in the guide, available at http://www.sdc.asi.it.software/cookbook, and in Chiappetti et al. 1998). The size of the box used for flux estimates is such maximize the signal-to-noise ratio given the local background, the source intensity and the local PSF.

At the end of the detection procedure, a total of 175 sources (excluded the targets of the observations) have been detected in the 4.5–10 keV energy range, with the faintest source having a flux of 3.6 $\times$ 10^{-14} erg cm^{-2} s^{-1}. The probability that they are not a poissonian fluctuation of the background has been assumed to be higher than 99.94

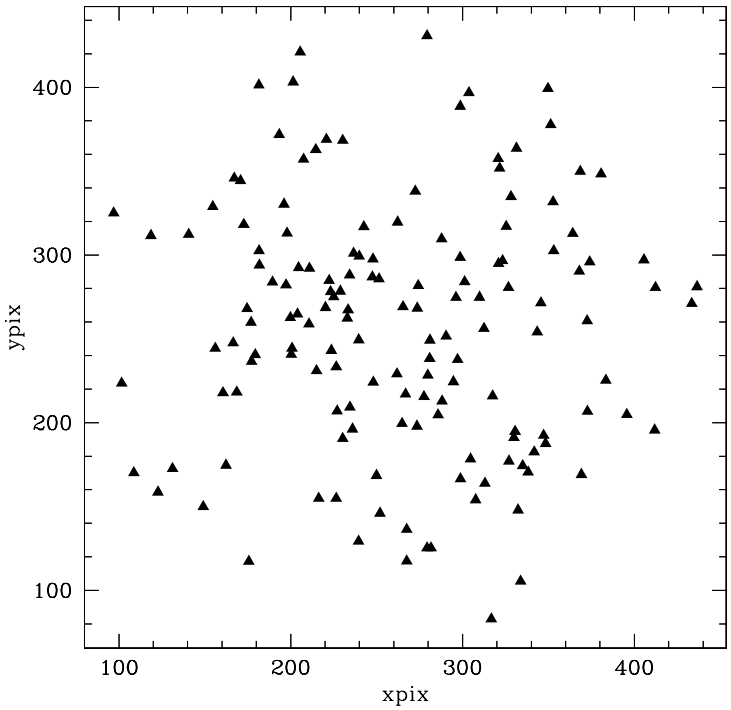

Figure 2.4: The distribution of the HELLAS sources in detector coordinates.

%, corresponding to a signal-to-noise ratio greater than ~ 3 (the exact value depending highly on the background level).

2.2.2 Count rate to flux conversion

Source count rates were accumulated in four bands:

T: TOTAL = **1.3–10 keV**

L: LOW BAND = **1.3–2.5 keV**

M: MEDIUM BAND = **2.5–4.5 keV**

H: HARD BAND = **4.5–10 keV**

The H band is the band covered by the HELLAS (i.e. that of the source detection). Counts in the L and M bands have been calculated around the centroid of the detection in the H band.

The count rates were corrected for the energy-dependent vignetting (see chapter 1), which was calibrated in orbit using several observation of the Crab nebula at different off-axis angles (Conti et al. 1997; Cusumano & Mineo 1998). The counts were also corrected for the position-dependence of the PSF, which was calibrated using an analytical approximation calibrated on ground and verified in orbit through pointed observations of Galactic compact sources and AGNs (Conti et al. 1997). All the corrections were made easier by the axis-symmetry of the PSF even at large off-axis angles.

For the faint sources (i.e. the sources having a signal-to-noise ratio < 4) all the corrections were applied at 6.4 keV, close to the mean energy for a power law spectrum with a slope $\Gamma = 1.6$. On the contrary, for the brighter sources the corrections were applied after convolving the energy- and position-dependent vignetting and PSF with the histogram of each source counts in the L, M and H bands (defined above).

The count rates were converted into fluxes using a fixed conversion factor, i.e. 7.8×10^{-11} erg cm^{-2} s^{-1} (5–10 keV) per one "3 MECS count" (4.5–10 keV). This factor is appropriate for a power law spectrum with a spectral slope $\Gamma = 1.6$. However, the conversion factor seems to change very little under different assumptions of the X–ray slope spectral index. In fact, it is 8.1×10^{-11} erg cm^{-2} s^{-1} and 7.6×10^{-11} erg cm^{-2} s^{-1} for $\Gamma = 1.4$ and $\Gamma = 1.8$, respectively. By assuming a power law spectrum with $\Gamma = 1.8$ (representative of the spectrum of the AGNs in the hard energy range, see Nandra et al. 1997) with $N_{\rm H} = 1,\ 10,\ 100 \times 10^{22}$ cm^{-2}, the conversion factor becomes 7.6, 8.1 and 11.3×10^{-11} erg cm^{-2} s^{-1}, respectively. In other words, the 5–10 keV fluxes are affected by X–ray absorption for column densities of the order (or greater) of 10^{23} cm^{-2}. For sources detected under the 550 μm Beryllium strongback (as described in chapter 1) a conversion factor of 9.9×10^{-11} erg cm^{-2} s^{-1} was applied to the counts, in order to account for the reduced detector sensitivity beneath the window support structure.

2.2.3 Sky coverage

In order to derive the sky coverage, the count rates as a function of the off-axis angle have been computed (see Fig. 2.5). Solid points

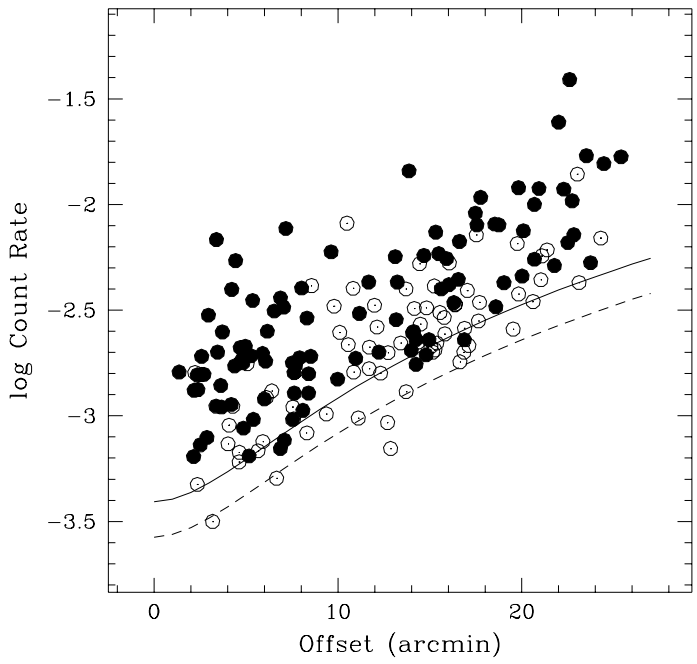

Figure 2.5: MECS count rate as a function of the off-axis angle. Solid points are from observations performed with 3 MECS units, while open circles indicate the ones performed with only 2 units. The solid (dashed) model line shows the minimum count rate detectable at the given threshold of 99.40 % for an exposure time of 100 ks in 2 (3) MECS units.

indicate the observations performed with the 3 MECS units, while the others (open circles) are related to 2 MECS units observations. The two model line (solid and dashed) represent the minimum detectable count rate achievable for an exposure time of 100 ks in 2 and 3 MECS units, respectively, at the given threshold applied to the whole survey (99.94 %). These model lines have been obtained using the latest in-flight calibrations of the telescope vignetting, of the background

(and its dependence on the position in the detector) and that of the Beryllium strongback. Their normalization are the results of extensive simulations, which have been performed for the whole survey assuming the *ASCA* 2–10 keV LogN-LogS (from Cagnoni, Della Ceca & Maccacaro 1998), a distribution of spectral shapes and the position of the HELLAS sources in the detector plane.

Then the sky coverage of the simulated survey has been computed by inverting the model curves and was adjusted until the input LogN-LogS was fully reproduced from the simulations. The adopted value for

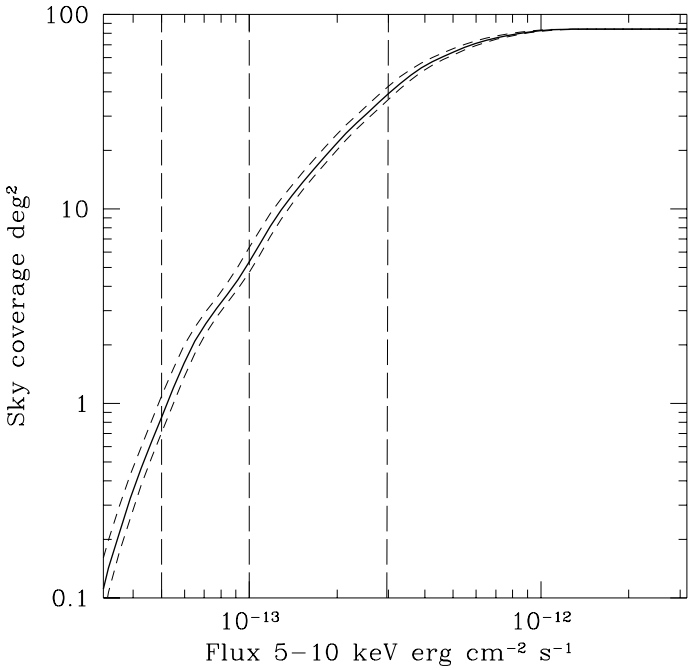

Figure 2.6: The HELLAS sky coverage for three different assumptions of the source spectral slope: $\Gamma = 1.6$ (solid line), $\Gamma = 1.2$ (lower dashed line) and $\Gamma = 2.0$ (upper dashed line).

the on-axis flux limit is $3 \times 10^{-14} \sqrt{(100/T(ks))}$ erg cm^{-2} s^{-1} (3 MECS units). At off-axis angles of 6 and 15 arcmin the flux limit becomes of the order of $5 \times 10^{-14} \sqrt{(100/T(ks))}$ and $1.5 \times 10^{-13} \sqrt{(100/T(ks))}$

erg cm^{-2} s^{-1}, respectively. This is caused by the vignetting: at large off-axis angles, only the bright sources can be detected, due to the rapidly decreasing effective area.

Fig. 2.6 shows the sky coverage, computed under different assumptions for the source spectral slopes: $\Gamma = 1.6$ (solid line), $\Gamma = 1.2$ (lower dashed line) and $\Gamma = 2.0$ (upper dashed line). Regions of 4, 6 and 8 arcmin around bright targets have been excluded from the sky coverage computation, as well as the sources detected in these regions. This radius has been calculated by imposing that the target count rate per square arcmin at a given off-axis angle was less than half of the local MECS background. In the same time, also those sources with a count rates smaller than that derived from the model curves in Fig. 2.5 (and normalized to the observation exposure time) have been excluded from the sample.

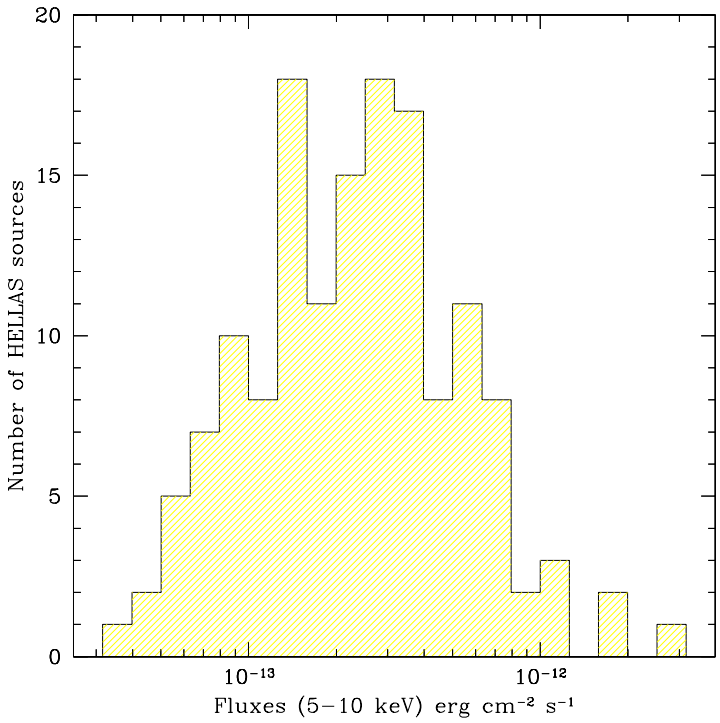

Figure 2.7: The flux distribution of the HELLAS sources in the 5–10 keV band.

The final number of hard X–ray detected sources is 147. Their flux distribution is showed in Fig. 2.7.

2.3 Parameters uncertainties

2.3.1 Flux and sky coverage uncertainties

The MECS flux was calibrated using several observations of the Crab nebula performed during the various years of *BeppoSAX* life. Assuming a power-law model to fit the Crab X–ray spectrum, the slope results to be $\Gamma = 2.088 \pm 0.002$ and the 2–10 keV flux $2.008 \pm 0.006 \times 10^{-8}$ erg cm^{-2} s^{-1}, with little differences between the repeated observations (Sacco 1999). As a consequence, since the MECS flux calibration appears stable in time, the main uncertainties on both the flux and the sky coverage derive from the unknown spectrum of the sources near the detection limit. This uncertainty has been evaluated by assuming different spectral slopes in computing the sky coverage, as described in the previous section (see also Fig. 2.6).

2.3.2 Source confusion

Source confusion is known to affect the data characterized by limited spatial resolution, which is the case of *BeppoSAX* MECS. In order to quantify the effect of source confusion on the following results, mainly on the LogN-LogS, the number of sources which are expected at the 5–10 keV flux of 2.5–5–10 $\times 10^{-14}$ erg cm^{-2} s^{-1} on the basis of the 2–10 keV ASCA LogN-LogS (Cagnoni et al. 1998; Ueda et al. 1998), converted to the HELLAS band, has been computed. 60, 20 and 7 sources per square degree, respectively, are expected. The probability of finding two sources with comparable fluxes equal to the above values within a box whose dimension is twice the typical slide-cell (i.e. 2–4 arcmin, depending on the source flux: faint sources can be detected only in the inner region of the detector, due to the vignetting, thus requiring a small cell to be detected) is 0.4, 0.05 and 0.1 % at these fluxes, respectively. The fraction of confused sources near the detection limit and in correspondence of the maximum of the flux distribution (most of the HELLAS sources have 5–10 keV fluxes of the order of 2–4 $\times 10^{-13}$ erg cm^{-2} s^{-1}, see Fig. 2.7) is estimated to be about 7–8 %.

An alternative check to estimate the fraction of confused sources with respect to the total has been performed by directly look at the spatial extension of the sources. Even though the MECS PSF is not the most suitable for this kind of analysis, about 20 sources for which there exists an indication of extension have been found, covering the full range of 5–10 keV fluxes. Among them, 6 clusters have been found, and some more objects can be extended too (e.g. nearby Seyfert galaxies, small groups of galaxies).

2.3.3 Spurious sources

Even though the source identification process will be discussed in chapter 6, it is useful to estimate the number or spurious sources starting from the source detection algorithm itself. Given a detection probability threshold P, the number of spurious sources is (1−P) × the number of independent (not overlapping) cells in the sky covered near a given flux limit. In the HELLAS the sensitivity is strongly dependent on the off-axis angle, as clearly evident in Fig. 2.5. In other word, a bright source can be near the flux limit for a typical exposure time at the edge of the detector, whereas the same source will be easily detected in the inner regions (or, better, on-axis). In this regard, the area of the extraction cell is a function of the off-axis angle, since also the PSF degradation with off-axis must be taken into account. In the inner part of the MECS (i.e. for typical off-axis angles lower than 8 arcmin) the area of the cell is about 0.004–0.005 square degrees, whereas at larger (> 16 arcmin) off-axis angles the extraction region is about 0.007–0.012 deg^2. At $F_{\rm X} = 5$–7×10^{-14} erg cm^{-2} s^{-1} the sky coverage is about 1–3 deg^2 and the typical extraction cell size is 0.004–0.005 deg^2. Therefore the number of spurious sources detected at the flux limit is about 0.15 and 0.45, respectively. At brighter fluxes, i.e. $F_{\rm X} = 5 \times 10^{-13}$ – 10^{-12} erg cm^{-2} s^{-1}, the sky coverage is about 65 and 84 squared degrees, respectively. Given the typical extraction cells at these fluxes, 0.007 (0.012) deg^2, the number of spurious sources is of the order of 5.7 (3.3) and 7.3 (4.3), respectively. Since the flux distribution of the HELLAS sources peaks at about 2–3 $\times 10^{-13}$ erg cm^{-2} s^{-1}, a reliable estimation of the number of spurious sources is about 7–8 %, which has been confirmed by simulations.

2.4 Position accuracy: causes and corrections

Several are the causes of the uncertainties in the location of an X–ray source by *BeppoSAX* MECS, the main being **(A)** the width of the MECS PSF, **(B)** the statistical uncertainty concerning the centroid of the photons distribution (especially in the low-statistics regime) and **(C)** the systematic errors in telescope pointing position reconstruction.

A *The width of the MECS PSF*

In the 4.5–10 keV band about half of the counts from an X–ray source is collected within a radius of 1.0–1.2 arcmin. For bright sources the uncertainty on the source centroid due to the PSF is about 13 arcsec (1 σ), which has been derived by multiple observations of the Galactic X–ray source LMC X-3 performed during the Science Verification Phase (SVP).

B *The statistical uncertainty on the centroid*

The second uncertainty is due to the problems in the determination of the centroid of a photons distribution when their number is relatively low. The minimum number of counts in an HELLAS source is about 30, against about 100 background counts. In these unfavorable situations (i.e. background-dominated sources) the statistical uncertainty on the source centroid is about 30–40 arcsec.

C *Systematic errors in telescope pointing position reconstruction*

These uncertainties represent the most relevant source of errors in the position localization of an X–ray source in *BeppoSAX* MECS. The magnitude of the implied errors can change from field to field.

The main sources of systematic errors are:

(1) the unavailability of the "z" star-tracker (the one which is co-aligned with the X–ray telescopes) for the whole observation. It happened in about 10 % of the observations. In these unlucky cases, the final error on the pointing position reconstruction can be as high as 2 arcmin;

(2) the unavailability of the "z" star-tracker for a part of each orbit. This causes "jumps" in the attitude reconstruction when the control is moved from one star-tracker to another. These "jumps" are caused by a non perfect calibration of the misalignment between the three star-trackers. In summer 1997 a 20 arcsec error in the on-board calibration of this misalignment was discovered, and then corrected in the on-board software in May 1999;

(3) uncertainties in the alignment of the X–ray telescopes with the satellite axis (and, as a consequence, with the star-trackers);

(4) since from August 1997 *BeppoSAX* is operating with only 1 gyroscope, for part of each orbit the satellite is controlled by one star-tracker and one gyro. All those configurations involving the "y" and the "-x" star-trackers plus the gyro produce a pointing accuracy worst than the configuration which includes simultaneously the 'y" and the "-x" star-trackers in the control loop. The best configuration being that in which the "z" star-tracker is in the control loop.

Just to understand the above discussed fonts of uncertainties in the position reconstruction, in Fig. 2.8 the deviations in right ascension (RA) and declination (DEC) between the *BeppoSAX* MECS positions and the optical (or radio) ones for a sample of about one hundred AGNs (targets or objects serendipitously found in some of the HELLAS fields) are plotted.

It is evident that the median deviation in DEC is zero. On the contrary, MECS RA are systematically smaller than RA found in catalogs by about 15 arcsec. The figure clearly shows that the typical error on the position is between 1 and 1.5 arcmin, when the "z" star-tracker is not in the control loop. Different errors are implied when the off-axis angle is higher. In fact, the radii encompassing 67 % and 90 % of the 79 sources observed with the "z" star-tracker and at off-axis angles < 3 arcmin are 43 and 56 arcsec, respectively.

This is the result of the relatively good PSF in the inner part of the MECS. When considering off-axis angles spanning from 7 to 23 arcmin, the above values become 63 and 85 arcsec, respectively,

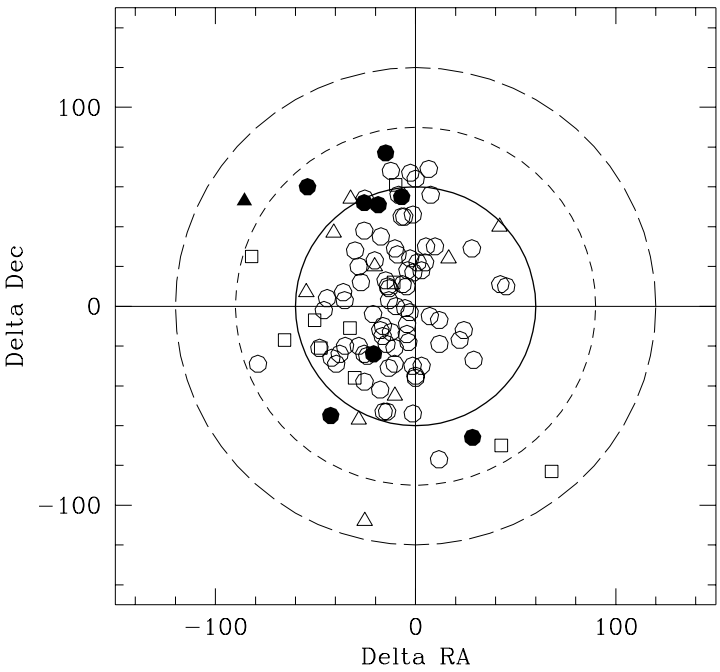

Figure 2.8: The deviations in RA and DEC between MECS positions and catalog positions for a sample of about one hundred AGNs (targets or sources serendipitously found in the HELLAS). The symbols indicate different conditions under which the observations were performed.
Filled symbols: sources observed without the "z" star-tracker in the control loop.
Open symbols: objects observed using (almost for a part of the observation) the "z" star-tracker.
Circles: sources detected at off-axis angles < 3 arcmin.
Squares: sources detected at off-axis angles $7 < R < 15$.
Triangles: sources detected at off-axis angles > 15 arcmin.
The three circles have radii of 1, 1.5 and 2 arcmin, respectively.

due to the MECS PSF degradation and to the presence of sources partially covered by the strongback supporting the MECS Beryllium window. Since at least half of the detected deviations in RA is ought to systematic errors in the position reconstruction, the sky position of

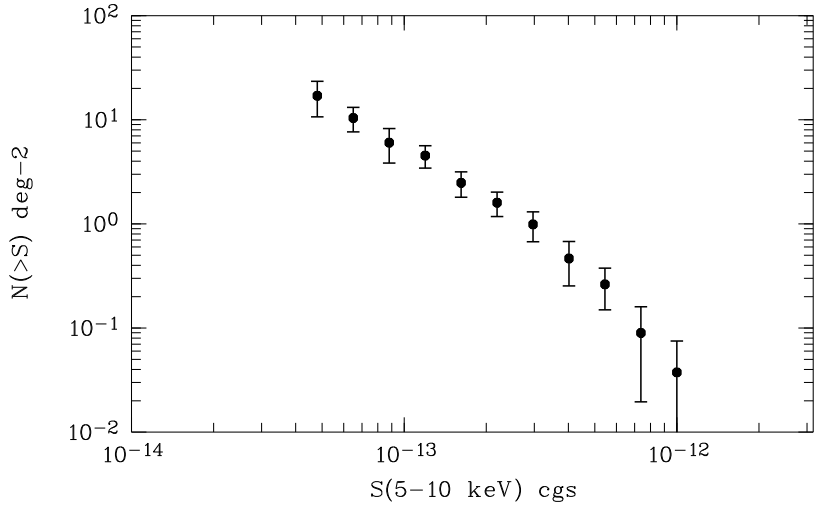

Figure 2.9: The HELLAS 5–10 keV LogN–LogS. The error bars include both 1 σ statistical interval and systematic uncertainties.

serendipitous sources in fields with a relatively bright target has been improved by applying a simple boresight correction. This consists in searching for identified sources (other than the HELLAS sources) in the MECS field of view (including the target, if bright enough) and then computing the best correction in right ascension and declination in order to well reproduce the sky positions of the identified objects. This correction cannot be applied to the errors related to the "roll" angle, because of the misalignment between the three star-trackers (discussed above). Anyway, this kind of errors is generally rather small.

2.5 The integral LogN–LogS

Fig. 2.9 presents the integral 5–10 keV LogN–LogS for the entire HELLAS sample assuming a power law with $\Gamma = 1.6$. The displayed errors include both statistical errors (at 1 σ confidence) and systematic uncertainties, mainly due to the lack of knowledge of the real spectrum of the faint sources (for which a photon index in the range 1.2–2.0 has been assumed). The best-fit power-law index at fluxes below 4 $\times$

10^{-13} erg cm^{-2} s^{-1} is q = -1.56 ± 0.14 (0.34), The normalization of the best-fit power law is 2.75×10^{-20} deg^{-2}. Above $\sim 4 \times 10^{-13}$ erg cm^{-2} s^{-1} the LogN–LogS curve significantly steepens, but this is probably a selection effect. In fact, the probability of finding a bright source near a relatively bright target is low, therefore the number of bright sources in a serendipitous survey like HELLAS is underestimated.

Several are the biases which may affect the shape of the LogN–LogS. The most important are:

(a) The Eddington Bias

Sources characterized by fluxes just below the flux limit can enter the survey owing to positive error fluctuations. This results in a steepening of the derived LogN–LogS.

This bias has probably a negligible effect on the present survey. Indeed the HELLAS, as being the result of a combination of observations with quite varied sensitivity (because of the different exposure times of the pointings and the large decrease of the sensitivity with the off-axis angle), should be poorly altered by this bias. Moreover, the flux limit changes from observation to observation, and in each field from on-axis positions to off-axis positions. Being this the case, the Eddington bias (Eddington 1940) should modify little the shape of the integral LogN–LogS, but its normalization could be enhanced artificially (Marshall 1985). In order to check and eventually quantify the influence of this bias on the final LogN–LogS, extensive simulations have been used to compute the sky coverage and to build the LogN–LogS. In these simulations, the flux limits (which are exposure- and off-axis–dependent) have been chosen in such a way to reproduce the input LogN–LogS. Simulations represent a good approach also in order to take care for the other biases which could affect the present survey.

(b) "Under-threshold" Bias

Two sources having about half of the flux limit can be detected in the same resolution element as a single brighter source. This produces a steepening of the LogN–LogS.

(c) Source Confusion

Two sources above the flux limit appear confused due to the MECS PSF. This bias produces a flattening of the LogN–LogS.

The points (b) and (c) have been widely discussed in the source confusion section. Their effect on the LogN–LogS shape and normalization should be very low.

2.6 The XRB model

Recently, the AGNs synthesis models for the XRB have been subjected to a renewed attention (Gilli, Risaliti & Salvati 1999; Wilman & Fabian 1999; Pompilio, La Franca & Matt 2000; Gilli, Salvati & Hasinger 2001) due to the increasing amount of observational data concerning both the XRB spectral intensity and the source counts in several energy ranges obtained by *ROSAT* , *ASCA* and *BeppoSAX* surveys (Lehmann et al. 2000; Akiyama et al. 2000; Fiore et al. 2000a). Further hints to a detailed modeling of the XRB have followed the first *Chandra* deep surveys (Mushotzky et al. 2000; Giacconi et al. 2001) and subsequent optical follow-up identifications. Even though a large fraction of the XRB spectral intensity and the source counts are fairly well reproduced by AGNs synthesis models (see Comastri 2000 for a review on the different approaches to this problem), a coherent self–consistent description of the XRB constituents has yet to be reached as most of its ingredients have to be extrapolated well beyond the present limits. Therefore, much stronger constraints are expected from the ongoing and future *Chandra* and XMM–*Newton* surveys.

The implications deriving from the 5–10 keV HELLAS LogN-LogS to the XRB modeling will be briefly described in the following. A full description can be found in Comastri et al. (2001).

For the present purposes, the C95 model is adopted, with a few variations and improvements. The spectrum of heavily absorbed AGNs (Compton-thick, i.e. $N_{\rm H} > 10^{24}$ cm^{-2}) is now computed taking into account Compton scattering effects by means of a Montecarlo code (Matt, Pompilio & La Franca 1999). The luminosity evolution, parameterized with the power-law model $L(z) = L(z=0) \times (1+z)^{2.6}$, stops at $z_{cut} = 1.8$, then remaining constant up to z_{max}=3. The choice

of these parameters is consistent with the more recent estimates of the high-redshift AGNs evolution and also finds observational support from the first *Chandra* measurements.

The input AGNs spectra, including the division in the $N_{\rm H}$ classes centered at Log$N_{\rm H}$ = 21.5, 22.5, 23.5, 24.5 cm^{-2}, are as described in C95, while the absorption distribution of obscured AGNs in the four $N_{\rm H}$ classes normalized to the space density of unobscured AGNs turns out to be 0.35, 1.5, 2.3, 2.0, which are slightly different from those reported previously by C95, due to the change of some input parameters and to the intensity of the *ASCA* 1–8 keV XRB spectrum, which is to be fitted by the model. The choice of the *ASCA* XRB spectrum is due to the large (about 30–40 %) discrepancy between *BeppoSAX* (Vecchi et al. 1999) and *HEAO–A2* (Marshall et al. 1980) XRB normalization, the former being higher, whereas *ASCA* normalization settles in the middle.

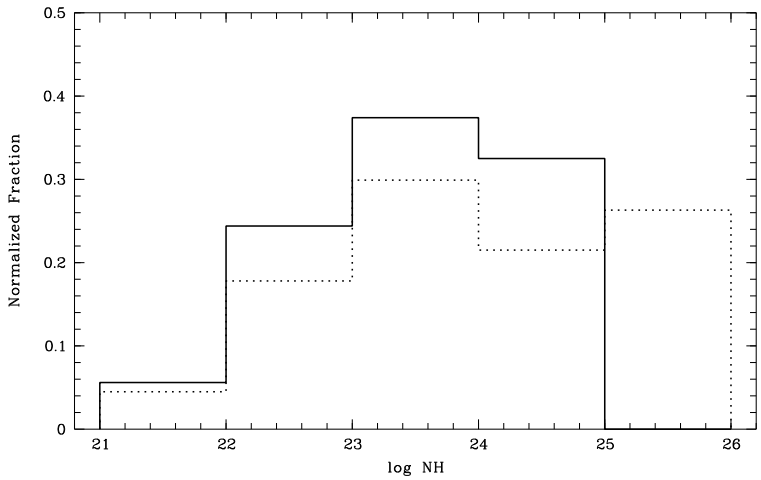

Figure 2.10: The model absorption distribution (solid line) compared with the observed $N_{\rm H}$ distribution for a sample of nearby Seyfert 2 galaxies (Risaliti et al. 1999). The two histograms are renormalized to the same ratio between obscured and unobscured objects.

The best-fit absorption distribution (Fig. 2.10) is in agreement

with that obtained by Risaliti, Maiolino & Salvati (1999) for the local Universe, the peak in both being in the $\mathrm{LogN_H} = 23$–24 $\mathrm{cm^{-2}}$ bin, with about 70–80 % of the objects lying in the $\mathrm{LogN_H} > 23$ $\mathrm{cm^{-2}}$ region. As a consequence, the large fraction of heavily obscured objects needed to fit the XRB spectral intensity is consistent with the absorption distribution of Seyfert 2 galaxies in the local Universe.

Compton-thick sources with column densities in excess to 10^{25} $\mathrm{cm^{-2}}$ are not included in the present model, as their contribution to the XRB is never energetically dominant (see e.g. Gilli et al. 1999), even though they could constitute a sizeable fraction of the obscured AGNs population.

2.7 The HELLAS LogN-LogS compared with model predictions

Fig. 2.11 shows the HELLAS 5–10 keV integral LogN-LogS previously described, with the 5–10 keV counts predicted by the present XRB model. The solid thick line includes the contributions from both AGNs and clusters of galaxies. The expected number counts relation for clusters has been computed assuming an average temperature kT = 6 keV and the local luminosity function of Piccinotti et al. (1982), with no evolution. However, as clearly visible in Fig. 2.11, clusters do provide a minor contribution to the 5–10 keV fluxes sampled by *BeppoSAX* .

The predicted hard X–ray counts are also consistent with the recent XMM–*Newton* observations in the Lockman hole, which reach 5–10 keV fluxes about an order of magnitude fainter (Hasinger et al. 2001).

The expectations of the same model are also compared with a compilation of number counts in the 2–10 keV band (Fig. 2.12) from *BeppoSAX* (Giommi et al. 2000), *ASCA* (Ueda et al. 1999a; Della Ceca et al. 1999) and Chandra (Mushotzky et al. 2000; Giacconi et al. 2001) surveys. A good agreement between model predictions and observations is obtained with the *BeppoSAX* and *ASCA* 2–10 keV number counts, and with the Mushotzky et al. (2000) *Chandra* counts, while the measurements of Giacconi et al. (2001) are slightly over-predicted.

The key parameter of all the XRB models is the space density of

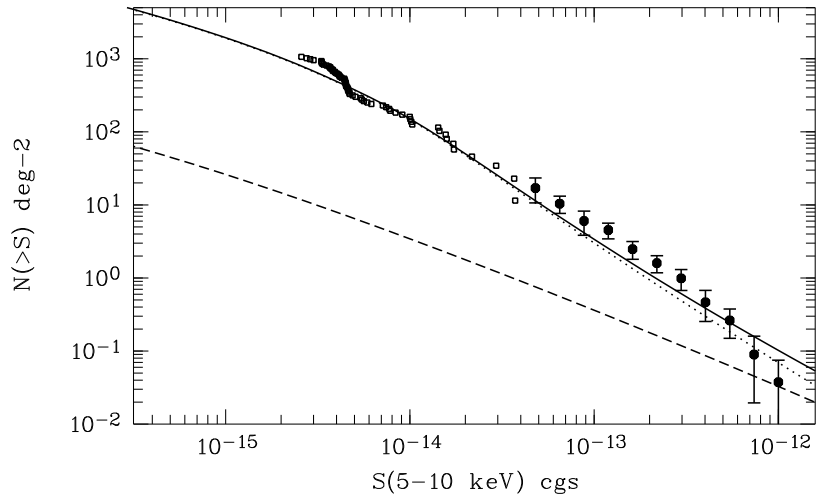

Figure 2.11: The HELLAS 5–10 keV integral LogN-LogS. Thick line = total (AGNs+clusters) 5–10 keV counts predicted by the present XRB synthesis model; dotted line = AGNs only; dashed line = clusters only.

obscured AGNs and their absorption distribution. The obscured-to-unobscured ratio is usually fixed to the value measured for samples of nearby (often optically–selected) Type 1 and 2 Seyfert galaxies. In the present model, this ratio is obtained by the XRB fitting procedure (see Fig. 2.10), therefore it depends upon the choice of the column density adopted to divide absorbed from unabsorbed objects. The obscured-to-unobscured ratio is about 4.3 if such a value is set to 10^{22} cm^{-2} and about 2.4 for $N_{\rm H} = 3 \times 10^{22}$ cm^{-2}. It is important to note that such a ratio (referred to the entire AGNs population responsible for the XRB intensity, fully recovered only when the whole XRB is resolved into single sources) is independent from optical classification, and therefore the relative fraction of X–ray obscured AGNs in a flux-limited survey could be different from the fraction of optically narrow-line Type 2 objects. The relation between the fraction of objects having a given column density actually included in a survey and the flux limit of the survey coupled with its energy range is shown in Fig. 2.13, where this fraction is plotted against 5–10 keV, 2–10 keV and 0.5–2 keV fluxes.

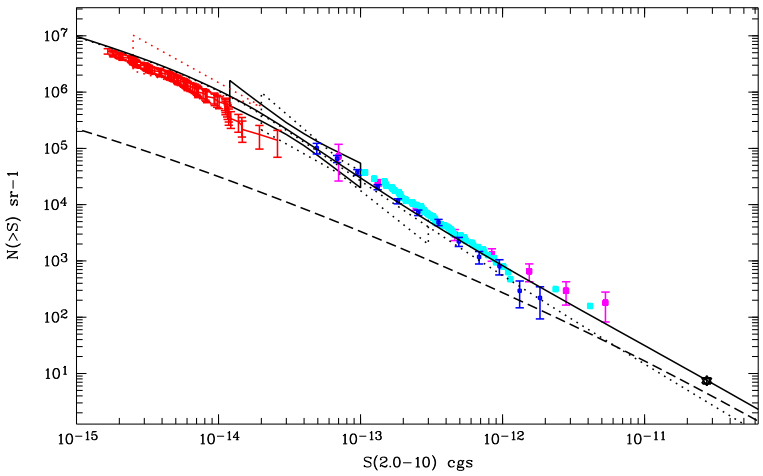

Figure 2.12: A compilation of the 2–10 keV logN-logS from different surveys. Blue dots = BeppoSAX (Giommi et al. 2000); magenta squares = ASCA (Ueda et al. 1999a); cyan squares = ASCA (Della Ceca et al. 1999); red error bars = Chandra (Giacconi et al. 2001); black star = HEAO1 (Piccinotti et al. 1982); black thick bow tie = the 1σ region delimited by the analysis of BeppoSAX fluctuations (Perri & Giommi 2000); black dot bow tie = the 1σ region delimited by the analysis of ASCA SIS fluctuations (Gendreau et al. 1998); red dot bow tie = Chandra logN-logS using eq. 2 of Mushotzky et al. (2000). Thick line = total (AGNs + clusters) 2–10 keV counts predicted by the XRB synthesis model; dotted line = AGNs only; dashed line = clusters only.

It appears evident that hard X–rays (e.g. 5–10 keV) are well suited to better probe the real fraction of obscured objects (e.g. at 5–10 keV fluxes of the order of 10^{-13} erg cm^{-2} s^{-1}, the fraction of objects in the Log$N_{\rm H}$ = 23–24 cm^{-2} bin is of the order of 25 %, becoming less that 15 % and negligible in the 2–10 and 0.5–2 keV bands, respectively). This is in agreement with XRB baseline model, where absorbed AGNs become progressively more important towards faint fluxes and hard energy ranges.

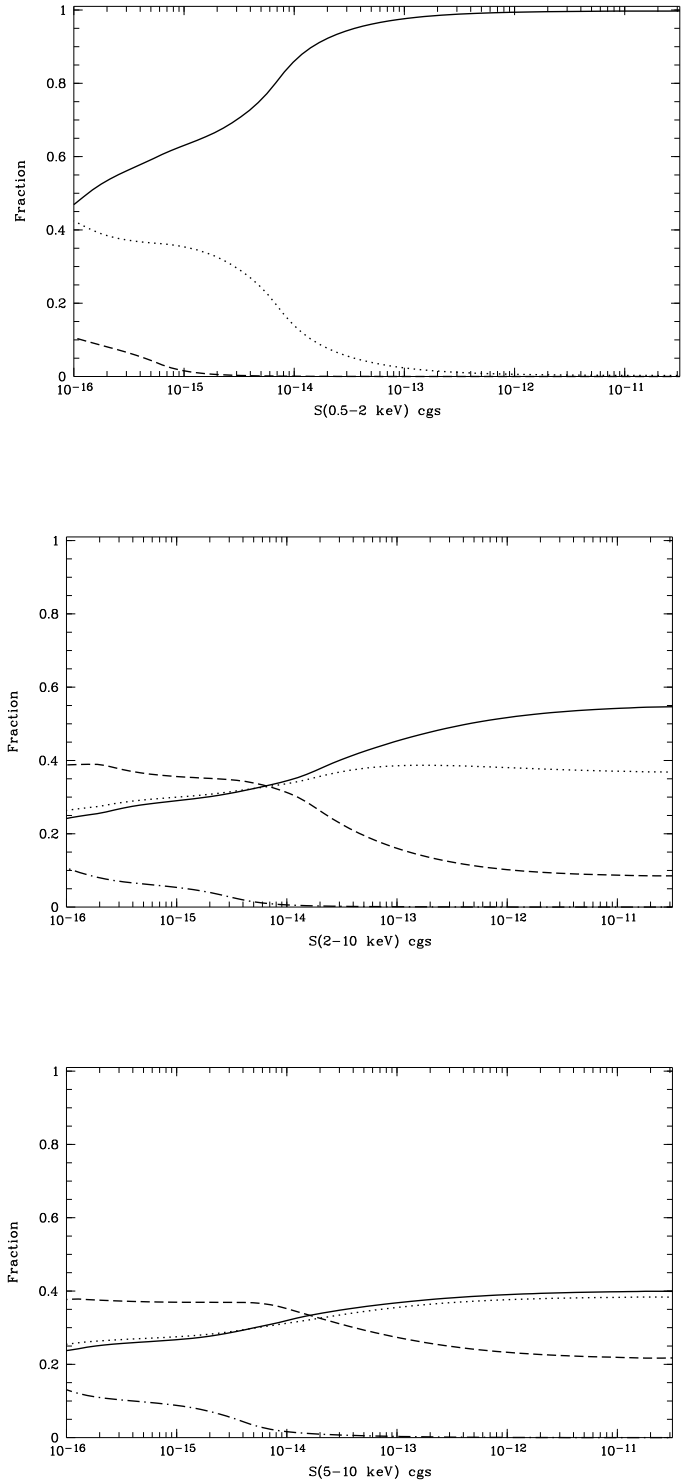

Figure 2.13: The relative fraction of unobscured (solid line) and obscured sources ($22 < \mathrm{Log\ N_H} < 23$: dotted line; $23 < \mathrm{Log\ N_H} < 24$: dashed line; $\mathrm{Log\ N_H} > 24$: dot-dashed line) as a function of the 0.5–2 keV, 2–10 keV and 5–10 keV flux.

BeppoSAX spectral analysis

3.1 Introduction

The large majority of the HELLAS sources do not allow to perform a standard X–ray spectral analysis, due to the low number of photons collected by MECS coupled to vignetting and PSF effects. Therefore all the spectral parameters (continuum slope, absorbing column densities, curvature in the spectra) are derived from the hardness ratio analysis, which can be considered the analog in the X–ray band of the optical colors. Even though the optical classification of the identified HELLAS sources will be discussed in chapter 6, it is interesting to introduce at this point the optical ID in order to compare the X–ray properties derived from the hardness ratio analysis with the optical ones.

A more comprehensive picture of broad-band, X–ray modeling of the HELLAS sources will be presented in chapter 8, after the analysis of the soft X–ray counterparts with *ROSAT* (chapter 4), along with a comparison with the results obtained from the *ASCA* Large Sky Survey (LSS, Akiyama et al. 2000).

3.2 X–ray spectral analysis

The full *BeppoSAX* MECS energy range (1.3–10 keV) has been divided into three bands: the low L = 1.3–2.5 keV, the medium M = 2.5–4.5 keV and the hard H = 4.5–10 keV band (the one in which the survey has been carried out).

For each source the softness ratio SR = (S−H)/(S+H) (where S = L+M) and the hardness ratios HR1 = (M−L)/(M+L) and HR2 = (H−M)/(H+M) have been computed. Since MECS1 is characterized

by a lower sensitivity than MECS2 and MECS3 at E $<$ 4 keV due to a thicker Kampton filter, the count ratios of sources observed with the three units have been corrected for this effect, even though the correction is generally very small and within the statistical errors.

The list of the **147** HELLAS sources, along with their X–ray positions, off-axis angles, fluxes and softness/hardness ratios, is reported in Table 3.1.

All those sources (19 out of 147) who lie close or under the Beryllium strongback supporting the MECS window have been excluded from the softness ratio analysis, because their colors may be systematically harder. This is due to the fact that the support structure has the effect of absorbing the photons at low energies.

In Fig. 3.1 the softness ratio SR is plotted as a function of the *BeppoSAX* 5–10 keV flux. It is interesting to note that many HELLAS sources are characterized by hard X–ray spectra, which may indicate very flat slopes or, more likely, the presence of strong absorption. Among the hardest sources (the ones in the lower region of the figure) there are objects classified as Type 1s, as well as Type 2s, but the majority is still unclassified.

In order to investigate the presence of X–ray absorption in the sources, a comparison between the counts observed in the S (1.3–4.5 keV) band and those predicted by extrapolating the assumed $\Gamma = 1.6$ hard power law to low energies has been carried out.

This method is clearly useful to provide a first, preliminary indication on the presence of X–ray obscuration, since the photoelectric absorption would depress the low-energy portion of the spectrum (the photoelectric cross-section is $\propto E^{-3}$). 36 out of the 128 sources have the 1.3–4.5 keV count rates lower than those expected for $\Gamma = 1.6$ at a confidence level $\geq$ 95 %, and 5 at a confidence level $\geq$ 99.7 %.

Is is worth noting that there is an apparent lack of faint hard X–ray sources (Fig. 3.1). This result goes in the opposite direction with respect to *ASCA* surveys, as described by Ueda et al. (1999a,b) and Ueda (2000), and by Della Ceca et al. (1999; 2000b). In particular, Della Ceca and collaborators find the brightest sources being characterized by $<\Gamma> = 1.87 \pm 0.08$, the faintest by $<\Gamma> = 1.36 \pm 0.14$. Keeping in mind the different selection bands (the HELLAS sources in the hard 4.5–10 keV energy interval, the *ASCA* ones in the 2–10 keV band), a deficit of very hard faint sources can be due to both an

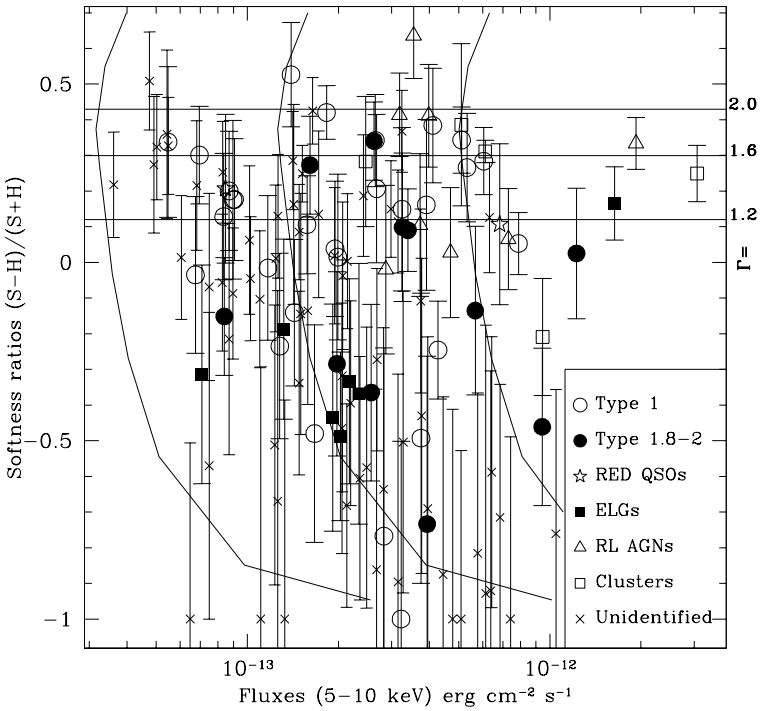

Figure 3.1: The softness ratio (S−H)/S+H) plotted as a function of the 5–10 keV flux for the 128 HELLAS sources which do not lie beneath the strongback support of the MECS window. The solid lines show the loci of equal 4.5–10 keV count rate, the straight solid lines indicate the spectral slopes corresponding to a few values of the softness ratio.

astrophysical and a technical reason.
The former could be a *redshift effect*: the observed softness ratio of sources with similar intrinsic column densities increases with redshift, as the cut-off energy moves towards lower energies.
The latter cause being an *instrumental effect, i.e. the reduced sensitivity at high energies* related to the rapid increase of the vignetting with the energy and the off-axis angles, which corresponds to a faster decrease of the sky coverage for the hard sources (having most of the photons in the hard X–rays, where the sensitivity goes down) than for the soft ones.

The solid lines in Fig. 3.1 can allow to quantify this instrumental

effect. They indicate the loci characterized by equal 4.5–10 keV count rates. The strong curvature of these lines towards low values of softness ratio is a clear indication of the strong vignetting affecting the X–ray data. Thus it is likely that the primary cause of the low number of very hard and faint sources is the vignetting. The MECS sensitivity is maximized with an unabsorbed power-law spectrum with a photon index $\sim$ 1.6–1.8.
Moreover, the bending of the same curves towards high fluxes for high SR values is due to the reduced MECS sensitivity for very soft sources due to the Beryllium window.

Recently, similar results (i.e. deficit of hard sources at faint fluxes) have been obtained by Georgantopoulos, Nandra & Ptak (2001) with the 5–10 keV *ASCA* GIS survey SHEEP (Search for the high energy extragalactic population).

More on the X–ray spectra can be inferred from the hardness ratio analysis, which indicates that the X–ray spectra of the majority of the HELLAS sources are more complex than a simple absorbed power law. This can be evaluated by plotting *BeppoSAX* HR1 vs. HR2 (Fig. 3.2) for the sources having a signal-to-noise ratio higher than 3.8 and which are not affected by the Be window support structure. Symbols are the same of Fig. 3.1.

Most of the sources lie at the left of the dashed lines, which indicate power-law models with increasing column densities ($N_{\rm H}$ = 10^{22}, 5 $\times$ 10^{22}, 10^{23}, 5 $\times$ 10^{23}, 10^{24} cm^{-2}) at redshifts z = 0 and 1.0, in an analogous way to that described by Della Ceca et al. (1999) for the *ASCA* Hard Serendipitous Survey (HSS) sources.

Fig. 3.2 suggests that (a) **substantial column densities** (spanning in the range Log $N_{\rm H}$ = 22–24 cm^{-2}) are present and (b) **soft components** are also common in the sample, resulting in a softer HR2. A partial covering model (where part of the nuclear component is seen as scattered radiation, while the remaining is suppressed by absorption) has been used to model an absorbed spectrum with a soft component. This is however only a simple parameterization, since different possibilities (like thermal emission from the host galaxy or from starburst regions) are also viable.

The two innermost solid lines represent the expectations of such a model, for a scattered fraction of 10 and 1 %, respectively. The evidence that soft X–ray components are present in hard X–ray selected samples

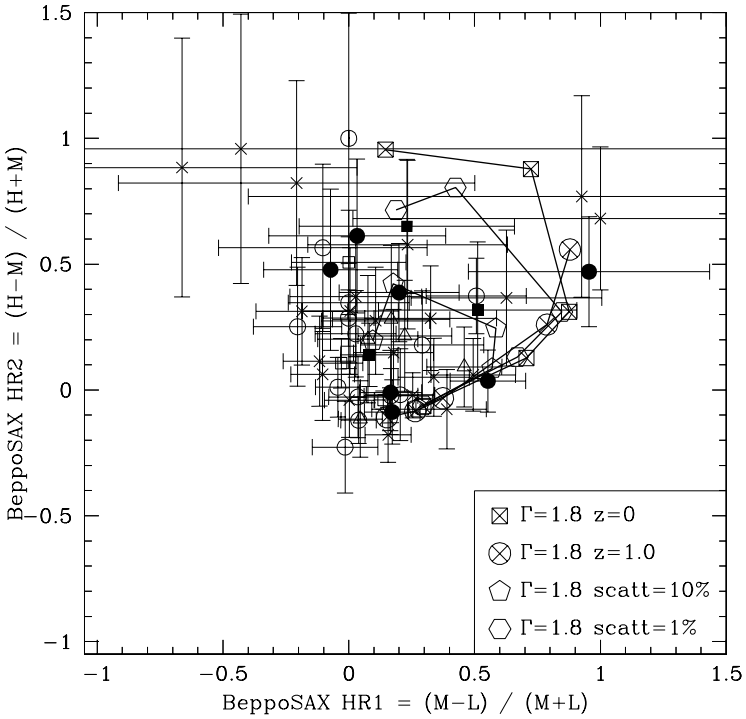

Figure 3.2: The hardness ratio HR1 = (M−L)/(M+L) vs. HR2 = (H−M)/(H+M) for the HELLAS sources having a signal-to-noise ratio > 3.8 and which do not lie beneath the Beryllium strongback. Symbols are the same of Fig. 3.1. The rightmost solid lines represent the expectations of a power-law model with slope $\Gamma = 1.8$ absorbed by a column density $N_{\rm H}$ = 10^{22}, 5×10^{22}, 10^{23}, 5×10^{23}, 10^{24} cm^{-2} at redshifts z = 0 and 1.0 (as indicated in the lower-right label). The two innermost curves (solid lines) represent the expectations of partial covering models with absorption as in previous cases and two different values for the scattered fraction: 10 and 1 %, respectively.

(Della Ceca et al. 1999; Giommi et al. 2000; Giacconi et al. 2001) is confirmed by the present results and will be discussed in more details through a comparison with *ROSAT* findings in chapter 4.

The above described models can account for the majority of the sources in Fig. 3.2 (almost within the large uncertainties concerning both HR1 and HR2). It is however interesting to note the presence of a

few isolated points in the upper left part of the diagram, characterized by the absence of photons in the medium (2.5–4.5 keV) band. This could imply a concave spectrum, where the soft X–rays are enhanced by the likely presence of an additional soft component, while the hard X–ray continuum is absorbed by a substantial amount of gas. The origin of the soft X–ray component (scattering, thermal, circum-nuclear starburst, etc.) cannot be addressed without further high-resolution imaging (as provided by *Chandra* and *XMM-Newton*).

In order to evaluate the absorbing column density of the HELLAS sources from the X–ray count ratio, the knowledge of the redshift of the source is required, under the assumption that the absorber is at the same redshift of the source (Fiore et al. 1998).

In Fig. 3.3 the softness ratio is plotted as a function of the redshift for all the HELLAS sources which do not lie beneath the MECS window support structure. Different symbols indicate different optical classification (through existing catalogs and by our follow-up observations, see chapter 6 for a full description of the optical counterparts), as in previous figures. The dotted lines indicate the softness ratios expected by assuming a $\Gamma = 1.8$ (upper line) and $\Gamma = 1.4$ (lower line) power-law model, respectively, with no intrinsic absorption. The short-dashed lines indicate the expectations of power-law continua absorbed by increasing column densities, ranging from 10^{23} cm^{-2} up to 10^{24} cm^{-2}, in the source rest-frame. As expected, the softness ratio of constant column density models strongly increases with the source redshift.

From Fig. 3.3 it appears evident that a large part of the identified HELLAS sources are not well parameterized by an unabsorbed power-law model, but substantial column densities are required in order to reproduce the *BeppoSAX* count ratios.

Not surprisingly, most of the sources with low softness ratios (the lower part of the diagram), i.e. characterized by absorption in the X–rays, have been classified as narrow-line, Type 1.8-2 objects (Fiore et al. 1999; Fiore et al. 2000a, 2001; La Franca et al., in preparation; see also chapter 6). Some emission-line galaxies (ELGs) are also present among the most absorbed sources.

Remarkably, many broad-line (Type 1, both radio-quiet and radio-loud) objects have softness ratios inconsistent with an unabsorbed X–ray spectrum, thus requiring the presence of large amounts of

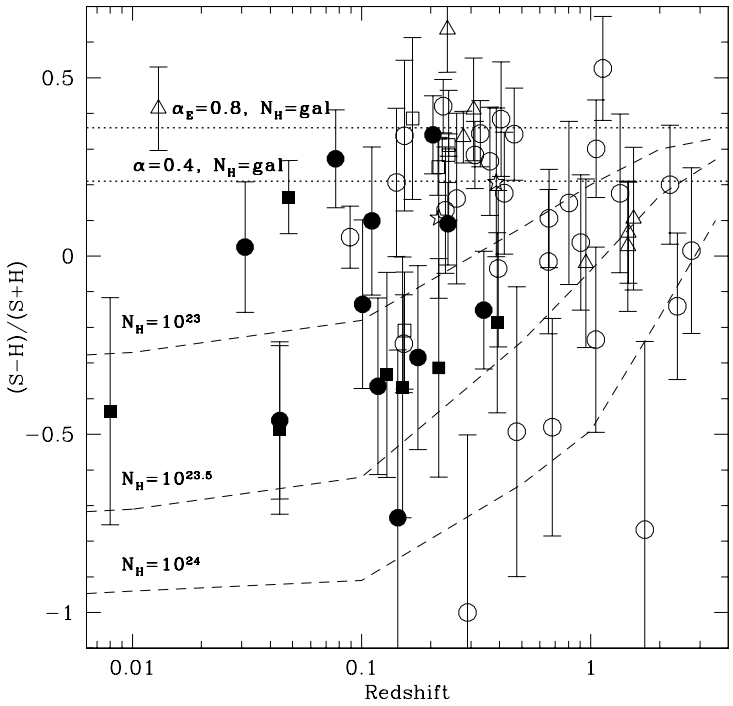

Figure 3.3: The *BeppoSAX* softness ratio as a function of redshift for the HELLAS sources which do not lie beneath the Be support structure of MECS. Different symbols identify different optical classifications as in previous figure. Dotted lines show the expected softness ratio for a power-law model with $\Gamma = 1.8$ (upper line) and $\Gamma = 1.4$ (lower line) and Galactic absorption only. The short-dashed lines indicate the softness ratios expected by assuming a power-law model absorbed by $N_{\rm H}$ spanning from 10^{23} up to 10^{24} cm^{-2} in the source rest-frame.

absorption ($N_{\rm H} \geq 10^{23}$ cm^{-2}) at their redshift. This effect is evident at z $>$ 0.3; the softness ratio is marginally anti-correlated with z (Spearman rank correlation coefficient of -0.27 for 34 degrees of freedom, corresponding to a probability of about 89 %).

Alternatively, the anticorrelation can be evaluated through the so-called running mean, i.e. the softness ratio (as a function of redshift) is computed dividing the sample of HELLAS Type 1 objects in small subsamples, each having in common with the previous one all but

one object. The softness ratio trend with redshift appears evident (Fig. 3.4).

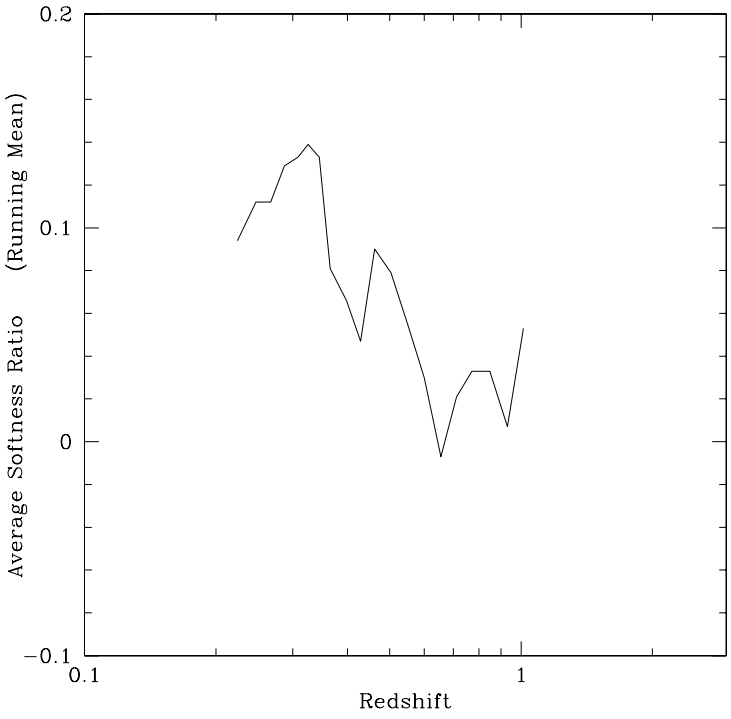

Figure 3.4: The softness ratio as a function of the redshift for the Type 1 objects computed through the method of the running mean.

The number of HELLAS sources having these properties is not so large to reach a definitive conclusion, but there is evidence that objects sharing the same properties are present also in the *ASCA* LSS (Akiyama et al. 2000), as described in chapter 4.

It must be noted that this correlation moves in the opposite direction than expected, since the ratio of the optical extinction (due to dust) to the X–ray obscuration (due to photoelectric absorption by gas) should scale as $(1+z)^4$. Therefore, highly X–ray obscured Type 1 objects can exist only assuming different dust-to-gas ratio with respect to the Galactic value or strongly different dust grain properties and sizes (see Maiolino 2000; Maiolino et al. 2001).

A more comprehensive picture will be presented in chapter 6

(concerning the optical identifications). *XMM-Newton* and *Chandra* pointed observations will easily confirm or disregard the presence of absorption in these high-redshift Type 1 objects.

3.3 The HELLAS average spectral properties compared with model predictions

In Fig. 3.5 the column density distribution inferred from Fig. 3.3 is compared with the baseline model predictions (cfr. § 2.6 for the XRB model). Given that the 5–10 keV band is not sensitive to column densities below $\sim 10^{23}$ cm^{-2}, sources with lower column densities are grouped in a single bin. The two BL Lac objects have been neglected in the calculation as this class of objects is not included in the synthesis model. The two boxes correspond to the observed fraction ($\pm$ 1 σ) of

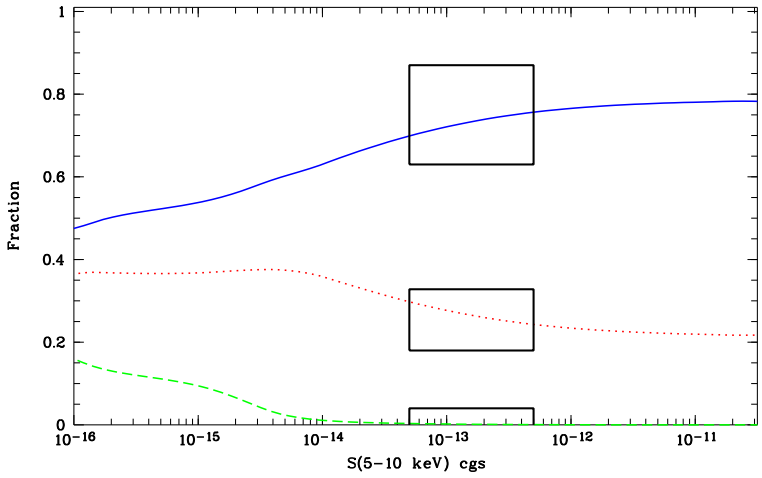

Figure 3.5: The model predicted fraction of relatively unobscured ($N_{\rm H} < 10^{23}$ cm^{-2}, solid line), highly absorbed ($10^{23} < N_{\rm H} < 10^{24}$ cm^{-2}, dotted line) and Compton-thick ($N_{\rm H} > 10^{24}$ cm^{-2}, dashed line) AGNs as a function of the 5–10 keV flux. The boxes correspond to the fraction of objects in the corresponding $N_{\rm H}$ classes as computed from the softness ratio vs. redshift diagram of Fig. 3.3.

HELLAS sources for each absorption class and cover the flux decade 5×10^{-14} – 5×10^{-13} erg cm^{-2} s^{-1}, corresponding to the fluxes of the large majority of the sources in Fig. 3.3. In order to take into account the relatively large errors in the softness ratio values, a source is included in the corresponding $N_{\rm H}$ class only if its softness ratio value plus one sigma error is below the $N_{\rm H}$ value indicated by the dashed lines in Fig. 3.3. According to this prescription, there is only one source with $N_{\rm H} \geq 10^{24}$ cm^{-2}, which is neglected since it does not belong to the final "restricted" sample of HELLAS sources (see section 6.8). The two sources with the "best-fit" column density $> 10^{24}$ cm^{-2} are assumed to be Compton-thick. It is important to note that the relatively good agreement between model predictions and observed $N_{\rm H}$ distribution is obtained without considering the optical classification.

Src. ID	RA (J2000)	DEC (J2000)	Off-axis (arcmin)	$F_{5-10\ keV}$ (erg cm^{-2} s^{-1})	SR	HR1	HR2
6	06 23 56.6	−69 21 12.7	6.1	1.3×10^{-13}	−1±0.61	0	1±0.58
8	06 25 31.3	−69 19 9.3	6.4	1.4×10^{-13}	0.16±0.28	−0.20±0.31	0.29±0.40
10	14 48 21.8	−69 20 29.8	11.7	4.2×10^{-13}	0.10±0.11	0.43±0.14	0.07±0.12
20	01 40 8.9	−67 48 12.7	8.0	2.8×10^{-13}	−0.41±0.32	−0.18±0.54	0.71±0.41
25	18 36 11.3	−65 07 19.9	22.8	4.4×10^{-13}	−0.88±0.50	−1±2.5	1±0.54
26	05 50 0.2	−61 02 22.2	5.9	9.0×10^{-14}	−0.09±0.18	0.33±0.26	0.29±0.21
30	05 52 6.1	−60 59 47.6	11.1	1.2×10^{-13}	−0.73±0.51	−0.22±1.58	0.89±0.56
31	05 52 51.3	−60 57 17.7	17.1	2.1×10^{-13}	−0.47±0.35	−0.66±0.70	0.88±0.51
32	05 48 41.3	−60 52 18.1	19.5	2.4×10^{-13}	0.19±0.17	0.22±0.15	0.06±0.21
35	23 16 9.8	−59 11 24.5	6.1	1.3×10^{-13}	−0.19±0.25	0.51±0.39	0.32±0.27
37	23 15 36.4	−59 03 39.7	8.3	2.0×10^{-13}	−0.49±0.24	0.23±0.43	0.65±0.27
39	01 21 56.8	−58 44 4.6	15.6	2.6×10^{-13}	−0.37±0.25	0.03±0.35	0.61±0.31
45	03 15 45.0	−55 29 25.5	14.5	2.6×10^{-13}	0.34±0.13	0.04±0.12	−0.03±0.16
46	03 17 32.4	−55 20 11.5	21.0	4.1×10^{-13}	0.38±0.16	0.04±0.12	−0.08±0.21
53	04 37 14.5	−47 30 57.9	16.0	2.7×10^{-13}	0.21±0.21	0.03±0.19	0.12±0.27
54	04 38 47.9	−47 29 6.4	20.1	4.7×10^{-13}	0.03±0.18	0.22±0.19	0.22±0.22
57	05 20 48.3	−45 42 0.0	9.6	5.9×10^{-13}	0.23±0.16	0.04±0.17	0.09±0.20
58	06 46 42.7	−44 32 29.0	19.0	2.7×10^{-13}	−0.27±0.26	0.63±0.40	0.37±0.27
65	06 46 39.3	−44 15 34.8	16.6	4.3×10^{-13}	−0.25±0.14	0.51±0.20	0.37±0.15
66	23 19 22.1	−42 41 50.0	21.4	5.7×10^{-13}	−0.14±0.24	−0.07±0.27	0.48±0.32
72	03 33 9.6	−36 19 39.6	15.2	4.0×10^{-13}	0.41±0.14	−0.01±0.13	−0.09±0.18
73	03 36 51.3	−36 15 56.7	14.7	3.7×10^{-13}	0.10±0.20	0.08±0.20	0.20±0.25
75	03 34 7.4	−36 04 21.7	5.1	1.9×10^{-13}	0.04±0.19	0.29±0.25	0.18±0.22
84	13 36 34.3	−33 57 47.0	21.8	3.2×10^{-13}	0.41±0.12	0.05±0.09	−0.12±0.15
85	22 03 0.5	−32 04 17.7	16.6	2.8×10^{-13}	−0.77±0.53	−1±1.59	1±0.64

Src. ID	RA (J2000)	DEC (J2000)	Off-axis (arcmin)	$F_{5-10\ keV}$ (erg cm^{-2} s^{-1})	SR	HR1	HR2
90	01 34 28.6	−30 06 33.7	12.2	1.3×10^{-13}	−0.34±0.28	0.49±0.44	0.47±0.30
91	01 34 51.9	−30 01 34.0	5.4	7.1×10^{-14}	−0.31±0.31	0.60±0.58	0.41±0.32
92	13 48 45.4	−30 29 36.2	14.4	5.1×10^{-13}	0.34±0.09	−0.04±0.09	0.01±0.12
93	01 34 33.3	−29 58 38.0	6.0	8.7×10^{-14}	0.20±0.17	−0.20±0.18	0.25±0.24
94	13 48 24.3	−30 25 47.1	14.8	3.1×10^{-13}	0.11±0.14	0.18±0.16	0.15±0.17
96	01 35 30.2	−29 51 21.0	8.4	9.0×10^{-14}	0.18±0.22	0.41±0.23	0±0.25
97	13 50 9.4	−30 19 54.9	10.8	5.1×10^{-13}	−0.28±0.15	0.60±0.25	0.38±0.15
99	01 34 14.3	−29 45 41.4	14.3	1.5×10^{-13}	−0.14±0.34	0.62±0.46	0.24±0.36
100	13 48 20.8	−30 11 5.9	14.4	2.2×10^{-13}	−0.33±0.29	0.54±0.51	0.44±0.30
101	13 48 37.9	−30 09 11.1	12.3	1.6×10^{-13}	−0.14±0.26	0.65±0.42	0.23±0.27
103_1	00 45 49.6	−25 15 13.0	23.7	3.3×10^{-13}	0.10±0.21	−0.31±0.19	0.41±0.33
107	00 48 5.8	−25 04 32.3	14.9	1.5×10^{-13}	−0.34±0.26	1±0.44	0.34±0.27
120	00 26 36.5	−19 44 13.2	13.2	3.4×10^{-13}	0.09±0.12	0.55±0.15	0.04±0.12
121	00 27 43.9	−19 30 28.8	11.0	1.6×10^{-13}	−0.34±0.29	0.25±0.45	0.53±0.34
124	00 27 9.9	−19 26 30.6	6.2	1.8×10^{-13}	0.42±0.08	0.04±0.07	−0.12±0.09
131	11 07 4.9	−18 16 27.5	7.7	1.2×10^{-13}	−0.51±0.39	−1±0.98	1±0.59
134	21 38 8.9	−14 33 12.8	7.0	2.3×10^{-13}	−0.37±0.37	−1±0.78	1±0.63
136	09 46 17.9	−14 10 26.6	10.9	2.0×10^{-13}	−0.89±0.40	1±2.80	0.89±0.39
137	09 46 32.8	−14 06 15.4	16.4	3.2×10^{-13}	−1±0.50	0	1±0.50
138	09 46 5.3	−14 02 59.2	15.8	2.8×10^{-13}	−0.64±0.45	−0.72±1.16	0.94±0.59
147	20 42 47.6	−10 38 30.5	21.1	5.3×10^{-13}	0.27±0.15	0.20±0.13	−0.02±0.18
149	20 44 34.8	−10 27 33.6	15.3	2.0×10^{-13}	0.02±0.23	−0.24±0.25	0.44±0.34
150	13 05 32.3	−10 32 35.4	22.0	1.9×10^{-12}	0.33±0.07	0.16±0.07	−0.08±0.09
151	13 04 24.3	−10 23 52.6	4.4	1.3×10^{-13}	−0.23±0.26	−0.10±0.41	0.57±0.33
155	13 04 38.2	−10 15 46.7	5.9	1.4×10^{-13}	−0.14±0.21	0.53±0.32	0.27±0.22

Src. ID	RA (J2000)	DEC (J2000)	Off-axis (arcmin)	$F_{5-10\ keV}$ (erg cm^{-2} s^{-1})	SR	HR1	HR2
157	12 56 9.9	−05 54 29.8	7.6	9.1×10^{-14}	0.18±0.17	0.48±0.19	−0.03±0.19
160	13 05 36.5	−05 43 30.0	22.7	6.4×10^{-13}	−0.59±0.38	−0.21±0.64	0.81±0.47
161	12 55 16.6	−05 39 22.5	16.3	2.2×10^{-13}	−0.39±0.29	0.23±0.40	0.58±0.34
162	13 04 45.1	−05 33 36.8	7.5	1.3×10^{-13}	−0.67±0.59	−1±2.28	1±0.77
167	12 40 26.0	−05 13 20.0	11.7	3.1×10^{-13}	0.16±0.14	0.17±0.16	0.10±0.17
169	12 40 29.6	−05 07 45.9	16.9	1.9×10^{-13}	−0.44±0.32	−0.56±0.54	0.84±0.46
171	14 11 58.7	−03 07 1.9	20.7	3.9×10^{-13}	−0.73±0.47	−1±1.10	1±0.60
172	02 42 1.8	00 00 45.6	10.0	1.5×10^{-13}	−0.02±0.17	0.28±0.22	0.24±0.19
174	02 42 9.4	00 02 29.2	7.5	6.8×10^{-14}	0.22±0.18	−0.14±0.18	0.20±0.25
176	13 42 59.3	00 01 37.9	20.6	3.2×10^{-13}	0.15±0.23	0.12±0.21	0.14±0.29
180	13 42 47.9	00 21 9.3	16.9	2.5×10^{-13}	−0.58±0.39	0.16±0.73	0.73±0.45
185	05 15 13.7	01 08 6.9	7.6	1.3×10^{-13}	0.13±0.17	0.27±0.20	0.10±0.20
186	12 29 23.7	01 51 37.7	14.1	1.6×10^{-13}	0.27±0.14	0.17±0.12	−0.01±0.17
187	16 52 12.5	02 11 29.0	15.8	2.4×10^{-13}	−0.61±0.34	−0.21±0.71	0.82±0.41
190	16 52 38.0	02 22 17.7	4.6	6.7×10^{-14}	−0.04±0.22	0.11±0.29	0.32±0.26
195	03 08 19.0	03 46 27.0	18.5	5.1×10^{-13}	−1±0.47	0	1±0.47
200	16 50 40.1	04 37 16.7	24.5	1.2×10^{-12}	0.03±0.18	0.32±0.22	0.18±0.21
201	16 49 57.9	04 53 32.3	19.8	9.5×10^{-13}	−0.21±0.16	0±0.23	0.51±0.21
203	04 32 27.9	05 13 4.7	15.0	2.1×10^{-13}	−0.32±0.33	−0.06±0.49	0.61±0.42
205	23 29 2.4	08 34 38.6	20.0	2.9×10^{-13}	−0.02±0.24	0.17±0.23	0.28±0.29
206	23 02 30.1	08 37 6.2	17.6	2.7×10^{-13}	−0.86±0.51	−0.43±2.64	0.96±0.54
207	23 27 37.1	08 38 55.8	7.9	1.5×10^{-13}	0.09±0.13	0.49±0.17	0.06±0.14
209	23 27 28.7	08 49 29.8	7.1	5.5×10^{-14}	0.34±0.21	0.32±0.20	−0.14±0.24
210	23 06 59.2	08 48 39.7	4.1	1.0×10^{-13}	0.06±0.21	−0.08±0.27	0.32±0.27
212	23 02 36.2	08 56 42.1	10.1	3.2×10^{-13}	−0.50±0.24	0.83±0.60	0.53±0.24

Src. ID	RA (J2000)	DEC (J2000)	Off-axis (arcmin)	$F_{5-10\ keV}$ (erg cm^{-2} s^{-1})	SR	HR1	HR2
213	22 31 49.6	11 32 8.3	15.2	1.9×10^{-13}	0.02±0.19	0.01±0.19	0.31±0.25
220	05 02 15.5	12 04 7.2	20.9	7.4×10^{-13}	−1±0.51	0	1±0.51
226	13 55 54.1	18 13 35.2	19.8	6.1×10^{-13}	−0.93±0.75	−1±6.31	1±0.78
228	13 53 54.6	18 20 32.8	17.5	6.8×10^{-13}	0.11±0.23	0.02±0.24	0.22±0.29
229	23 31 55.6	19 38 33.9	17.0	3.7×10^{-13}	−0.49±0.41	0.20±0.68	0.66±0.47
230_1	15 28 47.3	19 39 9.7	5.0	1.6×10^{-13}	0.11±0.14	0.03±0.16	0.22±0.17
230_2	15 28 46.0	19 45 10.0	4.7	1.6×10^{-13}	0.43±0.09	0.16±0.09	−0.18±0.11
237	22 26 30.3	21 11 56.3	13.7	3.9×10^{-13}	0.16±0.24	−0.27±0.27	0.33±0.35
239	14 17 12.5	24 59 28.1	12.9	6.9×10^{-14}	0.30±0.14	0.05±0.12	0.01±0.18
241	14 18 31.1	25 11 6.9	8.6	6.1×10^{-13}	0.31±0.03	0.14±0.03	−0.04±0.04
243	08 37 37.2	25 47 48.3	12.1	2.6×10^{-13}	0.19±0.17	0.28±0.18	0.03±0.19
246	08 38 59.9	26 08 13.0	23.0	1.6×10^{-12}	0.17±0.10	0.08±0.11	0.14±0.13
249	23 55 32.7	28 35 11.2	7.7	1.7×10^{-13}	0.14±0.23	−0.07±0.27	0.24±0.30
250	23 55 53.3	28 36 5.4	12.0	4.2×10^{-13}	0.22±0.18	0.26±0.19	0.01±0.20
252	12 04 7.6	28 08 30.5	16.1	5.1×10^{-13}	0.39±0.23	0.02±0.20	−0.07±0.29
254	22 42 51.5	29 35 31.7	7.6	1.0×10^{-13}	−0.05±0.17	−0.03±0.22	0.39±0.22
256	22 41 22.1	29 42 41.2	15.6	3.0×10^{-13}	0.15±0.14	0.34±0.14	0.05±0.15
258	22 44 11.4	29 51 14.1	23.1	3.9×10^{-13}	−0.69±0.48	0.04±1.13	0.83±0.53
264	12 18 55.0	29 58 12.0	12.7	2.0×10^{-13}	−0.28±0.26	1±0.48	0.28±0.26
265	12 17 50.3	30 07 7.9	19.8	3.5×10^{-13}	0.64±0.12	−0.04±0.08	−0.37±0.17
273	10 34 43.1	39 29 17.7	8.4	1.1×10^{-13}	−1±0.71	0	1±0.69
278	10 34 52.0	39 40 12.4	5.3	1.4×10^{-13}	0.29±0.14	−0.12±0.14	0.11±0.18
279	16 54 41.1	40 02 10.3	17.6	6.3×10^{-13}	0.13±0.15	−0.19±0.18	0.31±0.21
282	11 18 46.2	40 27 38.8	4.8	1.4×10^{-13}	0.53±0.15	−0.01±0.13	−0.23±0.18
283	11 18 11.9	40 28 32.9	4.2	8.5×10^{-14}	0.21±0.21	0.33±0.24	−0.01±0.23

Src. ID	RA (J2000)	DEC (J2000)	Off-axis (arcmin)	$F_{5-10\ keV}$ (erg cm^{-2} s^{-1})	SR	HR1	HR2
288	12 19 21.6	47 11 6.8	9.4	1.3×10^{-13}	-0.45 ± 0.29	1 ± 0.64	0.45 ± 0.29
290	12 19 45.7	47 20 42.4	7.5	1.2×10^{-13}	-0.02 ± 0.20	0 ± 0.24	0.35 ± 0.26
292	12 17 45.1	47 29 54.7	16.4	3.2×10^{-13}	0.37 ± 0.11	0 ± 0.10	-0.04 ± 0.15
295	13 38 34.1	48 21 5.0	4.3	1.2×10^{-13}	0.01 ± 0.21	0.27 ± 0.27	0.21 ± 0.24
296	18 15 17.5	49 44 51.4	9.8	3.5×10^{-13}	-0.95 ± 0.50	1 ± 8.73	0.95 ± 0.49
299	10 29 19.1	50 48 15.0	17.5	5.8×10^{-13}	-0.82 ± 0.45	1 ± 1.63	0.82 ± 0.45
300	10 32 15.8	50 51 3.0	10.4	3.1×10^{-13}	-0.66 ± 0.75	1 ± 3.00	0.66 ± 0.69
305	16 26 56.8	55 13 23.7	14.2	3.1×10^{-13}	-0.90 ± 0.58	1 ± 4.16	0.90 ± 0.58
307	16 26 59.9	55 28 20.1	10.5	1.2×10^{-12}	0.04 ± 0.09	0.18 ± 0.12	0.22 ± 0.10
319	10 54 19.8	57 25 8.6	13.4	2.6×10^{-13}	0.34 ± 0.11	0.17 ± 0.11	-0.09 ± 0.13
321	10 52 45.4	57 30 42.3	4.0	8.3×10^{-14}	-0.06 ± 0.19	0.03 ± 0.26	0.37 ± 0.24
323	10 54 21.7	57 36 24.4	16.6	2.1×10^{-13}	-0.68 ± 0.29	1 ± 0.98	0.68 ± 0.28
324	12 54 28.0	59 21 0.6	24.3	6.4×10^{-13}	-0.92 ± 0.62	-0.33 ± 5.10	0.97 ± 0.63
325	16 34 10.7	59 37 43.7	6.9	5.0×10^{-14}	0.32 ± 0.15	0.32 ± 0.14	-0.13 ± 0.17
327	16 34 11.8	59 45 28.6	3.4	8.4×10^{-14}	-0.15 ± 0.17	0.20 ± 0.24	0.39 ± 0.19
328	16 34 11.0	59 48 14.9	5.2	4.7×10^{-14}	0.51 ± 0.14	0.13 ± 0.11	-0.27 ± 0.17
337	18 19 39.5	60 53 25.6	3.7	8.3×10^{-14}	0.25 ± 0.14	0.39 ± 0.16	-0.08 ± 0.16
340_2	17 50 25.4	60 56 0.9	11.7	2.1×10^{-13}	-1 ± 0.61	0	1 ± 0.61
341	18 19 18.4	60 56 6.3	3.5	1.5×10^{-13}	0.25 ± 0.08	0.25 ± 0.09	-0.02 ± 0.09
345	18 19 35.5	60 58 45.9	2.2	4.9×10^{-14}	0.27 ± 0.19	0.40 ± 0.21	-0.10 ± 0.21
346_1	17 53 49.0	60 59 51.8	12.7	1.1×10^{-13}	-0.10 ± 0.19	1 ± 0.31	0.10 ± 0.19
346_2	17 51 30.3	61 00 43.2	6.7	5.5×10^{-14}	0.33 ± 0.14	-0.10 ± 0.13	0.06 ± 0.18
351_1	17 52 38.3	61 05 46.7	3.2	3.6×10^{-14}	0.22 ± 0.15	0.06 ± 0.16	0.10 ± 0.18
353	18 03 51.8	61 10 21.2	2.9	6.0×10^{-14}	0.01 ± 0.17	0.11 ± 0.22	0.27 ± 0.21
354	18 18 58.6	61 14 42.4	18.6	2.1×10^{-13}	-0.04 ± 0.21	0.32 ± 0.22	0.24 ± 0.24

Src. ID	RA (J2000)	DEC (J2000)	Off-axis (arcmin)	$F_{5-10\ keV}$ (erg cm^{-2} s^{-1})	SR	HR1	HR2
364	14 38 30.1	64 30 25.4	11.2	2.6×10^{-13}	0.17±0.14	0.69±0.17	−0.08±0.14
372	11 56 39.2	65 17 57.2	5.7	7.5×10^{-14}	−0.07±0.26	−0.10±0.34	0.44±0.35
374	11 57 1.7	65 27 23.8	15.4	2.1×10^{-13}	0±0.19	0.49±0.22	0.14±0.21
375	15 19 39.9	65 35 46.0	13.9	9.4×10^{-13}	−0.46±0.22	0.95±0.48	0.47±0.22
375_1	17 40 10.7	67 42 50.2	17.7	3.3×10^{-13}	−0.50±0.42	−0.72±0.85	0.91±0.62
375_2	17 42 36.3	68 00 43.8	10.6	2.8×10^{-13}	−1±0.50	0	1±0.50
380	11 34 52.7	70 23 8.8	15.5	3.8×10^{-13}	−0.43±0.44	1±0.86	0.43±0.44
385	07 21 29.6	71 14 4.0	8.1	8.4×10^{-14}	0.13±0.18	0.03±0.20	0.20±0.22
387	11 01 46.4	72 26 10.8	22.3	7.3×10^{-13}	0.07±0.14	0.46±0.15	0.09±0.16
389	11 06 14.0	72 43 16.0	8.5	1.7×10^{-13}	−0.48±0.31	0.18±0.59	0.66±0.35
390	11 02 37.2	72 46 37.6	20.7	7.9×10^{-13}	0.05±0.09	0±0.10	0.29±0.11
392	07 41 40.3	74 14 57.2	22.6	3.2×10^{-12}	0.25±0.08	−0.03±0.09	0.11±0.10
393	07 41 45.2	74 26 22.9	13.1	3.7×10^{-13}	−0.11±0.26	0.03±0.33	0.41±0.33
394	07 43 9.1	74 29 19.3	7.2	6.0×10^{-13}	0.28±0.09	0.17±0.11	−0.02±0.11
400	12 22 6.8	75 26 16.7	6.5	2.5×10^{-13}	0.28±0.18	−0.11±0.20	0.11±0.23
405	06 55 39.6	79 10 48.4	4.7	7.5×10^{-14}	−0.57±0.43	1±1.32	0.57±0.42
410	21 59 52.1	88 54 53.1	17.8	6.8×10^{-13}	−0.72±0.37	1±0.97	0.72±0.37
413	21 22 59.2	89 01 57.5	15.3	4.8×10^{-13}	−1±0.59	0	1±0.59
424	03 08 8.5	89 08 40.9	4.9	6.5×10^{-14}	−1±0.49	0	1±0.48
426	01 53 3.9	89 12 20.2	2.4	5.4×10^{-14}	0.36±0.24	0.22±0.23	−0.13±0.27
431	01 18 3.9	89 20 11.5	8.3	8.7×10^{-14}	−0.22±0.32	0.40±0.48	0.38±0.36
432	21 42 46.7	89 35 30.3	23.5	1.0×10^{-12}	−0.76±0.40	0.93±1.33	0.77±0.40

Table 3.1: The list of the **147** HELLAS sources and their X–ray parameters.

Studying the soft X–ray properties of the HELLAS sources with ROSAT

4.1 Introduction

The importance of extending the study of the HELLAS sources down to the *ROSAT* band is due the the fact that the 0.5–2 keV band is not fully achievable by the *BeppoSAX* MECS instruments (whose lower energy limit is about 1.3 keV). A broad-band view of hard X–ray selected sources would allow to better understand the mechanisms characterizing the X–ray emission, such as the importance of scattered nuclear components and the presence of non nuclear starburst-related emission, thus providing new hints for the AGN-starburst connection (Lawrence 1999; Veilleux 2000). The study of the broad-band spectrum of the hard X–ray selected sources is particularly important also for the AGNs synthesis models for the XRB. Soft X–ray components are either excluded from the XRB synthesis models (e.g. Comastri et al. 1995) or, if included, they do account for a small, energetically not relevant fraction of the XRB (e.g. Gilli et al. 1999). Indeed, there is increasing evidence that the broad-band spectral properties of the sources responsible for the hard XRB are characterized by more complex spectra than is expected from a simple absorbed power-law model (Della Ceca et al. 1999; Giommi et al. 2000), as confirmed by the presence of multi-components spectra in obscured nearby AGNs (Awaki et al. 2000). The possibility of the existence of such additional components must be taken into account when comparing surveys performed in different energy ranges and,

most important, at limiting fluxes differing by one (or more) order of magnitude. In this regard, archival *ROSAT* (PSPC, HRI and RASS) data for the full HELLAS sample have been searched for, in order to provide new clues on the nature of the sources responsible for the hard XRB and to verify whether additional soft X–ray components may be present (Vignali et al. 2001).

In the following section I will summarize the imaging and spectral performances of *ROSAT* , which are strictly related to the results presented in the chapter. Then the source detection algorithm and the reliability of the soft X–ray counterparts will be discussed. The findings will be compared to those obtained for a soft X–ray selected sample extracted from the *ROSAT* Deep Survey in the Lockman Hole (Hasinger et al. 1998; Schmidt et al. 1998; see also Lehmann et al. 2000 for the latest optical identifications).

4.2 The *ROSAT* satellite: a brief introduction

The *ROSAT* X–ray telescope (Trümper 1982) consists of two position-sensitive proportional counter (PSPC), one high-resolution image (HRI) and one wide-field camera (WFC). Most of the *ROSAT* archival observations which will be used in the following have been performed with the PSPC (Pfeffermann et al. 1987) in the focal plane. The PSPC provides a bandpass in the range 0.1–2.4 keV over an about 2° diameter field of view, with a moderate (about 45 % FWHM @ 0.93 keV) spectral resolution, but fairly good spatial resolution (about 15–20 arcsec on-axis). Due to uncertainties in the detector response matrix at energies above 2 keV, only results obtained in the 0.1–2 keV will be presented. Most of the observations have been obtained in the "wobble" mode: the detector is moved from the pointing direction with a period of about 400 s and an amplitude of about 3 arcmin. In such a way the effect of shadowing of the X–ray sources by the detector window structures, such as struts and wire mesh, is minimized.
The HRI instrument is less sensitive than PSPC and has no spectral resolution, but is characterized by a much better spatial resolution (about 5 arcsec on-axis).

4.3 The cross correlation

The *BeppoSAX* catalog was cross-correlated with the archival *ROSAT* data (PSPC, HRI and RASS). 108 out of the 147 sources are in *ROSAT* fields; for only 1 source RASS data have been used, due to the lack of pointed *ROSAT* observations. 4 sources lying beneath the PSPC detector window support structure will not be considered in the following discussions, therefore the useful number of HELLAS sources in *ROSAT* fields is 104. In those cases where multiple observations of the same HELLAS source are present, the one with the longest exposure time and/or the lowest off-axis angle was chosen, and the results checked by analyzing at least another image of the same field.

4.4 *ROSAT* fields

4.4.1 *ROSAT* source detection

The *ROSAT* data have been analyzed with the MIDAS/EXSAS package (Zimmermann et al. 1998). The *ROSAT* standard analysis (SASS, Voges 1992) performs several corrections to the individual PSPC and HRI photons, including detector linearization, optical distortions, boresight and attitude corrections. The sources have been detected by running the local detection algorithm LDETECT, the bicubic spline fit to the background map and the map detection algorithm MDETECT. The detection threshold of these algorithms was set at a likelihood of $L=-\ln(P_e)=10$, corresponding to a probability of 4.5×10^{-5} that the observed number of photons in the source cell is produced by a pure background fluctuation (about 4 σ detection, Cruddace, Hasinger & Schmitt 1988). The measured counts were then corrected for PSPC vignetting (particularly important for off-axis sources) and PSPC dead time, and the source parameters were determined by the maximum likelihood method (MAXLIK). The sources which partially fell under the PSPC window support structure and which were missed by the detection routine have also been analyzed, and the vignetting-corrected count rates have been obtained in the different energy bands. Even though the above described routines have been extensively applied in the past, the reliability of all the detections have been checked by running the slide-cell detection algorithm in XIMAGE (Giommi et al. 1991) in a similar way to that

described in Fiore et al. (2000a) for all the sources of the present sample, obtaining similar results within the errors. Most of the sources are also present in the WGA catalog (a point source catalog generated from all *ROSAT* PSPC pointed observations, see White, Giommi & Angelini 1994). The agreement between the present results and those from the WGA makes us further confident about the findings which will be described in the following sections.

Images were constructed in 4 energy bands: PI channels 11–41 (corresponding to 0.1–0.4 keV, band (a)), 52–201 (0.5–2 keV, (b)), 52–90 (0.5–0.9 keV, (c)) and 91-201 (0.9–2 keV, (d)), which correspond to S, H, H1 and H2 in Hasinger et al. (1998). The hardness ratios have been defined as follows: HR1=(b−a)/(b+a) and HR2=(d−c)/(d+c).

The soft X–ray fluxes have been computed in the full 0.5–2 keV energy range directly from the best-fit spectrum (when the statistics was high enough to allow a spectral modeling of the *ROSAT* counts) or by converting the count rates into fluxes under the assumption of a power-law slope with photon index 2.3 (the mean of the distribution of the present sample and within the width of the distribution of soft X–ray spectral slopes, e.g. Walter & Fink 1993), and Galactic absorption only.

In the following I will focus on the hardness ratio analysis, which is the most suitable way to obtain spectral information in the regimes of low-counting statistics.

4.4.2 *ROSAT* data analysis

Each *ROSAT* field has been analyzed searching for the soft X–ray counterpart of the *BeppoSAX* HELLAS sources, assuming a cross-correlation radius of 100 arcsec. Five *ROSAT* sources have been found at larger radii (see Fig. 4.1): four have been spectroscopically identified and the soft X–ray position coincide with the optical one within ~ 35 arcsec. This evidence, coupled with the errors which can be associated to *BeppoSAX* MECS pointing position reconstruction (mainly due to the unavailability of one star-tracker for a part of the observation, cfr. section 2.4 for a description of the problems related to *BeppoSAX* position reconstruction), make us confident that these associations are real. The fifth source belong to a high-Galactic field where *BeppoSAX* position recontruction was not possible due to the absence of either a bright known source or the target in the same field of view.

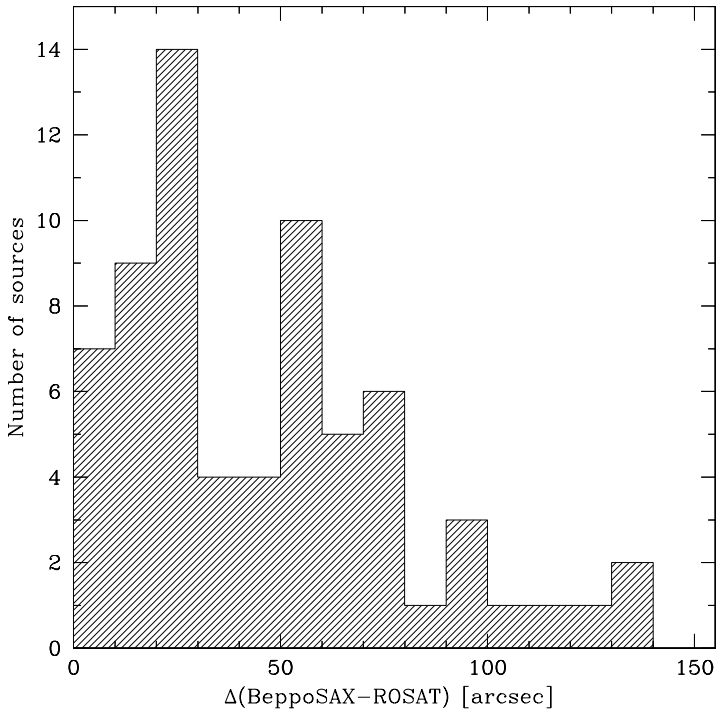

Figure 4.1: Distribution of the distances between *BeppoSAX* and *ROSAT* source positions.

For the majority of fields only one *ROSAT* source is present in each *BeppoSAX* error box. For the three cases in which more than one *ROSAT* source is present, the one closest to the center of *BeppoSAX* error box has been chosen. For these sources the soft X–ray emission is also associated to radio emission.

Given the large range of both *ROSAT* exposure times and off-axis angles distributions, the sensitivity limit is different from field to field. As a consequence, the number of spurious *ROSAT* – *BeppoSAX* associations has been derived by computing for each source the number of objects expected at its flux according to the 0.5–2 keV integral source counts (Hasinger et al. 1998) and adopting a searching radius of 100 arcsec. The final number of spurious associations is therefore the summed contribution of the chance coincidences expected for each field. With this approach, 2 associations by chance are expected.

68 out of the 104 HELLAS sources have a *ROSAT* soft X–ray counterpart, while 36 sources went undetected. The 5–10 keV flux distribution for the sources detected by *ROSAT* is not significantly different from that of the entire HELLAS sample (20 % confidence level according to the Kolmogorov-Smirnov test), see Fig. 4.2 for the comparison).

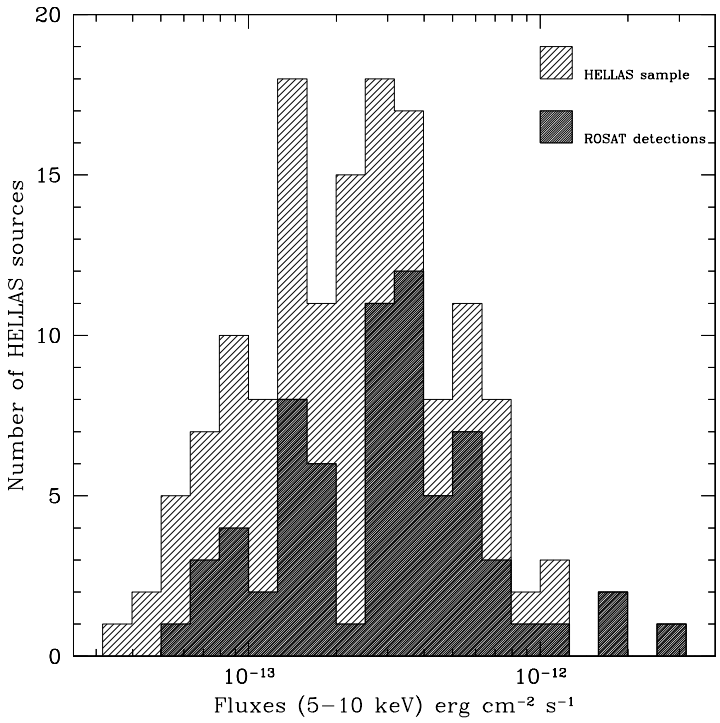

Figure 4.2: Flux distribution of the HELLAS sources with a soft X–ray counterpart with respect to the whole sample.

4.4.3 HELLAS sources detected by *ROSAT*

Among the 68 sources detected by *ROSAT* 51 have been identified with extra-galactic objects (see Table 4.1 for a comprehensive view on their soft X–ray properties), i.e. 35 Type 1 objects (including 5 radio-loud AGNs and 1 red quasar), 4 Type 1.8–2, 2 emission-line galaxies, 2 BL Lac objects, 1 radio-galaxy and 6 clusters. Moreover, one source is

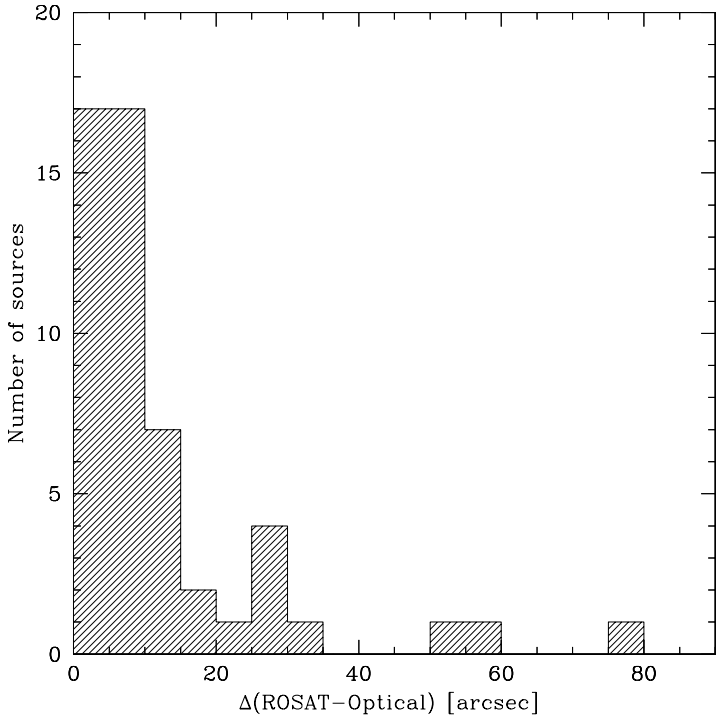

Figure 4.3: Distribution of the distances between *ROSAT* and optical positions for the HELLAS sources.

associated with a bright K star.

All the radio-loud AGNs and the clusters, and about one third of the Type 1 objects have been identified through existing catalogs, while the remaining have been spectroscopically identified by our group (see La Franca et al. 2001). In several cases the *ROSAT –BeppoSAX* association has been used in the spectroscopic identification process.

For what concerns the *ROSAT*-optical association, the X–ray source has been considered physically associated with the optically identified object if the distance between the X–ray and the optical position is below 40 arcsec (which should take into account the dependence of the PSPC point-spread function with the off-axis angle and the possible error in aspect reconstruction). The *ROSAT* sources of the present sample have typical distances (see Fig. 4.3) of about 10–20 arcsec from the optical position (which is consistent with the values

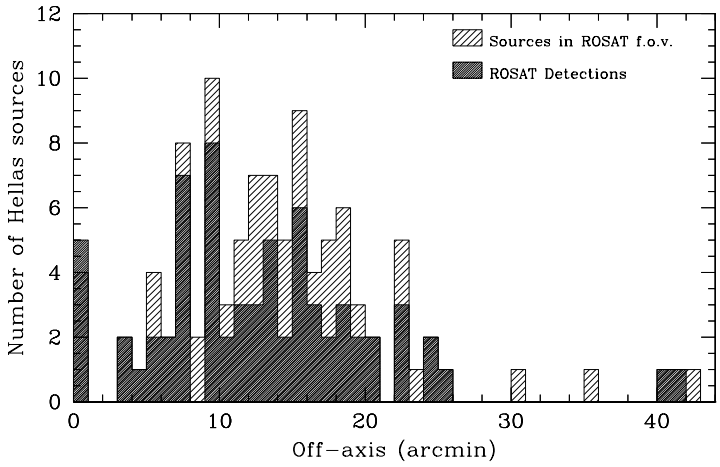

Figure 4.4: Distribution of the off-axis angles for the HELLAS sources detected by *ROSAT* with respect to the total.

found by Voges et al. 1999 for point-like sources). Only for three sources the optical and the *ROSAT* positions seem to be different: in one case the most likely explanation is that the X–ray emission comes from a group of galaxies (the likely counterpart of the HELLAS source) and not from a single object (which is confirmed by the presence of some optical emission-line objects in the BeppoSAX error box). In the other cases, the X–ray sources are clearly extended and identified as a Type 1.9 AGNs and a cluster.

4.4.4 HELLAS sources undetected by *ROSAT*

The off-axis angles (Fig. 4.4) and the exposure times (Fig. 4.5) distributions of the 68 detected sources are not statistically different from those of the 36 undetected sources (within the intrinsic width of the distribution, confidence level of 13 and 49 %, respectively – according to the Kolmogorov-Smirnov test – that the two subsamples are drawn from the same parent population).

Indeed, the average off-axis angle for the detected (undetected) subsample is 13.5 arcmin (16.4), with a dispersion of 8 (9.2) arcmin. The same applies to the exposure times, that for the *ROSAT*-detected sources being 12.8 ks (against 12.6 ks for the undetected ones).

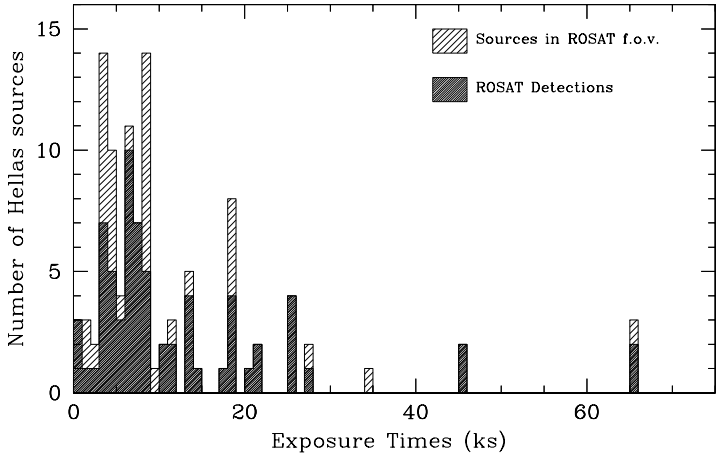

Figure 4.5: Distribution of the exposure times for the HELLAS sources detected by *ROSAT* with respect to the total.

X–ray absorption is likely to play a major role in "hiding" a fraction of objects, thus making them extremely faint or even absent in the soft X–rays. This is confirmed by computing the average *BeppoSAX* softness ratio (SR=(S−H)/(S+H), where S=1.3–4.5 keV and H=4.5–10 keV band) for the subsamples which are detected and undetected by *ROSAT*, the former having SR = 0.037 (dispersion=0.363), the latter SR = −0.314 (dispersion = 0.424), this value corresponding to $N_{\rm H}$ $> 10^{23}$ cm^{-2} at any redshift. This is a further clear indication that absorption plays a major role in the soft X–ray detection/undetection of the HELLAS sources.

Among the 12 sources which are spectroscopically identified without being detected by *ROSAT* , there are 2 high-z Type 1 objects (z = 0.953 and z = 2.386), 3 emission-line galaxies, 1 red quasar and 6 Type 1.8-2. These objects, on the basis of the X–ray analysis performed with *BeppoSAX* , are likely to be affected by absorption, their mean softness ratio being <SR> $\simeq -0.228$ ($N_{\rm H} > 10^{23}$ cm^{-2} at z > 0.015).

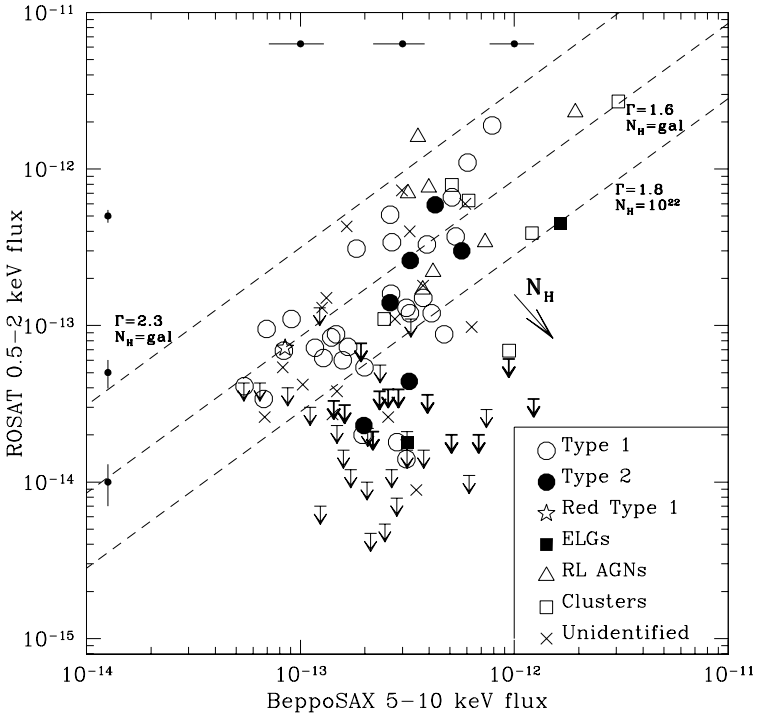

Figure 4.6: *BeppoSAX* 5–10 keV flux against *ROSAT* 0.5–2 keV flux. The upper limits for the spectroscopically identified sources appear thicker in the plot. The dashed lines indicate the expectations for Γ=2.3, 1.6 and Galactic absorption, and Γ=1.8 plus $N_{\rm H}$=10^{22} cm^{-2}, from top to bottom. Errors are plotted separately (for three flux intervals). The errors associated to *BeppoSAX* and *ROSAT* fluxes are plotted separately (for three flux intervals).

4.5 *ROSAT* results

4.5.1 Absorption

The *BeppoSAX* 5–10 keV and *ROSAT* 0.5–2 keV fluxes are reported in Fig. 4.6. The dashed lines indicate the fluxes expected for a spectral slope of Γ=2.3 and Γ=1.6 (with the average Galactic absorption of the present distribution: $\sim 3\times10^{20}$ cm^{-2}), and Γ=1.8 plus $N_{\rm H}$=10^{22} cm^{-2}, from top to bottom. It appears clear that for a significant fraction

of the objects intrinsic absorption and/or flatter spectral slopes are required in order to reproduce the observed flux ratio. It must be kept in mind that the values derived from Fig. 4.6 are only indicative and may be considered as lower limits on the presence of X–ray absorption, since any additional component in the *ROSAT* energy range would increase the soft X–ray flux, and that source variability between the observations with the two satellites may affect the results. However, since the amplitude of nuclear variability scales as (about) the inverse of the luminosity (Nandra et al. 1997), for the majority of the objects of the present subsample (with an average 0.5–2 keV luminosity of $\sim 10^{44}$ erg s^{-1}) variability is unlikely to significantly affect the present results.

In order to provide a further evidence of the presence of strong absorption in the HELLAS sources, the upper limits for the sources which went undetected in the *ROSAT* band are also plotted in Fig. 4.6. The thicker upper limits are relative to the 12 spectroscopically identified sources (cfr. § 4.4.4). It can be seen that the upper limits are extremely concentrated in the region characterized by high absorbing column densities: this is a further indication of the role of absorption in hiding the HELLAS sources, despite of their optical classification.

Similar results can be obtained by plotting the 5–10 keV to 0.5–2 keV flux ratios as a function of redshift (Fig. 4.7) for Type 1 and Type 2 sources. In order to provide an estimate of the absorption at the source redshift, three curves corresponding to Log$N_{\rm H}$ = 22, 22.5 and 23 cm^{-2} are also plotted. The underlying assumed spectrum is a power law with $\Gamma = 1.8$. It is evident that about half of the sources require absorption in excess to 10^{22} cm^{-2} and, among them, many are associated to broad-line objects (Seyfert galaxies and quasars). Viceversa, 3 out of 4 Type 2 AGNs are consistent with $N_{\rm H} < 10^{22}$ cm^{-2}. We also note a trend of increasing hardness with redshift, which is more pronounced for Type 1 objects.

A similar trend can be found by adding *ASCA* Large Sky Survey (Akiyama et al. 2000) broad-line objects (open symbols in Fig. 4.8) to the HELLAS ones. The increasing hardness with redshift, parameterized by the relation $F_{\rm hard}/F_{\rm soft} \propto z^{0.7}$, is particular evident at z > 0.3 and could be ascribed to a flattening of the primary X–ray spectral slope at moderate/high redshift, as tentatively suggested by Vignali et al. (1999) for a small sample of high-z radio-quiet quasars.

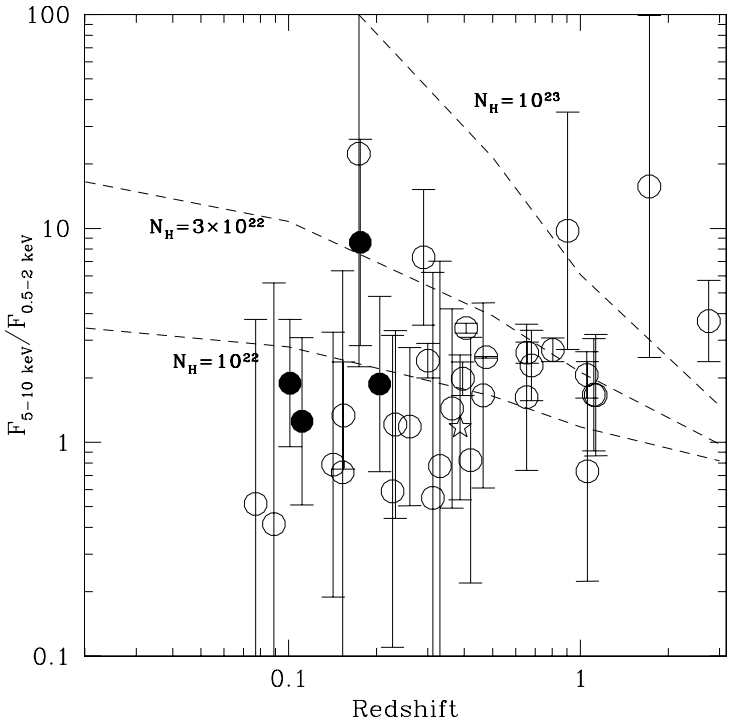

Figure 4.7: *BeppoSAX* 5–10 keV to *ROSAT* 0.5–2 keV flux ratios as a function of redshift. Only the HELLAS sources classified as Type 1 (radio-quiet), Type 2 and the red quasar are plotted (symbols are as in the previous figure), along with three curves representing different column densities ($N_{\rm H}$ = 10^{22}, 3×10^{22} and 10^{23} cm^{-2}, assuming a power-law spectrum with Γ = 1.8).

Even though the large majority of Type 1 objects of Fig. 4.8 can be parameterized by a variety of spectral slopes ranging from Γ = 1.0 to Γ = 2.0 (the short-long dashed lines), the flux ratios of some sources are not well reproduced, clearly suggesting that absorption is a better explanation, in line with *BeppoSAX* softness ratio predictions. A combination of both these effect, absorption and flattening with redshift, is also plausible.

The presence of absorbed Type 1 can be suggested by Fig. 4.6, where for a large fraction of *BeppoSAX* sources optically identified as broad-line objects the hard and soft X–ray fluxes suggest spectral

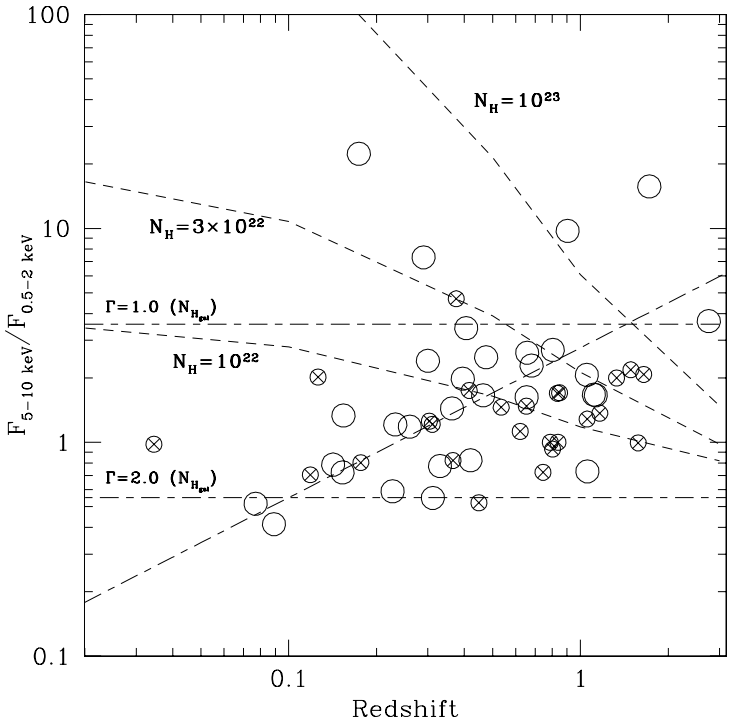

Figure 4.8: 5–10 keV to 0.5–2 keV flux ratios for the HELLAS (as in the previous figure, big open symbols) and the *ASCA* LSS broad-line objects (small crossed symbols). The long dashed line shows the best-fit $F_{\rm hard}/F_{\rm soft}$ – redshift correlation for Type 1 objects of both the samples, while the short-long dashed lines indicate the flux ratios expected for a Γ=1.0 and 2.0 power-law and Galactic absorption.

slopes much harder than $\Gamma = 1.6$. This finding could indicate that the X–ray obscuration is uncorrelated with the optical reddening, thus pointing towards a more complex picture of the Active Galactic Nuclei properties (Comastri et al. 2000; Vignali, Comastri & Fiore 2000b).

4.5.2 Soft X–ray components

The broad-band X–ray spectrum has been investigated by selecting a subsample of 12 HELLAS sources spectroscopically identified as broad-line (radio-quiet) objects, whose softness ratio (as a function

of redshift) indicates the presence of substantial intrinsic absorption ($N_{\rm H} > 5 \times 10^{22}$ cm^{-2} at the source rest frame). For these sources the 0.5–2 keV flux which is expected by extrapolating the *BeppoSAX* flux in the *ROSAT* band (under the assumption of a $\Gamma = 1.8$ power-law continuum absorbed by the $N_{\rm H}$ obtained by the softness ratio analysis with *BeppoSAX*) has been calculated. These values have been subsequently compared to the observed 0.5–2 keV fluxes obtained directly from the present analysis.

Among the 12 Type 1 objects, 5 sources have *ROSAT* fluxes which agree with the predicted ones within 10 %, while for 6 of the remaining objects, in order to reproduce the observed *ROSAT* flux, an additional component is strongly required, with a moderate/high fraction (from 25 to 65 %) of the nuclear (5–10 keV) radiation being reprocessed in soft X–ray radiation and re-emitted. The remaining source is characterized by a soft X–ray flux higher than the 5–10 keV flux, clearly pointing towards a prominent soft excess in this object.

Similar values (from 5 to 35 %) have been obtained for the 2 Type 2 objects which appear absorbed in *BeppoSAX* and which are detected by *ROSAT* .

The true nature of the soft component is far from being clear: it could be due to nuclear photons spilling from a partial covering screen, or reflected by a warm/hot medium or, alternatively, it could be thermal emission from starburst regions and winds. At the present it is difficult to shed light on the nature of this component on the basis of these X–ray data only, unless *Chandra* or *XMM-Newton* follow-up observations will be performed.

4.6 Comparison with the *ROSAT* Deep Survey sample

In order to further investigate the soft X–ray properties and the nature of the HELLAS hard X–ray selected sources, the present sample has been compared to that of similar size extracted from the *ROSAT* Deep Survey in the Lockman Hole (hereafter RDS, Hasinger et al. 1998; Schmidt et al. 1998; Lehmann et al. 2000) which is soft X–ray-selected and fully identified at a limiting X–ray flux of 5.5×10^{-15} erg cm^{-2} s^{-1} (0.5–2 keV).

Figure 4.9 shows the redshift distribution of the HELLAS

subsample detected by *ROSAT* with that of the RDS sample, the latter peaking at higher z, whereas Fig. 4.10 and Fig. 4.11 show the location of the sources in the 0.5–2 keV – redshift plane.

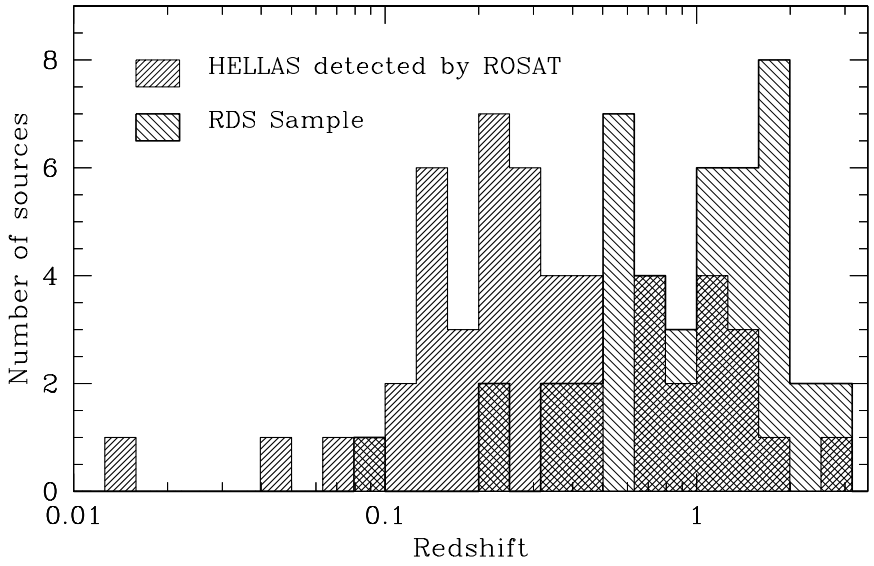

Figure 4.9: Redshift distribution of the HELLAS and the RDS sources.

The X–ray properties of the two samples have been then compared by means of hardness ratios HR1 and HR2 (cfr. Sect. 4.4.1). Figure 4.12 and Fig. 4.13 show the plot of the hardness ratios HR1 vs. HR2 for the HELLAS and the RDS sources, respectively.

It appears clear that most of the HELLAS sources populate the hardest region (HR1 > 0, HR2 > 0) of the diagram. A comparison of this diagram with the results from the Lockman Hole sources indicates that the X–ray colors are generally harder for the HELLAS sources.

A two-dimensional Kolmogorov-Smirnov test performed on the hardness ratios of the two samples statistically confirms the previous finding by providing a probability of 3×10^{-6} that the RDS and the HELLAS sources belong to the same parent population.

It must be noted, however, that HR1 is very sensitive even to relatively small values of the Galactic absorption (Fig. 4.14). While the Lockman Hole sources are absorbed only by a Galactic column

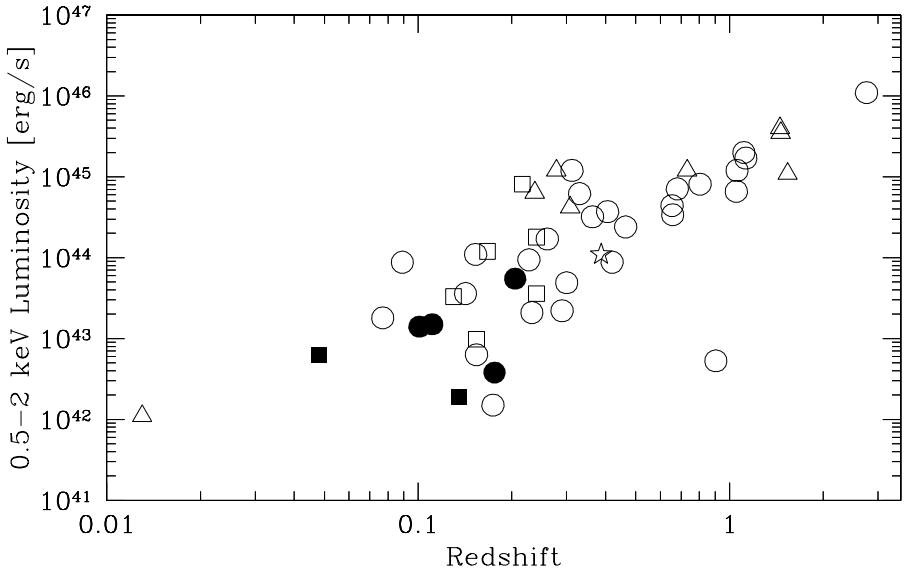

Figure 4.10: 0.5–2 keV Luminosity vs. Redshift for the HELLAS sources.

density of the order of 5.7×10^{19} cm^{-2}, the HELLAS sample spans a wide range of Galactic $N_{\rm H}$, from 5.7×10^{19} cm^{-2} (two sources detected in the Lockman Hole) to 1.1×10^{21} cm^{-2} (only one source having this $N_{\rm H}$), with an average column density of 2.6×10^{20} cm^{-2} (see Fig. 4.15 for the distribution of the sources as a function of the Galactic $N_{\rm H}$). This means that a simple comparison of HR1 hardness ratios for the two samples, as showed in Fig. 4.16, should take into account the effect due to the different $N_{\rm H}$ distribution, the net effect being a shift of the HR1 distribution up to 0.5–0.6 (Fig. 4.14). Therefore, since a meaningful comparison between HR1 for the two samples is not possible, a more reliable result can be obtained by comparing HR2, which is much less sensible to the Galactic absorption. Indeed, given the HELLAS $N_{\rm H}$ distribution, the effect of absorption is only marginal and could give rise to an increase in HR2 of only 0.05–0.1 (Fig. 4.17), a value which is within the statistical errors. The result is that the HR2 distribution of the HELLAS sample is intrinsically different from that obtained for the Lockman Hole sources (Fig. 4.18), as confirmed by the Kolmogorov-Smirnov test (probability of 10^{-6} that the two samples derive from the

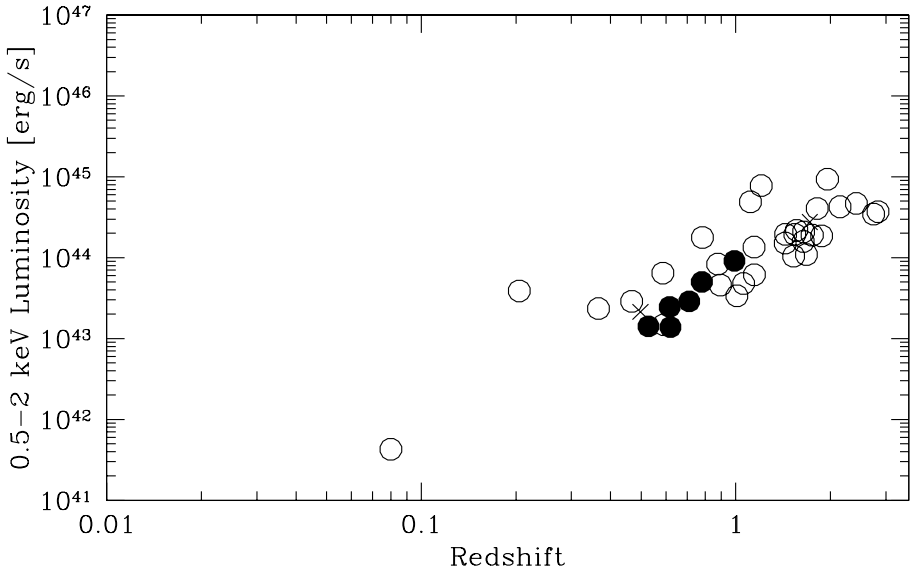

Figure 4.11: 0.5–2 keV Luminosity vs. Redshift for the RDS sources. Open circles: Type 1 objects (classes "a, b, c" in Lehmann et al. 2000); filled circles: Type 1.8–2 objects (class "d"); crosses: groups & galaxies (class "e").

same parent population). The differences observed in the color-color diagram between the two samples are also evident in the color-redshift distribution. In particular, the HR2 of the HELLAS sources (Fig. 4.19) populates, on average, a harder region of the diagram than the RDS sources (Fig. 4.20). This result confirms again we are sampling the hard (absorbed) tail of the distribution of the sources responsible for the XRB.

It is interesting to note that the hardest HELLAS sources show a large variety of optical identifications, including both Type 1 AGNs and Type 2s. This result is corroborated by plotting the *BeppoSAX* softness ratio vs. *ROSAT* HR2 (Fig. 4.21), where the hardest sources populate the lower right region.

This variety may be found, even though based on a smaller number of objects, in the Lockman Hole sample, where in the hardest part of the color-color diagram (Fig. 4.13) there are two Type 2 objects,

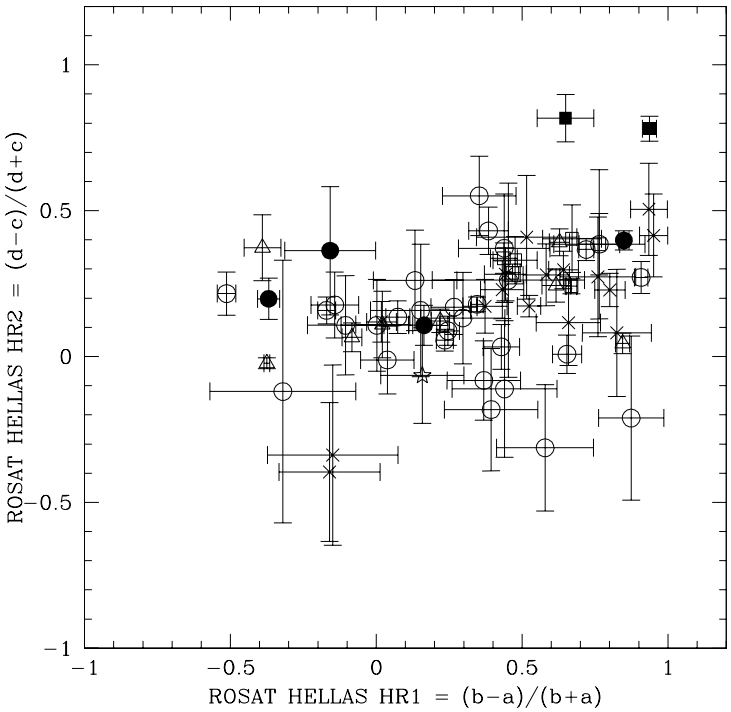

Figure 4.12: *ROSAT* HR1 vs. HR2 for the HELLAS sources.

two R−K > 5–6 sources (candidate EROs, Extremely Red Galaxies; see Lehmann et al. 2000 for a detailed discussion) and two Type 1 objects, whose redshifts (1.561 and 2.832) and hard X–ray colors seem to confirm *BeppoSAX* findings about X–ray absorbed Type 1s. All the previous results indicate that hard X–ray selection provides a significant fraction of absorbed objects, characterized by varied optical properties and classifications (broad-line AGNs, narrow-line AGNs, emission-line galaxies). X–ray absorbed objects are however present also in soft X–ray selected samples, even though at a lower level. Most interesting, a large fraction of hard X–ray-selected objects is present in *ROSAT* : the obscured constituents of the XRB progressively show up going to fainter fluxes and harder energy ranges.

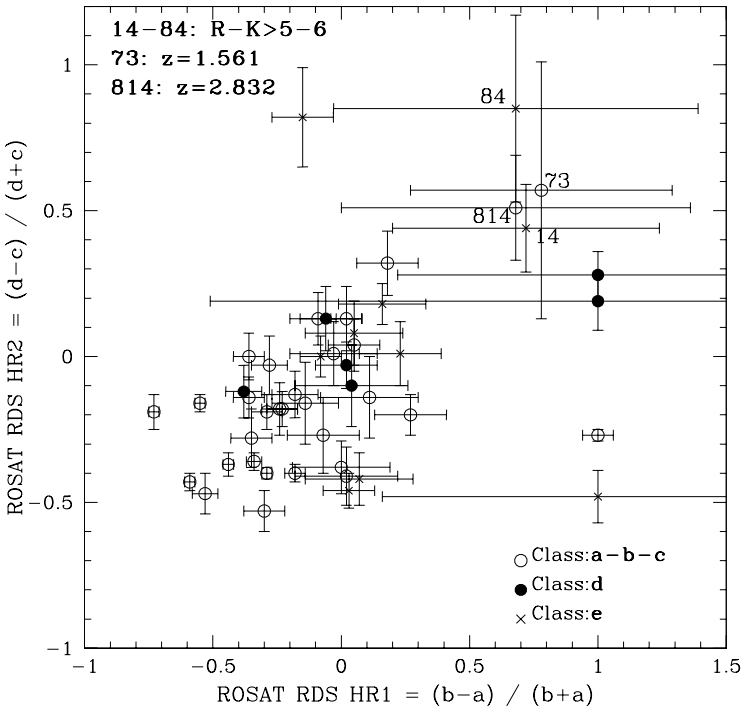

Figure 4.13: *ROSAT* HR1 vs. HR2 for the Lockman Hole sources. Symbols are as in Fig. 4.11.

4.7 Discussion and conclusions

The recent hard X–ray surveys performed by *ASCA*, *BeppoSAX* and *Chandra* have revealed that the population responsible for the hard X–ray background has quite varied multi-wavelength properties. According to AGNs synthesis models (i.e. Comastri et al. 1995), these sources must be characterized by a spectral energy density spanning a wide range of luminosities and absorption column densities, in order to reproduce both the XRB spectrum and the source counts in different energy ranges. In particular, the energetically dominant contribution comes from sources around the knee of the X–ray luminosity function ($L_{\rm X} \sim$ a few 10^{44} erg s^{-1} at z = 1) and with absorbing column densities of the order of 10^{23} cm^{-2} (Comastri 2000). These objects, the so-called "QSO 2", i.e. quasars with optical narrow-emission lines, have been

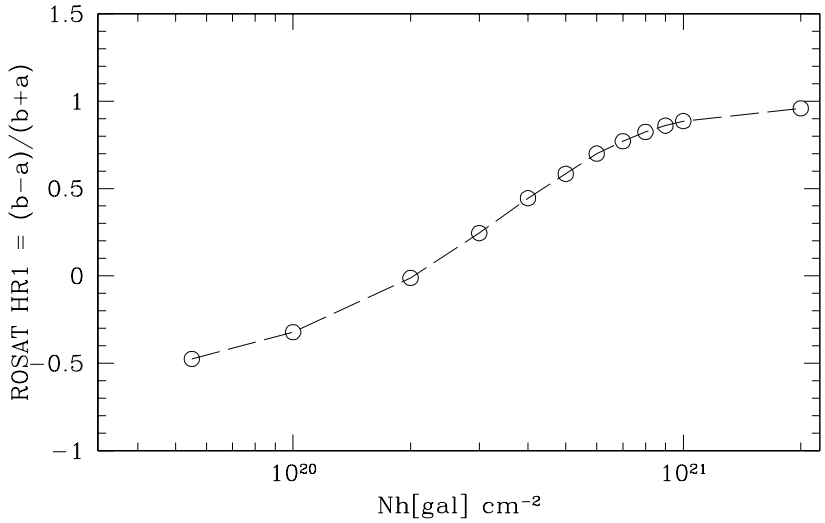

Figure 4.14: *ROSAT* HR1 as a function of Galactic column density.

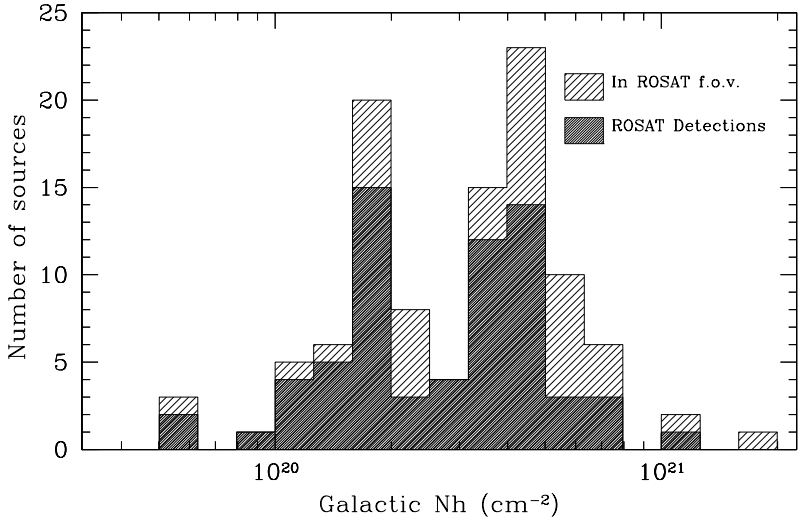

Figure 4.15: Distribution of the sources (detected: red; full *ROSAT* sample: yellow) as a function of Galactic absorption.

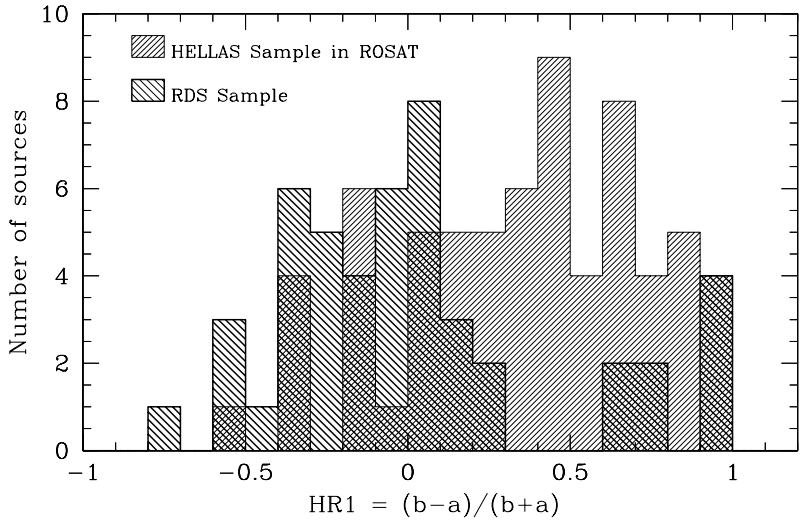

Figure 4.16: *ROSAT* HR1 distribution for the HELLAS and the RDS sources.

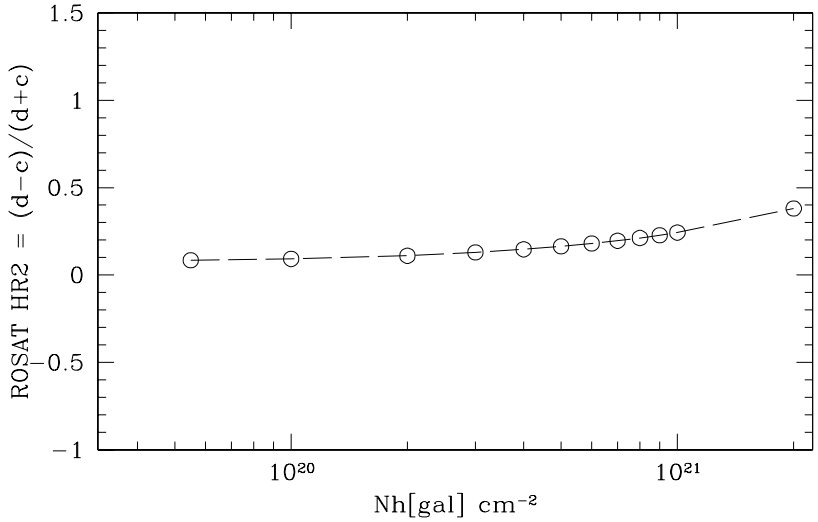

Figure 4.17: *ROSAT* HR2 as a function of Galactic column density.

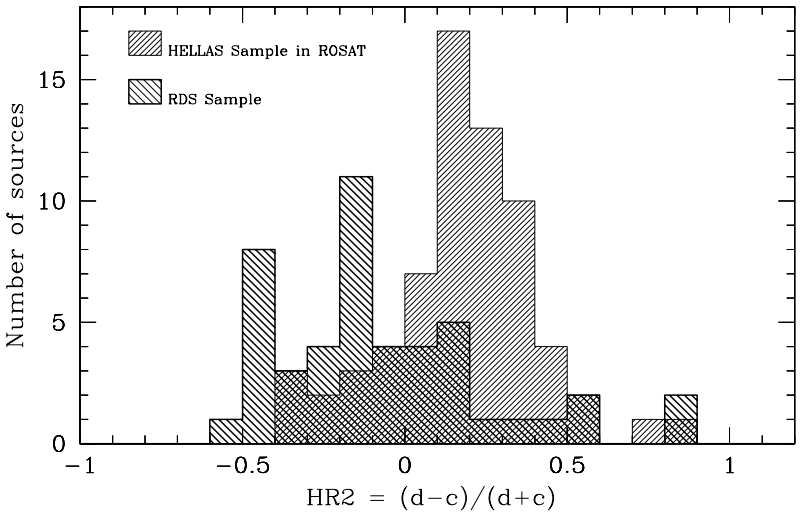

Figure 4.18: *ROSAT* HR2 distribution for the HELLAS and the RDS sources.

extensively searched, but, at present, only a handful of candidates have been found (Ohta et al. 1996; Akiyama et al. 2000; Della Ceca et al. 2000a). Results from recent hard X–ray surveys and the ones presented in this chapter indicate that X–ray absorption is not correlated with the optical reddening, hence the classical statement of unobscured Type 1 – obscured Type 2 objects is far from being always valid. Indeed, Type 1 AGNs characterized by hard X–ray colors, likely to be absorbed by column density of the order of 5×10^{22} cm^{-2} or greater, have been found by both *BeppoSAX* and *ASCA* surveys (and through pointed observations, see Brandt, Laor & Wills 2000b), and their role in contributing to the XRB may be exactly the same of the postulated Type 2 QSOs.

Analogously, the fact that the optical appearance of X–ray obscured sources is far different from what expected (i.e. narrow line AGNs) has been recently confirmed by the discovery by Fiore et al. (2000b) of a galaxy which is inactive in the optical but extremely emitting in the X–rays.

The emerging picture is that the zoo of the hard X–ray-selected sources is characterized by more complex properties than previously

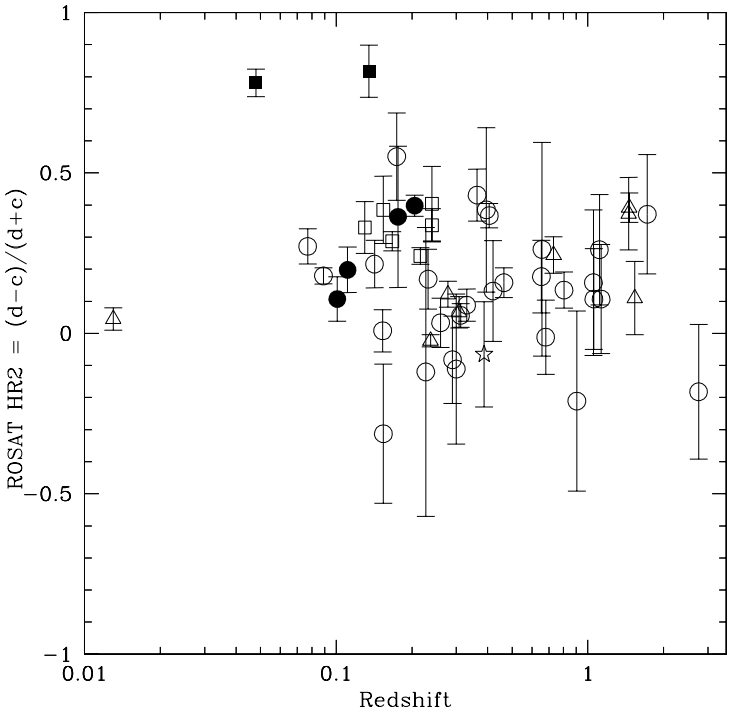

Figure 4.19: HR2 vs. redshift for the HELLAS sources.

thought (Comastri et al. 2000; Vignali et al. 2000b).

Another interesting result comes from the relatively high number of HELLAS hard X–ray selected sources revealed by *ROSAT* . This is due to a combination of effects, the most important being the high sensitivity of *ROSAT* also at faint flux levels and the presence of soft X–ray emission also in strongly obscured AGNs. The most important implication is that the same highly absorbed sources responsible for a sizeable fraction of the hard XRB emit in the soft X–rays (Giommi et al. 2000; Giacconi et al. 2001), where they confirm their hardness. In some cases it was found that this emission is enhanced, with respect to the extrapolation at low energies of the absorbed higher energy component, by Compton down-scattering or through a thermal component. For a subsample of HELLAS sources it has been possible to provide an estimate of the relative fraction of this scattered component with respect to the nuclear flux, spanning from a few to 65 per cent.

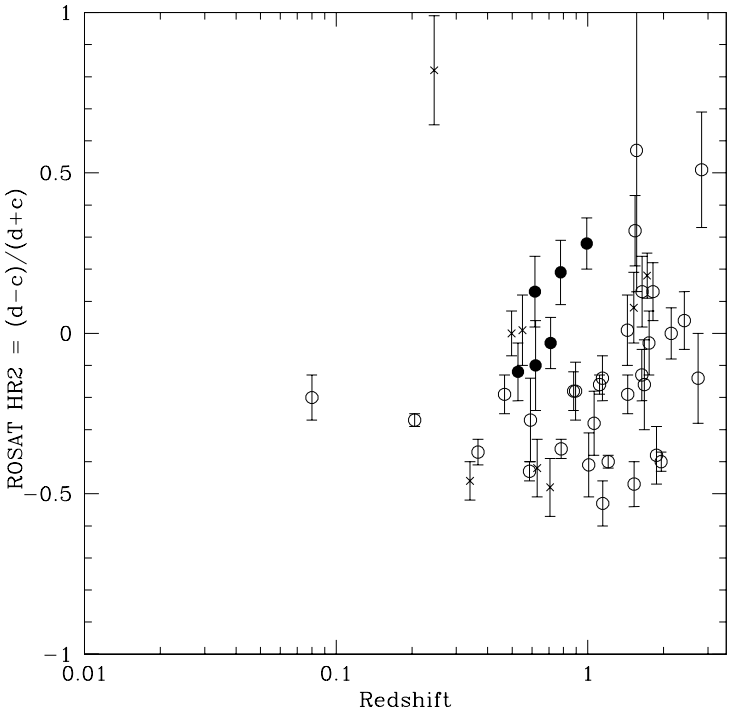

Figure 4.20: HR2 vs. redshift for the Lockman Hole objects.

Although this component is not energetically dominant (indeed it is not present in the XRB synthesis model by Comastri et al. 1995), it could be important when comparing surveys performed in different energy ranges and, most important, at limiting fluxes differing by one (or more) order of magnitude. This has interesting consequences also in the computation of the X–ray luminosity function for the sources responsible for the XRB, since the contribution from this additional component is taken into account as it was of nuclear origin, not due either to reprocessing of the primary radiation or to thermal emission.

Remarkably, the *ROSAT* analysis indicates that a significant number of HELLAS sources are characterized by hard X–ray colors also in soft X–rays. The broad-band analysis of the sources which are not detected by *ROSAT* (upper limits in Fig. 4.6) suggests that truly hard sources (where the soft X–ray emission is extremely faint or totally absent) do exist. There are evidences that such sources have also been

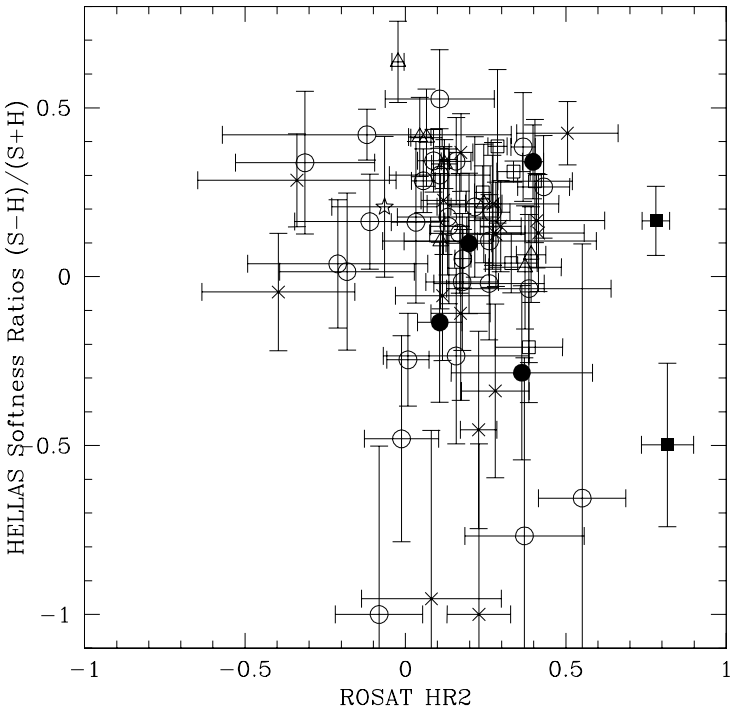

Figure 4.21: HR2 vs. *BeppoSAX* Softness Ratio for the HELLAS sources.

detected by *XMM-Newton* in the Lockman Hole (Hasinger et al. 2001).

The comparison of the color-color properties of the present sample with those of the ROSAT Deep Survey (Hasinger et al. 1998) in the Lockman Hole confirms that we are sampling the hard tail of the distribution of the sources responsible for the XRB, where the hardness of the spectrum may be ascribed to a flat continuum or, more convincingly, to large amounts of X–ray absorption, or to a combination of both the factors. Even though the HELLAS sources are harder in soft X–rays than the RDS objects, it is straightforward to note a continuity of properties between the two samples, with a optically varied population of hard sources in both.

Source ID	RA (J2000)	DEC (J2000)	Class.	Count Rate ($\times 10^{-2}$ c/s)	$F_{0.5-2\ keV}$ ($\times 10^{-13}$ cgs)	HR1	HR2	ROR #	Off-axis (arcmin)	Exposure (ks)	$N_{H_{gal}}$
20	01 40 14.7	−67 48 55.2	⋆	0.20±0.04	0.22	0.159±0.200	−0.252±0.194	300043p	6.2	14.8	
45	03 15 47.5	−55 29 5.2	1	1.24±0.06	1.6	−0.170±0.031	0.158±0.046	701036p	15.6	45.8	2.88
46	03 17 32.7	−55 20 24.9	1	1.22±0.06	1.2	0.720±0.026	0.367±0.038	701036p	20.7	45.8	2.88
53	04 37 11.9	−47 31 43.2	1	2.36±0.24	3.4	−0.513±0.032	0.216±0.074	701184p	19.7	6.1	1.74
54	04 38 46.2	−47 27 56.9	RLQ	1.09±0.17	0.88	−0.390±0.063	0.373±0.113	701184p	22.2	6.1	1.78
57	05 20 49.0	−45 41 31.2		5.24±0.37	6.0	0.018±0.051	0.119±0.070	700057p	12.6	4.4	4.09
65	06 46 38.0	−44 15 34.8	1	4.92±0.32	5.9	0.654±0.050	0.008±0.066	300226p	15.9	5.5	6.19
66	23 19 31.2	−42 42 11.1	1.8	2.16±0.22	3.0	0.164±0.053	0.107±0.069	700333p	22.8	7.2	1.96
72	03 33 12.4	−36 19 46.7	Bl Lac	6.07±0.30	7.6	−0.083±0.034	0.066±0.049	700921p-1	12.3	7.7	1.47
73	03 36 55.9	−36 15 55.9	RLQ	2.71±0.30	1.7	0.021±0.091	0.110±0.114	700921p-1	41.0	7.7	1.40
75	03 34 6.9	−36 03 55.3	1	0.19±0.05	0.20	0.874±0.112	−0.211±0.281	700921p-1	7.7	7.7	1.37
84	13 36 39.2	−33 57 52.4	RadGal	4.84±0.17	7.0	0.845±0.024	0.045±0.035	600268p-1	0	18.4	4.10
85	22 02 59.9	−32 04 37.4	1	0.20±0.05	0.18	0.439±0.157	0.371±0.186	800419p-1	13.3	13.5	1.62
92	13 48 45.1	−30 29 40.3	1	5.57±0.10	6.6	0.246±0.039	0.088±0.050	700907p	13.3	8.2	4.39
103_1	00 45 44.4	−25 15 29.9	1.9	1.10±0.13	2.6	−0.369±0.038	0.198±0.071	600087p-0	25.3	11.6	1.42
107	00 48 8.4	−25 04 56.0		0.32±0.06	0.38	0.583±0.079	0.280±0.106	600087p-0	14.5	11.6	1.52
124	00 27 9.5	−19 26 16.0	1	6.18±1.72	3.1	−0.320±0.250	−0.120±0.450		††	0.3	1.85
137	09 46 37.4	−14 07 46.0	1	0.44±0.06	0.44	0.369±0.126	−0.082±0.136	701458p	17.8	18.6	4.10
147	20 42 52.9	−10 38 33.0	1	3.69±0.41	3.7	0.385±0.068	0.431±0.081	701362p	20.7	3.3	4.10
149	20 44 34.7	−10 27 54.4	1	0.44±0.13	0.54	0.394±0.160	−0.182±0.210	701362p	16.5	3.3	4.20
150	13 05 32.9	−10 33 15.9	RLQ	19.8±0.08	23.0	0.220±0.031	0.122±0.040	701195p	0	3.2	3.33
151	13 04 33.0	−10 24 37.6	1	0.61±0.17	0.62	0.152±0.172	0.158±0.227	701195p	19.6	3.2	3.35
157	12 56 12.8	−05 56 28.2	1	0.94±0.15	1.1	0.279±0.144	0.132±0.157	700305p-0	9.1	4.9	2.25
167	12 40 27.3	−05 13 57.5	1	1.41±0.36	1.3	0.440±0.180	−0.111±0.234	701012p	13.8	1.3	2.28
172	02 42 1.2	00 00 26.6	1	0.64±0.12	0.88	0.133±0.143	0.261±0.172	150021p-2	9.9	5.5	3.45

Source ID	RA (J2000)	DEC (J2000)	Class.	Count Rate ($\times 10^{-2}$ c/s)	$F_{0.5-2\ keV}$ ($\times 10^{-13}$ cgs)	HR1	HR2	ROR #	Off-axis (arcmin)	Exposure (ks)	$N_{H_{gal}}$
174	02 42 11.0	00 02 2.2		0.37±0.09	0.26	0.760±0.130	0.273±0.205	150021p-2	7.9	5.5	3.46
176	13 42 56.5	00 00 57.0		0.95±0.07	1.2	0.074±0.041	0.135±0.056	701000p-1	17.3	27.8	1.91
185	05 15 15.7	01 09 19.5		1.24±0.20	1.3	0.951±0.048	0.415±0.142	300352p	7.7	3.1	10.9
190	16 52 38.4	02 22 3.9	1	0.44±0.13	0.34	0.765±0.156	0.385±0.256	701035p-1	5.7	3.2	5.75
201	16 49 59.2	04 53 37.6	Cl.	0.75±0.13	0.69	0.765±0.070	0.385±0.105	701611p	18.2	8.1	6.35
209	23 27 29.2	08 49 28.0	1	0.52±0.13	0.41	0.579±0.166	−0.313±0.217	600234p	7.7	3.9	5.21
212	23 02 33.0	08 57 1.2	ELG	0.23±0.04	0.18	0.649±0.097	0.817±0.081	700423p	11.3	18.6	4.91
229	23 31 54.7	19 38 29.0	1	0.64±0.14	1.5	†	†	201697h	15.6	6.3	4.29
230_1	15 28 48.1	19 38 52.7	1	0.94±0.36	0.60	0.453±0.261	0.262±0.333	180175p	5.8	0.8	4.60
230_2	15 28 45.1	19 44 34.0		3.69±0.72	4.3	0.935±0.063	0.505±0.158	180175p	6.6	0.8	4.62
237	22 26 31.6	21 11 33.3	1	2.95±0.23	3.3	0.429±0.062	0.033±0.077	700856p	14.0	6.4	4.44
239	14 17 16.9	24 59 17.3	1	0.49±0.08	0.95	0.002±0.123	0.107±0.157	700536p	13.3	10.9	1.70
241	14 18 30.4	25 10 52.3	Cl.	3.51±0.19	6.3	0.438±0.046	0.337±0.052	600200p	7.3	6.6	1.70
243	08 37 37.3	25 47 50.8	1	4.24±0.27	5.1	0.908±0.023	0.271±0.055	600200p	10.9	6.6	3.64
246	08 38 58.3	26 08 18.6	ELG	3.33±0.28	4.5	0.937±0.024	0.781±0.043	600200p	24.6	6.6	3.61
250	23 55 54.0	28 35 53.6	RLQ	1.86±0.11	2.2	0.617±0.049	0.244±0.057	200002p	11.5	18.0	4.98
252	12 04 3.8	28 07 8.7	Cl.	5.51±0.17	7.9	0.467±0.027	0.287±0.030	700232p	15.8	26.0	1.68
254	22 42 47.2	29 34 18.5		0.41±0.11	0.42	−0.160±0.173	−0.396±0.238	701597p	9.7	4.3	6.35
256	22 41 23.5	29 42 45.0		6.23±0.42	7.3	0.642±0.051	0.297±0.064	701597p	16.3	4.3	6.45
264	12 18 54.8	29 59 44.1	1.9	0.16±0.03	0.23	−0.158±0.156	0.363±0.220	700221p	15.8	21.6	1.70
265	12 17 52.3	30 07 4.3	Bl Lac	13.9±0.26	16.0	−0.375±0.010	−0.023±0.019	700221p	0	21.6	1.69
278	10 34 57.0	39 39 43.1		0.52±0.16	0.27	−0.149±0.224	−0.338±0.309	700551p	3.4	4.6	0.95
279	16 54 42.0	40 01 18.6		2.00±0.22	0.98	0.443±0.072	0.282±0.091	700130p	18.3	7.6	1.81
282	11 18 47.7	40 26 46.9	1	0.56±0.10	0.84	−0.105±0.131	0.107±0.170	700801p	3.3	6.5	1.92
283	11 18 14.0	40 28 34.3	1 red	0.61±0.10	0.72	0.158±0.143	−0.065±0.164	700801p	4.3	6.5	1.91

Source ID	RA (J2000)	DEC (J2000)	Class.	Count Rate ($\times 10^{-2}$ c/s)	$F_{0.5-2\ keV}$ ($\times 10^{-13}$ cgs)	HR1	HR2	ROR #	Off-axis (arcmin)	Exposure (ks)	$N_{H_{gal}}$
288	12 19 23.2	47 09 42.6		1.29±0.07	1.5	0.801±0.052	0.228±0.057	600546p	9.9	25.7	1.15
290	12 19 52.1	47 21 0.0	1	0.34±0.04	0.72	−0.142±0.082	0.177±0.113	600546p	9.5	25.7	1.16
292	12 17 43.3	47 29 15.8		2.99±0.12	4.0	0.524±0.040	0.173±0.037	600546p	16.5	25.7	1.21
296	18 15 13.5	49 44 15.0		0.10±0.03	0.09	0.825±0.118	0.081±0.218	300067p-1	11.6	18.0	4.34
300	10 32 15.6	50 51 12.0	1	0.22±0.05	0.14	0.353±0.126	0.551±0.136	701544p	9.2	10.8	1.18
307	16 26 59.7	55 28 16.2	Cl.	6.49±0.57	3.9	0.476±0.076	0.330±0.081	701372p	9.6	2.3	1.85
319	10 54 20.2	57 25 43.1	1.8	1.17±0.05	1.4	0.849±0.018	0.398±0.033	900029p-2	18.6	65.6	0.57
321	10 32 38.3	57 31 3.4		0.17±0.02	0.54	0.659±0.110	0.116±0.147	900029p-2	9.9	65.6	0.56
364	14 38 22.0	64 31 17.9		0.21±0.06	0.26	0.516±0.172	0.409±0.212	200069p	14.5	7.4	1.68
375_2	17 43 0.0	68 00 46.3		2.75±0.33	1.1	0.432±0.074	0.229±0.099	999995p	41.5	6.4	4.38
385	07 21 36.9	71 13 25.5	1	0.60±0.06	0.69	0.267±0.079	0.169±0.093	700210p	7.1	20.7	3.84
387	11 01 48.8	72 25 44.1	RLQ	2.74±0.19	3.4	0.628±0.035	0.392±0.046	700872p	24.3	13.1	3.16
389	11 06 16.6	72 44 10.5	1	0.65±0.08	0.73	0.038±0.092	−0.012±0.116	700872p	10.3	13.1	3.17
390	11 02 37.2	72 46 38.1	1	15.5±0.04	19.0	0.346±0.020	0.179±0.025	700872p	22.4	13.1	3.36
392	07 41 44.6	74 14 41.6	Cl.	17.0±0.05	27.0	0.669±0.019	0.241±0.016	800230p	0	8.8	3.49
393	07 42 2.4	74 26 21.9		1.55±0.14	1.8	0.373±0.076	0.172±0.092	800230p	11.4	8.8	3.52
394	07 43 12.0	74 29 34.0	1	9.53±0.36	11.0	0.235±0.029	0.056±0.037	800230p	15.6	8.8	3.53
400	12 22 6.9	75 26 17.4	Cl.	1.01±0.12	1.1	0.671±0.101	0.404±0.116	700434p-1	7.8	7.4	2.97

Table 4.1: The HELLAS sources detected by *ROSAT*. † HRI data; †† RASS (*ROSAT* All Sky Survey); Galactic $N_{\rm H}$ from Dickey & Lockman (1990) in units of 10^{20} cm^{-2}; Class: 1: broad-line AGN; 1 red: broad-line QSO with a red continuum; 1.8-2: narrow-line AGN; ELG: emission-line galaxy; BL Lac: BL Lac object; RLQ: radio-loud QSO; RadGal: radio-galaxy; Cl.: cluster; ⋆: star.

Hard X–ray properties of the HELLAS sources in archival ASCA fields

5.1 Introduction

In this chapter the X–ray properties of the HELLAS sources which have been found in archival *ASCA* GIS (Gas Scintillation Spectrometers) images will be discussed. Surveys with the *ASCA* satellite have been extensively carried out in the last few years (Ogasaka et al. 1998; Della Ceca et al. 1999; Ueda et al. 1999a,b), so the aim of the present work is to obtain a better knowledge of the physics of the fraction of HELLAS sources for which the counting statistics is high enough to allow a spectral modeling over the *ASCA* energy range ($\sim$ 0.7–10 keV). In this regard, no hardness ratio analysis similar to that carried out with *BeppoSAX* data will be performed. The main reason of this approach being the intrinsically different properties characterizing *ASCA* GIS and *BeppoSAX* MECS (PSF, vignetting, sensitivity), in particular the effective area which is different between the two detectors at high energies (that of MECS being far larger than the GIS one). Practically, the low GIS effective area at E $>$ 7 keV (see Fig. 2.2) prevents from obtaining a hard X–ray survey like that performed by MECS.

Therefore, I will briefly discuss the properties of the HELLAS sources in *ASCA* fields and then I will focus on those sources characterized by relatively good statistics to ensure a spectral analysis over the 0.7–10 keV band of the GIS instrument. Among the sources detected by *ASCA* with high significance (thus allowing a spectral

analysis, 17 sources) there are Type 1s (both radio-loud and radio-quiet) and Type 2s objects, 1 cluster of galaxies and, most interesting, some sources still unidentified which seem to be characterized by complex X–ray spectra.

In Section 5.5 the X–ray properties of two objects (one red quasar and one Seyfert 1.9 galaxy) which have been deeply investigated through a multi-wavelength approach and, in particular, with pointed follow-up *ASCA* observations, will be extensively discussed.

5.2 The HELLAS sources in archival *ASCA* data

In order to further investigate the X–ray properties of the HELLAS sources, the counterparts in archival *ASCA* data have been searched for. Among the 147 sources of the *BeppoSAX* catalog, only **68** are present in *ASCA* fields. A search radius of about 2 arcmin has been assumed in the cross-correlation procedure to take into account the relative uncertainties in the position in both *BeppoSAX* MECS and *ASCA* GIS. The detections have been carried in several bands, *in primis* in the HELLAS band (4.5–10 keV) and then in the 0.7–7 keV energy interval (to enhance both the probability of detecting the sources and to minimize the contribution of the background). The detection threshold is about 3 σ for all the *ASCA* fields.

50 HELLAS sources have been detected by *ASCA* , 36 of which spectroscopically identified. There are 18 Type 1 objects (Seyfert 1 galaxies and quasars), all detected by *ASCA*, 7 Type 1.8-2 (4 detections), 5 emission-line galaxies (ELGs, including both LINERs and starburst galaxies); among these, only 3 were detected by *ASCA*), 6 RL-AGNs (6 detections), 3 clusters of galaxies (3 detections) and 1 star (which was not detected). It is important to note that in the already identified subsample, the sources which preferably went undetected are among the ELGs and the Type 1.8-2. Some checks were also performed in order to understand why some sources have not been detected by *ASCA*, even setting the detection threshold at a low level. The possible causes may be: **(a)** large off-axis angle in *ASCA* observations; **(b)** relatively low exposure time, and **(c)** the extreme hardness of the sources (as derived from *BeppoSAX* softness ratio analysis).

In Fig. 5.1 the distribution of the off-axis angles of the HELLAS sources in the *ASCA* observations are shown. It is evident that the

distribution of the detected sources vs. the undetected is similar, the mean off-axis angle being 11.8 arcmin for the former class and 13.1 arcmin for the latter. These values are consistent within the dispersions of the two distributions (about 6.5 arcmin).

Analogously, the exposure time distribution of the detected vs. undetected sources is similar enough, the former peaking at 45.3 ks, the latter at 38.5 ks. The relative histogram distribution is shown in Fig. 5.2.

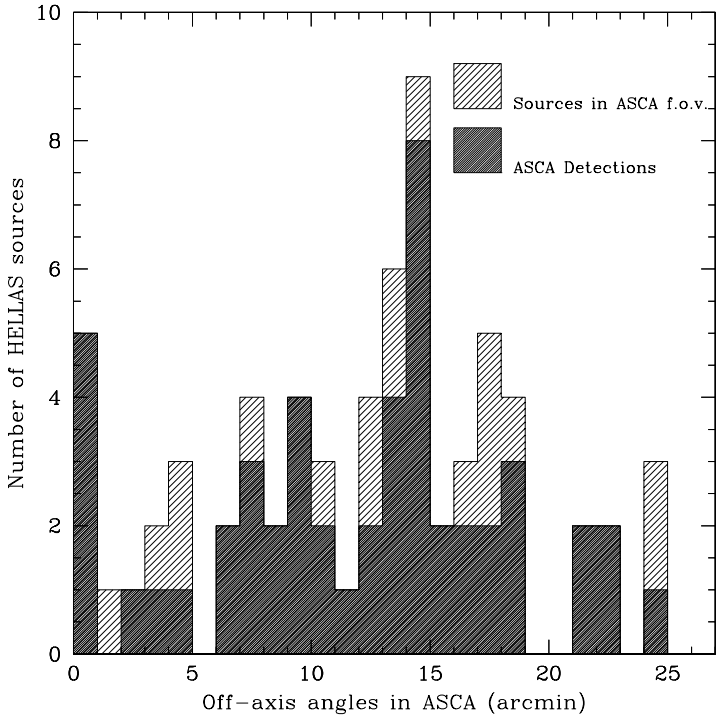

Figure 5.1: Distribution of the off-axis angles of the HELLAS sources detected by *ASCA* with respect to the total in *ASCA* field of view (f.o.v.). Note that the off-axis angles are calculated assuming the center of the GIS as its aim point (the difference being generally within a few arcmin).

Finally, the check was performed on the *BeppoSAX* softness ratio distribution (Fig. 5.3), confirming the selection bias already seen in *ROSAT*. A simple average indicates that the sources detected by *ASCA* are generally soft (mean softness ratio SR $\simeq -0.04$), whereas those

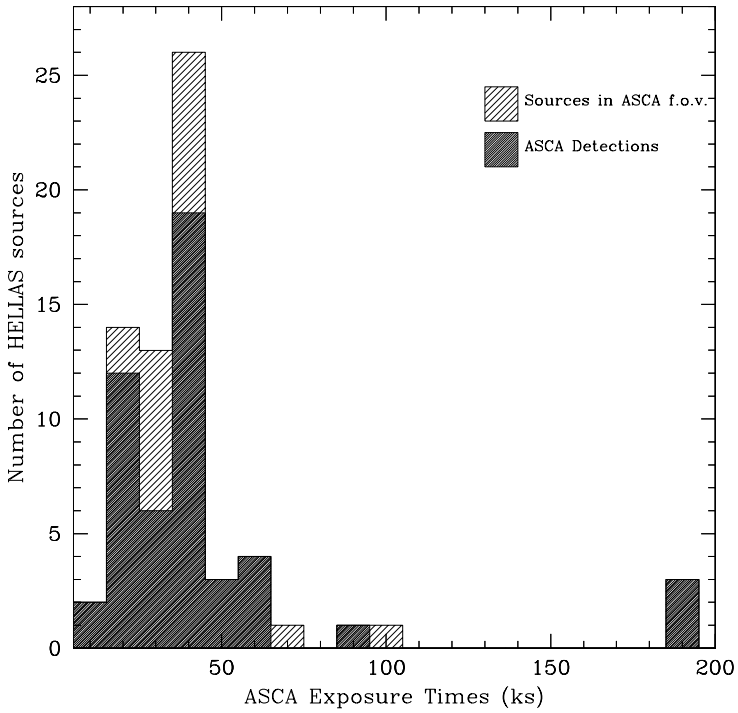

Figure 5.2: Distribution of the exposure times of the HELLAS sources detected by *ASCA* with respect to the total.

undetected are characterized by SR $\simeq -0.36$. Low (negative) values of softness ratio may be due to flat hard X–ray slopes or/and absorption (in this case greater than 10^{23} cm^{-2} at any redshift). Moreover, it must be stressed that the shape of the effective area of GIS on board *ASCA* are not well suitable to detect such hard (absorbed) objects.

5.3 *ASCA* data reduction

The *ASCA* (Tanaka, Inoue & Holt 1994) focal plane instruments consist of two solid-state imaging spectrometers (SIS, Gendreau 1995) and two gas scintillation imaging spectrometers (GIS, Makishima et al. 1996), which provide a good spectral resolution (nominal FWHM $\sim$ 2 % and $\sim$ 8 % at 5.9 keV, respectively, when the satellite was

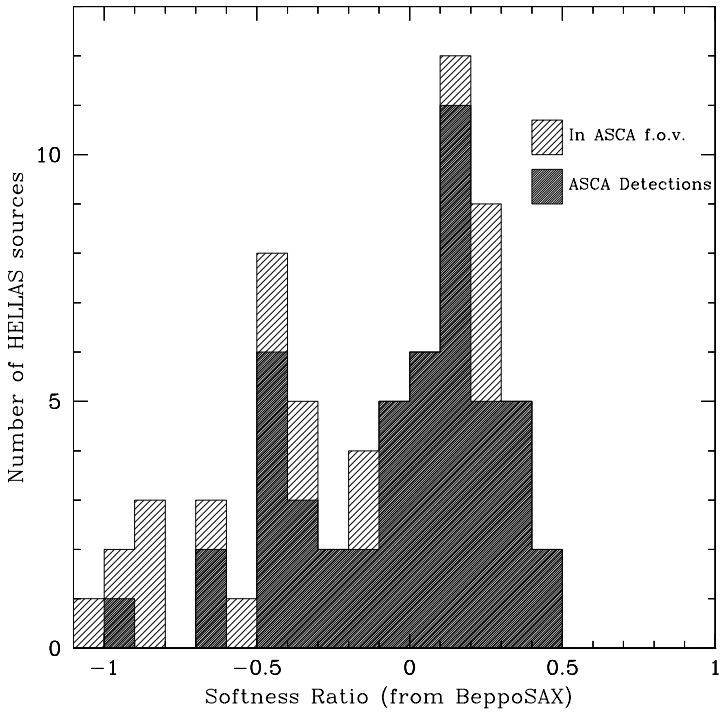

Figure 5.3: Distribution of the softness ratio (SR) of the HELLAS sources detected by *ASCA* with respect to the total.

launched), broad band ($\sim$ 0.5–10 keV) capabilities and a large (about 20 arcmin radius) field-of-view. All but three of the results concerning the HELLAS sources observed by *ASCA* have been obtained with the GIS instruments, due to the small field-of-view of the SIS instruments (11 arcmin for each square chip). For three HELLAS source GIS+SIS data are available, since these were the targets of the *ASCA* pointings. The two *ASCA* follow-up observations will be discussed apart (§ 5.5). The observations which have been used in the spectral analysis of the HELLAS sources were generally performed in FAINT mode and then corrected for dark frame error and echo uncertainties (Otani & Dotani 1994). The data were screened with the version 2.0 of the XSELECT package, in order to include only data collected when: the spacecraft was outside the South Atlantic Anomaly; the radiation belt monitor was less than 100 counts s^{-1}; the magnetic cut-off rigidity was greater

than 6 GeV c^{-1} for SIS and 4 GeV c^{-1} for GIS; the elevation angle above the Earth limb greater than 5° and the angle above the Sun-illuminated Earth limb greater than 15°. For the GIS data, the recently available method of rejecting "hard particle flares" using the so-called HO2 count rate was employed, as well as the standard "rise-time" criteria. "Hot" and flickering pixels were removed from the SIS using the standard algorithm. SIS grades 0, 2, 3 and 4 were considered in the data reduction. The source counts were extracted from regions of sizes different from observation to observation, to maximize the signal-to-noise ratio. In order to find the best-extraction radius, each *ASCA* image has been smoothed (following the procedure described in section 2.2.1). In such a way, the radius maximizing the source counts has been derived quite easily, generally spanning in the range 3–6 arcmin for the GIS and being ~ 3.5 arcmin for the SIS. Background spectra were extracted from source-free regions of the same field-of-view for GIS and from the same CCD chip for SIS. For the SIS datasets, appropriate detector redistribution matrices were generated using the ftool sisrmg (v1.1). For the GIS data, the 1995 response matrices gis2v4_0.rmf and gis3v4_0.rmf were used, while ancillary response files were created with the ftool ascaarf (v3.0). Spectral analysis has been carried out with version 11.0 of the XSPEC program (Arnaud 1996).

5.4 Spectral analysis and results

For a subsample of HELLAS sources it has been possible to perform a spectral analysis due to their relatively high *ASCA* 2–10 keV fluxes ($> 3 \times 10^{-13}$ erg cm^{-2} s^{-1}). Given the small number of sources expected in this bright flux range (about 1/deg^2) and the assumed radius for the *BeppoSAX* -*ASCA* cross-correlation, it is plausible to assume that all these sources are really the counterparts of the HELLAS sources. In the following spectral analysis, the objects will be divided according to their optical and radio classification even though the optical and radio properties of the HELLAS sources will be considered in chapters 6 and 7, respectively.

For the large majority of the HELLAS sources, whose X-ray spectral analysis will be described in the following, the statistics is clearly dominated by the source photons. However, since at energies above 6–7 keV background subtraction may play a crucial role, in order

to minimize this effect, more than one background spectrum has been checked before performing subtraction.

The first step of the spectral analysis has been carried out by fitting the GIS2 and the GIS3 (the two gas scintillation proportional counters) separately. When the source statistics was the same in the two detectors and the spectral analysis provided similar results (within the errors), the final fitting procedure was carried out by applying the ADDASCASPEC ftool procedure. This routine consists in summing the data of the two instruments bin per bin, after applying different weights in order to take into account any difference in the exposure times (which may exist, owing to the screening procedure described above). In the same way, also the background spectra and the ancillary response files (ARF) are combined, while the final redistribution matrix files (RMF) is either that of GIS2 or GIS3, since for two detectors there exists no difference in the channel-to-energy conversion. In some cases major problems with the GIS3 detector prevented from a jointed fit.

GIS spectra were binned with more than 20 counts per bin in order to apply χ^2 statistics. In the cases of relatively poor statistics, the number of binned counts was set to 15.

Throughout the chapter, errors are given at 90% confidence level for one interesting parameter ($\Delta\chi^2 = 2.71$, Avni 1976). Cosmic abundances have been derived by Anders and Grevesse (1989), cross sections from Balucinska-Church & McCammon (1992) and Galactic column density by Dickey and Lockman (1990). $H_0 = 50$ km s^{-1} Mpc^{-1} and $q_0 = 0.0$ are assumed throughout.

In Table 5.1 there is a summary of the main X–ray properties (best-fit spectral slope, absorption, flux and luminosity) of the HELLAS/ASCA sample.

5.4.1 The radio-loud objects

HELLAS #72: BL Lac, z=0.308

The *ASCA* spectrum of this source (Fig. 5.4) is characterized by a steep continuum ($\Gamma = 1.93^{+0.14}_{-0.10}$), typical of this class of objects (Wolter et al. 1998), with no evidence of excess absorption above the Galactic value ($N_{\rm H} = 1.47 \times 10^{20}$ cm^{-2}). The fit at E $>$ 5 keV seems to improve

Source	z	Count Rate[a] (10^{-2} c/s)	Exposure (ks)	Off-axis (arcmin)	Γ[b]/kT (keV)	$N_{\rm H}$[c] (10^{21} cm^{-2})	χ^2/dof	$F_{2-10\ keV}$ (10^{-13} cgs)	$L_{2-10\ keV}$ (10^{44} cgs)	$F_{5-10\ keV}$ (10^{-13} cgs)
RL-AGNs										
H 72	0.308	2.66±0.08	36.6	9.2	$1.93^{+0.14}_{-0.10}$	< 1.39	115/102	13.0	7.1	6.4
H 73	1.537	0.98±0.09	37.7	8.1	$1.46^{+0.56}_{-0.42}$	< 83.6	29.6/34	9.6	190	5.2
H 387	1.46	0.85±0.02	185.5	22.2	$1.60^{+0.14}_{-0.09}$	< 10.8	165/190	18.0	340	9.4
H 84†	0.013	3.76±0.15	40.2	0	$1.74^{+0.26}_{-0.29}$/0.62±0.06	$3.87^{+1.00}_{-1.13}$	253/226	12.0	8.1×10^{-3}	5.4
Cluster										
H 392†	0.216	9.97±0.22	15.7	0	.../$5.18^{+0.62}_{-0.64}$	< 1.03	209/225	42.0	11	16.0
Type 1s										
H 167	0.300	1.35±0.06	33.5	8.1	$1.88^{+0.37}_{-0.26}$	< 6.18	71.4/63	7.7	3.8	3.5
H 176	0.804	0.45±0.05	87.9	17.6	$2.18^{+1.29}_{-0.69}$	< 40.3	36.5/55	3.8	20.0	1.6
H 390	0.089	1.29±0.02	185.5	24.7	$2.14^{+0.14}_{-0.10}$	< 1.19	211/225	19.0	0.71	7.7
H 394	0.312	1.70±0.09	15.7	15.4	$2.22^{+0.26}_{-0.23}$	< 1.98	29.9/28	11.0	6.4	4.2
H 228†	0.217	0.74±0.04	62.8	0	$1.28^{+0.23}_{-0.28}$	$6.14^{+2.10}_{-4.56}$	168/157	6.2	1.3	3.5
Type 1.8–2										
H 264	0.176	0.69±0.05	36.0	11.1	$1.10^{+0.51}_{-0.32}$	< 13.5	29.7/38	7.4	1.0	4.6
H 319	0.205	0.72±0.04	59.0	6.9	$1.54^{+0.39}_{-0.32}$	< 6.62	93.5/81	10.0	2.0	5.3
H 375	0.044	1.20±0.06	50.8	0	$1.18^{+0.48}_{-0.69}$	153^{+44}_{-61}	145/116	25.0	0.38	20.0
Unid.										
H 254		0.78±0.05	50.9	1.0	1.3 unc.††	531 unc.	18.3/19	5.2		2.9
H 256		1.25±0.04	50.9	21.8	$2.31^{+0.25}_{-0.15}$	< 2.06	69.4/71	10.0		3.8
H 296		0.74±0.06	38.4	7.3	$0.23^{+0.27}$††	< 5.48	69.1/73	9.5		7.4
H 393		0.75±0.07	15.7	13.8	$1.63^{+0.78}_{-0.48}$	< 7.27	28.7/25	5.8		3.2

Table 5.1: *ASCA* spectral results obtained for the highest signal-to-noise ratio HELLAS sources.

[a] The count rates (with relative 90 % statistical errors) are given for the summed GIS2+GIS3 observation, when available.
[b] The spectral slope in the table is that of the hard (primary) power-law component.
[c] When the source redshift is known, the column density is given at the source rest frame.
† Both SIS and GIS data. The count rate is referred to GIS data.
†† See text for a more comprehensive description of the adopted model.

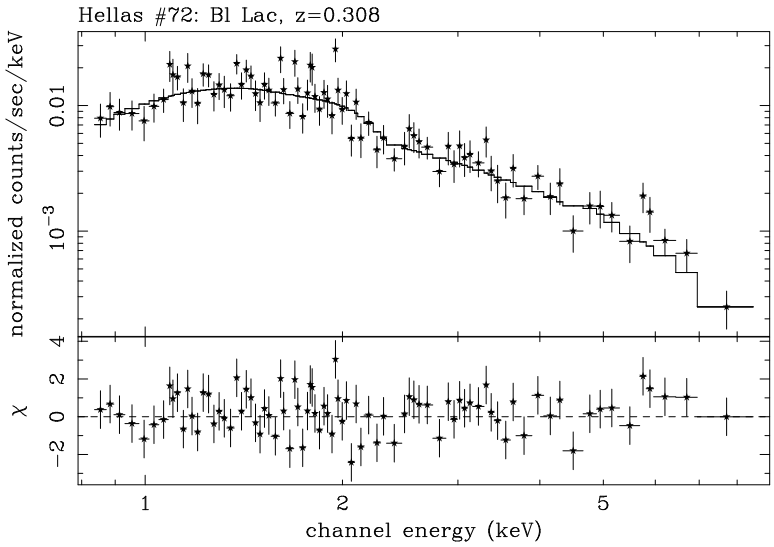

Figure 5.4: Power-law fit to the *ASCA* GIS2+GIS3 data of the HELLAS source #72 (BL Lac, z=0.308) and relative data/model ratio. The data points have 3 σ significance.

when the X–ray continuum is fitted with a double power-law model (with the higher energy power law steeper than the low-energy one), but the improvement is not statistically relevant. The 2–10 keV flux is 1.3×10^{-12} erg cm^{-2} s^{-1}, the corresponding (unabsorbed) luminosity 7.1×10^{44} erg s^{-1}. Not surprisingly, the 5–10 keV flux is a factor 1.6 higher than that derived by *BeppoSAX*, a likely explanation being the variability characterizing BL Lac objects also in the X–rays.

HELLAS #73: RLQ, z=1.537
HELLAS #387: RLQ, z=1.46

Due to the very low statistics of HELLAS #73 in the GIS3 instrument, only GIS2 data have been used in the spectral analysis. The *ASCA* spectra of HELLAS #73 and HELLAS #387 are both fitted by a flat continuum ($\Gamma \simeq 1.5$–1.6) up to 15 keV (see Fig. 5.5 and 5.6). The flatness of the slope may be ascribed to the beamed synchrotron self-Compton component related to the radio source (jet) (see Cappi et al. 1997 for a comprehensive overview on radio-loud quasars). Indeed, it

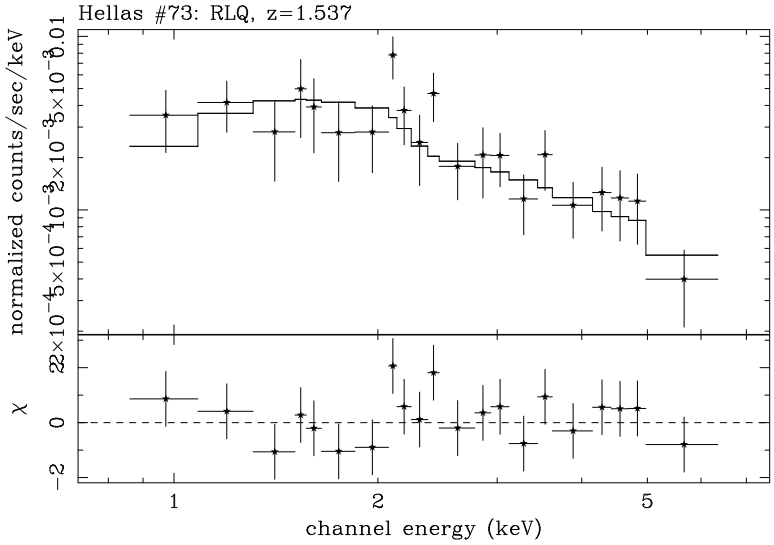

Figure 5.5: Power-law fit to the *ASCA* GIS2 data of the HELLAS source #73 (RLQ, z=1.537) and relative data/model ratio. The data points have 2 σ significance.

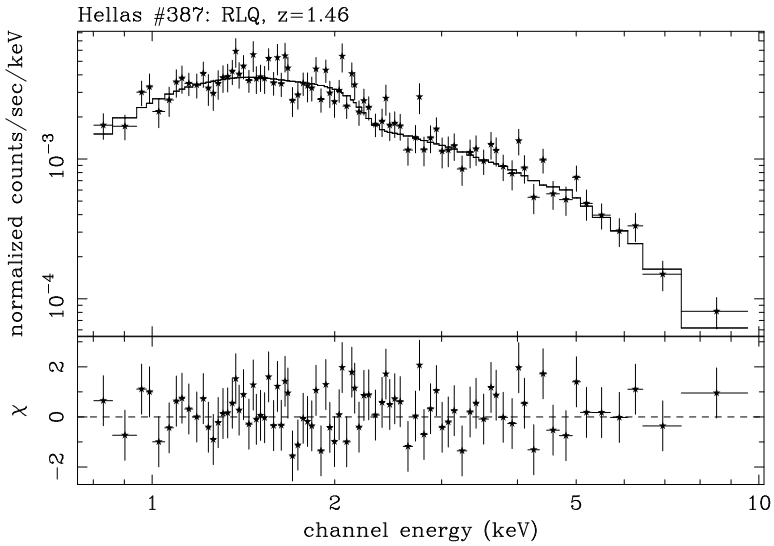

Figure 5.6: Power-law fit to the *ASCA* GIS2+GIS3 data of the HELLAS source #387 (RLQ, z=1.46) and relative data/model ratio. The data points have 4 σ significance.

is well known that radio-loud quasars (RLQs) have flatter slopes in the X–rays with respect to radio-quiet ones (RQQs, e.g. Vignali et al. 1999). Absorption at the source redshift cannot be excluded by the present spectral analysis, but it seems not required by the data.

The *ASCA* 2–10 keV flux (luminosity) of HELLAS #73 is 9.6×10^{-13} erg cm^{-2} s^{-1} (1.9×10^{46} erg s^{-1}), about half of which coming from the 5–10 keV emission (observer frame), while that of HELLAS #387 (1.8×10^{-12} erg cm^{-2} s^{-1}, corresponding to a luminosity of 3.4 $\times 10^{46}$ erg s^{-1}) makes this objects one of the brightest among the HELLAS objects.

HELLAS #84: Radio-galaxy, z=0.013

HELLAS #84, i.e. the "weak-line" radio-galaxy (WLRG) IC 4296, has been observed by *ASCA* with a pointed observation. This means that for this object data from both the GIS and the SIS instruments are available. Therefore the data have been combined (after checking the consistency of their individual spectral results), allowing the relative normalizations free to vary in order to account for eventual residual discrepancies in the absolute flux calibration. WLRGs, i.e. with galaxies weak or absent optical lines, are known X–ray emitters, even if at a lower level (about 2 orders of magnitude) with respect to the broad-line (BLRGs) and narrow-line radio galaxies (NLRGs). In fact, IC 4296 2–10 keV X–ray flux (luminosity) is $\sim 1.2 \times 10^{-12}$ erg cm^{-2} s^{-1} (8.1×10^{41} erg s^{-1}). As extensively discussed by Sambruna and collaborators (1999), the WLRGs seem to share common properties, the most interesting ones being the presence of a soft thermal component with kT $\simeq$ 1 keV and a hard flat X–ray spectral slope ($\Gamma \simeq 1.3$–1.7). IC 4296 belongs to this class: the soft X–ray emission is well modeled by a RAYMOND-SMITH (Raymond & Smith 1977) or a MEKAL thermal plasma model (Mewe, Gronenschild & van den Oord 1985) with a temperature of 0.62 ± 0.06 keV and a power law with $\Gamma = 1.74^{+0.26}_{-0.29}$, which do agree with the values found by Sambruna et al. (1999). There is also evidence of excess absorption above the Galactic value ($N_{\rm H} = 3.87^{+1.00}_{-1.13} \times 10^{21}$ cm^{-2}), but absorption by the torus may easily account for such a value (Urry & Padovani 1995). The soft X–ray emission confirms the previous results from *ROSAT* and *Einstein* that

radio galaxies are embedded in a hot, diffuse medium (Fabbiano 1989; Worrall et al. 1994; Trussoni et al. 1997; Crawford et al. 1999,), as well as more recent results obtained by *BeppoSAX* (Padovani et al. 1999). Even though *ASCA* is not the most suitable instrument to study the morphology of the thermal component with good angular resolution, its sensitivity at low energies, where this component normally peaks, is high enough to allow a good determination of its spectral parameters. The hard X–ray power law, $\Gamma \simeq 1.7$, can be either due to the presence

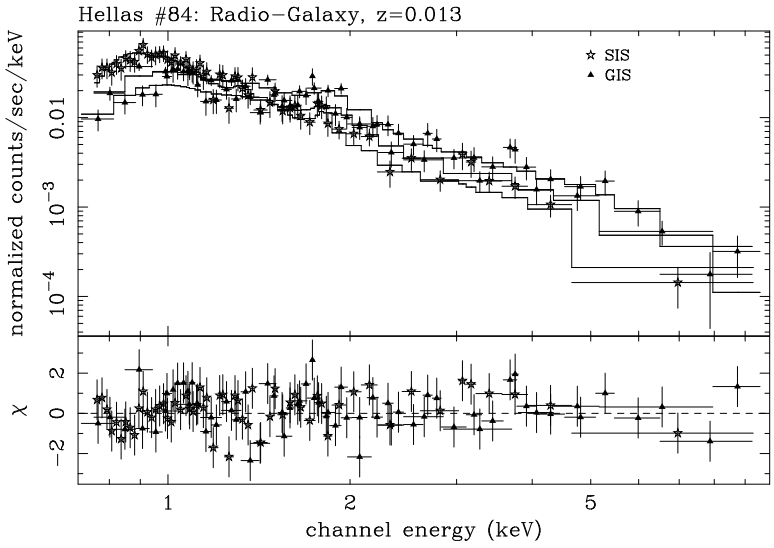

Figure 5.7: Power law + thermal fit to the *ASCA* SIS+GIS data of the HELLAS source #84 (the radio-galaxy IC 4296, z=0.013) and relative data/model ratio. The data points have 3 σ significance.

of a very weak AGN in the core of the radio-galaxy (it has been suggested that the majority of the WLRGs may represent the radio-loud analogs of LINERs), or to the contribution of the radio jet (even though a large part of its emission is probably beamed away from the line of sight, as IC 4296 is a lobe-dominated radio-galaxy), or to an ADAF ("Advection-Dominated" Accretion Flow, Ichimaru 1977; Rees et al. 1982; Narayan & Yi 1994; Narayan, Mahadevan & Quataert 1998) regime. In this case, the Coulomb collisions between ions and electrons are inefficient cooling mechanism, and the plasma settles into a two-temperatures phase, the ions being much hotter (then energetically dominant) than the electrons ($T_{ions} \sim 10^{11}$ K, $T_e \sim 10^9$

K). The ions take most of the potential energy and advect it into the black hole (characterized by a very low accretion rate with respect to the Eddington one). On the contrary, the colder electrons radiate a small portion of the full energy via synchrotron, inverse Compton and bremsstrahlung emission in the radio, optical and hard X–rays, respectively. In the ADAF regime, the X–ray spectrum is a sensitive function of the accretion rate (see Narayan et al. 1998 for a recent review).

There is no evidence of a Fe Kα emission line in the X–ray spectrum of IC 4296, thus confirming the results obtained for similar objects by Sambruna et al. (1999) and suggesting that the ADAF hypothesis might be tenable. *ASCA* SIS+GIS spectrum of IC 4296 is shown in Fig. 5.7.

5.4.2 The clusters

HELLAS #392: Cluster, z=0.216

HELLAS #392 (MS 0735+74) was identified as a candidate "cooling flow" by Donahue and collaborators (1992) because its central galaxy has extended Hα emission and low-ionization emission lines. These nebulae typically extend about 10–100 kpc from the central brightest galaxy in the cluster and are found to be associated exclusively with cluster cooling flows (Baum 1992; Heckman et al. 1989); moreover, they are quite luminous, and their emission in the Hα line only is up to 10^{42} erg s^{-1} (7.3×10^{40} erg s^{-1} for MS 0735+74, Donahue & Stocke 1995). The radio emission from the cluster is clearly dominated by the presence of the strong radio-galaxy 4C 74.13, which is characterized by an amorphous morphology and a steep spectrum, similarly to most of the central radio sources associated with cooling flow (Ball, Burns & Loken 1993). The larger scale X–ray emission and the radio emission are nearly co-spatial and appear oriented in similar directions.

Since a detailed, radial-dependent study of this cluster is beyond the scope of the present discussion, I will briefly summarize the main results obtained by simply fitting the whole 0.7–10 keV *ASCA* SIS+GIS spectrum. A Raymond-Smith (or, alternatively, a MEKAL model) provides a good parameterization of the source spectrum, where the temperature (kT $\simeq$ 5.2 keV) and metallicity (Z $\simeq$ 0.34 Z$_\odot$) are

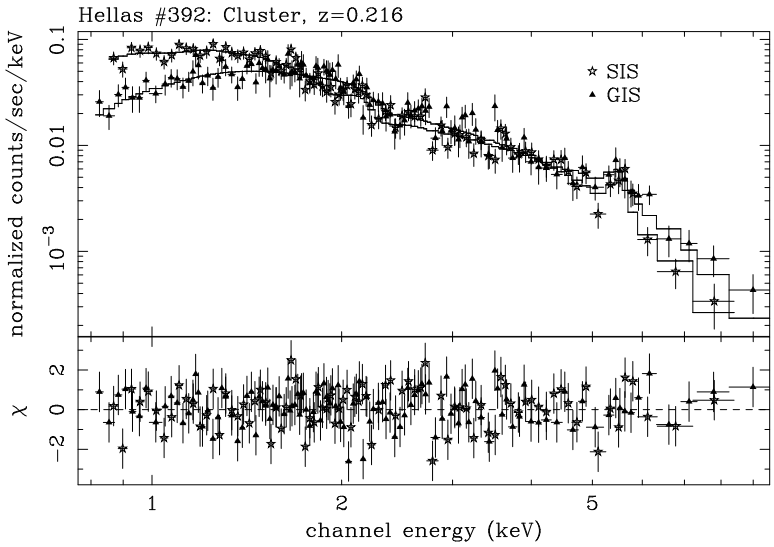

Figure 5.8: Thermal fit to the *ASCA* SIS+GIS data of the HELLAS source #392 (cluster, z=0.216) and relative data/model ratio. The data points have 4 σ significance.

consistent with the values found by Irwin & Bregman (2000) for a sample of clusters observed by *BeppoSAX*. The 2–10 keV flux is 4.2 $\times$ 10^{-12} erg cm^{-2} s^{-1}, corresponding to an X–ray luminosity of 1.1 $\times$ 10^{45} erg s^{-1}. The *ASCA* spectrum is shown in Fig. 5.8.

5.4.3 The radio-quiet objects

HELLAS #167: Type 1, z=0.300
HELLAS #176: Type 1, z=0.804
HELLAS #390: Type 1, z=0.089
HELLAS #394: Type 1, z=0.312

The X–ray spectrum of the HELLAS source #167 is well parameterized (Fig. 5.9) by a single power law whose spectral slope, $\Gamma \simeq 1.9$, is typical of Seyfert 1 galaxies and radio-quiet quasars (Nandra & Pounds 1994; Gondek et al. 1996; Nandra et al. 1997; George et al. 2000; see also Piro et al. 2000 for a review on recent results obtained by *BeppoSAX*). The same applies to HELLAS #176 ($\Gamma \simeq 2.1$, but with

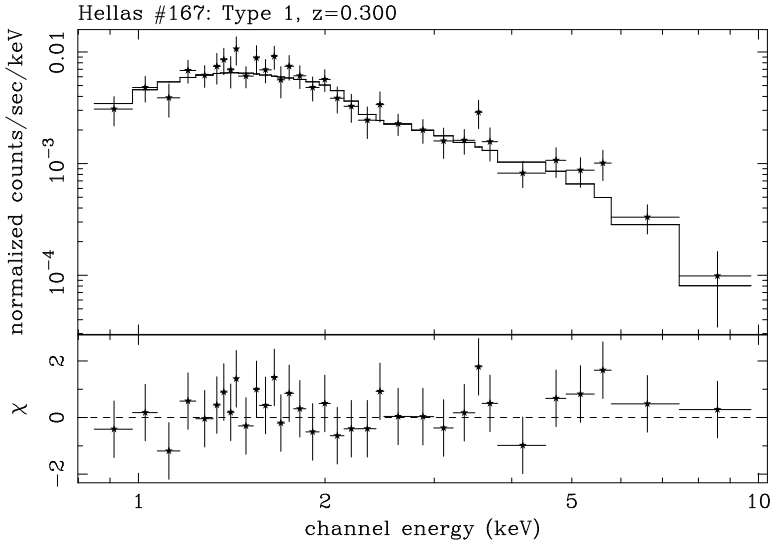

Figure 5.9: Power-law fit to the *ASCA* GIS2+GIS3 data of the HELLAS source #167 (Type 1 at z=0.300) and relative data/model ratio. The data points have 3 σ significance.

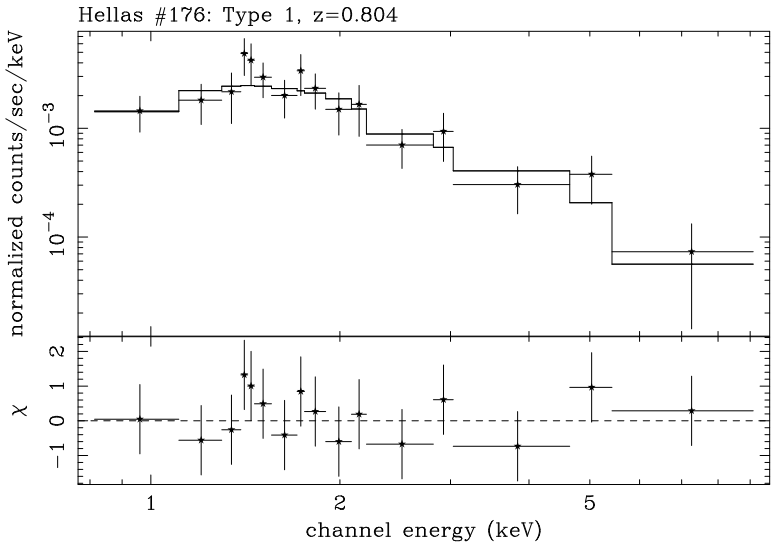

Figure 5.10: Power-law fit to the *ASCA* GIS2 data of the HELLAS source #176 (Type 1 at z=0.804) and relative data/model ratio. The data points have 2 σ significance.

larger uncertainties due to the relatively poor statistics in the GIS, see Fig. 5.10), to HELLAS #390 ($\Gamma \simeq 2.1$, Fig. 5.11) and to HELLAS #394 ($\Gamma \simeq 2.2$, Fig. 5.12).

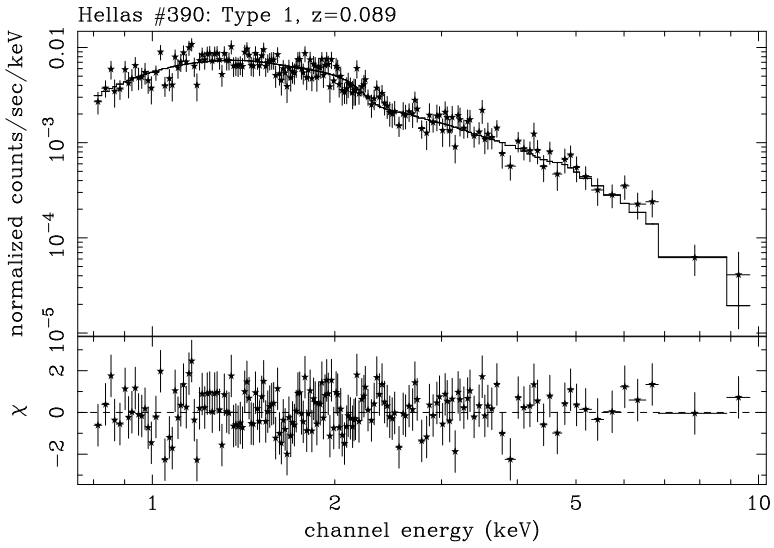

Figure 5.11: Power-law fit to the *ASCA* GIS2+GIS3 data of the HELLAS source #390 (Type 1 at z=0.089) and relative data/model ratio. The data points have 3 σ significance.

Any more complex model seems not to be required by the present *ASCA* data for all these sources but HELLAS #394, where an additional, likely thermal soft X–ray component seems to be present in GIS2 data, with a temperature of about 1 keV, probably related to the emission from the galaxy hosting the active nucleus. No evidence of this component is present in GIS3 data, but its lower statistics (about half of GIS2) can account for this discrepancy between the two detectors.

A bump at about 6.4 keV (observer frame) is visible in HELLAS #167 X–ray residuals, but the relatively low statistics prevents from a deep investigation on the line properties, if any.

Soft X–ray absorption, which is suggested by *BeppoSAX* softness ratio analysis of HELLAS #176, cannot be confirmed or ruled out by the present data, due to the low-counting statistics.

HELLAS #264: Type 1.9, z=0.176

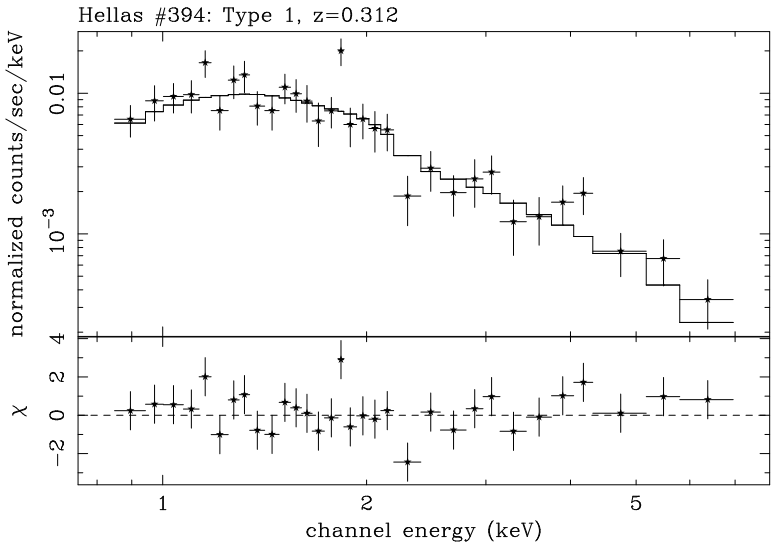

Figure 5.12: Power-law fit to the *ASCA* GIS2+GIS3 data of the HELLAS source #394 (Type 1 at z=0.312) and relative data/model ratio. The data points have 3 σ significance.

The *ASCA* spectrum of the Seyfert 1.9 galaxy HELLAS #264 (Fig. 5.13) is well described by a flat power-law continuum ($\Gamma \simeq 1.1$) plus several narrow emission line.

Even though the low statistics characterizing this spectrum (and the poor energy resolution of the GIS instruments) prevents from a detailed description of the various components, it is possible to reveal:

(a) an iron Kα emission line whose significance is at about 68 % level (as derived from the confidence contours). Its rest frame energy is compatible with a neutral or moderately warm origin (E $\simeq$ 6.4$\pm$0.3 keV, EW $\simeq$ 650 eV). Due to the *ASCA* limited energy bandpass, it is difficult to reveal any reflection component associated to this line;

(b) an emission line (68 % significance) at E $\simeq$ 2.3$\pm$0.15 keV (rest frame), probably a S–Si line (or blend of lines), and an emission line (90 % significance) at E $\simeq$ 5.0$\pm$0.2 keV, possibly associated to Ca emission.

It must be noted that none of the present emission lines is highly significant. Undoubtedly, the main property of HELLAS #264 X–ray

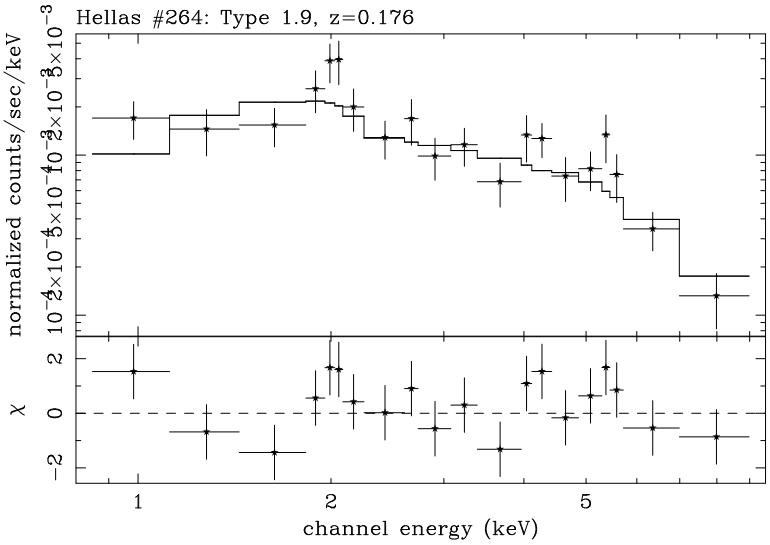

Figure 5.13: *ASCA* GIS2+GIS3 data of the HELLAS source #264 (Type 1.9, z=0.176) fitted with a simple power-law model. There is evidence of some unresolved features, possibly ascribed to blended emission-lines (lower panel). The data points have 3 σ significance.

spectrum is given by the extremely flat power-law index, which may be partly ascribed to the presence of a strong absorption at the source's redshift. From the present data, however, it is possible to derive only an upper limit to the column density, of the order of 10^{22} cm^{-2}, whereas *BeppoSAX* softness ratio analysis suggests a very a strong absorption, of the order of 5×10^{23} cm^{-2}. If the X–ray slope were similar to that of the Seyfert 1 galaxies (i.e. $\Gamma \simeq 1.9$), then the derived column density is $N_{\rm H} = 1.76^{+0.54}_{-0.60} \times 10^{22}$ cm^{-2}.

HELLAS #319: Type 1.8, z=0.205

The X–ray spectrum (Fig. 5.14) of the Seyfert 1.8 galaxy HELLAS #319 is well fitted with a simple power-law component, showing a rather flat spectral slope ($\Gamma \simeq 1.5 \pm 0.3$), which is in agreement with *BeppoSAX* findings.

Some residuals at low energies (E $<$ 2 keV) seem to indicate the presence of an additional spectral component, but the relatively poor

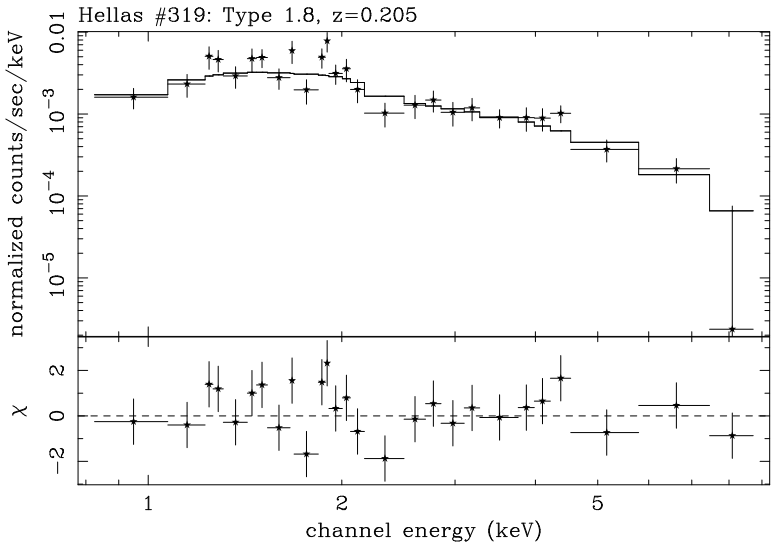

Figure 5.14: Power-law fit to the *ASCA* GIS2+GIS3 spectrum of the HELLAS source #319 (Type 1.8, z=0.205) and relative data/model ratio. The data points have 3 σ significance.

statistics makes further investigations quite difficult.

HELLAS #254: unidentified

Among the HELLAS sources observed by *ASCA*, also still unidentified objects are present. As a consequence, the study of the X–ray properties of this class of objects could provide useful information about the nature of these sources and also on their redshift.

In this regard, HELLAS #254 (Fig. 5.15) is a quite interesting object: even though the off-axis angle of the source is high, the statistics relatively low (in fact, only GIS2 data are useful) and its vicinity to the bright Narrow-Line Seyfert 1 (NLS1) Ark 564 obliges to extract the source counts from a very small region, some remarkable features appear to be present in the X–ray spectrum:

(a) a steep ($\Gamma \simeq 2.7$) continuum fits well the E < 5 keV data, the only exception being some counts excess at about 3 keV, possibly due to a blend of soft X–ray lines (S, Si);

(b) an absorbed ($N_{\rm H} \simeq 5.3 \times 10^{23}$ cm^{-2}), hard X–ray component parameterized by a power law with $\Gamma \simeq 1.3$. Both the X–ray spectral slope and the column density are largely unconstrained, owing to the limited energy bandpass provided by *ASCA*; if the hard X–ray slope is fixed to $\Gamma = 1.9$, the derived upper limit on the absorption is $N_{\rm H} = 1.65 \times 10^{24}$ cm^{-2}

(c) an emission line feature at E $\simeq 4.8 \pm 0.2$ keV (90 % significance). In this were a a neutral Kα line, then the source's redshift would be $\sim$ 0.3–0.4. The equivalent width (EW) is about 4.7 keV.

The X–ray spectrum so far described can be tentatively explained by assuming that the source is a Seyfert 2 (or intermediate) galaxy whose E < 5 keV spectrum is due to a scattered component (or to the thermal contribution by the host galaxy: in this case, the feature at about 3 keV could be more easily explained), where the scattering medium is related to the $N_{\rm H} \simeq 5 \times 10^{23}$ cm^{-2} absorber. On the contrary, the hard X–ray emission is due to the nuclear component which escapes only at higher energies. Its flatness, if confirmed, could be ascribed to reflection, as well as the presence of the emission line

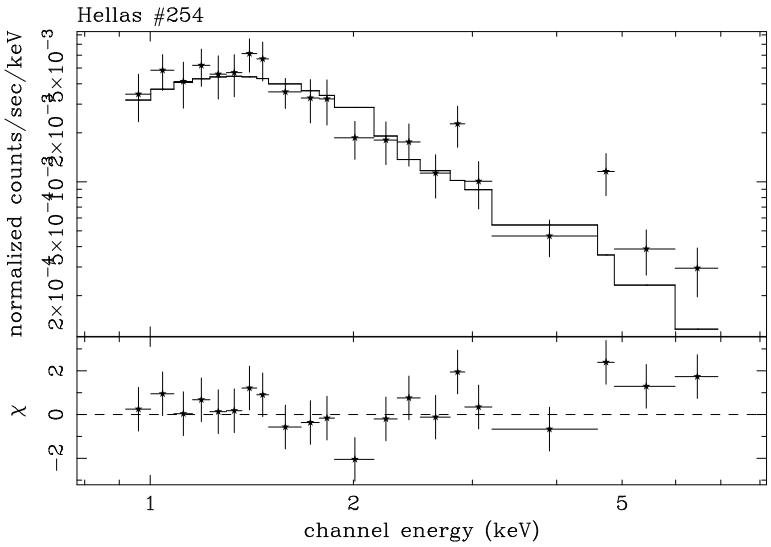

Figure 5.15: *ASCA* GIS2 spectrum of the HELLAS source #254 fitted with a single power-law model, in order to enhance the presence of additional features (lower panel). The data points have 3 σ significance.

at about 4.8 keV in the observer frame. In the same way, the EW of this line results to be extremely high because it is measured against a suppressed (absorbed) continuum. This tentative fully-comprehensive picture makes this source a good candidate to be a border-line object between "classical" Seyfert 2 galaxies and "Compton-thick" Seyfert 2, i.e. objects characterized by $N_{\rm H} > 1.5 \times 10^{24}$ cm^{-2} (Risaliti et al. 1999; see also Matt et al. 2000 for a recent review on *BeppoSAX* results). What makes these results particularly noteworthy is the fact that the Type 2 classification of this galaxy and its redshift may result directly from the X–ray data. This kind of approach has been already successfully applied to X–ray data by Della Ceca et al. (2000a).

HELLAS #256: unidentified
HELLAS #393: unidentified

The 0.9–6 keV X–ray spectrum of the HELLAS source #256 is best parameterized by a steep power-law continuum ($\Gamma \simeq 2.3\pm0.2$), with

no evident feature or additional component. The *ASCA* GIS2+GIS3 spectrum is shown in Fig. 5.16.

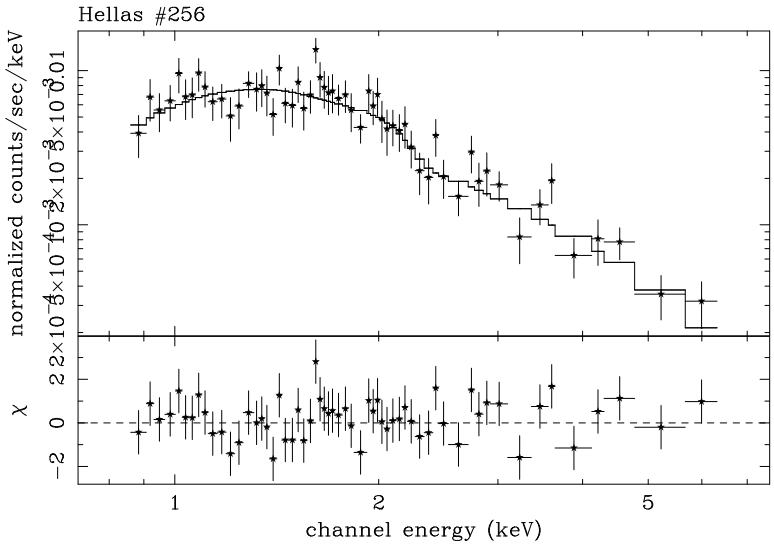

Figure 5.16: Single power-law fit to the *ASCA* GIS2+GIS3 spectrum of the HELLAS source #256 and relative data/model ratio. The data points have 3 σ significance.

On the contrary, a flatter spectrum is required by the HELLAS source #393, which can be can be modeled either by a flat power-law continuum ($\Gamma \simeq 1.6$, with large uncertainties) or by a thermal model (kT $\simeq$ 4 keV). The latter model provides a better description of the X–ray spectrum of the source, but requires abundances largely higher than the Solar ones. The best-fit spectrum is shown in Fig. 5.17.

HELLAS #296: unidentified

The *ASCA* spectrum of HELLAS #296, even though poorly defined due to the small photon counts accumulated by the GIS instruments, seems to show a more complex spectrum than a simple power law. At first, the X–ray spectrum was fitted with an absorbed power law: this model gives an acceptable χ^2, but the slope is very flat ($\Gamma \simeq 0.2\pm0.3$) and some residuals are apparent. In particular, an additional low-energy component (which is hardly constrained by the fit) and a

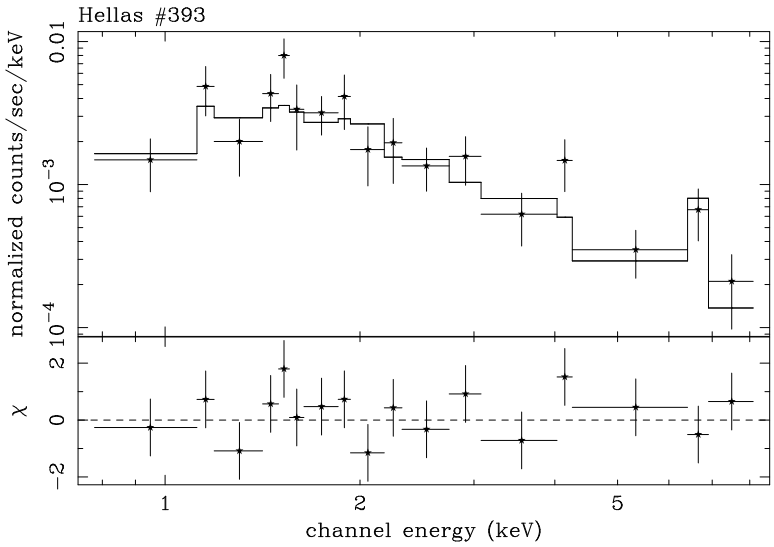

Figure 5.17: Thermal fit to the *ASCA* GIS2+GIS3 spectrum of the HELLAS source #393 and relative data/model ratio. The data points have 2 σ significance.

narrow line (only 68 % significance) at E = $6.16^{+0.34}_{-0.22}$ keV seem to be present (Fig. 5.18).

The line can be due to iron emission: if neutral, the source's redshift should be of the order of 0.08. The equivalent width of this line is $\sim$ 480$\pm$340 eV. Due to the limited energy bandwidth provided by *ASCA* and to the low quality of the present data, it is not possible to verify the existence of any reflection component.

Moreover, it is worth noting that HELLAS #296 is one of the hardest sources in the HELLAS sample. The present *ASCA* data confirms this finding: the 2–10 keV flux of the source is 9.5 $\times$ 10^{-13} erg cm^{-2} s^{-1}, the large part of it coming from the 5–10 keV band (flux of 7.4 $\times$ 10^{-13} erg cm^{-2} s^{-1}). Having this in mind, it is possible to suggest that the *ASCA* spectrum of HELLAS #296 is only the scattered/reflected part of the nuclear continuum, likely peaking at higher energies, thus unreachable by the present data.

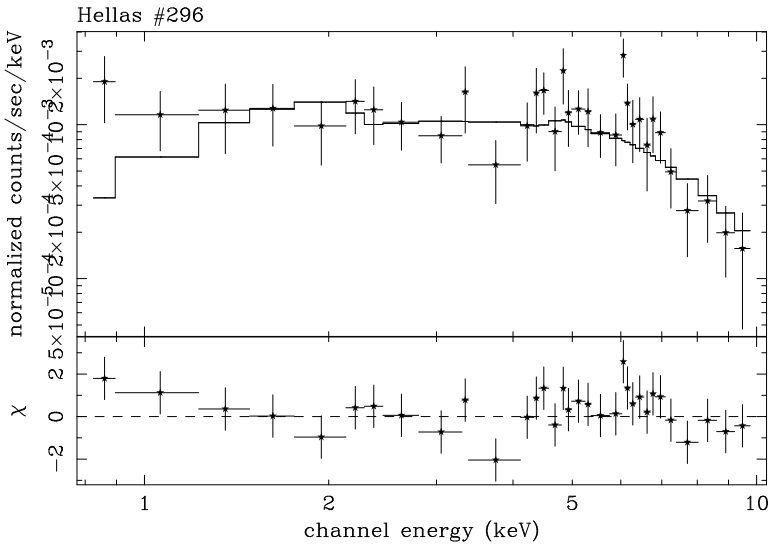

Figure 5.18: *ASCA* GIS spectrum of the HELLAS source #296 fitted with a simple power-law model. The residuals are plotted in the lower panel.

5.5 Follow-up observations

SAXJ 1519.5+6535 and SAXJ 1353.9+1820 belong to a small subsample of HELLAS sources for which a multi-wavelength follow-up program has been started, in order to investigate both their emission and absorption properties (Vignali et al. 2000a,b). In particular, in this section I will focus on their hard X–ray properties as discovered by pointed, follow-up *ASCA* observations. Their multi-wavelength study will be discussed in chapter 6.

HELLAS #375: Type 1.9, z=0.044

The ASCA X–ray emission of the Seyfert 1.9 SAXJ 1519.5+6535 (CGCG 319-007, z = 0.044) is well fitted by a flat ($\Gamma = 1.18^{+0.48}_{-0.69}$) and highly absorbed power law ($N_H = 1.53^{+0.44}_{-0.61} \times 10^{23}$ cm^{-2}). The GIS spectrum of the source is shown in Fig 5.19. If Γ=1.9 is assumed,

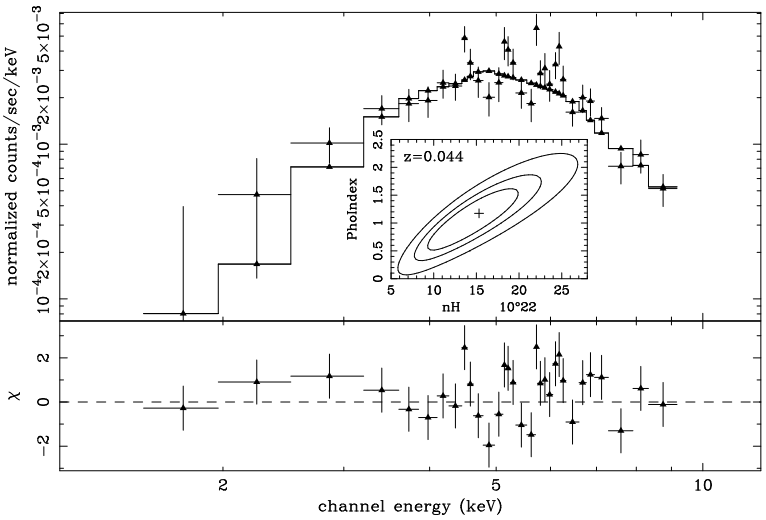

Figure 5.19: SAXJ 1519.5+6535 (HELLAS #375) best-fit spectrum with residuals. The Γ–N_H confidence contours are showed in the insert.

N_H is $\sim 2 \times 10^{23}$ cm^{-2}. A neutral iron Kα emission line seems to be present (EW $\simeq$ 190 eV), even if not statistically relevant (68 %). The

2–10 keV flux (luminosity) is 2.5×10^{-12} erg cm^{-2} s^{-1} (3.8×10^{43} erg s^{-1}).

Interesting enough, the *ASCA* intensity levels indicate that part of the hard X–ray emission is given by the companion galaxy MCG +11−19−005 (RA: 15h19m21.7s, DEC: +65d34m40s, z=0.0444), which is located south-west with respect to HELLAS #375. The X–ray intensity levels overlaid on the POSS image are shown in Fig. 5.20. It is also possible that some (minor) part of the hard X–ray emission is due to warm intra-galaxy medium around the two sources. *Chandra* and/or *XMM-Newton* observations are required to assess or discard this issue.

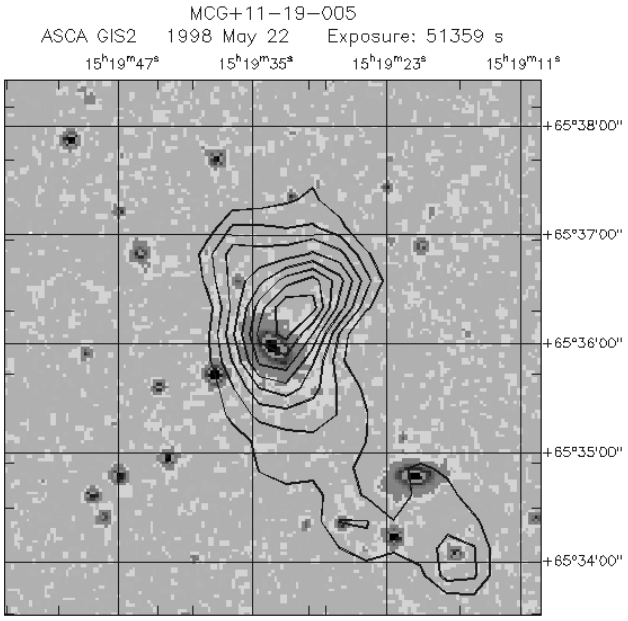

Figure 5.20: *ASCA* hard X–ray intensity levels regarding SAXJ 1519.5+6535 overlaid on the POSS image. A tail towards the companion galaxy MCG +11−19−005 is also apparent. The shift between the X–ray sources and the optical counterparts is due to *ASCA* pointing position uncertainties.

HELLAS #228: Red QSO, z=0.217

SAXJ 1353.9+1820 was observed with the *ASCA* satellite in January 1999 for about 60 ks. The screening criteria described in detail at the beginning of the present chapter (cfr. § 5.3) were applied. Both SIS and GIS spectra were grouped with almost 20 photons for each spectral bin in order to apply χ^2 statistics. Calibration uncertainties in the soft X–ray band have been avoided by selecting only data at energies higher than 0.9 keV. No discrepancies have been found between SIS and GIS spectral analysis, therefore all the data have been fitted together allowing the relative normalizations to be free of varying in order to take into account for residual calibration uncertainties between SIS and GIS. The uncertainties introduced by background subtraction have been carefully checked using both local and blank–sky background spectra and also varying their normalizations by ± 10 per cent. The lack of significant variations for the source count rate and spectral shape makes us confident on the robustness of the results that will be presented in the following.

Model	Γ	$N_{\rm H}$ (10^{21} cm^{-2})	CvrFract (%)	χ^2/dof
(a)	$1.28^{+0.23}_{-0.28}$	$6.14^{+2.10}_{-4.56}$	...	168/157
(b)	1.9 (frozen)	$15.4^{+3.70}_{-3.20}$	...	181/158
(c)	$1.28^{+0.43}_{-0.30}$	$8.55^{+24.0}_{-6.89}$	81^{+19}_{-44}	168/156
(d)	1.9 (frozen)	$28.7^{+17.2}_{-5.90}$	80^{+11}_{-8}	171/157

Table 5.2: *ASCA* SIS+GIS spectral fits to SAXJ 1353.9+1820 in the 0.9–10 keV energy range (observer frame).

A simple power-law model plus Galactic absorption ($N_{\rm H} \simeq 2.05 \times 10^{20}$ cm^{-2}, Dickey & Lockman 1990) leaves some residuals in the fit (χ^2 = 174/158) and gives a very flat slope ($\Gamma < 0.9$). Therefore an extra cold absorber at the redshift of the source (model (a) in Table 5.2) has been added to the previous model, significantly improving the fit: the continuum X–ray spectral slope is now $\Gamma = 1.28^{+0.23}_{-0.28}$, attenuated by a column density $N_{\rm H} = 6.14^{+2.10}_{-4.56} \times 10^{21}$ cm^{-2}. The best-fitting spectrum and the confidence contours for the absorbed power-law model are

presented in Fig. 5.21 and Fig. 5.22, respectively. The unabsorbed 2–

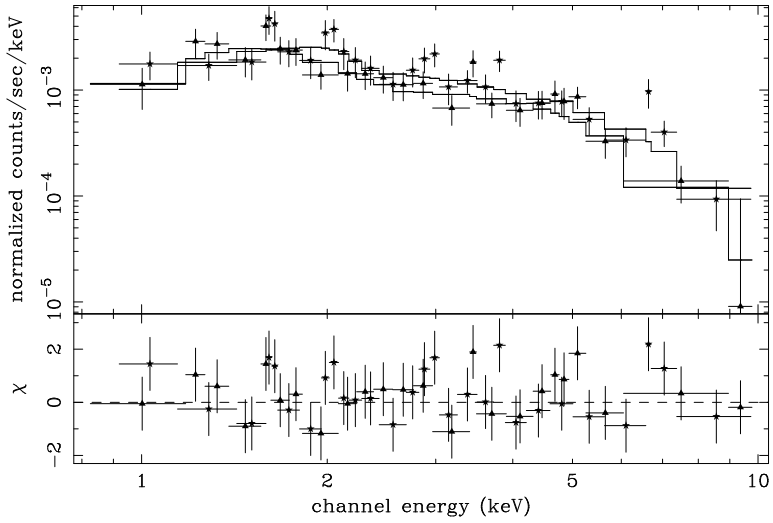

Figure 5.21: *ASCA* SIS+GIS spectrum of SAXJ 1353.9+1820 and relative data/model ratio for the absorbed power-law model (model (a) in Table 5.2).

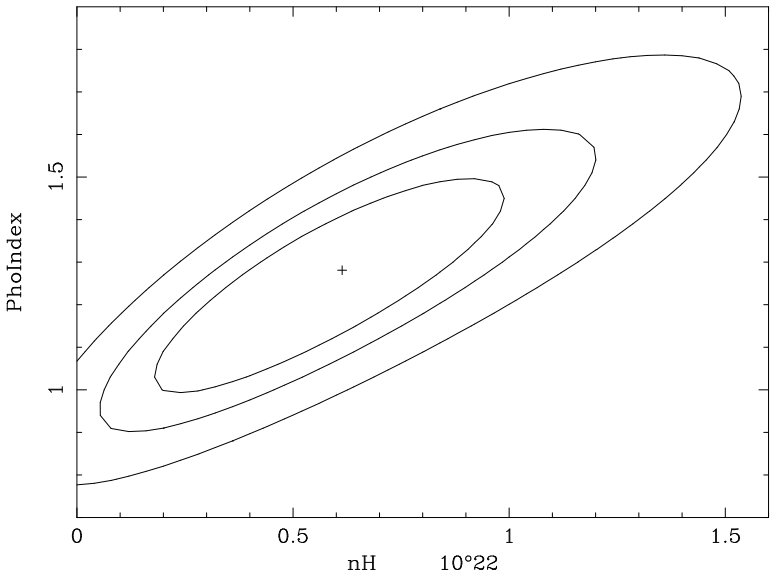

Figure 5.22: *ASCA* confidence contours in the Γ – $N_{\mathrm{H_{int}}}$ space parameters for the source SAXJ 1353.9+1820.

10 keV flux and luminosity are $\sim 6.2 \times 10^{-13}$ erg cm^{-2} s^{-1} and $\sim 1.3 \times 10^{44}$ erg s^{-1}. The *ASCA* 5–10 keV flux is about 40 per cent lower than in *BeppoSAX*. X–ray variability and/or cross–calibration uncertainties could provide a likely explanation.

SAXJ 1353.9+1820 does not show any particular feature or any other indication of reprocessed radiation. Neither the iron Kα emission line (the 90 per cent upper limit on the equivalent width being 330 eV) nor the reflection component (which is basically unconstrained by the present data) do improve the fit. The $N_{\rm H}$ value (which has been fixed at the quasar redshift but which could lie along the line of sight to the quasar) is in agreement with the value found by the softness ratio analysis performed with *BeppoSAX* data.

The best-fitting slope is extremely hard and significantly flatter than the average slope of Seyfert Galaxies and quasars with similar luminosities and redshifts (Nandra & Pounds 1994; Reeves et al. 1997; George et al. 2000; Reeves & Lawson 2000). Indeed, assuming a 'canonical' $\Gamma = 1.9$ value, it is not possible to obtain a good fit as relatively large residuals remain present at high energies (model (b)). The underlying continuum spectrum could be either intrinsically flat or flattened by a complex (multicolumn and/or leaky) absorber (Hayashi et al. 1996; Vignali et al. 1998; Malaguti et al. 1999; Turner et al. 2000).

In order to check this hypothesis, a partial covering model (models (c) and (d) in Table 5.2) was fitted to the data. According to this model, part (1 − CvrFract in Table 5.2) of the direct component escapes as scattered radiation without being absorbed. While the best-fitting model still requires a flat slope, a steeper continuum partially absorbed by a column density of $\sim 3 \times 10^{22}$ cm^{-2} does provide a good fit to the observed spectrum.

SAXJ 1353.9+1820 was also serendipitously observed for about 120 ks at large off-axis angle during the *ASCA* observation of the spectroscopic binary HD 121370. Even though the quality of the data is worse than the one concerning the pointed observation, it is possible to confirm a very flat X–ray continuum (Fig. 5.23), $\Gamma = 1.16^{+0.36}_{-0.23}$, attenuated by a column density whose upper limit is $N_{\rm H} = 3.9 \times 10^{21}$ cm^{-2} at z = 0.217. There is no flux variability between the two *ASCA* observations.

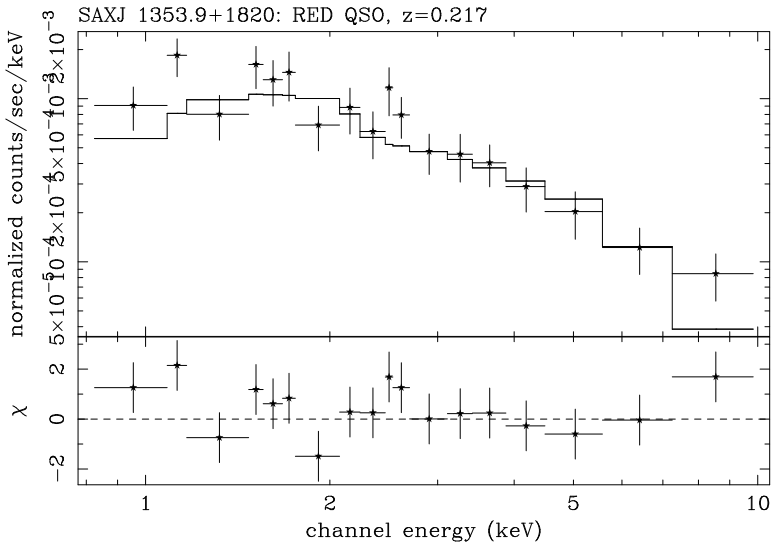

Figure 5.23: *ASCA* GIS spectrum of SAXJ 1353.9+1820, serendipitously observed in the field of view of the spectroscopic binary HD 121370.

5.6 Conclusions

The analysis of the *ASCA* fields presented in this chapter provides additional spectral information and nicely complements the broad-band coverage obtained with *ROSAT* and *BeppoSAX*, as the GIS effective area peaks between PSPC and MECS effective areas.

ASCA was able to detect all the HELLAS Seyfert 1 galaxies which fell in its field of view. The broad-line, blue-continuum Type 1 objects show a "classical" X–ray spectrum (Nandra & Pounds 1994; Nandra et al. 1997), with $\Gamma \simeq 1.9$–2.2, and no evidence for X–ray absorption. Among these sources, H #176 and H #390 seem to be absorbed through *BeppoSAX* softness ratio analysis ($N_{\rm H} \simeq 5 \times 10^{22}$ cm^{-2}). Comparing results obtained with different instruments is not obvious. In this regard, the different X–ray absorption value found between *BeppoSAX* and *ASCA* results may be due to the higher effective area of the MECS instruments with respect to the GIS. As a consequence, the softness ratio in *BeppoSAX* tends to be lower, since a large number of hard X–ray photons is collected. Moreover, the two sources have been observed at large off-axis angles in *ASCA*: the vignetting is high enough to prevent from a detailed modeling of the hard tail of the X–

ray spectrum. Even though the errors associated to *BeppoSAX* softness ratios are generally large (therefore the difference between absorption of a few $\times$ 10^{22} cm^{-2} and no absorption at all may be small), it is however interesting to note that for the red quasar H #228 the *ASCA* pointed-observation results (flat spectrum with moderate absorption, see § 5.5) do agree with *BeppoSAX* findings. The same applies to the Type 1.9 object H #375 (the other follow-up observation, see below).

Radio-loud AGNs show the typical spectra of their class: a steep power-law continuum for the BL Lac object and flat slopes for the RLQs, with no evidence of absorption. The radio galaxy is characterized by a more complex spectrum, with a prominent soft X–ray component (possibly due to thermal plasma) and a $\Gamma \simeq 1.7$ power law, with moderate absorption at the source redshift ($N_{\rm H} \simeq 4 \times 10^{21}$ cm^{-2}).

A thermal model with sub-solar abundances is a good representation of the X–ray spectrum of the cluster H #392.

The Type 1.8-2 sources (4 detections, two sources undetected) are described by flat X–ray spectra, absorption being the most plausible cause of this behavior. Only for H #375 (§ 5.5) it has been possible to associate the flatness of the X–ray spectrum with the presence of strong X–ray absorption. This is not surprising, since for this source a moderately long follow-up observation with *ASCA* was carried out.

Among the four still unidentified objects, complex X–ray spectra seem to be present in two objects. The present low-counting statistics prevents from a detailed modeling of the spectrum. However, it is interesting to note that flat X–ray spectra seem to provide the best-fit for these two sources, which can be considered good candidates to belong to the class of Compton-thick Seyfert 2 galaxies.

Within the uncertainties in the modeling of the X–ray spectra of the HELLAS sources with the GIS instruments, some issues appear evident: the presence of absorption for the objects for which *ASCA* follow-up observations have been carried out, and the flatness of the X–ray spectra for the Type 1.8-2 objects observed by *ASCA* . Absorption is thought to play the major role in the X–ray flatness. Similar evidences have been found in a couple of still unidentified HELLAS sources.

The comparison of *BeppoSAX* softness ratios with those obtained by *ASCA* (in the same energy ranges) clearly stress the hard X–ray

capabilities of MECS detectors to detect hard X–ray photons. Indeed, *ASCA* softness ratios are about 50–60 % higher (for the bright sample described above) than *BeppoSAX* , but, interestingly, the HELLAS hard sources are among the hardest also in *ASCA* (see Fig. 5.24, keeping in mind the difference, which can be considered as a shift in the scale).

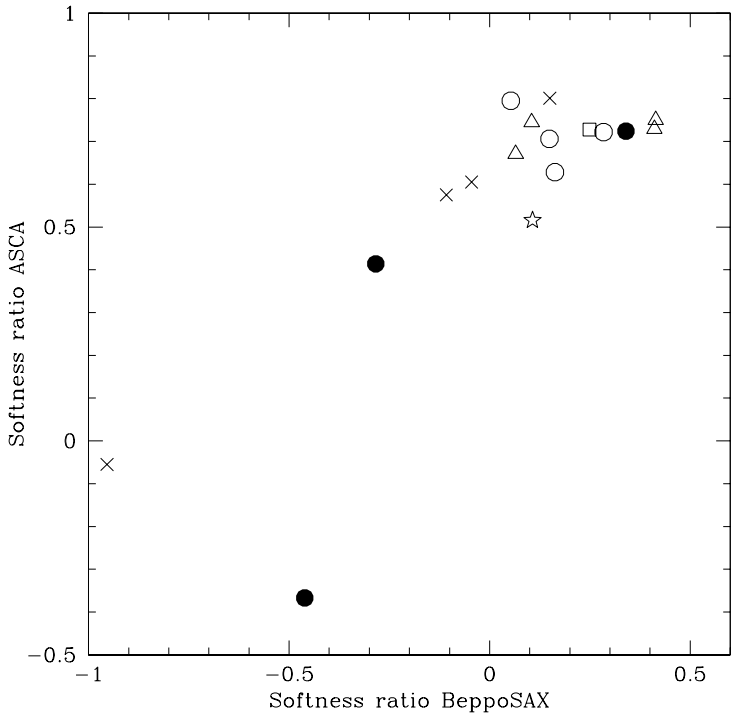

Figure 5.24: *BeppoSAX* vs. *ASCA* softness ratio for the "bright" HELLAS sample. Symbols are as in previous figures.

Optical and near-infrared properties of the HELLAS sources

6.1 Introduction

The nature of the HELLAS sources responsible for about 20–30 % of the hard X–ray background (XRB) has been investigated through a multi-wavelength approach. In particular, along with the spectroscopic identification follow-up observations, photometric studies in the optical and in the near-infrared bands have been carried out in order to provide further information on their colors and morphologies, when possible. The optical properties have then been compared to those emerging from the hard X–rays and described in chapter 3.

This approach should also help in evaluating the quite varied properties of the zoo of the hard X–ray selected sources, and in investigating their nature, with important consequences for the AGNs synthesis models for the XRB.

In the last part of the present chapter some works in progress on the "restricted" HELLAS sample will be presented. From the original sample a restricted portion of sky has been excluded ($5^h < \alpha < 6.5^h$ and $16.9^h < \alpha < 20^h$ plus $-90° < \delta < -59°$ and $+80° < \delta < +90°$), thus reducing the number of HELLAS sources to 115, the only excluded identified object being the star. Moreover, a R magnitude limit has been applied (different from one class of objects to another, to take into account the different surface density of the sources), in order to

reduce the number of possible spurious identifications. In this case only 7 optically identified extra-galactic HELLAS sources are "lost" (2 Type 1, 3 Type 2 and 2 emission-line galaxies, ELGs).

In the following I will present the optical and near-infrared results obtained with the full HELLAS sample. When drawing the conclusions and determining the number of Type 2/Type 1 objects, only the "restricted" HELLAS sample (i.e. that obtained by applying a limiting R-magnitude) will be used.

At the end of the chapter a brief review on the recent sub-millimeter results on hard X–ray selected sources will be presented, in order to quantify the contribution of these sources to the sub-mm background.

6.2 Spectroscopic runs

The spectroscopic follow-up observations have been carried out using the RC spectrograph (RCSP) at the Kitt Peak 4-m telescope (on March 1998, eight sources), the FAST Spectrograph at the Whipple 60-inch telescope (1998, one source), the Hawaii 88-inch telescope (1998, two sources), and EFOSC2 at the ESO 3.6-m (all the remaining identifications, dating from 1998 to July 2000). Long-slit spectra and multi-object spectroscopy have been performed with a resolution between 7 and 26 $\AA$, in the wavelength range spanning from 3450 to 8500 $\AA$ (RCSP) and from $\sim$ 3800–8000 $\AA$ for the other instruments. The data have been reduced using standard MIDAS tasks (Banse et al. 1983). The raw data were sky-subtracted and corrected for pixel-to-pixel variations by dividing them with a suitably normalized flat-field spectrum. Wavelength calibrations were carried out by comparison with exposures of He-Ar and Ne lamps, while flux calibrations by observations of spectrophotometric standard stars (Oke 1990).

6.2.1 Spectroscopic identifications and results

At present, 71 out of the 147 HELLAS sources have been spectroscopically identified, 45 through follow-up observations and 26 from existing catalogs. Table 6.1 lists the optical counterparts of the HELLAS sources, with their position, offset with respect to *BeppoSAX* centroid error box, their 5–10 keV flux, B and R magnitude (from

Source ID	RA (J2000)	DEC (J2000)	Δ_{X-Ott} (arcsec)	$F_{5-10\ keV}$ (erg cm^{-2} s^{-1})	R (USNO)	B (USNO)	Spec. ID	z	Notes
120	00 26 36.1	−19 44 16	6.2	3.4×10^{-13}	17.3	19.2	AGN 2	0.238	
124	00 27 09.8	−19 26 12.6	17.7	1.8×10^{-13}	17.3	18.0	AGN 1	0.227	
103_1	00 45 46.3	−25 15 50	87.4	3.3×10^{-13}	17.5	19.7	AGN 1.9	0.111	Gr. ?
39	01 21 56.9	−58 44 41	36.4	2.6×10^{-13}	16.8	18.5	AGN 1.9	0.118	
93	01 34 33.8	−29 58 15	23.9	8.7×10^{-14}	19.0	19.0	AGN 1	2.217	
⇒**91**	01 34 45.4	−30 00 49.4	95.5	7.1×10^{-14}	18.1	19.4	ELG	0.217	
96	01 35 32.7	−29 52 02	52.5	9.0×10^{-14}	18.2	18.3	AGN 1	1.344	
⇒**20**	01 40 14.7	−67 48 54	54.0	2.8×10^{-13}	12.4	12.9	star		
75	03 34 07.5	−36 04 03	19.4	1.9×10^{-13}	.....	.....	AGN 1	0.904	
53	04 37 11.8	−47 31 47.2	57.1	2.7×10^{-13}	16.4	16.1	AGN 1	0.142	
54	04 38 47.0	−47 28 0.3	66.7	4.7×10^{-13}	19.7	20.5	AGN 1	1.453	APM mag.
65	06 46 37.6	−44 15 34.9	18.4	4.3×10^{-13}	18.0	17.7	AGN 1	0.153	
243	08 37 37.1	25 47 49.7	2.0	2.6×10^{-13}	16.1	18.0	AGN 1	0.077	
246	08 38 59.2	26 08 12.4	29.6	1.6×10^{-12}	12.4	15.8	ELG	0.048	
137	09 46 37.5	−14 07 47.4	113.8	3.2×10^{-13}	19.5	20.3	AGN 1	0.290	
300	10 32 16.1	50 51 21	77.2	3.1×10^{-13}	15.8	16.9	AGN 1	0.174	
283	11 18 13.8	40 28 38	23.6	8.5×10^{-14}	18.3	20.7	RED AGN 1	0.387	
282	11 18 48.7	40 26 48	58.4	1.4×10^{-13}	18.6	18.6	AGN 1	1.129	
264	12 18 52.5	29 59 01	70.3	2.0×10^{-13}	18.7	20.7	AGN 1.9	0.176	
⇒**186**	12 29 21.7	01 49 44.0	118	1.6×10^{-13}	19.3	20.1	AGN 2	0.077	
167	12 40 27.8	−05 14 02	92.0	3.1×10^{-13}	18.8	20.9	AGN 1	0.300	
169	12 40 36.4	−05 07 52	106.5	1.9×10^{-13}	11.0	11.3	ELG	0.008	NED

Source ID	RA (J2000)	DEC (J2000)	Δ_{X-Ott} (arcsec)	$F_{5-10\ keV}$ (erg cm^{-2} s^{-1})	R (USNO)	B (USNO)	Spec. ID	z	Notes
151	13 04 32.5	−10 24 36.7	127.5	1.3×10^{-13}	18.8	18.8	AGN 1	1.052	
155	13 04 35.5	−10 15 48.6	39.9	1.4×10^{-13}	19.0	20.5	AGN 1	2.386	
100	13 48 19.5	−30 11 55	51.9	2.2×10^{-13}	16.7	18.2	ELG	0.128	
92	13 48 44.7	−30 29 44.4	12.2	5.1×10^{-13}	17.0	17.5	AGN 1	0.330	
97	13 50 15.4	−30 20 9.9	52.5	5.1×10^{-13}	14.9	18.8	AGN 2	0.074	
228	13 53 54.4	18 20 16	17.0	6.8×10^{-13}	17.0	19.7	RED AGN 1	0.217	
⇒171	14 11 59	−03 06 27.0	33.2	3.9×10^{-13}	19.5	21.7	AGN 2	0.144	APM mag. ; Gr. ?
375	15 19 33.7	65 35 58	41.1	9.4×10^{-13}	10.1	11.5	AGN 1.9	0.044	
230_1	15 28 47.7	19 38 53	17.6	1.6×10^{-13}	20.3	20.6	AGN 1	0.657	mag. from G98
327	16 34 18.5	59 45 43	53.4	8.4×10^{-14}	17.8	18.3	AGN 1.8	0.341	
200	16 50 42.7	04 36 18	70.4	1.2×10^{-12}	11.2	13.9	AGN 1.9	0.031	
⇒190	16 52 37.5	02 22 6.0	13.9	6.7×10^{-14}	.....	.....	AGN 1	0.395	
147	20 42 53.0	−10 38 26	79.9	5.3×10^{-13}	17.8	18.8	AGN 1	0.363	APM mag.
149	20 44 34.8	−10 28 08	34.4	2.0×10^{-13}	.....	.....	AGN 1	2.755	
134	21 38 15.2	−14 33 54	100.5	2.3×10^{-13}	17.0	19.8	ELG	0.151	
⇒85	22 03 00.7	−32 04 46.0	28.4	2.8×10^{-13}	.....	.....	AGN 1	1.723	
237	22 26 31.7	21 11 35	27.1	3.9×10^{-13}	17.2	17.7	AGN 1	0.260	
212a	23 02 29.0	08 57 47	125.1	3.2×10^{-13}	18.3	20.3	ELG	0.135	APM mag. ; Gr. ?
212b	23 02 32.0	08 55 30	95.3	3.2×10^{-13}	16.9	17.3	ELG	0.132	Gr. ?
⇒35	23 16 8.8	−59 11 23.0	8.7	1.3×10^{-13}	19.4	21.3	ELG	0.391	APM mag.
66	23 19 32.0	−42 42 27	156.9	5.7×10^{-13}	17.1	17.2	AGN 1.8	0.101	Gr. ?
209	23 27 28.7	08 49 26	4.1	5.5×10^{-14}	18.7	20.6	AGN 1	0.154	
205	23 29 05.8	08 34 15.2	83.6	2.9×10^{-13}	.....	.....	AGN 1	0.953	
229	23 31 54.3	19 38 34.6	18.5	3.7×10^{-13}	19.1	20.2	AGN 1	0.475	

Source ID	RA (J2000)	DEC (J2000)	Δ_{X-Ott} (arcsec)	$F_{5-10\ keV}$ (erg cm^{-2} s^{-1})	R (USNO)	B (USNO)	Spec. ID	z	Notes
172	02 42 00.7	00 00 21	28	1.5×10^{-13}	18.4	18.6	AGN 1	1.112	
45	03 15 47.5	−55 29 03	31.1	2.7×10^{-13}	19.7	22.1	AGN 1	0.464	SC mag.
46	03 17 32.7	−55 20 25	13.7	4.1×10^{-13}	17.5	18.0	AGN 1	0.406	
72	03 33 12.9	−36 19 47	41.1	4.0×10^{-13}	18.5	20.4	BL Lac	0.308	
73	03 36 54.0	−36 16 07	34.4	3.7×10^{-13}	18.9	19.6	RLQSO	1.537	
385	07 21 36.0	71 13 22	86.2	8.4×10^{-14}	17.7	18.8	AGN 1	0.232	
392	07 41 50.0	74 14 48	41.2	3.1×10^{-12}			Cluster	0.216	
394	07 43 12.6	74 29 36	22.1	6.0×10^{-13}	16.2	17.0	AGN 1	0.312	
319	10 54 21.2	57 25 45	37.9	2.6×10^{-13}	18.4	21.0	AGN 1.8	0.205	
387	11 01 48.8	72 25 37	35.5	7.3×10^{-13}	17.1	17.3	RLQSO	1.460	
390	11 02 36.9	72 46 38	1	7.9×10^{-13}	15.2	16.7	AGN 1	0.089	
389	11 06 16.1	72 44 13	82.2	1.7×10^{-13}	18.6	19.2	AGN 1	0.68	
252	12 04 04.0	28 07 24	77.9	5.1×10^{-13}			Cluster	0.167	
265	12 17 52.1	30 07 01	24.4	3.5×10^{-13}	14.4	14.9	BL Lac	0.237	
290	12 19 52.3	47 20 57	68.1	1.2×10^{-13}	18.8	19.6	AGN 1	0.654	
400	12 22 07.0	75 26 17	0.8	2.5×10^{-13}			Cluster	0.240	
157	12 56 12.8	−05 56 29.3	126.6	9.1×10^{-14}	19.6	20.3	AGN 1	0.420	
150	13 05 33.0	−10 33 19	44.8	1.9×10^{-12}	14.9	15.0	RLQSO	0.278	
84	13 36 39.0	−33 57 57	66.7	3.2×10^{-13}	10.5	11.1	RadioGal.	0.013	
176	13 42 56.5	00 00 57	58.6	3.2×10^{-13}	19.3	19.6	AGN 1	0.804	APM mag.
239	14 17 18.8	24 59 30	82.3	6.9×10^{-14}	19.8	20.2	AGN 1	1.057	
241	14 18 31.2	25 10 50	16.9	6.1×10^{-13}			Cluster	0.240	
307	16 26 59.0	55 27 24	59.3	1.2×10^{-12}			Cluster	0.130	
201	16 50 00.0	04 54 00	41.9	9.5×10^{-13}			Cluster	0.154	
37	23 15 46.8	−59 03 14	86	2.0×10^{-13}	10.1	11.3	ELG	0.044	Int. gal.
250	23 55 54.3	28 35 58	14	4.2×10^{-13}	18.1	18.1	RLQSO	0.731	

Table 6.1: Optically identified HELLAS sources. The last part of this table concerns the classifications by catalogs. *Gr. ?* indicates the possibility for the HELLAS source of being a member of a group. *APM mag.* or SuperCOSMOS (SC) mag. are used when USNO mag. are not available. *G98*: magnitudes from Gorosabel et al. (1998). *Z92*: magnitudes from Zitelli et al. (1992). The sources indicated by ⇒ do not belong to the Final ("restricted") sample (with a limiting R magnitude and a restriction in RA and DEC).

Optical ID	Total	Final[a]	New ID		From cat.
			Total	Final[a]	
Type 1 AGNs	33	31	22	20	11
Red QSOs	2	2	2	2	0
Type 1.8-2 AGNs	12	10	11	9	1
Em.line gal. (ELGs)	8	6	7	5	1
Radio-loud QSOs (RLQSOs)	6	6	2	2	4
BL Lacs	2	2	0	0	2
Radio Gal.	1	1	0	0	1
Clusters	6	6	0	0	6
Stars	1	0	1	0	0
	71	**64**	45	38	26

Table 6.2: Summary of spectroscopic identifications.
[a] Sources with R magnitude greater than the chosen magnitude limit (different from one class to another) or lost after the selection of sky regions (the star).

USNO catalog, Monet et al. 1997, Monet 1998, and from APM in few cases, Maddox et al. 1990a,b, only one case with the SuperCOSMOS, Knox et al. 1998), spectroscopic classification and redshift, while a summary is shown in Table 6.2.

Given the uncertainties in *BeppoSAX* positions along with the MECS PSF width (as described in chapters 1 and 2), error boxes of the order of 1.5 arcmin of radius have been chosen in searching for the candidate optical counterparts of the HELLAS sources during the spectroscopic follow-up observations and by catalogs.

Histogram in Fig. 6.1 shows the distribution of the offset between the center of *BeppoSAX* error box and the position of the optical counterpart. The average distance, after the boresight correction of the *BeppoSAX* positions, is 51.1 arcsec.

It appears evident that in some cases the X–ray position is far from being consistent with the optical one (with offsets as large as $\sim$ 160 arcsec), the principal cause of this behavior being a non perfect position reconstruction due to some problems with the star-trackers (cfr. § 2.4) or the off-axis angle of the sources in the MECS detectors which, combined with the faintness of most sources, could lead to this error position. The effects of the off-axis angle and that of the 5–10

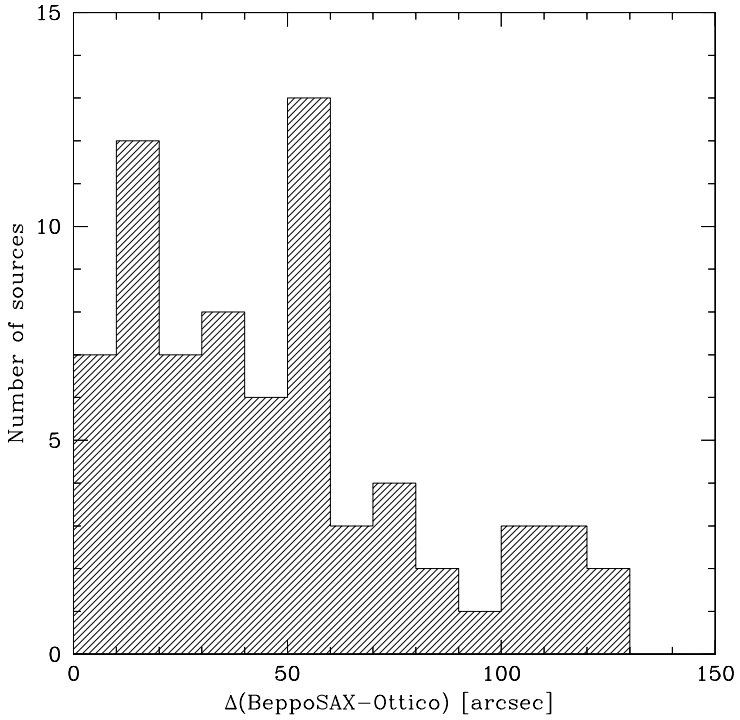

Figure 6.1: The offset distribution between the X–ray and the optical positions for all the identified HELLAS sources.

keV flux have been checked for all the identified sources. The result is that an important contribution to the relative difference between hard X–ray and optical positions is due to the sources at off-axis angles $10' < R < 15'$ (probably due to the presence of the Be strongback) and at $R > 20'$ (offset *BeppoSAX* – optical of about 1 arcmin), as well as by sources with fluxes below $\sim 4\times 10^{-13}$ erg cm^{-2} s^{-1}. Their individual effect is shown in Fig. 6.2 and 6.3, respectively.

It must be noted, however, that optical misidentifications can still be present, and will be discussed in the last part of this chapter.

In a limited number of cases (eight) the optical counterpart is not present in the error boxes (even if assumed larger than 90 arcsec) down to R=20.5–21: these represent the so called "blank-fields".

The HELLAS identified subsample can be considered a good representation of the full sample in terms of hard (5–10 keV) X–ray

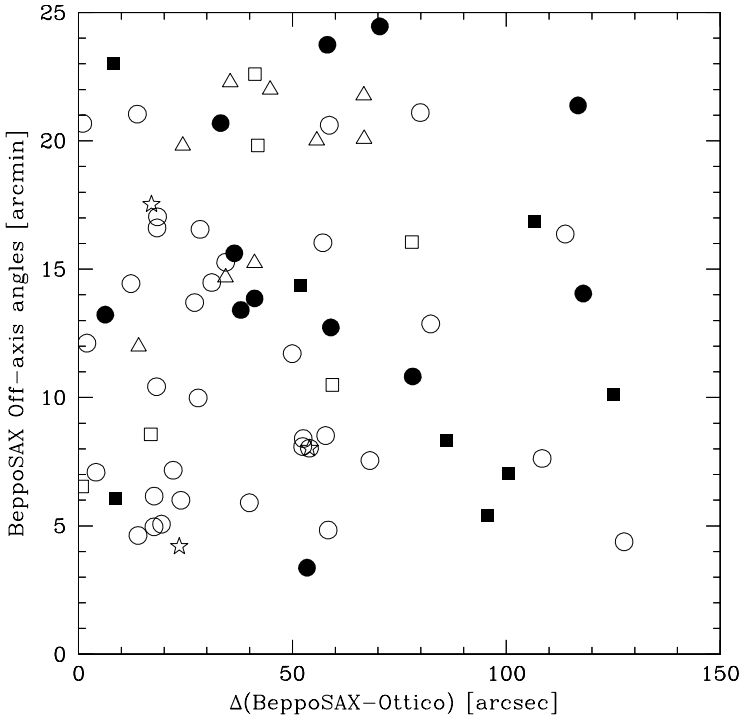

Figure 6.2: The offset distribution between the X–ray and the optical positions as a function of the off-axis angles in *BeppoSAX* . Symbols are as in previous figures, while the CIRCLED $\star$ indicates the unique HELLAS object identified as star.

flux, as shown in Fig. 6.4. The redshift distribution of the HELLAS sources (Fig. 6.5) indicates that most of the identified sources are at redshift greater than 0.2 and, among them, the most numerous are broad-line objects (radio-loud and radio-quiet). The finding of many moderate/high-redshift broad-line objects is a consequence of their high nuclear luminosity, as shown in Fig. 6.6, where the 5–10 keV luminosity is plotted as a function of redshift.

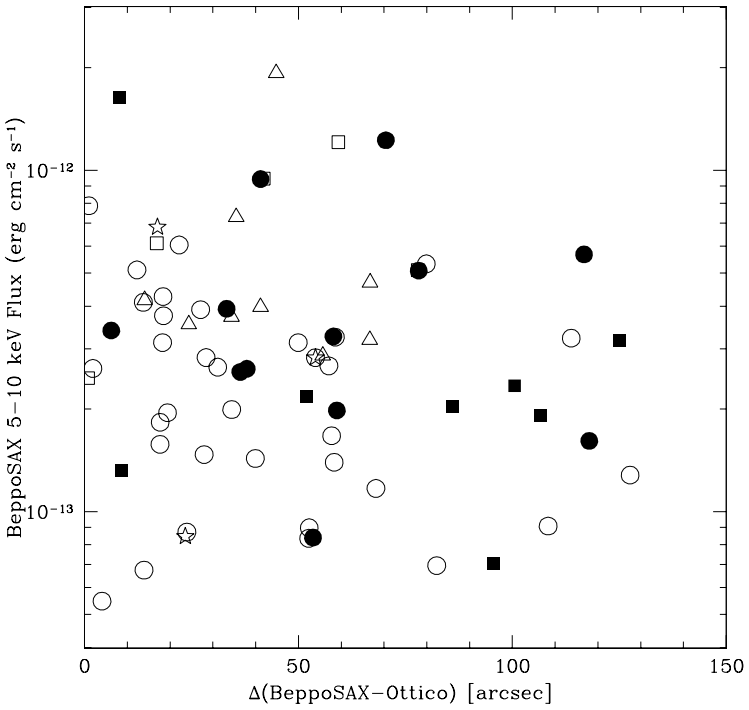

Figure 6.3: The offset distribution between the X–ray and the optical positions as a function of the 5–10 keV flux.

6.3 Photometric runs

Photometric follow-up observations of the HELLAS fields have been performed from 1998 to 2000, in order to get reliable information about optical and near-infrared colors, and to make possible a detailed study of a subsample of objects characterized by interesting and rather extreme hard X–ray properties.

Optical photometric observations have been performed at the 1.5-m telescope of S. Pedro Martir (Mexico, on October 1998) and at the 3.5-m National Telescope Galileo (TNG) in the Canary Islands (June 1999 and 2000).

Across the end of 1998 and June 2000 near-infrared (NIR) observations have been carried out with the infrared camera ARNICA at the TNG. Only one object has been observed in the near-infrared

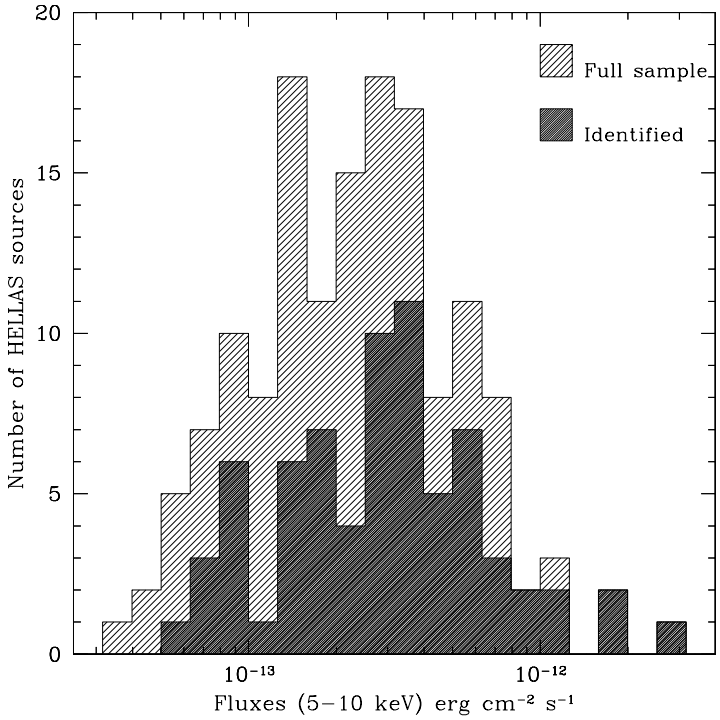

Figure 6.4: The 5–10 keV flux distribution of the HELLAS identified sources with respect to the full sample. The identified subsample well reproduces the flux distribution of the full sample.

with the NIRC (Matthews & Soifer 1994) at Keck I.

The result of this broad-band approach is such to make possible a modeling of the continuum emission for a subsample of HELLAS sources from the near-infrared up to the UV band and, by comparison with galaxy templates, to determine the relative importance of the host galaxy with respect to the AGN. This aspect will be extensively discussed in the following.

6.3.1 Optical and Near-Infrared data reduction

Most of the results presented in this section have been obtained through the Optical Imager Galileo (OIG) and the Arcetri Near-Infrared Camera (ARNICA) at the Italian National Telescope Galileo

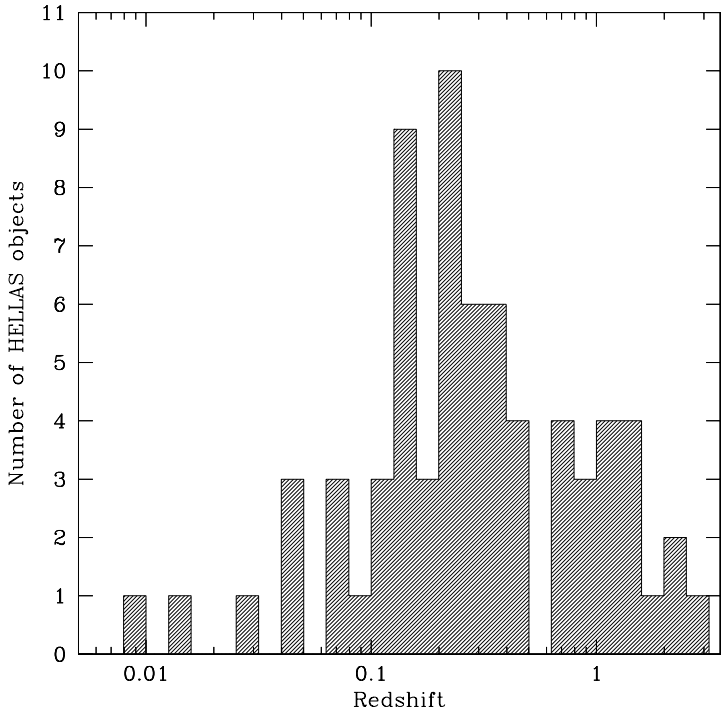

Figure 6.5: The redshift distribution of the HELLAS sources optically identified either through existing catalogs of by follow-up observations.

(TNG) at La Palma in the last two years.

Optical broad-band imaging was carried out in the Johnson–Kron–Cousins–Gunn *U, B, V, R* and *I* filters. For the 1999 observations (whose results will be the principal subject of this section) the seeing ranges from 0.9 arcsec (FWHM) in the reddest band to 1.3 arcsec in the ultraviolet, with a steady increase through the optical bands giving evidence that the blurring is mainly due to atmospheric causes. The observations performed in June 2000 have been carried out at a seeing typically varying from 1.2 up to 2 arcsec (FWHM). The frames relative to the 1998 observing run have been observed at airmass $\leq$ 1.5, the more recent ones at airmass $\leq$ 1.8. The data reduction and analysis has been performed in a standard way using IRAF routines. Bias exposures taken at the beginning and at the end of the night were stacked, checked for consistency with the overscan region of the

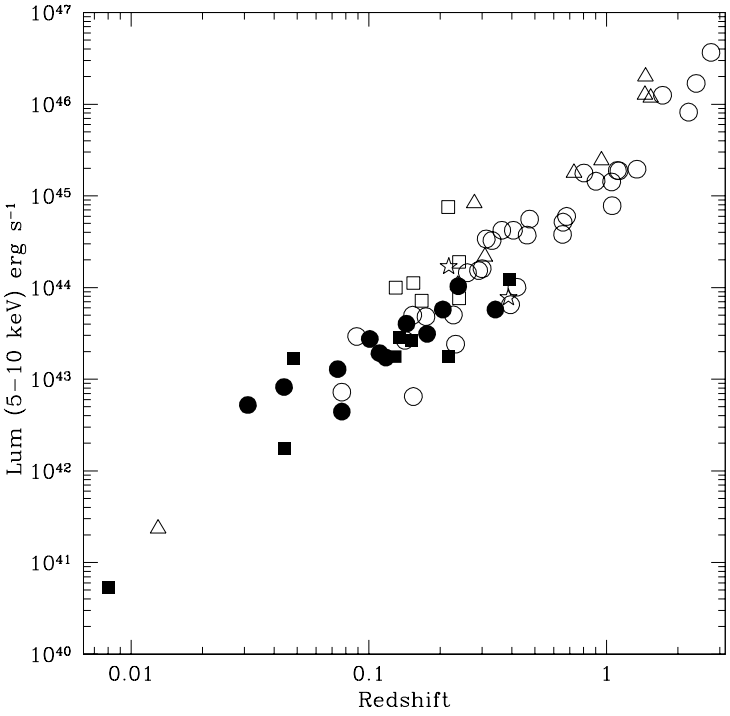

Figure 6.6: The 5–10 keV luminosity of the HELLAS sources as a function of their redshift. The symbols are as in previous chapters. Among the X–ray brightest objects the major role is played by Type 1 objects and radio-loud AGNs (BL Lacs and radio-loud quasars).

scientific images and subtracted out. The bias–subtracted frames were then flat–fielded using sky flats. The cosmic rays of the CCD region around the target have been interactively identified and removed by fitting of the neighboring pixels (through the COSMICRAYS routine) or, alternatively, by using the XZAP task implemented in the IRAF context.

The photometry has been performed using `apphot`, the Aperture Photometry Package available in IRAF.

Most of the NIR images were obtained with the ARNICA camera (Lisi et al. 1996), only one object has been observed with the NIRC at Keck I. The objects were observed at K-short (~ 2.16 μm) and at J (~ 1.25 μm), with a seeing ranging between 0.4 and 1 arcsec for 1998–1999

observations, and between 0.9 and 1.8 for June 2000 observations.

The observations were performed by mosaicing the field every minute, and by applying offsets of about 10–20 arcsec around the source, in order to sample the background and to minimize the effects of artifacts in the array. The data reduction pipeline was similar to that described in Hunt et al. (1994). Each image was divided by a differential flat-field made out of sky twilight images. Then images of each mosaic were aligned by means of field stars and co-added with a average sigma clipping rejection to exclude both hot and dead temporary pixels, not accounted for by the bad pixel mask.

The photometric results from TNG observations are presented in Table 6.3, while those performed at the 1.5-m telescope at S. Pedro Martir (Mexico) are listed in Table 6.4, along with the magnitudes in the R filter obtained at the 3.6-m telescope at La Silla through the acquisition images taken before spectroscopy.

6.4 Probing the nature of the Optical+NIR continuum in a subsample of HELLAS sources

In order to shed light on the nature of the optical and NIR continuum of the HELLAS sources, a subsample of 15 objects was studied in detail through the 1998–1999 follow-up observations described above. It must be noted that this subsample was not selected with a specific criterion, but it was drawn from the early HELLAS identifications known and accessible at the time of those observations. This subsample includes six "classical" broad-line objects with a blue continuum (objects 149, 167, 176, 230_1, 239 and 282), five Type 1.8-2 AGNs (objects 103_1, 200, 264, 327 and 375), two "red" broad-line quasars (228 and 283), characterized by a red underlying continuum, one of which has been investigated in great detail in the hard X–rays (chapter 5) and will be treated apart in the following, and two objects classified as emission line galaxies (ELGs, objects 134 and 169). This "random" selection samples well both the classes of AGNs (Type 1, intermediate AGNs, emission-line galaxies) and the redshift range of the HELLAS sample. Thus, even if it is not statistically solid because of the small size, it still contains information on the general properties of the HELLAS sources. About half of this subsample of 15 objects have already been extensively analyzed and the results are presented in Maiolino et al. (2000). I discuss the preliminary

Source ID	Optical Photometry					Near-Infrared Photometry	
	U	**B**	**V**	**R**	**i**[a]	**J**	**K_S**[b]
103_1						16.38±0.05	15.27±0.07
283	19.54±0.08	20.19±0.06	19.62±0.05	18.71±0.04	17.88±0.04	16.48±0.05	14.97±0.07
282	18.30±0.07	19.24±0.05	18.93±0.04	18.54±0.04	18.39±0.04	17.98±0.10	16.69±0.15
264	21.08±0.15	20.69±0.05	19.26±0.04	18.58±0.03	17.75±0.04	16.51±0.05	15.14±0.07
167		20.53±0.05	19.70±0.05	18.77±0.04	17.88±0.05	16.65±0.07	15.02±0.07
169[c]	17.01±0.07	16.75±0.05	16.00±0.04	15.15±0.03	14.47±0.04	11.56±0.05	10.43±0.02
176	18.54±0.07	19.21±0.05	18.99±0.04	18.72±0.04	18.35±0.04	17.82±0.09	17.46±0.17
228	19.98±0.07	19.55±0.03	18.15±0.03	17.32±0.02	16.62±0.04	15.26±0.05	13.90±0.07
239	19.08±0.07	19.97±0.05	19.76±0.04	19.31±0.04	18.73±0.04	18.55±0.11	17.88±0.23
375	16.27±0.04	15.98±0.01	15.00±0.01	14.39±0.01	13.70±0.01		
375[d]	17.50±0.04	17.24±0.01	16.19±0.01	15.56±0.01	14.84±0.01		11.38±0.07
230_1							15.94±0.07
327		20.31±0.01	20.03±0.02	19.52±0.02	19.27±0.04	18.89±0.16	17.26±0.28
200	16.70±0.07	16.38±0.05	15.33±0.04	14.64±0.03	13.98±0.04	12.90±0.06	11.55±0.02
149	17.56±0.07	18.04±0.05	18.01±0.04	17.76±0.03	16.74±0.04	16.25±0.05	14.91±0.05
134	21.06±0.08	19.49±0.05	18.13±0.04	17.23±0.03	16.44±0.04	15.59±0.03	14.59±0.03

Table 6.3: Optical and NIR magnitudes obtained through follow-up observations (TNG).
[a] Gunn-i filter.
[b] K-short band (2.16 μm).
[c] Inner 4.6 arcsec.
[d] Inner 2.5 arcsec.

Source ID	Tel.	Optical Photometry		
		B	**R**	**I**[a]
120	E		18.1±0.10	
93	E		18.0±0.10	
91	E		20.1±0.10	
96	E		19.1±0.10	
172	M	19.49±0.15	18.58±0.07	18.53±0.11
75	E		20.1±0.10	
53	E		17.3±0.10	
54	E		20.5±0.10	
65	E		16.6±0.10	
243	E		16.9±0.10	
246	E		15.3±0.10	
137	E		19.6±0.10	
151	E		18.8±0.10	
155	E		20.1±0.10	
92	E		17.1±0.10	
97	E		16.5±0.10	
171	E		20.5±0.10	
190	E		20.7±0.10	
147	E		17.9±0.10	
134	M	19.50±0.04	17.31±0.04	16.45±0.04
85	E		21.7±0.10	
237	M	18.42±0.04	17.59±0.05	16.98±0.06
212a	M	19.82±0.05	18.62±0.04	17.90±0.05
212b	M	19.84±0.05	17.84±0.03	16.93±0.03
35	E		19.6±0.10	
205	E		20.3±0.10	
229	E		18.8±0.10	

Table 6.4: Optical magnitudes obtained at the 1.5-m Mexican telescope at S. Pedro Martir (M) and with EFOSC2 acquisition images at ESO 3.6-m (E).
[a] Cousins-I filter.

results obtained by enlarging the old subsample with "new" objects observed at TNG in 2000.

It must be noted that for two objects of Table 6.3 (the HELLAS source 230_1 and 103_1) the optical magnitudes are available only from catalogs (see Table 6.1), therefore some uncertainties on the derived colors may be possible.

The most remarkable result is that all the intermediate-Type 2 AGNs and the red QSOs show extended emission indicative of a significant NIR contribution from the host galaxy. Moreover, one emission-line galaxy (out of two) and two blue-continuum quasars also show extended emission, both in the optical and in the NIR. Furthermore, the B−K_s colors are not clustered around the value of

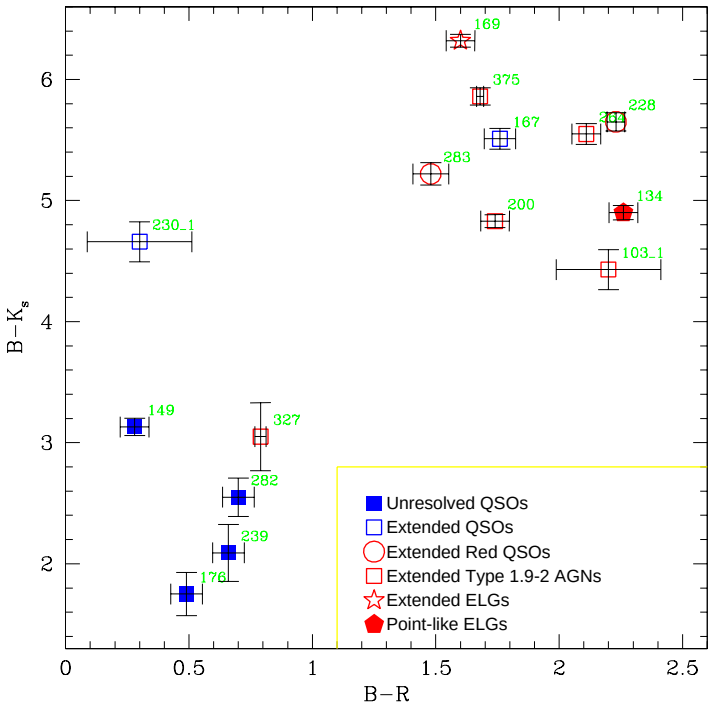

Figure 6.7: B−R plotted against B−K_S for a subsample of 15 HELLAS sources (blue-continuum QSOs, red-continuum QSOs, Type 1.8-2 AGNs and emission-line galaxies). The filled symbols indicate the point-like objects, the open ones the extended sources.

$\sim$ 2, which can be considered typical of color–selected QSOs at high redshift, but extend to very red values up to B$-$K $\sim$ 5 (Fig. 6.7), in analogy with the radio selected AGNs (Webster et al. 1995; Francis, Whiting & Webster 2000). Therefore, it seems plausible that our "red" AGNs are the radio-quiet counterparts of red AGNs found in the radio surveys.

The color-color diagram in Fig. 6.7 show that the objects characterized by extended emission populate the upper region of the B$-$R vs. B$-$K$_S$ diagram, the unique exception being the Sey 1.8 galaxy HELLAS 327, which is in the region populated by blue-continuum (point-like) quasars. It is possible that the contribution from the host galaxy is moderate.

In the upper right part of the color-color diagram there are Type 1.8-2 objects, one extended Type 1 and also two emission-line galaxies, both characterized by red colors in the optical and in the NIR (B$-$K$_S$ $\sim$ 4–6).

The average B$-$K$_S$ is 5.1 and 2.9 for the extended and the point-like objects, respectively. Also the B$-$R color shows a similar behavior, with the extended objects having an average B$-$R $\sim$ 1.6, the unresolved ones 0.88. A possible source of uncertainty is given by the optical photometry for two objects (which is derived by catalogs) and by the fact that for some sources the optical and NIR data belong to different periods, so variability may play a role.

Four blue AGNs (out of six) are unresolved: this is a consequence of the dominance of the AGN component and, possibly, of their higher redshift. Indeed, the two blue QSOs showing extended emission are those at lower redshift.

In order to check and quantify the contribution from the host galaxies, a QSO template spectrum (derived from a combination of the average spectra given in Elvis et al. 1994a and Francis et al. 1991) and galaxy templates from Bruzual & Charlot (1993), with solar abundances and a Salpeter IMF, were assumed in order to reproduce the observed color-color diagram.

The free parameters of the model are the reddening of the QSO, the age of the stellar population and the relative contribution of these two components. The observed optical to NIR photometric data and optical spectra of each object have been compared with those expected from (reddened) QSOs and from evolved stellar populations. An example

of this method for a specific object will be presented in the following subsection.

The combination of the (reddened) AGN spectral template and that related to the host galaxy component should give an acceptable fit of the observed photometric points. The maximum tolerance between the model and the observed optical spectrum is 30 %, to account for all the uncertainties introduced by the non-parallactic angle of the slit. In the same way, an attempt to fit the equivalent width (EW) of the observed broad hydrogen lines was performed (within a factor of two, given the EW spread in the optical samples of QSOs).

It must be noted that a QSO template cannot explain all our data, irrespective of the assumed amount of reddening. Instead, the reddest objects have colors similar to those expected from an evolved stellar population.

Fig. 6.8 shows examples of the spectral fits, corresponding to three representative classes of AGNs: one blue continuum quasar, one AGN 1.9 and one quasar with a red continuum.

The thin solid line in the upper panels is the best-fit QSO + galaxy model, the two thick lines indicate the shape (and spread) of the line-free continuum observed in the optical spectra, while points with error-bars are the photometric fluxes normalized to R band. It appears evident that the red, spatially resolved sources are characterized by the 4000 Å break, with a discernible progression from the "transition" sources to the very red ones. The B−R colors and the preferred age for the model population increase in the same way (from ~ 1 to ~ 2.8, and from 10^9 to 10^{10} years, respectively). The fractional contribution of the reddened AGN (to the rest frame V-band) decreases from 100 % in the bluest objects to a few percent in the red ones. Although a small contribution from a reddened AGN is required even in the reddest objects, this cannot dominate their red colors, as shown in the lower panel of Fig. 6.8, where it is evident that a (reddened) QSO template cannot account for both the continuum shape and the photometric points (which are poorly fitted).

Remarkably, the best-model fitting to the photometry and spectral shape perfectly agrees with the imaging results, in the sense that the contribution of the host galaxy is generally dominant in those sources which appear extended.

Finally, it is interesting to note that the best-fitting stellar

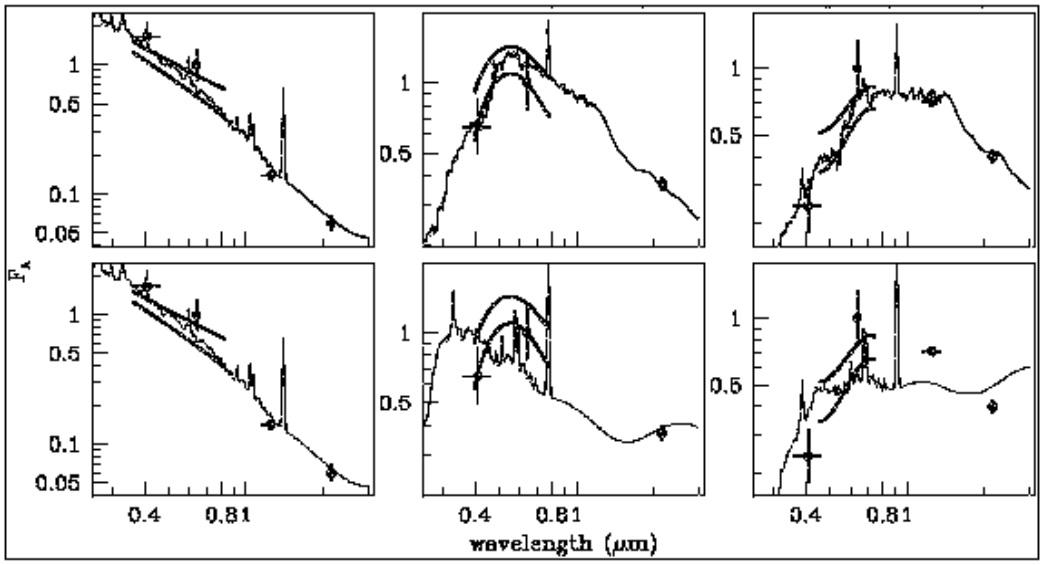

Figure 6.8: Comparison between photometric measurements (black dots with error-bars) and observed optical spectral shapes (thick lines) with the best-fit models for three representative objects (one blue quasar, one AGN 1.9 and one red quasar, respectively). Models in the upper panels (thin solid lines) include both the contribution from a reddened QSO and from an evolved stellar population (which appears to be dominant in the Type 1.9 AGN–t$\sim 10^9$ yrs and in the red QSO–t$\sim 10^{10}$ yrs). The dotted lines in the lower panels represent the best-fit using only a quasar template with the appropriate reddening.

populations are generally old/evolved. However, one should bear in mind that in certain cases different models such as a reddened 10^9 year-old population or a reddened continuous burst provide also an acceptable fit to the data, indicating some degree of degeneracy.

Red, absorbed AGNs are about 25–30 % of the identified sources in the HELLAS sample. This fraction increases to about 38 % if one assumes that the optical counterparts in the "blank fields" are strongly absorbed AGNs. It is possible that the fraction of obscured AGNs is higher at fainter X-ray fluxes, where the remaining 70–80 % of the hard X-ray background is produced (Gilli et al. 1999).

The present results suggest that a large fraction of the hard XRB contributors have optical/near-IR counterparts which appear as

"normal" galaxies (possibly with narrow AGN–like emission lines). A population of red AGNs similar to that analyzed in this section but at z > 1 would probably remain undetected at R=20–21: these could be the counterparts of the HELLAS sources for which no optical identification was found.

6.5 SAXJ 1353.9+1820 (HELLAS 228): a red quasar

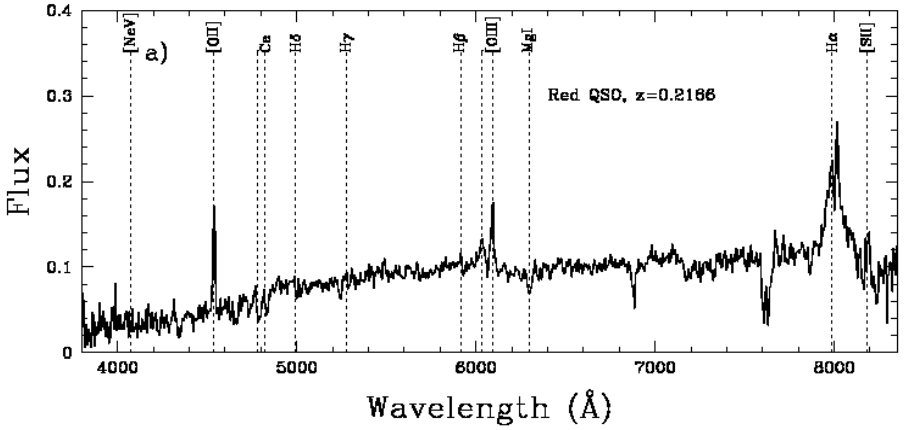

Figure 6.9: The optical spectrum of the red quasar SAXJ 1353.9+1820.

The optical spectrum (Fig. 6.9) of the z = 0.217 red quasar SAXJ 1353.9+1820 (Vignali et al. 2000a) is dominated by starlight, as the presence of H and K plus Mg I absorption lines clearly indicates. The Hα equivalent width (about 90 $\AA$), the absence of the Hβ and the *BeppoSAX* softness ratio (SR $\simeq$ 0.11) are suggestive of reddening of the nuclear radiation (see also chapter 5 for the *ASCA* observations). The *BeppoSAX* hard X–ray luminosity, $L_{5-10\ keV} \sim 1.4 \times 10^{44}$ erg s^{-1}, the

presence of a broad Balmer line and the optical spectrum properties allow to classify this object as a fairly low-luminosity, red quasar.
This class of objects, originally discovered in radio–selected samples (Smith & Spinrad 1980), is characterized by red optical colors ($B-K$ up to 8, Webster et al. 1995; Francis et al. 2000). From *ROSAT* PSPC observations and optical spectroscopy Kim & Elvis (1999) pointed out that a significant fraction (from a few percent up to 20 per cent) of soft X–ray selected radio–quiet quasars belong to this class. The origin of the observed 'redness' may be ascribed to dust absorption, to intrinsic red colors ($\geq$ 70 per cent of the red sources of the Parkes sample has $\leq$ 30 per cent of contribution to B−K by their host galaxies, Masci, Webster & Francis 1998) or to an excess of light in K band rather than a dust-induced deficit in B (Benn et al. 1998). Whatever is the origin of the red colors, it is likely that a large fraction of quasars could have been missed by the usual selection techniques in the optical band (Webster et al. 1995). If this is the case, red quasars could constitute a sizeable fraction of the absorbed AGNs population needed to explain the hard X–ray background spectrum (i.e. Comastri et al. 1995). Hard X–ray observations provide the most efficient way to select these objects; indeed two candidates have been found in the course of the optical identification program (Fiore et al. 1999).

6.5.1 Optical and NIR photometry

SAXJ 1353.9+1820 has been observed at the 3.5-m National Telescope Galileo with the OIG and ARNICA instruments (Table 6.3). The object is clearly extended ($\sim$ 8 arcsec, corresponding to a projected distance of about 15 h_{50}^{-1} kpc at the redshift of the source).

The surface brightness (SB) profiles in the U, B, V, R and I filters have been estimated computing a curve of growth for each passband with increasing circular apertures (Fig. 6.10). An effective radius of $\sim$ 1.5 arcsec was independently derived from all but one fits (for the I–band the profile is slightly more concentrated). The dashed line in Fig. 6.10 represents the $r^{1/4}$ law, which fits very well the observed profiles outside of the seeing-dominated region down to the faintest flux levels. The SB profiles are typical for elliptical galaxies suggesting that at optical wavelengths there is no evidence of an unresolved nucleus in SAXJ 1353.9+1820.

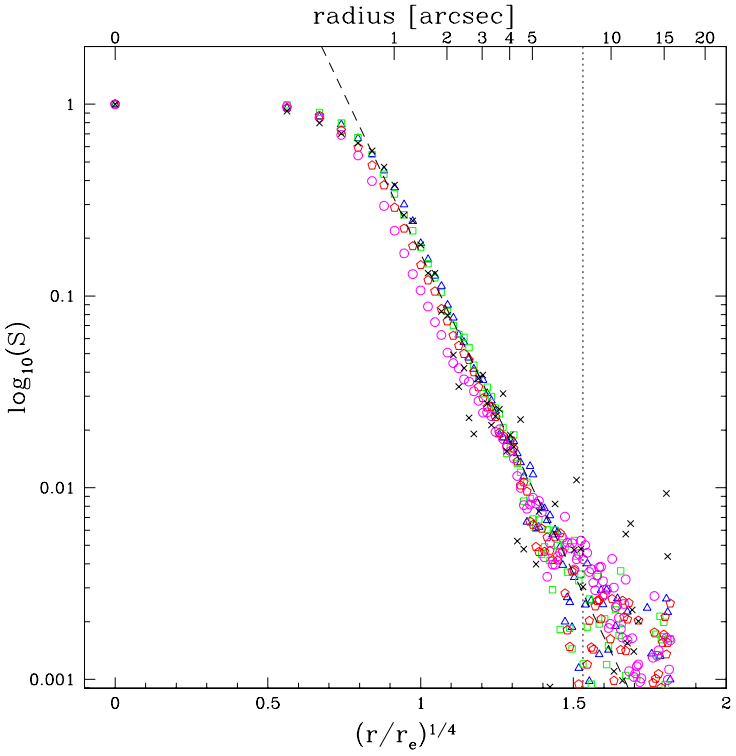

Figure 6.10: The optical surface brightness profiles of SAXJ 1353.9+1820 fitted with a de Vaucouleurs $r^{1/4}$ law (dashed line). Different symbols are referred to different filters. The vertical dotted line represents the adopted aperture radius.

6.5.2 X–ray absorption

The *ASCA* observation confirms the presence of a bright and moderately absorbed ($N_{\rm H} \sim 6 \times 10^{21}$ cm^{-2}) nucleus with a flat hard X–ray spectrum, in agreement with the BeppoSAX softness ratio analysis. Assuming for the underlying continuum slope the average value of quasars in the same energy range (i.e. Γ=1.8–1.9), the absorption column density could be as high as $N_{\rm H} \sim 3 \times 10^{22}$ cm^{-2} if some 20 per cent of the nuclear radiation is not absorbed. Even if the X–ray data alone does not allow to distinguish between the two possibilities, SAXJ 1353.9+1820 harbors a mildly obscured, luminous ($L_{2-10\rm keV} \simeq 1.3 \times 10^{44}$ erg s^{-1}) active nucleus.

Not surprisingly high energy observations of quasars characterized by similar dust reddened optical continua do reveal the presence of absorption by cold (IRAS 23060+0505, Brandt et al. 1997a) and/or warm (IRAS 13349+2438, Brandt et al. 1997b) gas.

6.5.3 The nature of SAXJ 1353.9+1820

The surface brightness profiles are consistent with those of an elliptical galaxy, and the optical colors (U−B = 0.43, B−V = 1.40, V−R = 0.83 and R−I = 0.70) agree with the properties of a early-type galaxy at $z = 0.2$ (Fukugita, Shimasaku & Ichikawa 1995). The optical colors provides a first, clear indication of the presence of a strong contribution from the host galaxy.

A more comprehensive picture of the optical–NIR properties of SAXJ 1353.9+1820 can be obtained by fitting the photometric points (cfr. § 6.4) with a two-components model consisting of an old stellar population template (10^{10} yr, Bruzual & Charlot 1993) and a moderately absorbed ($A_V \simeq 2$ mag, corresponding to $N_H \simeq 4 \times 10^{21}$ cm^{-2} for Galactic dust–to–gas ratio, i.e. Bohlin, Savage & Drake 1978) quasar spectrum template (Elvis et al. 1994a; Francis et al. 1991), in a similar way to that described in section 6.4.

As shown in Fig. 6.11, the combination of these two spectra provides a good description of the observed data (possibly with the exception of the J photometry, which deviates by 1.4 sigma). The quality of the fit is acceptable ($\chi^2_r = 1.3$ when both the uncertainties in the photometric data and in the template spectra are taken into account) indicating that most of the optical and near–IR flux is dominated by starlight.

The importance of the host galaxy can be alternatively evaluated also by locating SAXJ 1353.9+1820 in the color-color diagram obtained for the extended objects in the Marano Field (Zamorani et al. 1999) in the same range of B magnitude (Fig. 6.12). It can be clearly seen that the red quasar optical properties, although not extreme, are such to populate neither the region of high-z red quasars nor that of low-z UV-selected QSOs.

The present results add further evidence on the hypothesis of substantial gas and dust absorption as an explanation of the observed properties of this red quasar. Even more interesting is that the active nucleus peers only at X–ray energies and possibly at

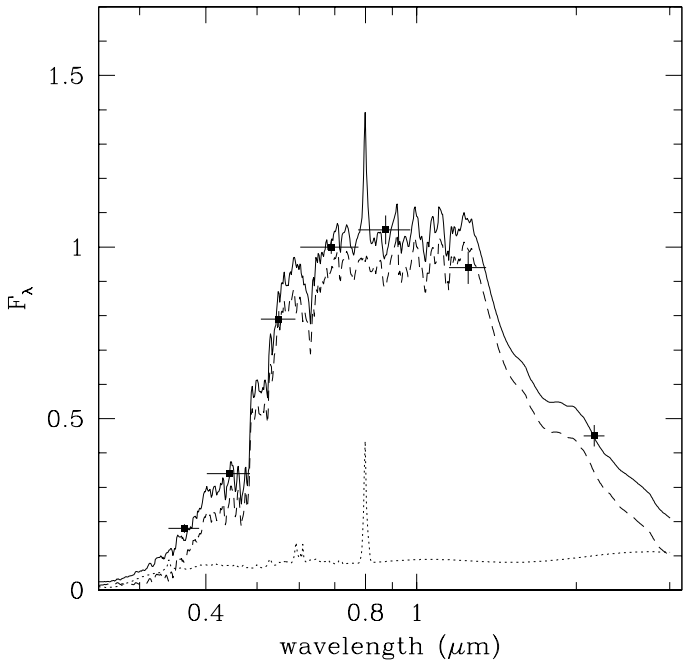

Figure 6.11: SAXJ 1353.9+1820 photometric (optical + NIR) points fitted with a synthetic model of an evolved early-type galaxy (dashed line) plus the contribution of a moderately absorbed quasar (dotted line). The sum is given by the solid line.

wavelengths longward of 2 μm (Fig. 6.11), while at optical wavelengths SAXJ 1353.9+1820 looks like a normal evolved elliptical galaxy.

If this behavior applies also to other objects it may well be that a significant fraction of obscured AGNs resides in otherwise normal passive galaxies. These nuclei would have been completely missed in optical quasar surveys because of their extended morphology and galaxy-like colors. If the column density is of the order of 10^{22} cm^{-2} or higher, their fraction could be underestimated also in soft X–ray surveys. If this is the case, the fraction of red objects among radio-quiet quasars ($\sim$ 3–20 per cent, Kim & Elvis 1999) should be considered as a lower limit. This may have strong implications for the XRB synthesis models, which in their simplest version (i.e. Madau et al.

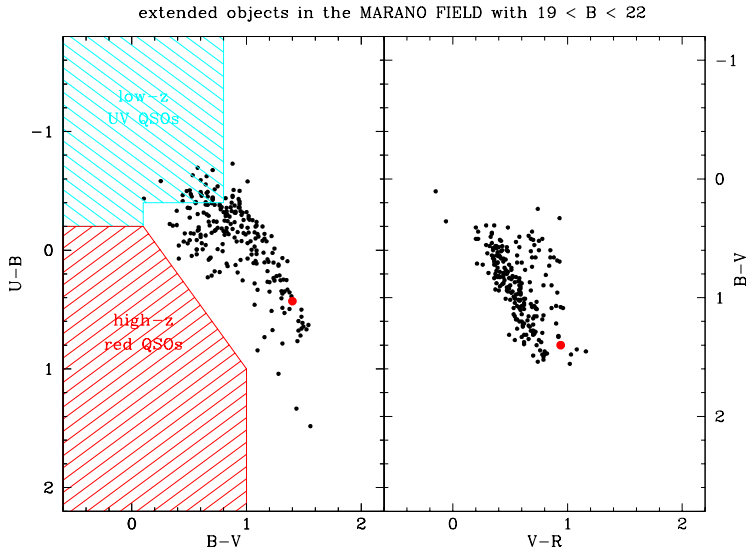

Figure 6.12: The B−V vs. U−B and V−R vs. B−V diagram for all the extended objects which populate the Marano field in the B magnitude range 19–22. It is interesting to note that the "normal" selection criteria adopting to select high-z red quasars and low-z UV-selected QSOs would fail with SAXJ 1353.9+1820.

1994; Comastri et al. 1995) predict a large number of high-luminosity absorbed quasars (called type 2 QSOs). Despite intensive optical searches, these objects appears to be elusive indicating a much lower space density than that of lower luminosity Seyfert 2 galaxies (Halpern, Eracleous & Forster 1998) and calling for a substantial revision of AGNs synthesis models for the XRB (Gilli et al. 1999).

An alternative possibility (see Comastri 2000) is that X–ray obscured AGNs show a large variety of optical properties including those of SAXJ 1353.9+1820. It is worth noting that column densities as high as $10^{23.5}$ cm^{-2} have been detected in Broad Absorption Line QSOs (Gallagher et al. 1999), in some UV bright soft X–ray weak QSOs (Brandt et al. 2000b), in bright PG quasars (Gallagher et al. 2001), and in a few HELLAS sources optically identified with broad line blue quasars (chapter 3). It is thus possible that the sources responsible for a large fraction of the XRB energy density are characterized by a large spread in their optical to X–ray properties. The α_{ox} spectral

index, defined as the slope joining the 2500 $\AA$ and the 2 keV flux densities, is usually employed to measure the optical to X–ray ratio. Not surprisingly, absorbed objects are characterized by values of α_{ox} ($>$ 1.8) much steeper than the average value of bright unabsorbed quasars and Seyfert galaxies, $\alpha_{ox} \simeq 1.5$ (Laor et al. 1997; Yuan et al. 1998), while the faint nuclear UV flux density and the relatively bright 2 keV flux of SAXJ 1353.9+1820 correspond to $\alpha_{ox} \simeq 1$, which is quite flat but not unusual for red quasars (Kim & Elvis 1999).

As far as the X–ray spectral properties and the bolometric luminosity of $\simeq 10^{45}$ erg s^{-1} (estimated using the average SED of Elvis et al. 1994a with the measured α_{ox}) are concerned, SAXJ 1353+1820 can be classified as a high–luminosity absorbed AGN.

6.6 Optical properties of the HELLAS sample Comparison with hard X–ray properties

Figure 6.13 shows the B−R distribution for the HELLAS Type 1, Type 1.8-2, red quasars and emission-line galaxies identified either by our follow-up observations or by existing catalogs (see Table 6.2 for a summary). The optical magnitudes are taken mainly from the USNO 1.0 (2.0) catalog (Monet et al. 1997; Monet 1998), as in Table 6.1, and partly from our photometric follow-up observations.

It is evident that Type 1 AGNs (with a blue optical continuum) populate a different region with respect to Type 1.8-2 AGNs (i.e. narrow-line). This is confirmed by computing the average <B−R> = 0.81 (with a dispersion $\sigma = 0.65$) for the former class and <B−R> = 1.81 ($\sigma = 0.97$) for the latter. Also the two red quasars and most of the ELGs are among the reddest sources. This confirms the results previously presented about the optical + NIR observations of a subsample of objects. It must be kept in mind that even though some uncertainties in the optical R and B magnitudes derived from catalogs may exist, Type 2 objects are generally redder than Type 1 but appear also more dispersed, as evident from the low B−R tail populated by narrow-line objects as well as broad-line sources.

Similar evidences can be drawn from the *BeppoSAX* softness ratio analysis (chapter 3). Indeed, the average softness ratio is <SR> = 0.055 ($\sigma = 0.344$) and <SR> = −0.132 ($\sigma = 0.314$) for Type 1 and Type 2, respectively. One again, the large uncertainties on the

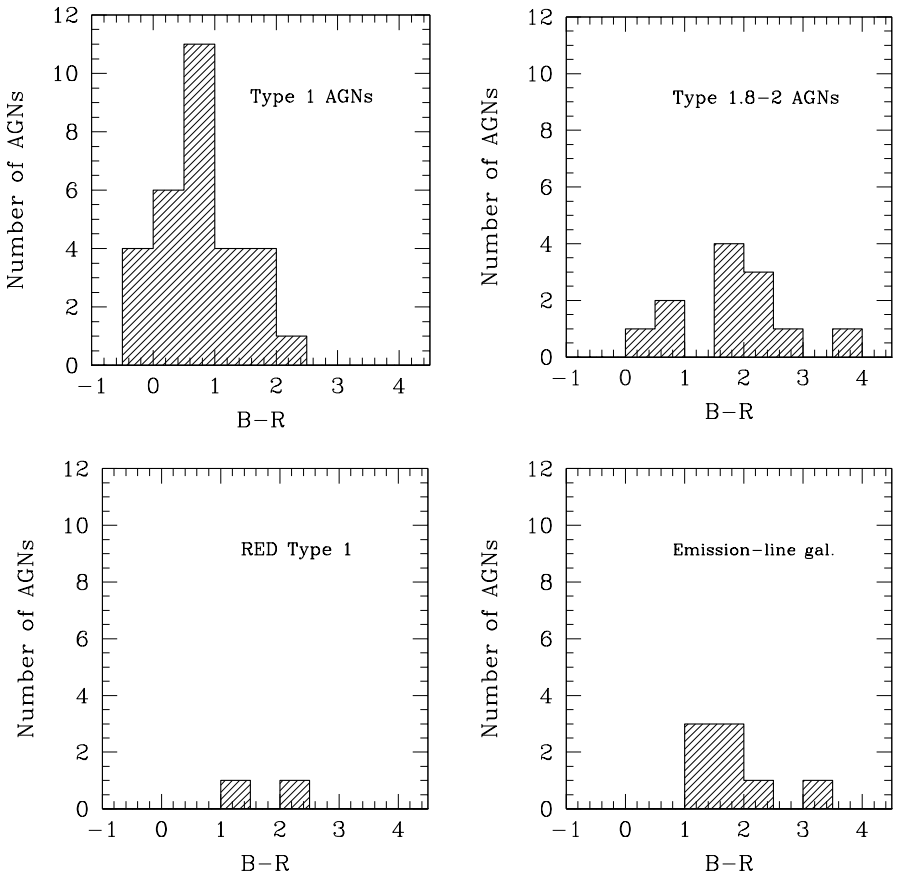

Figure 6.13: The B−R distribution of the HELLAS sources which have been spectroscopically identified as Type 1 AGNs, Type 1.8-2 AGNs, red quasars and emission-line galaxies. Magnitudes are drawn from catalogs (see text) and from follow-up photometric observations.

softness ratio deserves further investigations, possibly with instruments characterized by higher sensitivity than *BeppoSAX* (e.g. *Chandra* and *XMM-Newton*). X–ray spectra even harder (flatter or more absorbed continuum) are required by the objects classified as emission-line galaxies (ELGs), with <SR> $= -0.307$ ($\sigma = 0.216$). Anyway, there is a clear trend for the hardest sources to be characterized by red optical

colors on average. Note that broad-line AGNs (except for a few objects) are generally well separated from the narrow-line in the softness ratio vs. B−R diagram plotted in Fig. 6.14, although the scatter in both the classes is large. For comparison, also the other identified extra-galactic sources (excluding the clusters) are plotted in the same figure.

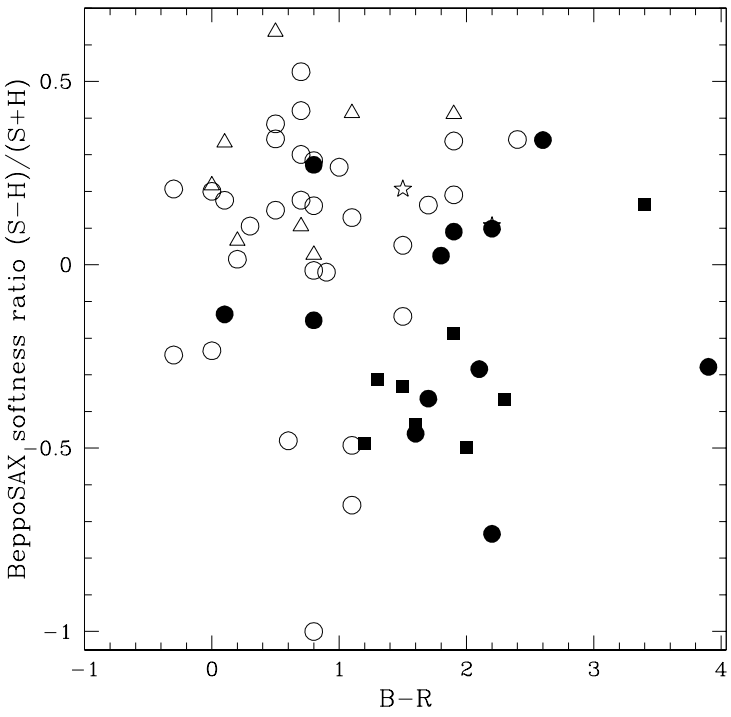

Figure 6.14: The *BeppoSAX* softness ratio vs. the optical B−R color.

Fig. 6.15 shows the X–ray-to-optical ratio as a function of the 5–10 keV flux for the HELLAS identified sources. The dashed lines identify the regions of constant apparent R magnitude. For comparison, different classes of local luminous AGNs are also indicated in the figure. The X–ray-to-optical ratio of the HELLAS sources is similar to that of the X–ray brightest objects in the local Universe.

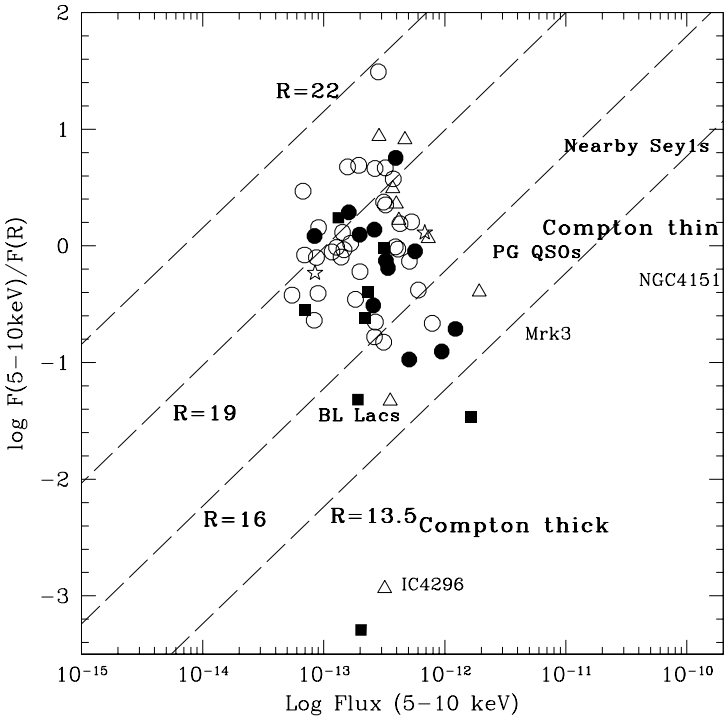

Figure 6.15: The X–ray-to-optical ratio vs. the 5–10 keV flux for the HELLAS identified sources. The loci of equal R magnitudes are plotted, along with the regions populated by the principal classes of nearby AGNs (Seyfert 1 galaxies, Compton-thin Seyfert 2s, Compton-thick sources, PG QSOs, and BL Lac objects). Some intermediate objects (NGC 4151, Mrk 3) are also plotted for comparison.

6.7 The role of small galaxy groups

An interesting result of the *BeppoSAX* follow-up identification program is that at least six of the HELLAS sources lie in small groups and/or in interacting couples. Most interesting, all of these have been identified as narrow-line objects, in particular four as Type 1.8-2 objects (the HELLAS sources 66, 103_1, 171 and 375, the last one being detailly analyzed in the X–rays in chapter 5), while the remaining two as ELGs (212 and 37, the latter being associated with interacting galaxies, Bergvall & Johansson 1985). Also the HELLAS source 230_2 seems to

belong to a small group of galaxies, but its optical identification is still not clear.

This is not surprising: according to Fischer et al. (1998), the optical counterparts of a large fraction of ROSAT sources (selected on the basis of a hard spectrum possibly due to soft X–ray absorption) are coincident with interacting galaxies or reside in small groups, some of the companions galaxies themselves showing indication of activity, possibly enhanced star formation by merging or tidal interactions (Hasinger et al. 1997). However, the excess of companion galaxies associated to Seyfert 2s is still a matter of debate. A plausible explanation (Dultzin-Hacyan et al. 1999; Corbin 2000), which would provide a challenge to the unification schemes, requires that Seyfert 2 galaxies are as Seyfert 1s obscured because of interactions: strong interaction with a companion of comparable size enhances overall star formation and drives molecular gas towards the center of the galaxy, which may in turn obscure the active nucleus' broad-line regions. An observational check is given by the finding of a larger number of circumnuclear star-forming regions around Seyfert 2 galaxies than Seyfert 1s, both in the optical (Gonzalez-Delgado & Perez 1993) and in the infrared (Maiolino & Rieke 1995; Maiolino et al. 1997). The triggering hypothesis has also been suggested to explain the different behavior of radio-loud quasars with respect to radio-quiet ones, the former populating, on average, richer environments than the latter (Yee & Green 1987; Lehnert et al. 1999).

6.8 The "restricted" HELLAS sample: choosing a magnitude limit

Since the spectroscopic follow-up observations did not cover uniformly the α–δ plane (but was particularly concentrated towards southern objects, see Table 6.1), a selection has been applied to the MECS fields, by choosing only those at $-60^\circ < \delta < +79^\circ$ and excluding the regions having $5^h < \alpha < 6.5^h$ and $16.9^h < \alpha < 20^h$. By applying this selection, the number of remaining MECS fields is 110 (out of 142) and the sky coverage is about 55 and 0.5 square degrees at a 5–10 keV flux of the order of 5×10^{-13} and 3.6×10^{-14} erg cm^{-2} s^{-1}, respectively. The number of identified sources is preserved (with the star being the only exception), since the excluded fields are basically the ones at high/low

declination with very poor information in general. The number of HELLAS sources in the reduced sample is 115.

In order to keep the number of spurious identifications in the reduced sample as low as 3–4 (La Franca et al. 2001), a limiting magnitude was chosen for each class of objects, such to limit the optical identification process only to objects with a surface density < 40 deg^2: R = 20.5 for broad-line AGNs (Type 1-1.5), R = 19.0 for narrow-line AGNs (Type 1.8-2), and R = 17.5 for emission-line galaxies (ELGs, i.e. LINERs and starbursts).

The surface density of quasars at R = 20.5 is 30–40 deg^{-2} (Zitelli et al. 1992) and given the assumed *BeppoSAX* error box (about 90 arcsec radius) and the number of observed fields (with an optical Type 1 AGN counterpart), the expected number of chance coincidences is 1.3–1.7. The surface density of galaxies at R $\leq$ 19 is about 500 deg^{-2} (Lilly et al. 1995). Tresse and collaborators (1996) found that about 8–17 % of the galaxies at z < 0.3 in the Canada-France Redshift Survey (CFRS) host Seyfert 1.8–2 or LINER nuclei. Similar results ($\sim$ 13 % at z < 0.5) have been obtained by Hammer et al. (1997). Therefore the expected chance coincidences of narrow-emission line objects (AGNs + LINERs) is about 1.2–2.5.

According to the applied magnitude limits, 6 out of the 70 sources spectroscopically identified as extra-galactic objects (Table 6.1) are "lost": they are 2 Type 1, 2 Type 1.8-2 and 2 ELGs, which are indicated by a $\Rightarrow$ in Table 6.1.

Fig. 6.16 shows the flux distribution for the HELLAS identified sources (red dashed region) in the "final" catalog (blue solid line) with respect to the original sample (yellow dashed region). The final identified subsample has the same distribution of the final HELLAS sample at the 37 % confidence level according to the Kolmogorov-Smirnov test.

The results presented in this chapter remain substantially unchanged when considering the "restricted" HELLAS sample, which has been used to evaluate the Type 1-to-Type 2 ratio, in order to be sure that spurious sources play a marginal role in this context.

It is interesting to note (Table 6.2) that all but one of the narrow-line AGNs do not belong to any existing catalog, as well as the majority of ELGs. This can be explained by the fact that no large catalogs of such objects do exist at the present time. As a consequence,

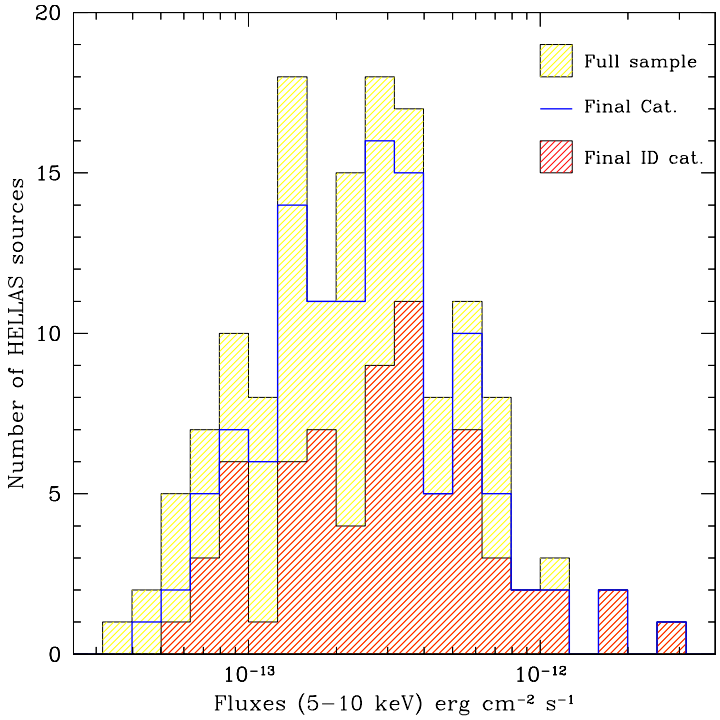

Figure 6.16: The flux distribution of the subsample of 115 sources (blue continuous line) with respect to the original HELLAS sample (yellow dashed region), and that of the 63 spectroscopically identified sources (red dashed region).

a bias is introduced in the observed fractions of the populations of the identified sources against Type 2 AGNs and narrow-emission line galaxies. Given the similar flux distributions of the subsample of 26 sources identified through cross-correlations with catalogs, that of the 38 sources identified by follow-up observations and the "final" HELLAS sample of 115 sources (according to the Kolmogorov-Smirnov test), it is possible to correct the bias in a simply way, by taking into account the different fractions for each class of objects identified by catalog or by spectroscopic follow-up programs.

The relative fraction of Type 1 objects (including both the radio-quiet and the radio-loud) is 62 %, while Type 1.8-2's is 19.0 %. If the ELGs are also taken into account, the final fraction of narrow-line

objects is 30.0 %. The Type 2-to-Type 1 ratio, ~ 0.48, is higher than in previous soft (0.24, Lehmann et al. 2000) and medium-hard X–ray selected surveys (0.20, Akiyama et al. 2000), and becomes higher ($\sim$ 0.63) if all the "blank fields" host a Type 2 object. Then it is possible to argue that hard X–ray surveys like the HELLAS are the most suitable way to pick up a large fraction of obscured objects.

It is interesting to note that this is only an estimate on the real ratio of Type 1 and Type 2 objects. In fact, the present sample is biased against high-z Type 2 AGNs (the highest redshift being 0.341), which are indeed fainter than the assumed spectroscopic limit of R = 19 for narrow-line AGNs (Seyfert 1.8-2), and R = 17.5 for emission-line galaxies. A first preliminary estimate can be drawn by taking into account only the AGNs at redshifts < 0.2; in this case, the Type 2(+ELGs)-to-Type 1 ratio is about 3 ± 1.5, which is consistent to the unified models for AGNs (Comastri et al. 1995). A more accurate analysis via model predictions from the evolution of Type 1 and Type 2 AGNs is underway (La Franca et al., in preparation).

6.9 The contribution of the HELLAS sources to the sub-mm background

Obscured AGNs are thought to contribute a large fraction of the hard X–ray background (see the introduction), and have also been proposed as the power-house of a fraction of SCUBA (i.e. sub-millimeter) sources, which make most of the 850 μm background. From the strong similarity existing between the broad-band background spectrum and that of obscured AGNs (Vignati et al. 1999) it is possible to argue that absorbed AGNs do significantly contribute to the IR background by reprocessing of primary radiation into longer wavelengths, from the far infrared to the sub-mm regions. Even though the exact shape of the infrared–sub-mm spectrum of such sources is rather uncertain in most cases, the integrated luminosity can be estimated by the X–ray one. The result is that the absorbed AGNs could account for a substantial fraction of the sub-mm radiation, ranging from 20 up to 50 % (Almaini, Lawrence & Boyle 1999) if the reprocessing material were sufficiently cold. Therefore AGNs could be the link between the two spectral windows. However, the nature of the energy powering strong IR and sub-mm galaxies is still matter of debate, especially after ISO

results (Genzel et al. 1998; Lutz et al. 1998), which suggest that star-formation provides most of the energy output at these wavelengths. On the other hand, some high-z SCUBA sources appear to host an active nucleus (Ivison et al. 2000).

In order to tackle this issue, four HELLAS sources plus several more hard X–ray sources have been observed in the sub-mm (Severgnini et al. 2000). None has a counterpart at 850 μm , except for a *Chandra* source which is likely to be associated with a highly obscured Type 2 object at high redshift.

In particular, the 2–10 keV sources with fluxes greater than 10^{-15} erg cm^{-2} s^{-1} (which make about 75 % of the hard X–ray background, Mushotzky et al. 2000) contribute for less than 7 % to the sub-mm background. Moreover, the $F_{850\mu m}/F_{5\ keV}$ ratio derived from the sub-mm sources without a hard X–ray counterpart do suggest that either strong starburst activity or a Compton-thick AGN (with an absorbing column density exceeding 10^{25} cm^{-2}) can be responsible of the sub-mm emission.

The latter hypothesis has been developed extensively through a different approach by Brusa, Comastri & Vignali (in preparation), with similar results.

Radio observations of the HELLAS sources

7.1 Introduction

The multi-wavelength analysis of the HELLAS sources has been completed by radio follow-up observations which, combined with cross-correlations with *NVSS* and *FIRST* archival data, has allowed a further investigation on the emitting properties of the hard X–ray selected HELLAS sample.

7.2 Radio follow-up observations and data reduction

20 HELLAS sources with declination lower than $-40°$ have been observed with the Australia Telescope Compact Array (*ATCA*) in June 1999 with the 6.0A configuration at 6 cm (bandwidth of 128 MHz). Each source was observed for about 25 minutes, reaching a 5 σ flux limit of about 0.5 mJy.

The sources with declination higher than $-40°$ have been observed at the *VLA* with the C configuration (April 2000), at 4.86 GHz (bandwidth of 50 MHz). In this configuration, the synthesized beam size (full width at half power, FWHP) is about 4 arcsec, which should allow to pinpoint optical identifications to a few arcsec, except for asymmetric multicomponent sources. The FWHP of the primary beam is about 9 arcmin, which should allow to study the radio counterparts of the HELLAS sources (if any) and their environment, which is needed to compute the field source density and to estimate a reliable

number of spurious coincidences. The final 5 σ flux limit is about 0.4 mJy, considerably deeper than the *NVSS* and *FIRST* surveys. The frequency of 4.85 GHz and the flux limit can be considered a good compromise between a deep survey and the necessity of avoiding strong contamination of spurious sources within the X–ray error box. Indeed, at 0.4 mJy the surface density of the 6 cm radio sources population is $\sim 70/\mathrm{deg}^2$, while at 0.1 mJy level it becomes about $365/\mathrm{deg}^2$, thus drastically increasing the number of chance associations. At 20 cm the situation is much more critical, since at 0.1 mJy the surface density increases to 1000 sources/deg^2.

7.2.1 Data reduction

ATCA data were calibrated against PKS 1934−638 (having a flux density of 6.26 Jy at 6 cm) and analyzed through the MIRIAD software package, while for *VLA* data the NRAO AIPS reduction package was used and 3C 286 was chosen as primary flux density calibrator (assuming a flux of 7.41 Jy at 4.85 GHz). The task `UVFLAG` was used to "flag" (delete) the corrupted data (*e.g.* bad integration, non operating antennas, high amplitudes due to interferences), while the tasks `VLACALIB` and `GETJY` were used to calibrate the data and to determine the source flux densities. Finally each observation was cleaned using the task `IMAGR`.

The rms noise of each pointing was estimated using the amplitude distribution of the pixel values in the cleaned map before correcting for primary-beam attenuation. The rms of the noise distribution alone is assumed to be nearly equal to the rms of that distribution obtainable by reflecting the negative flux portion of the observed amplitude distribution. A good agreement is obtained between the observed and the theoretical rms noise levels. Some fields show a slightly higher than average rms value, this being caused by the presence of nearby strong radio objects. No evident structures or irregularities were found in the rms maps.

7.2.2 Regions for the source extraction

The radio sources have been searched in a square central region of 8 $\times$ 8 arcmin. In each region the rms used for source extraction is the highest rms in the region. In this way we are confident that all the

sources extracted are above the fixed threshold in the region. Within each region, the radio sources up to a peak flux density ≥ 5 times the rms value of the region have been selected and for each source the flux, the position and the size are estimated using a least square Gaussian fit (Condon 1997).

For what concerns multiple sources, the ones separated by less than two times the value of the synthesized beam size and with a flux ratio lower than 2 have been considered as a unique source. This criterion has been adopted since the component flux density ratio of physically doubles is usually small ($\lesssim 2$), while the projection pairs can have arbitrarily large flux density ratio (Condon, Condon and Hazard, 1982).

7.3 Cross-correlation with NVSS and FIRST

In order to extend the knowledge of the radio properties of the HELLAS sources at 20 cm, the sample has been cross-correlated with the NVSS and the FIRST on-line catalogs with a searching radius of 90 arcsec.

The NRAO/VLA Sky Survey (NVSS), carried out with the National Radio Astronomy Observatory's Very Large Array at 20 cm (1.4 GHz), covers the sky north of -40° with a resolution of 45 arcsec (Condon et al. 1998). The catalog contains sources with a peak brightness in excess of 2.5 mJy/beam (5 σ), and provides further information on the detected radio sources such as sizes and linear polarization (which have not been considered in the following analysis).

The Faint Images of the Radio Sky at Twenty-cm (FIRST: Becker, White & Helfand 1995) is a project designed to produce the equivalent in the radio band of the Palomar Observatory Sky Survey. The nominal frequency of this survey is 1.4 GHz (like the NVSS), with the limiting flux being considerably lower (1 mJy at 5 σ confidence) than NVSS, as well as with a better spatial resolution (about 5 arcsec).

7.4 The HELLAS sources at radio wavelengths

As said above, all the HELLAS fields have been covered by radio follow-up observations, except for 4 fields (for which only NVSS data are available). The *BeppoSAX* error box has been assumed to be of about 90 arcsec, in order to be absolutely conservative in the cross-correlation

process, even though it must be noted that on average *BeppoSAX* positions of the HELLAS sources are better defined than 90 arcsec (cfr., for comparison, chapter 6). For the low number of high-Galactic latitude fields with neither the target nor a known source in the same field-of-view the error box has been assumed to be of 2 arcmin (since no correction to the astrometry was possible).

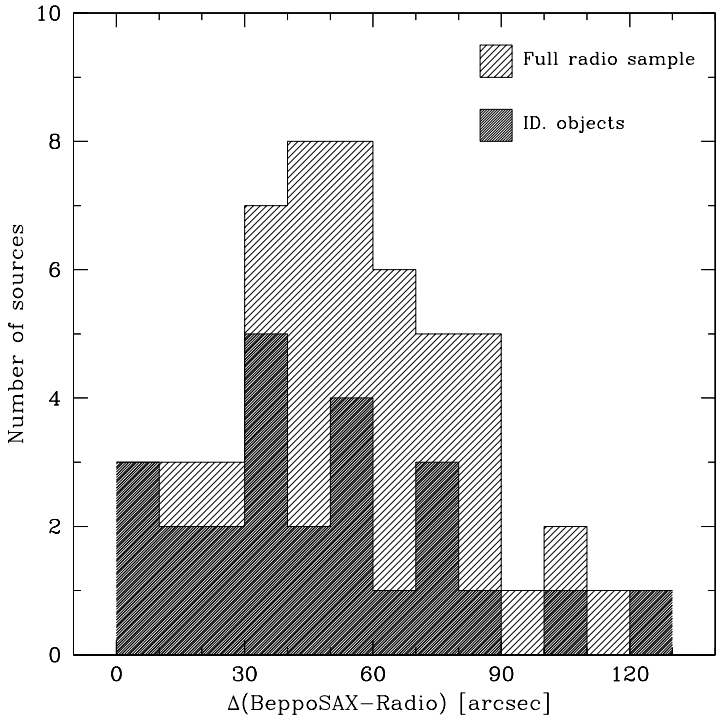

Figure 7.1: Distribution of the distances between radio and X–ray (*BeppoSAX*) position. The spectroscopically identified sources are marked differently.

Given these assumptions, 63 X–ray/radio coincidences have been found. The radio positions for 10 sources are quite different from the optical ones (assumed to be the real position of the X–ray sources). Some of these sources have a soft X–ray counterpart in *ROSAT*, whose coordinates are consistent with the optical position. Thus we are confident that these 10 sources are really spurious associations, the final number of radio/X–ray associations being therefore $53/147 \sim 36$

% of the HELLAS sample. In Fig. 7.1 the distribution of the distances between X–ray and radio position is showed. In particular, the radio source having larger distance than 2 arcmin from the X–ray centroid is associated with a a radio-galaxy in a cluster.

Considering the frequency and the flux limit of the present survey (6 cm and 0.4 mJy, respectively), the expected number of spurious sources using an error box of 90 arcsec is ~ 20, considering a surface density of $N(S) = 0.42 \times (S/30)^{-1.18}$, where N(S) is the number of objects per arcmin^2 and S the flux in μJy (Fomalont et al. 1991).

In 7 fields more than one radio source is present in the X–ray error box: in these situations, the radio source nearest to the X–ray position and/or present both at 6 cm and at 20 cm (in order to be more confident on the detection of the source) has been chosen.

5 sources have only a 20 cm flux measurement, 22 sources only at 6 cm, while for the remaining 26 objects a clear detection (above 5 σ) is present at both the wavelengths. In these cases, assuming no source variability in the time elapsing between 20 and 6 cm observations, it has been possible to compute a radio spectral slope, which is reported in Table 7.1 along with source positions, flux densities and the radio-to-optical and optical-to-X spectral indices (described below). The average radio slope is $\alpha = 0.8$ (where the flux density $S_\nu \propto \nu^{-\alpha}$).

Interestingly enough, the likely radio counterparts of HELLAS 321 and 323 (Lockman Hole) and HELLAS 353 consist of 5 components. In particular, the radio source in HELLAS 321 error box (Fig. 7.2) is an absorption-line galaxy at z = 0.469 (RDS 116 A, see Lehmann et al. 2000), but in the neighboring region there are also a Type 2 object at a (photometric) redshift of 1.94 (Pozzetti, private communication) and another emission line galaxy (Lehmann et al. 2000), which can be associated to the *BeppoSAX* source.

The 6 cm fluxes (in mJy, see Table 7.1) are plotted in Fig. 7.3 as a function of the 5–10 keV *BeppoSAX* fluxes. Among the radio brightest sources we have the 2 BL Lac objects (HELLAS 72 and 265), the radio-loud AGNs previously known by catalog and two Type 1 objects discovered in the course of the survey (HELLAS 54 and 205). The 4 cluster (out of 6 which are present in the HELLAS survey) have their radio emission associated with a radio galaxy (HELLAS 307, 392 and 400) or a small group of galaxies (HELLAS 241).

The radio-loudness of the two Type 1 objects HELLAS 54 and 205

Source ID	RA (J2000)	DEC (J2000)	$F_{20\ cm}$ (mJy)	$F_{6\ cm}$ (mJy)	$\alpha_{\rm R}$	$\Delta_{radio-X}$ (arcsec)	$\Delta_{radio-ott}$ (arcsec)	$\alpha_{\rm RO}$	$\alpha_{\rm OX}$
6	06 23 50.91	−69 20 8.1		0.59±0.10		71.5	0.8	0.15	1.62
10	14 48 25.59	−69 19 52.2		0.95±0.10		42.8	2.8	0.15	1.51
26	05 50 6.61	−61 01 23.3		0.97±0.10		76.9	2.5	−0.05	2.18
37	23 15 46.73	−59 03 15.8		15.4±0.10		83.4	2.9	−0.18	2.80
54	04 38 47.01	−47 28 0.9		132.3±1.0		66.1	0.6	0.76	1.06
57	05 20 44.78	−45 41 27.3		4.9±0.10		49.6	5.3	0.53	0.94
72	03 33 12.54	−36 19 47.5	14.7±1.0	not obs.		36.6	4.6	0.36	1.39
73	03 36 54.01	−36 16 5.1	501.3±15	not obs.		34.0	1.9	0.67	1.34
84	13 36 39.00	−33 57 57.4		239.1±0.8		60.0	6.7	0.06	2.66
90	01 34 25.61	−30 05 50.9	4.6±0.5	0.41±0.05	2.03	57.8		> 0.45	< 1.34
97	13 50 15.40	−30 20 9.6		0.69±0.11		79.3	1.3	0.04	1.66
100	13 48 19.51	−30 11 54.0	11.5±1.0	4.68±0.13	0.75	50.9	1.0	0.21	1.77
136	09 46 21.89	−14 10 45.0		0.37±0.05		62.7	12.7	0.09	1.60
149	20 44 34.95	−10 28 9.1	9.0±0.5	4.30±0.17	0.61	35.6	2.5	0.28	1.62
150	13 05 33.00	−10 33 19.1	711.7±21.4	1150±1.0	−0.4	44.9	0.1	0.52	1.68
160	13 05 36.10	−05 42 0.3	6.8±0.5	2.10±0.11	0.98	89.9		> 0.39	< 1.08
162	13 04 44.20	−05 33 40.2		0.58±0.05		13.5		> 0.28	< 1.36
169	12 40 36.89	−05 07 52.8	40.3±2.3			109.2	3.6	0.19	2.03
174	02 42 14.53	00 02 51.9		1.65±0.20		80.2	1.5	0.25	1.70
180	13 42 46.03	00 20 28.3	97.6±3.5	29.5±0.5	0.99	49.7		> 0.60	< 1.24
185	05 15 11.83	01 08 21.0		0.48±0.05		31.4		> 0.27	< 1.36

Source ID	RA (J2000)	DEC (J2000)	$F_{20\ cm}$ (mJy)	$F_{6\ cm}$ (mJy)	$\alpha_{\rm R}$	$\Delta_{radio-X}$ (arcsec)	$\Delta_{radio-ott}$ (arcsec)	$\alpha_{\rm RO}$	$\alpha_{\rm OX}$
200	16 50 42.77	04 36 18.4		1.63±0.10		70.7	1.1	−0.03	1.81
205	23 29 5.79	08 34 16.4	173.4±5.2	197.8±0.4	−0.11	55.0	1.3	0.78	1.17
228	13 53 54.43	18 20 16.6		0.43±0.05		16.4	0.7	0.06	1.49
230_2	15 28 44.59	19 44 34.9	1.26±0.16	1.16±0.05	0.07	40.4	1.0	0.41	1.17
241	14 18 32.38	25 12 1.0	38.9±1.6	12.8±0.21	0.92	56.8	4.0	0.39	
243	08 37 37.03	25 47 50.5	1.18±0.20	1.07±0.15	0.08	3.2	1.2	0.10	1.71
246	08 38 59.27	26 08 13.1	7.4±0.5	1.89±0.15	1.13	8.5	0.8	0.03	1.65
250	23 55 53.90	28 35 54.0	697.2±24.6	286.7±0.5	0.74	13.9	5.6	0.64	1.45
256	22 41 27.56	39 43 33.9		0.84±0.11		88.9		> 0.31	< 1.21
265	12 17 52.08	30 07 0.3	572.7±21.4	384.8±3.1	0.33	24.3	0.8	0.39	2.04
278	10 34 56.41	39 39 40.8	1.6±0.2			60.4	0.8	0.03	1.87
279	16 54 43.03	40 02 46.2	81.5±3.0	36.3±0.35	0.67	42.2	2.4	0.23	1.89
288	12 19 21.27	47 12 13.4	9.1±0.2			66.7		> 0.43	< 1.35
290	12 19 52.40	47 20 58.7	3.4±0.6	1.21±0.05	0.86	70.1	2.3	0.26	1.55
292	12 17 51.07	47 30 13.6		0.41±0.07		63.9	5.7	0.21	1.29
307	12 26 46.75	55 29 7.0	8.3±0.6	2.34±0.12	1.05	122.5	0.7	0.06	
319	10 54 21.14	57 25 44.6	1.4±0.2	0.50±0.05	0.86	37.7	0.5	0.15	1.48
321	10 52 37.39	57 31 4.1	65.9±2.4	16.09±0.15	1.17	69.0	0.1	0.61	1.32
323	10 54 26.24	57 36 48.2	192.9±6.8	37.30±0.15	1.36	44.1	1.5	0.44	1.65
328	16 34 12.53	59 49 13.7		0.87±0.15		60.0	1.3	0.14	1.88
340_2	17 50 38.81	60 56 42.5	4.7±0.5	2.11±0.11	0.67	108.9		> 0.39	< 1.27

Source ID	RA (J2000)	DEC (J2000)	$F_{20\ cm}$ (mJy)	$F_{6\ cm}$ (mJy)	$\alpha_{\rm R}$	$\Delta_{radio-X}$ (arcsec)	$\Delta_{radio-ott}$ (arcsec)	$\alpha_{\rm RO}$	$\alpha_{\rm OX}$
346_1	17 53 47.71	60 58 58.8		0.47±0.10		53.9		> 0.27	< 1.38
353	18 03 47.38	61 09 22.2	133.2±5.0	39.0±0.5	1.02	67.2		> 0.62	< 1.48
354	18 18 51.06	61 14 18.4		2.54±0.06		59.9		> 0.40	< 1.27
364	14 38 26.71	64 28 59.8		0.65±0.05		88.5	0.2	0.08	1.68
375	15 19 33.69	65 35 0.8		1.08±0.20		42.1	2.8	0.01	1.70
375_1	17 40 22.32	67 41 38.1	4.2±0.5	5.57±0.06	−0.23	99.3		> 0.47	< 1.19
375_2	17 42 50.51	67 59 33.5	7.4±0.5	2.71±0.09	0.84	110.5		> 0.41	< 1.22
387	11 01 48.92	72 25 38.0	1245.6±37.4	864.1±1.3	0.30	34.8	1.4	0.66	1.51
392	07 41 44.70	74 14 39.8	22.7±1.6	1.50±0.15	2.26	25.2	2.0	0.06	
400	12 22 6.50	75 26 14.9		1.60±0.05		2.15	0.1	0.14	
413	21 21 36.16	89 02 16.4	61.0±1.9	19.5±0.17	0.96	29.5			

Table 7.1: Properties of the radio counterparts of the HELLAS sources. The spectroscopically identified objects in the table are in boldface. For the remaining unidentified sources, the R magnitude (from USNO catalog) of the nearest optical object (if any) has been assumed in the computation of the indices.
For the cluster, the $\alpha_{\rm OX}$ has not been computed since the X–ray emission is likely to have also a diffuse thermal component.

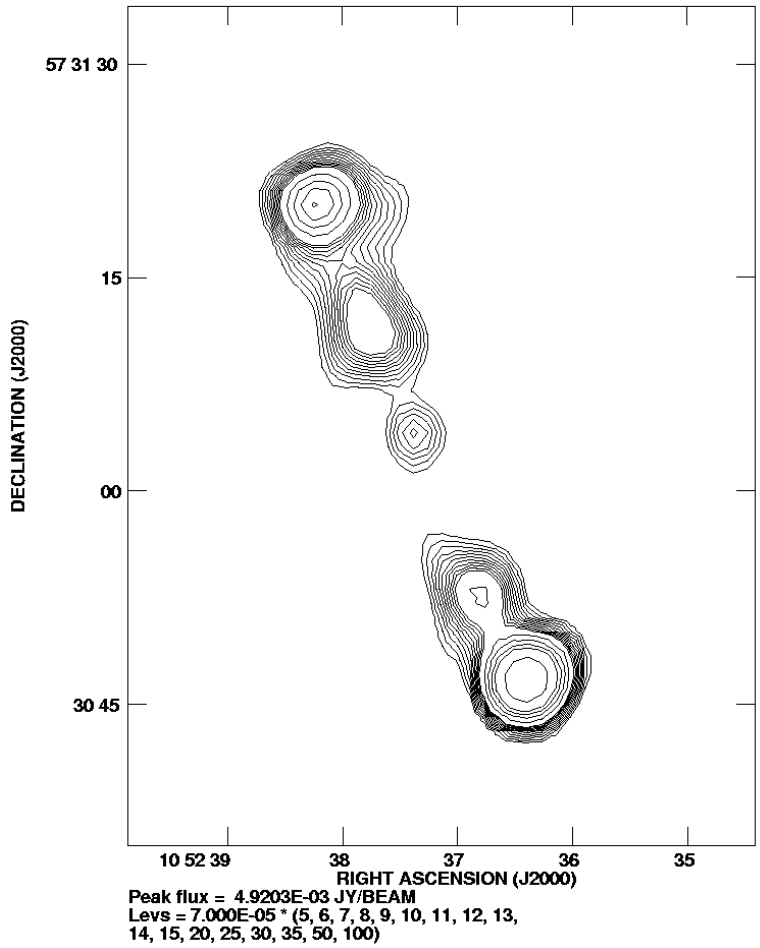

Figure 7.2: The radio contours for the HELLAS source 321 obtained at the *VLA* (6 cm).

is confirmed by computing and plotting (Fig. 7.4) the broad-band two frequencies spectral indices defined as:

$$\alpha_{\rm RO} = \mathsf{Log}\ (\mathsf{F}_{5\ GHz}/\mathsf{F}_{2200\ \mathring{A}})/5.38$$
$$\alpha_{\rm OX} = \mathsf{Log}\ (\mathsf{F}_{2200\ \mathring{A}}/\mathsf{F}_{2\ keV})/2.605$$

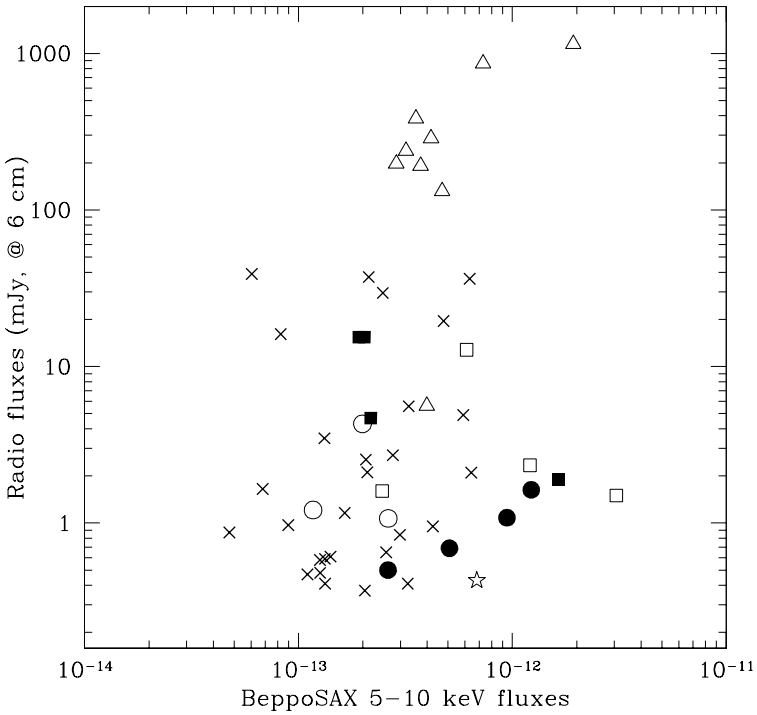

Figure 7.3: Radio fluxes (at 6 cm) against 5–10 keV flux. Symbols are as in previous chapters. Crosses indicate the unidentified HELLAS sources.

The radio flux at 6 cm is obtained by the present observations or by extrapolating the 20 cm flux density with a power-law slope with $\alpha = 0.8$ (the average of the distribution). The optical 2200 $\mathring{A}$ flux is derived by the R magnitude (when possible, obtained by photometric follow-up observations, otherwise from the USNO catalog, see chapter 6) with an optical slope of $\alpha = 0.5$. For the unidentified HELLAS sources, the optical object nearest to the radio position has been chosen in computing the indices (14 cases). The upper limits in the $\alpha_{\rm RO} - \alpha_{\rm OX}$ plane are calculated assuming R = 20, i.e. the optical magnitude limit of the plates (13 sources). The 2 keV monochromatic flux is derived from the measured *BeppoSAX* 5–10 keV flux and assuming an X–ray slope $\alpha = 0.6$ ($\alpha = \Gamma - 1$).

Two Type 1 objects (HELLAS 149 and 290) are in the intermediate region between radio-quiet and radio-loud objects, which is indicated

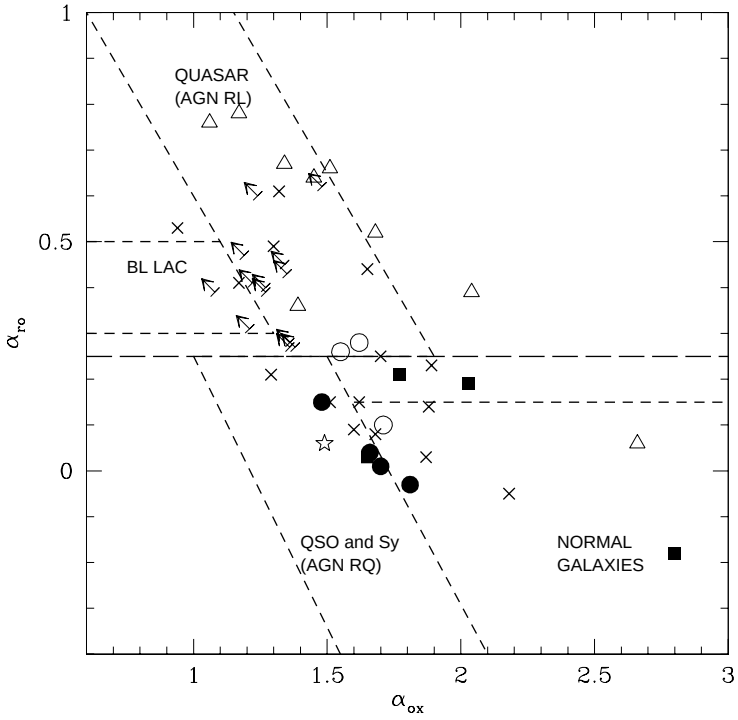

Figure 7.4: $\alpha_{\rm RO}$ vs. $\alpha_{\rm OX}$ index for the majority of the HELLAS sources whose radio properties are listed in Table 7.1. The short-dashed lines indicate the areas typically occupied by different classes of extra-galactic objects. This diagram can be used as a preliminary classifier for X–ray sources prior to optical spectroscopy. The horizontal long-dashed line is an indicative dividing line between the radio-quiet and the radio-loud population (Giommi et al. 1999).

in Fig. 7.4 by the long-dashed horizontal line ($\alpha_{\rm RO} \simeq 0.25$, Giommi, Menna & Padovani 1999). The short-dashed lines show the typical areas occupied by different classes of extra-galactic objects and can be used as a preliminary classifier for X–ray sources. It is interesting to note the position of the bright, optically dull radio-galaxy IC 4296, which lies in the extreme $\alpha_{\rm OX}$ region. Most of the unidentified objects are located in the radio-loud region, in particular that populated by the radio-loud quasars (see Fig. 7.2).

Survey	F_X limit (erg/cm^2 s)	$F_{1\ keV}$ (μJy)	F_R limit (mJy)	$F_R/F_{1\ keV}$ ($\times 10^3$)	% Radio/X associations	References
Marano + 20 cm ATCA	4×10^{-15}	0.00110	0.20	181	(4/50) $\sim$ 8 %	Zamorani et al. (1999)
LOCKMAN + 6 cm VLA	1×10^{-15}	0.00030	0.05	167	(9/75) $\sim$ 12 %	Ciliegi et al. (2000)
CRSS + 20 cm VLA	2×10^{-14}	0.00596	0.70	117	(7/80) $\sim$ 9 %	Ciliegi et al. (1995)
LOCKMAN + 20 cm VLA	5×10^{-15}	0.00149	0.12	81	(16/135) $\sim$ 12 %	de Ruiter et al. (1997)
EMSS + 6 cm VLA	8×10^{-14}	0.01340	0.80	60	(167/625) $\sim$ 27 %	Stocke et al. (1991)
LSS ASCA + FIRST	1×10^{-13}	0.02200	1.00	45	(12/34) $\sim$ 35 %	Akiyama et al. (2000)
HELLAS + 6 cm + 20 cm	5×10^{-14}	0.02450	0.50	20	(53/147) $\sim$ 36 %	Ciliegi et al. (in prep.)

Table 7.2: Summary of the results concerning radio/X–ray associations from previous X–ray surveys and the present one.

7.5 Comparison with other X–ray samples

Previous radio follow-up of X–ray selected samples have shown different percentages of radio/X–ray associations. Using 20 cm observations of *ROSAT* X–ray selected samples, Ciliegi et al. (1995), de Ruiter et al. (1997) and Zamorani et al. (1999) found only $\sim$ 10 % of radio/X–ray coincidences, while Stocke et al. (1991) found a significantly higher fraction (about 27 %) for the X–ray sources in the Extended Medium Sensitivity Survey (EMSS). The value obtained for the HELLAS sources, about 36 % (i.e. 53/147), is comparable to that obtained by Akiyama et al. (2000) in the course of the *ASCA* Large Sky Survey ($\sim$ 35 %), which is medium-hard X–ray selected. The percentage of radio/X associations is a function of the flux limits ratio: the lower this ratio is (i.e. deeper radio data in comparison to the X–ray flux limit) the higher is the fraction of X–ray objects with a likely radio counterpart. It seems also plausible to suggest a dependence on the X–ray energy band: the hardest the band is, the highest the probability of an association to a radio source is, i.e. at hard X–ray energies it is likely to pick up a higher fraction of AGNs. It must be kept in mind, however, that the high percentage is to be intended as an upper limit, due to the number of possible spurious coincidences (as described in the previous section).

In Table 7.2 some X–ray surveys with radio follow-up observations are shown, along with the radio-to-X–ray limit ratio. The ratio of $\sim 20 \times 10^3$ is about an order of magnitude larger that the typical radio-to-X–ray ratio of the radio-quiet AGNs (Elvis et al. 1994), but within the scatter of the radio-quiet population. Thus, when the radio-to-X–ray flux limits ratio becomes lower than 20×10^3 it is possible to

start seeing also some radio-quiet AGNs in addition to the radio-loud population, as shown in Fig. 7.4.

Most important, the HELLAS sample is the first (very) hard X–ray selected sample so far to be completely observed at radio wavelengths. In fact, previous studies about the X–ray/radio coincidence were based almost exclusively on samples of soft X–ray selected objects (e.g. Boyle et al. 1993; Hamilton & Helfand 1993), the sole exception being the *ASCA* LSS (Akiyama et al. 2000).

If the nature of hard X–ray selected sources is really different (Type 2 quasars, red AGNs, etc.) from that of soft X–ray selected AGNs, radio observation may help in understanding the true nature of these objects. Further radio investigation, possibly in polarization, are required to assess the nature of X–ray obscured objects and the fraction of scattered emission, which has been tentatively suggested (chapter 4) to explain the soft X–ray properties of the HELLAS sources.

Conclusions

The HELLAS sources provide the first hard X–ray selected sample obtained with an imaging instrument in the 5–10 keV energy range, as previous $ASCA$ surveys were carried out primarily in the softer 0.7–7 and 2–10 keV bands (Ueda et al. 1999a,b; Della Ceca et al. 1999). At the flux limit of about 5 $\times$ 10^{-14} erg cm^{-2} s^{-1}, the integrated flux of the HELLAS sources account for about 30 % of the XRB. The sky coverage sampled by $BeppoSAX$ is high enough to allow to find sizeable samples of rare objects (red quasars, X–ray active but optically dull galaxies, narrow-line quasars), whose optical counterparts can be spectroscopically identified in order to investigate their broad-band properties and to reliably test AGNs synthesis models.

A significant fraction of AGNs are though to be obscured and escaped from traditional selection criteria. Such population of obscured objects will appear significantly either in the hard X–rays (which are able to pass through obscuring) or in the radio band. Since radio-selected AGNs are dominated by radio-loud active nuclei, which are only about one-tenth of the radio-quiet population (Osterbrock 1991), hard X–ray selection is the best way to pick up AGNs without bias against absorbed AGNs, and to unveil the "accretion history" of the Universe. Indeed, the $BeppoSAX$ hardness ratio analysis do reveal the presence of X–ray absorption in a sizeable number of objects, despite of their optical classification.

The most important results discussed in this thesis are summarized in the following.

The HELLAS 5–10 keV integral LogN-LogS slope, q $= -1.56 \pm 0.14$ (where N($>$S) $\propto$ S^{-q}), is consistent with being Euclidean. The extrapolation of the HELLAS counts towards fainter 5–10 keV fluxes agrees with the recent XMM-$Newton$ results in the Lockman Hole (Hasinger et al. 2001). A good match is also obtained with $ASCA$ (Ueda et al. 1999a; Della Ceca et al.

1999) and recent *Chandra* (Mushotzky et al. 2000) source counts in the 2–10 keV energy range assuming a $\Gamma = 1.6$ spectral slope. This means that over three decades in X–ray fluxes the LogN-LogS is consistent with an Euclidean slope.

Another striking result, strictly related to the choice of the detection band, is the finding of a high number of hard X–ray sources. Both the softness ratio diagram (chapter 3) and the comparison of soft to hard X–ray fluxes (chapter 4) clearly indicate that a sizeable number of *BeppoSAX* sources require a flat slope and/or absorption column densities in excess to the Galactic one, often larger than 10^{22}–10^{23} cm^{-2}. This allows to test in a quantitative way the AGNs synthesis models for the XRB, which indeed require a mixing of absorbed and unabsorbed objects to reproduce both the shape of the XRB and the source counts (e.g. Comastri et al. 1995).

Interesting enough, a fraction of sources which in the hard X–rays suggest the presence of substantial X–ray absorption (despite of their optical identification), are characterized by hard colors also in soft X–rays. This means that even with lower efficiency it is possible to pick up absorbed objects also in the soft X–rays. Evidences of absorbed objects have also been drawn, even though in a lower number of cases, from the *ROSAT* Deep Survey in the Lockman Hole (Hasinger et al. 1998; Lehmann et al. 2000), where some "extreme" sources in the hardness ratios diagram appear as the "tip of the iceberg" of that hard X–ray population which is better sampled by *BeppoSAX* .

Both *BeppoSAX* and *ROSAT* analysis of the HELLAS sources reveal that the average spectral properties are not well accounted for by a simple absorbed power-law model. More complex spectra are required in a high number of cases, and this is particularly true for very absorbed objects. Reprocessing by means of scattering radiation and/or starburst components are required, in most cases involving about 10–50 % of the primary radiation. Similar evidences have been obtained also from *ASCA* (Della Ceca et al. 1999) and *Chandra* (Giacconi et al. 2001) surveys.

The presence of a soft component not directly related to the nuclear emission might easily lead to a wrong estimate of the intrinsic soft X–ray luminosity, especially for heavily absorbed sources. According to the XRB synthesis models, absorbed AGNs become progressively more important towards faint fluxes and thus spurious evolutionary terms can be introduced in the luminosity function derived from soft X–ray selected samples. An estimate of the importance of this bias is not straightforward and also

strongly model-dependent (see Miyaji, Hasinger & Schmidt 2000 for a detailed discussion). The nature of this additional component will be probed by *Chandra* and *XMM-Newton* observations.

The Type 1/Type 2(+ELGs) ratio (calculated on the "restricted" HELLAS sample, i.e. applying a magnitude limit to each class of objects) is about 0.48, higher than in previous soft (0.24, Lehmann et al. 2000) and medium-hard X–ray selected surveys (0.20, Akiyama et al. 2000), and becomes higher if all the "blank fields" host a Type 2 object.

The optical follow-up spectroscopy identification program has revealed that while at redshift lower than 0.3–0.4 the HELLAS sources are associated to absorbed Type 2 AGNs and narrow-line emission line galaxies, along with unabsorbed Type 1 AGNs (Seyfert galaxies and quasars), at higher redshifts the presence of X–ray absorption in a sizeable fraction of Type 1 AGNs represents a new, intriguing issue to be demanded to further *Chandra* and *XMM-Newton* observations, and clearly indicates that AGNs properties cannot be exhaustively interpreted without a multi-wavelength approach, which can be the only plausible way to explain the decoupling between their optical and X–ray properties. In fact, since the dust is responsible for optical attenuation, while gas for soft X–ray absorption, the presence of broad-line objects with large amount of absorption in the X–rays suggests dust-to-gas ratio far lower than the Galactic one or the existence of dust grains with different properties than previously known or thought (Maiolino et al. 2001). An alternative but viable explanation for this behavior consists in assuming the presence of a "warm absorber", a plasma photo-ionized by the AGN radiation, which has been extensively observed and studied in nearby Seyfert galaxies (Reynolds 1997). The typical ionization state of these warm absorbers in Seyfert galaxies is such that oxygen is highly ionized. Since transitions in the optical band disappear when plasma is highly ionized, the optical absorption would not take place. However, it must be assumed that the radiation field of this kind of objects is high enough that dust sublimates at high rates and its contribution to optical extinction is very low. Optical spectropolarimetry observations should allow to probe the presence and quantify the importance of dust scattering in these sources.

Strong X–ray absorption ($N_{\rm H} > 10^{23}$ cm^{-2}) in high-redshift broad-line AGNs has also been reported in 4 objects detected in the course of the *ASCA* Large Sky Survey (Akiyama et al. 2000), and recent results from *Chandra* observations seem to confirm this result at much lower X–

ray fluxes (Fiore et al. 2000b; Gilli, private communication). The present results involve both the not dominant population of radio-loud objects, which past and recent observations revealed to be absorbed in the X–rays in a large number of cases (Elvis et al. 1994b; Cappi et al. 1997; Fiore et al. 1998; Yuan et al. 2000), and the population of radio-quiet quasars. It must be also noted that the broad-absorption line quasars spectral properties suggest the presence of large amount of absorption in the X–rays (Gallagher et al. 1999; Brandt et al. 2000b).

According to AGNs synthesis models (i.e. Comastri et al. 1995), the sources responsible for the XRB must be characterized by a spectral energy density spanning a wide range of luminosities and absorption column densities, in order to reproduce both the XRB spectrum and the source counts in different energy ranges. In particular, the energetically dominant contribution comes from sources around the knee of the X–ray luminosity function ($L_{\rm X} \sim$ a few 10^{44} erg s^{-1} at z=1) and with absorbing column densities of the order of 10^{23} cm^{-2} (Comastri 2000). These objects, the so-called "QSO 2", i.e. quasars with optical narrow-emission lines, have been extensively searched, but, at present, only a handful of candidates have been found, the most interesting of which being the z = 0.9 quasar AX J08494+4454, lacking both optical (Ohta et al. 1996) and near-infrared broad lines (Nakanishi et al. 2000). The results obtained by HELLAS suggest that if the the classical statement of obscured Type 2 $\equiv$ narrow optical lines is removed, the moderate/high-redshift absorbed Type 1 objects could have the same role of the so far elusive class of Type 2 AGNs in contributing to the XRB.

Remarkable results have also been obtained by the photometric follow-up observations of a subsample of HELLAS sources. Interesting enough, the optical and the near-infrared properties of a fraction of intermediate (1.8–1.9) and Type 2 objects (Maiolino et al. 2000), as well as red quasars (Vignali et al. 2000a), are dominated by the stellar component of the galaxies hosting the (obscured) X–ray active nucleus. This result has straightforward consequences, since it implies that a fraction of sources responsible for the hard XRB may be hosted by normal, passively-evolving galaxies and could have been missed by previous optical surveys based on color-selection criteria.

Finally, HELLAS represents a complementary probe of the hard X–ray Universe with respect to the more recent, pencil-beam *Chandra* and *XMM-Newton* surveys. Indeed, even though these surveys provide a factor

50 increase in sensitivity in the 2–10 keV energy range (reaching a flux limit $F_{2-10\ keV} \sim 3 \times 10^{-15}$ erg cm^{-2} s^{-1}, where 70–90 % of the hard XRB is resolved into discrete sources), they are effectively limited by the small portion of sky surveyed: 0.1–0.2 deg^2 for Chandra (Mushotzky et al. 2000; Giacconi et al. 2001) and 0.2 deg^2 for XMM-Newton (Hasinger et al. 2001).

The hard X–ray sky view drawn from $BeppoSAX$, i.e. the extremely varied properties of the sources contributing to the hard XRB, is being confirmed and extended to lower fluxes by $Chandra$ and $XMM\text{-}Newton$ findings, suggesting that AGNs synthesis models might be tenable if the zoo of hard X–ray sources is populated also by absorbed broad-line AGNs and by obscured objects hosted by passively evolving galaxies and without any evidence of activity in the optical band.

Bibliography

[1] AKIYAMA M., OHTA K., YAMADA T., ET AL., 1998, *Ap.J.* **500**, 173.

[2] AKIYAMA M., OHTA K., YAMADA T., ET AL., 2000, *Ap.J.* **532**, 700.

[3] ALMAINI O., SHANKS T., BOYLE B. J., GRIFFITHS R. E., ROCHE N., STEWART G. C., GEORGANTOPOULOS I., 1996, *M.N.R.A.S.* **282**, 295.

[4] ALMAINI O., LAWRENCE A., BOYLE B. J., 1999, *M.N.R.A.S.* **305**, 59.

[5] ANDERS E., GREVESSE N., 1989, GEOCHIMICA ET COSMOCHIMICA ACTA **53**, 197.

[6] ARNAUD K. A., 1996, IN "ASTRONOMICAL DATA ANALYSIS SOFTWARE AND SYSTEMS V", JACOBY G. & BARNES J. EDS., *ASP Conf. Ser.* **101**, 17.

[7] AVNI Y., 1976, *Ap.J.* **210**, 642.

[8] AWAKI H., UENO S. TANIGUCHI Y., WEAVER K. A., 2000, *Ap.J.* **542**, 175.

[9] BALL R., BURNS J., LOKEN C., 1993, *A.J.* **105**, 53.

[10] BALUCINSKA-CHURCH M., MCCAMMON D., 1992, *Ap.J.* **400**, 699.

[11] BANSE K., CRANE P., GROSBOL P., MIDDLEBURG F., OUNNAS C., PONZ D., WALDTHAUSEN H., 1983, *ESO Messenger* **31**, 26.

[12] BARGER A. J., COWIE L. L., MUSHOTZKY R. F., RICHARDS E. A., 2001, *A.J.* **121**, 662.

[13] BAUM S. A., 1992, *P.A.S.P.* **104**, 848.

[14] BECKER R. H., WHITE R. L., HELFAND D. J., 1995, *Ap.J.* **450**, 559.

[15] BENN C. S., VIGOTTI M., CARBALLO R., GONZALEZ-SERRANO J. I., SANCHEZ S. F., 1998, *M.N.R.A.S.* **295**, 451.

[16] BERGVALL N., JOHANSSON L., 1985, *A.&A.* **149**, 481.

[17] BOELLA G., BUTLER R. C., PEROLA G. C., ET AL., 1997A, *A.&A.S.* **122**, 299.

[18] BOELLA G., CHIAPPETTI L., CONTI G., ET AL., 1997B, *A.&A.S.* **122**, 327.

[19] BOHLIN R. C., SAVAGE B. D., DRAKE J. F., 1978, *Ap.J.* **224**, 291.

[20] BOYLE B. J., STAVELEY-SMITH L., STEWART G. C., GEORGANTOPOULOS I., SHANKS T., GRIFFITHS R. E., 1993, *M.N.R.A.S.* **265**, 501.

[21] BOYLE B. J., SHANKS T., GEORGANTOPOULOS I., STEWART G. C., GRIFFITHS R. E., 1994, *M.N.R.A.S.* **271**, 639.

[22] BRANDT W. N., FABIAN A. C., TAKAHASHI K., FUJIMOTO R., YAMASHITA A., INOUE H., OGASAKA Y., 1997A, *M.N.R.A.S.* **290**, 617.

[23] BRANDT W. N., MATHUR S., REYNOLDS C. S., ELVIS M., 1997B, *M.N.R.A.S.* **292**, 407.

[24] BRANDT W. N., HORNSCHEMEIER A. E., SCHNEIDER D. P., ET AL., 2000A, *A.J.* **119**, 2349.

[25] BRANDT W. N., LAOR A., WILLS B. J., 2000B, *Ap.J.* **528**, 637.

[26] BRUSA M., COMASTRI A., VIGNALI C., IN PREPARATION.

[27] BRUZUAL A. G., CHARLOT S., 1993, *Ap.J.* **405**, 538.

[28] BUTCHER J. A., STEWART G. C., WARWICK R. S., ET AL., 1997, *M.N.R.A.S.* **291**, 437.

[29] CAGNONI I, DELLA CECA R., MACCACARO T., 1998, *Ap.J.* **493**, 5.

[30] CAPPI M., MATSUOKA M., COMASTRI A., BRINKMANN W., ELVIS M., PALUMBO G. G. C., VIGNALI C, 1997, *Ap.J.* **478**, 492.

[31] CHEN L.-W., FABIAN A. C., GENDREAU K. C., 1997, *M.N.R.A.S.* **285**, 449.

[32] CHIAPPETTI L., CUSUMANO G., DEL SORDO S., MACCARONE M. C., MINEO T., MOLENDI S., 1998, IN "THE ACTIVE X–RAY SKY: RESULTS FROM BEPPOSAX AND RXTE", SCARSI L., BRADT H., GIOMMI P. & FIORE F. EDS., *Nuclear Physics B* (PROC. SUPPL.) **69/1-3**, 610.

[33] CILIEGI P., ELVIS M., WILKES B. J., BOYLE B. J., MCMAHON R. G., MACCACARO T., 1995, *M.N.R.A.S.* **277**, 1463.

[34] CILIEGI P., ZAMORANI G., GRUPPIONI, C., HASINGER G., LEHMANN I., WILSON G., 2000, IN "LARGE SCALE STRUCTURE IN THE X–RAY UNIVERSE", PLIONIS M. & GEORGANTOPOULOS I. EDS., P. 347.

[35] CILIEGI P., VIGNALI C., COMASTRI A., FIORE F., MATT G., LA FRANCA F., *M.N.R.A.S*, IN PREPARATION.

[36] CITTERIO O., CONTI G., MATTAINI E., SANTAMBROGIO E., SACCO B., 1986, IN "X–RAY INSTRUMENTATION IN ASTRONOMY", *Proc. SPIE* **597**, 102.

[37] COMASTRI A., SETTI G., ZAMORANI G., HASINGER G., 1995, *A.&A.* **296**, 1.

[38] COMASTRI A., 2000, IN "X–RAY ASTRONOMY '999: STELLAR ENDPOINTS, AGN AND THE DIFFUSE X–RAY BACKGROUND", MALAGUTI G., PALUMBO G. & WHITE N. EDS. (ASTRO-PH/0003437).

[39] COMASTRI A., FIORE F., VIGNALI C., LA FRANCA F., MATT G., 2000, IN "LARGE SCALE STRUCTURE IN THE X–RAY UNIVERSE", PLIONIS M. & GEORGANTOPOULOS I. EDS., P. 227.

[40] COMASTRI A., FIORE F., VIGNALI C., MATT G., PEROLA G. C., LA FRANCA F., 2001, *M.N.R.A.S.*, SUBMITTED.

[41] CONDON J. J., 1997, *P.A.S.P.* **109**, 166.

[42] CONDON J. J., CONDON M. A., HAZARD C., 1982, *A.J.* **87**, 739.

[43] CONDON J. J., COTTON W. D., GREISEN E. W., YIN Q. F., PERLEY R. A., TAYLOR G. B., BRODERICK J. J., 1998, *A.J.* **115**, 1693.

[44] CONTI G., MATTAINI E., SANTAMBROGIO E., ET AL., 1994, IN "ADVANCES IN MULTILAYER AND GRAZING INCIDENCE X–RAY/EUV/FUV OPTICS", HOOVER R. B. & WALKER A. B. EDS., *Proc. SPIE* **2279**, 101.

[45] CONTI G., CHIAPPETTI L., MOLENDI S., ET AL., 1997, IN "GRAZING INCIDENCE AND MULTILAYER X–RAY OPTICAL SYSTEMS", HOOVER R. B. & WALKER A. B. EDS., *Proc. SPIE* **3113**, 394.

[46] CORBIN M. R., 2000, *Ap.J.* **536**, L73.

[47] CRAWFORD C. S., LEHMANN I., FABIAN A. C., BREMER M. N., HASINGER G., 1999, *M.N.R.A.S.* **308**, 1159.

[48] CRAWFORD C. S., FABIAN A. C., GANDHI P., WILMAN R. J., JOHNSTONE R. M., 2001, *M.N.R.A.S*, SUBMITTED (ASTRO-PH/0005242).

[49] CRUDDACE R. G., HASINGER G., SCHMITT J. H., 1988, IN "ASTRONOMY FROM LARGE DATABASES: SCIENTIFIC OBJECTIVES AND METHODOLOGICAL APPROACHES", P. 177.

[50] CUSUMANO G., MINEO T., 1998, *Technical Report* (AVAILABLE AT HTTP://WWW.SDC.ASI.IT/PUB/SAX/DOC/REPORTS/VIGNETTING_REP.PS.GZ).

[51] DELLA CECA R., CASTELLI G., BRAITO V., CAGNONI I., MACCACARO T., 1999, *Ap.J.* **524**, 674.

[52] DELLA CECA R., MACCACARO T., ROSATI P., BRAITO V., 2000A, *A.&A.* **355**, 121.

[53] DELLA CECA R., BRAITO V., CAGNONI I., MACCACARO T., 2000B, IN "AGN NEL 2000", *Mem. Soc. Astr. It.* , IN PRESS.

[54] DE RUITER H. R., ZAMORANI G., PARMA P., ET AL., 1997, *A.&A.* **319**, 7.

[55] DICKEY J. M., LOCKMAN F. J., 1990, *A.R.A.&A.* **28**, 215.

[56] DONAHUE M., STOCKE J. T., GIOIA I. M., 1992, *Ap.J.* **385**, 49.

[57] DONAHUE M., STOCKE J. T., 1995, *Ap.J.* **554**, 566.

[58] DOS SANTOS J. M. F., CONDE C. A. N., BENTO A. C. S., 1993, *NIM* **A324**, 611.

[59] DULTZIN-HACYAN D., KRONGOLD Y., FUENTES-GURIDI I., MARZIANI P., 1999, *Ap.J.* **513**, L111.

[60] EDDINGTON A. S., 1940, *M.N.R.A.S.* **100**, 354.

[61] ELVIS M., WILKES B. J., MCDOWELL J. C., ET AL., 1994A, *Ap.J.S.S.* **95**, 1.

[62] ELVIS M., FIORE F., WILKES B. J., MCDOWELL J. C., BECHTOLD J., 1994B, *Ap.J.* **422**, 60.

[63] FABBIANO G., 1989, *A.R.A.&A.* **27**, 87.

[64] FABIAN A. C., BARCONS X., 1992, *A.R.A.&A.* **30**, 429.

[65] FABIAN A. C., BARCONS X., ALMAINI O., IWASAWA K., 1998, *M.N.R.A.S.* **297**, L11.

[66] FABIAN A. C., 1999, *M.N.R.A.S.* **308**, L39.

[67] FABIAN A. C., IWASAWA K., 1999, *M.N.R.A.S.* **303**, L34.

[68] FIORE F., GUAINAZZI M., GRANDI P., 1997, "HANDBOOK FOR *BeppoSAX* NFI SPECTRAL ANALYSIS" (FTP://WWW.SDC.ASI.IT/PUB/SAX/DOC/SOFTWARE_DOCS/SAXABC_V1.2.PS.GZ).

[69] FIORE F., ELVIS M., GIOMMI P., PADOVANI P., 1998, *Ap.J.* **492**, 79.

[70] FIORE F., LA FRANCA F., GIOMMI P., ELVIS M., MATT G., COMASTRI A., MOLENDI S., GIOIA I. M., 1999, *M.N.R.A.S.* **306**, L55.

[71] FIORE F., ANTONELLI L. A., CILIEGI P., COMASTRI A., GIOMMI P., LA FRANCA F., MAIOLINO R., MATT G., MOLENDI S., PEROLA G. C., VIGNALI C., 2000A, IN "X–RAY ASTRONOMY '999: STELLAR ENDPOINTS, AGN, AND THE DIFFUSE BACKGROUND", MALAGUTI G., PALUMBO G. & WHITE N. EDS. (ASTRO-PH/0007118).

[72] FIORE F., LA FRANCA F., VIGNALI C., COMASTRI A., MATT G., PEROLA G. C., CAPPI M., ELVIS M., NICASTRO F., 2000B, *New Astronomy* **5**, 143.

[73] FIORE F., GIOMMI P., VIGNALI C., COMASTRI A., MATT G., PEROLA G. C., LA FRANCA F., MOLENDI S., TAMBURELLI F., ANTONELLI A., 2001, *M.N.R.A.S.*, SUBMITTED.

[74] FISCHER J.-U., HASINGER G., SCHWOPE A. D., BRUNNER H., BOLLER TH., TRÜMPER J., VOGES W., NEIZVESTNY S., 1998, *Astron. Nachr.* **347**, 368.

[75] FOMALONT E. B., WINDHORST R. A., KRISTIAN J. A., KELLERMAN K. I., 1991, *A.J.* **102**, 1258.

[76] FRANCIS P. J., HEWETT P. C., FOLTZ C. B., CHAFFEE F. H., WEYMANN R. J., MORRIS S. L., 1991, *Ap.J.* **373**, 465.

[77] FRANCIS P. J., WHITING M. T., WEBSTER R. L., 2000, *P.A.S.A.* **17**, 56.

[78] FRONTERA F., COSTA E., PIRO L., ET AL., 1997, *A.&A.S.* **122**, 357.

[79] FUKUGITA M., SHIMASAKU K., ICHIKAWA T., 1995, *P.A.S.P.* **107**, 945.

[80] GALLAGHER S. C., BRANDT W. N., SAMBRUNA R. M., MATHUR S., YAMASAKI N., 1999, *Ap.J.* **519**, 549.

[81] GALLAGHER S. C., BRANDT W. N., LAOR A., ELVIS M., MATHUR S., WILLS B. J., IYOMOTO N., 2001, *Ap.J.* **546**, 795.

[82] GENDREAU K. C., 1995, PHD THESIS, MASSACHUSSETS INSTITUTE OF TECHNOLOGY.

[83] GENDREAU K. C., BARCONS X., FABIAN A. C., 1998, *M.N.R.A.S.* **297**, 41.

[84] GENZEL R., LUTZ D., STURM E., ET AL., 1998, *Ap.J.* **498**, 579.

[85] GEORGANTOPOULOS I, NANDRA K., PTAK A., 2001, IN "X–RAY ASTRONOMY 2000", GIACCONI R., STELLA L. & SERIO S. EDS., *ASP Conf. Ser.* (ASTRO-PH/0101077).

[86] GEORGE I. M., TURNER T. J., YAQOOB T., NETZER H., LAOR A., MUSHOTZKY R. F., NANDRA K., TAKAHASHI T., 2000, *Ap.J.* **531**, 52.

[87] GIACCONI R., GURSKY H., PAOLINI F., ROSSI B., 1962, *Phys. Rev. Lett.* **9**, 439.

[88] GIACCONI R., BECHTOLD J., BRANDUARDI G., ET AL., 1979, *Ap.J.* **234**, L1.

[89] GIACCONI R., ROSATI P., TOZZI P., ET AL., 2001, *Ap.J*, SUBMITTED (ASTRO-PH/0007240).

[90] GILLI R., RISALITI G., SALVATI M., 1999, *A.&A.* **347**, 424.

[91] GILLI R., SALVATI M., HASINGER G., 2001, *A.&A.* **366**, 407.

[92] GIOIA I. M., MACCACARO T., SCHILD R. E., STOCKE J. T., LIEBERT J. W., DANZIGER I. J., KUNTH D., LUB J., 1984, *Ap.J.* **283**, 495.

[93] GIOIA I. M., MACCACARO T., SCHILD R. E., WOLTER A., STOCKE J. T., MORRIS S. L., HENRY J. P., 1990, *Ap.J.S.S.* **72**, 567.

[94] GIOMMI P., TAGLIAFERRI G., BEUERMANN K., ET AL., 1991, *Ap.J.* **378**, 77.

[95] GIOMMI P., MENNA M. T., PADOVANI P., 1999, *M.N.R.A.S.* **310**, 456.

[96] GIOMMI P., PERRI M., FIORE F., 2000, *A.&A.S.* **362**, 799.

[97] GONDEK D., ZDZIARSKI A. A., JOHNSON W. N., GEORGE I. M., MCNARON-BROWN K., MAGDZIARZ P., SMITH D., GRUBER D. E., 1996, *M.N.R.A.S.* **282**, 646.

[98] GONZALEZ-DELGADO R. M., PEREZ E., 1993, *Ap.J.S.S.* **205**, 127.

[99] GOROSABEL J., CASTRO-TIRADO A. J., WOLF C., ET AL., 1998, *A.&A.* **339**, 719.

[100] HALPERN J. P., ERACLEOUS M., FORSTER K., 1998, *Ap.J.* **501**, 103.

[101] HAMILTON T. T., HELFAND D. J., 1993, *Ap.J.* **418**, 55.

[102] HAMMER F., FLORES H., LILLY S. J., ET AL., 1997, *Ap.J.* **481**, 49.

[103] HASINGER G., 1992, IN "THE X–RAY BACKGROUND", BARCONS X. & FABIAN A. C. EDS., P. 229.

[104] HASINGER G., BURG R., GIACCONI R., HARTNER G., SCHMIDT M., TRÜMPER J., ZAMORANI G., 1993, *A.&A.* **275**, 1.

[105] HASINGER G., FISCHER J.-U., SCHWOPE A. D., BOLLER TH., TRÜMPER J., VOGES W., 1997, *Astron. Nachr.* **329**, 334.

[106] HASINGER G., BURG R., GIACCONI R., SCHMIDT M., TRÜMPER J., ZAMORANI G., 1998, *A.&A.* **329**, 482.

[107] HASINGER G., LEHMANN I., GIACCONI R., SCHMIDT M., TRÜMPER J., ZAMORANI G., 2000, IN "X–RAY ASTRONOMY '999: STELLAR ENDPOINTS, AGN AND THE DIFFUSE X–RAY BACKGROUND", MALAGUTI G., PALUMBO G. & WHITE N. EDS. (ASTRO-PH/9901103).

[108] HASINGER G., ALTIERI B., ARNAUD M, ET AL. 2001, *A.&A.* **365**, L45.

[109] HAYASHI I., KOYAMA K., AWAKI H., YAMAUCHI S., UENO S., 1996, *P.A.S.J.* **48**, 219.

[110] HAYASHIDA K., 1990, PHD THESIS, UNIVERSITY OF TOKYO, ISAS RESEARCH NOTE 466.

[111] HAYASHIDA K., INOUE H., KII T., 1992, IN "FRONTIER OF X–RAY ASTRONOMY", TANAKA Y. & KOYAMA K. EDS., P. 653.

[112] HECKMAN T. M., BAUM S. A., VAN BREUGEL W. M., MCCARTHY P., 1989, *Ap.J.* **338**, 48.

[113] HUNT L., TESTI L., BORELLI S., MAIOLINO R., MORIONDO G., 1994, *Arcetri Technical Report* **4**.

[114] KIM D.-W., ELVIS M., 1999, *Ap.J.* **516**, 9.

[115] KNOX R. A., HAMBLY N. C., HAWKINS M. R. S., MACGILLIVRAY H. T., 1998, *M.N.R.A.S.* **297**, 839.

[116] KONDO H., 1990, PHD THESIS, UNIVERSITY OF TOKYO, ISAS RESEARCH NOTE 494.

[117] KOYAMA K., 1989, *P.A.S.J.* **41**, 665.

[118] ICHIMARU S., 1977, *Ap.J.* **214**, 840.

[119] IRWIN J. A., BREGMAN J. N., 2000, *Ap.J.* **538**, 543.

[120] IVISON R., SMAIL I., BARGER A., ET AL., 2000, *M.N.R.A.S.* **315**, 209.

[121] JAGER R., MELS W. A., BRINKMANN A. C., ET AL., 1997, *A.&A.S.* **125**, 557.

[122] JANSEN F., LUMB D., ALTIERI B., ET AL., 2001, *A.&A.* **365**, L1.

[123] LA FRANCA F., FIORE F., VIGNALI C., COMASTRI A., POMPILIO F., 2001, IN "THE NEW ERA OF WIDE FIELD ASTRONOMY", CLOWES R. G., ADAMSON A. J. & BROMAGE G. E. EDS., ASP CONF. SERIES (ASTRO-PH/0011008).

[124] LA FRANCA F., FIORE F., COMASTRI A., GIOMMI P., MATT G., MOLENDI S., PEROLA S., POMPILIO F., VIGNALI C., *M.N.R.A.S.*, IN PREPARATION.

[125] LAOR A., FIORE F., ELVIS M., WILKES B. J., MCDOWELL J. C., 1997, *Ap.J.* **477**, 93.

[126] LAWRENCE A., 1999, *Adv. Space Res.* **23**, 1167.

[127] LEHMANN I., HASINGER G., SCHMIDT M., ET AL., 2000, *A.&A.* **354**, 35.

[128] LEHNERT M. D., MILEY G. K., SPARKS W. B., ET AL., 2000, *Ap.J.S.S.* **123**, 351.

[129] LILLY S. J., LE FEVRE O., CRAMPTON D., HAMMER F., TRESSE L., 1995, *Ap.J.* **455**, 50.

[130] LISI F., BAFFA C., BILOTTI V., ET AL., 1996, *P.A.S.P.* **108**, 364.

[131] LUTZ D., SPOON H. W. W., RIGOPOULOU D., MOORWOOD A. F. M., GENZEL R., 1998, *Ap.J.* **505**, L103.

[132] MACCACARO T., DELLA CECA R., GIOIA I. M., MORRIS S. L., STOCKE J. T., WOLTER A., 1991, *Ap.J.* **374**, 117.

[133] MADAU P., GHISELLINI G., FABIAN, A. C., 1994, *M.N.R.A.S.* **270**, L17.

[134] MADDOX S. J., EFSTATHIOU G., SUTHERLAND W. J., LOVEDAY J., 1990A, *M.N.R.A.S.* **243**, 692.

[135] MADDOX S. J., EFSTATHIOU G., SUTHERLAND W. J., 1990B, *M.N.R.A.S.* **246**, 433.

[136] MAKISHIMA K., TASHIRO M., EBISAWA K., ET AL., 1996, *P.A.S.J.* **48**, 171.

[137] MAIOLINO R., RIEKE G. H., 1995, *Ap.J.* **454**, 95.

[138] MAIOLINO R., RUIZ M., RIEKE G. H., PAPADOPOULOS P., 1997, *Ap.J.* **485**, 552.

[139] MAIOLINO R., 2000, IN "X–RAY ASTRONOMY '999: STELLAR ENDPOINTS, AGN, AND THE DIFFUSE X–RAY BACKGROUND", MALAGUTI G., PALUMBO G. & WHITE N. EDS. (ASTRO-PH/0007473).

[140] MAIOLINO R., SALVATI M., ANTONELLI A., COMASTRI A., FIORE F., GHINASSI F., GILLI R., LA FRANCA F., MANNUCCI F., RISALITI G., THOMPSON D., VIGNALI C., 2000, *A.&A.* **355**, L47.

[141] MAIOLINO R., MARCONI A., OLIVA E., 2001, *A.&A.* **365**, 37.

[142] MALAGUTI G., BASSANI L., CAPPI M., ET AL. 1999, *A.&A.* **342**, L41.

[143] MANZO G., GIARRUSSO S., SANTANGELO A., ET AL., 1997, *A.&A.* **122**, 341.

[144] MARSHALL F. E., BOLDT E. A., HOLT S. S., MILLER R. B., MUSHOTZKY R. F., ROSE L. A., ROTHSCHILD R. E., SERLEMITSOS P. J., 1980, *Ap.J.* **235**, 4.

[145] MARSHALL H. L., 1985, *Ap.J.* **289**, 457.

[146] MASCI F. J., WEBSTER R. L., FRANCIS P. J., 1998, *M.N.R.A.S.* **301**, 975.

[147] MATHER J. C., CHENG E. S., EPLEE R. E., ET AL., 1990, *Ap.J.* **354**, L37.

[148] MATHER J. C., CHENG E. S., COTTINGHAM D. A., ET AL., 1994, *Ap.J.* **420**, 439.

[149] MATT G., FABIAN A. C., 1994, *M.N.R.A.S.* **267**, 187.

[150] MATT G., POMPILIO F., LA FRANCA F., 1999, *New Astronomy* **4**, 191.

[151] MATT G., FABIAN A. C., GUAINAZZI M., IWASAWA K., BASSANI L., MALAGUTI G., 2000, *M.N.R.A.S.* **318**, 173.

[152] MATTHEWS K., SOIFER B. T., 1994, IN "INFRARED ASTRONOMY WITH ARRAYS", MCLEAN I. ED., P. 239.

[153] MCHARDY I. M., JONES L. R., MERRIFIELD M. R., ET AL., 1998, *M.N.R.A.S.* **295**, 641.

[154] MEWE R., GRONENSCHILD E. H. B. M., VAN DEN OORD G. H. J., 1985, *A.&A.S.* **62**, 197.

[155] MIYAJI T., HASINGER G., SCHMIDT M., 2000, *A.&A.* **353**, 25.

[156] MONET D., ET AL., 1997, THE PPM USNO-A1.0 CATALOG.

[157] MONET D., 1998, *Amer. Astr. Soc. Meeting* **190**, 120.03.

[158] MUSHOTZKY R. F., COWIE L. L., BARGER A. J., ARNAUD K. A., 2000, *Nature* **404**, 459.

[159] NAKANISHI K., AKIYAMA M., OHTA K., YAMADA T., 2000, *Ap.J.* **534**, 587.

[160] NANDRA K., POUNDS K. A., 1994, *M.N.R.A.S.* **268**, 405.

[161] NANDRA K., GEORGE I. M., MUSHOTZKY R. F., TURNER T. J., YAQOOB T., 1997, *Ap.J.* **476**, 70.

[162] NARAYAN R., YI I., 1994, *Ap.J.* **428**, L13.

[163] NARAYAN R., MAHADEVAN R., QUATAERT E., 1998, IN "THE THEORY OF BLACK HOLE ACCRETION DISKS", ABRAMOWICZ G., BJORNSSON G. & PRINGLE J. E. EDS., P. 148.

[164] OGASAKA Y., KII T., UEDA Y., ET AL., 1998, *Astron. Nachr.* **319**, 430.

[165] OHTA K., YAMADA T., NAKANISHI K., OGASAKA Y., KII T., HAYASHIDA K., 1996, *Ap.J.* **458**, L70.

[166] OKE J. B., 1990, *A.J.* **99**, 1621.

[167] OSTERBROCK D. E., 1991, *Rep. Prog. Phys.* **54**, 579.

[168] OTANI C., DOTANI T., 1994, *ASCA Newsl.* **2**, 25.

[169] PADOVANI P., MORGANTI R., SIEBERT J., VAGNETTI F., CIMATTI A., 1999, *M.N.R.A.S.* **304**, 829.

[170] PARMAR A. N., MARTIN D. D. E., BAVDAZ M., ET AL., 1997, *A.&A.* **122**, 309.

[171] PERRI M., GIOMMI P., 2000, *A.&A.* **362**, L57.

[172] PFEFFERMANN E., BRIEL U. G., HIPPMANN H., ET AL., 1987, IN "SOFT X–RAY OPTICS AND TECHNOLOGY", *Proc. SPIE* **733**, 519.

[173] PICCINOTTI G., MUSHOTZKY R. F., BOLDT E. A., HOLT S. S., MARSHALL F. E., SERLEMITSOS P. J., SHAFER R. A., 1982, *Ap.J.* **253**, 485.

[174] PIRO L., DE ROSA A., DADINA M., ET AL., 2000, *Adv. Space Res.* **25**, 453.

[175] POMPILIO F., LA FRANCA F., MATT G., 2000, *A.&A.* **353**, 440.

[176] RAMSEY B. D., AUSTIN R. A., DECHER R., 1994, *Space Sci. Rev.* **69**, 139.

[177] RAYMOND J. C., SMITH B. W., 1977, *Ap.J.S.S.* **35**, 419.

[178] REES M. J., BEGELMAN M. C., BLANDFORD R. D., PHINNEY E. S., 1982, *Nature* **295**, 17.

[179] REEVES J. N., TURNER M. J. L., OHASHI T., KII T., 1997, *M.N.R.A.S.* **292**, 468.

[180] REEVES J. N., TURNER M. J. L., 2000, *M.N.R.A.S.* **316**, 234.

[181] REYNOLDS C. S., 1997, *M.N.R.A.S.* **286**, 513.

[182] RICCI D., FIORE F., GIOMMI P., 1998, IN "THE ACTIVE X–RAY SKY: RESULTS FROM BEPPOSAX AND RXTE", SCARSI L., BRADT H., GIOMMI P. & FIORE F. EDS., *Nuclear Physics B* (PROC. SUPPL.) **69/1-3**, 618.

[183] RISALITI G., MAIOLINO R., SALVATI M., 1999, *Ap.J.* **522**, 157.

[184] ROTHSCHILD R. E., BAITY W. A., GRUBER D. E., MATTESON J. L., PETERSON L. E., MUSHOTZKY R. F., 1983, *Ap.J.* **269**, 423.

[185] SACCO B., 1999, *BeppoSAX* EIWG MEETING REPORT.

[186] SAKANO M., KOYAMA K., TSURU T., ET AL., 1998, *Ap.J.* **505**, 129.

[187] SAMBRUNA M. R., ERACLEOUS M., MUSHOTZKY R. F., 1999, *Ap.J.* **526**, 60.

[188] SCHMIDT M., HASINGER G., GUNN J., ET AL., 1998, *A.&A.* **329**, 495.

[189] SETTI G., WOLTJER L., 1989, *A.&A.* **224**, L21.

[190] SEVERGNINI P., MAIOLINO R., SALVATI M., AXON D., CIMATTI A., FIORE F., GILLI R., LA FRANCA F., MARCONI A., MATT G., RISALITI G., VIGNALI C., 2000, *A.&A.* **360**, 457.

[191] SHAFER R. A., 1983, PHD THESIS, UNIVERSITY OF MARYLAND, NASA TM 85029.

[192] SHANKS T., GEORGANTOPULOS I., STEWART G. C., POUNDS K. A., BOYLE B. J., GRIFFITHS R. E., 1991, *Nature* **353**, 315.

[193] SMITH H. E., SPINRAD H., 1980, *Ap.J.* **236**, 419.

[194] STOCKE J. T., MORRIS S. L., GIOIA I. M., MACCACARO T., SCHILD R., WOLTER A., FLEMING T. A., HENRY J. P., 1991, *Ap.J.S.S.* **76**, 813.

[195] TAKAHASHI T., UEDA Y., ISHISAKI Y, OHASHI T., MAKISHIMA K., 1998, *Astron. Nachr.* **319**, 91.

[196] TANAKA Y., BLEEKER J. A. M., 1977, *Space Sci. Rev.* **20**, 815.

[197] TANAKA Y., INOUE H., HOLT S. S., 1994, *P.A.S.J.* **46**, L37.

[198] TRESSE L., ROLA C., HAMMER F., STASINSKA G., LE FEVRE O., LILLY S. J., CRAMPTON D., 1996, *M.N.R.A.S.* **281**, 847.

[199] TRÜMPER J., 1982, *Adv. Space Res.* **2**, 241.

[200] TRUSSONI E., MASSAGLIA S., FERRARI R., FANTI R., FERETTI L., PARMA P., BRINKMANN W., 1997, *A.&A.* **327**, 27.

[201] TURNER T. J., POUNDS K. A., 1989, *M.N.R.A.S.* **240**, 833.

[202] TURNER T. J., PEROLA G. C., FIORE F., MATT G., GEORGE I. M., PIRO L., BASSANI L., 2000, *Ap.J.* **531**, 245.

[203] UEDA Y, TAKAHASHI T., INOUE H., ET AL., 1998, *Nature* **391**, 866.

[204] UEDA Y., TAKAHASHI T., INOUE H., ET AL., 1999A, *Ap.J.* **518**, 656.

[205] UEDA Y., TAKAHASHI T., ISHISAKI Y., OHASHI T., MAKISHIMA K., 1999B, *Ap.J.* **524**, L11.

[206] UEDA Y., 2000, IN "X–RAY ASTRONOMY '999: STELLAR ENDPOINTS, AGN, AND THE DIFFUSE X–RAY BACKGROUND", MALAGUTI G., PALUMBO G. & WHITE N. EDS. (ASTRO-PH/9912084).

[207] URRY C. M., PADOVANI P., 1995, *P.A.S.P.* **107**, 803.

[208] VECCHI A., MOLENDI S., GUAINAZZI M., FIORE F., PARMAR A. N., 1999, *A.&A.* **349**, L73.

[209] VEILLEUX S., 2000, IN "STARBURSTS – NEAR AND FAR" (ASTRO-PH/0012121).

[210] VIGNALI C., COMASTRI A., STIRPE G. M., CAPPI M., PALUMBO G. G. C., MATSUOKA M., MALAGUTI G., BASSANI L., 1998, *A.&A.* **333**, 411.

[211] VIGNALI C., COMASTRI A., CAPPI M., PALUMBO G. G. C., MATSUOKA M., KUBO H., 1999, *Ap.J.* **516**, 582.

[212] VIGNALI C., MIGNOLI M., COMASTRI A., MAIOLINO R., FIORE F., 2000A, *M.N.R.A.S.* **314**, L11.

[213] VIGNALI C., COMASTRI A., FIORE F., 2000B, IN "LARGE SCALE STRUCTURE IN THE X–RAY UNIVERSE", PLIONIS M. & GEORGANTOPOULOS I. EDS., P. 269.

[214] VIGNALI C., COMASTRI A., FIORE F., LA FRANCA F., 2001, *A.&A.*, IN PRESS.

[215] VIGNATI P., MOLENDI S., MATT G., ET AL., 1999, *A.&A.* **349**, L57.

[216] VIKHLININ A., FORMAN W., JONES C., MURRAY S., 1995, *Ap.J.* **451**, 564.

[217] VOGES W., 1992, PROCEEDINGS ESA ISY CONFERENCE, ESA ISY-3, P. 3.

[218] VOGES W., ASCHENBACH B., BOLLER TH., ET AL., 1999, *A.&A.* **349**, 389.

[219] WANG Q. D., MCCRAY R., 1993, *Ap.J.* **409**, L37.

[220] WALTER R., FINK H. H., 1993, *A.&A.* **274**, 105.

[221] WEBSTER R. L., FRANCIS P. J., PETERSON B. A., DRINKWATER M. J., MASCI F. J., 1995, *Nature* **375**, 469.

[222] WEISSKOPF M. C., O'DELL S. L., VAN SPEYBROECK L. P., 1996, *Proc. SPIE* **2805**, 2.

[223] WHITE N. E., 1985, *EXOSAT Expr.* **11**, 51.

[224] WHITE N. E., GIOMMI P., ANGELINI L., 1994, *Amer. Astr. Soc. Meeting* **185**, 4111.

[225] WILMAN R. J., FABIAN A. C., 1999, *M.N.R.A.S.* **309**, 862.

[226] WILMAN R. J., FABIAN A. C., NULSEN P. E. J., 2000, *M.N.R.A.S.* **319**, 583.

[227] WOLTER A., COMASTRI A., GHISELLINI G., ET AL., 1998, *A.&A.* **335**, 899.

[228] WORRALL D. M., LAWRENCE C. R., PEARSON T. J., READHEAD A. C. S., 1994, *Ap.J.* **420**, L17.

[229] WRIGHT E. L., MATHER J. C., FIXSEN D. J., 1994, *Ap.J.* **420**, 450.

[230] YEE H. K. C., GREEN R. F., 1987, *Ap.J.* **319**, 28.

[231] YUAN W., BRINKMANN W., SIEBERT J., VOGES W., 1998, *A.&A.* **330**, 108.

[232] YUAN W., MATSUOKA M., WANG T., UENO S., KUBO H., MIHARA T., 2000, *Ap.J.* **545**, 625.

[233] ZAMORANI G., MIGNOLI M., HASINGER G., ET AL., 1999, *A.&A.* **346**, 731.

[234] ZIMMERMANN H. U., BOESE G., BECKER W., BELLONI T., DÖBEREINER S., IZZO C., KAHABKA P., SCHWENTKER O., 1998, *MPE Report.*

[235] ZITELLI V., MIGNOLI M., ZAMORANI G., MARANO B., BOYLE B. J., 1992, *M.N.R.A.S.* **256**, 349.

Related Publications

• Ciliegi P., Vignali C., Comastri A., Fiore F., Matt G., La Franca F., *M.N.R.A.S*, in preparation
The BeppoSAX High Energy Large Area Survey – VI: the radio properties of the HELLAS sources

• Comastri A., Fiore F., Vignali C., La Franca F., Matt G., 2000, in "Large scale structure in the X–ray Universe", Plionis M. & Georgantopoulos I. eds., p. 227
The BeppoSAX High Energy Large Area Survey (HELLAS): a progress report

• Comastri A., Fiore F., Vignali C., Matt G., Perola G. C., La Franca F., 2001, *M.N.R.A.S.*, submitted
The BeppoSAX High Energy Large Area Survey – III: testing synthesis models for the X–ray background

• Fiore F., La Franca F., Giommi P., Elvis M., Matt G., Comastri A., Molendi S., Gioia I. M., 1999, *M.N.R.A.S.* **306**, L55
The contribution of faint active galactic nuclei to the hard X-ray background

• Fiore F., Antonelli L. A., Ciliegi P., Comastri A., Giommi P., La Franca F., Maiolino R., Matt G., Molendi S., Perola G. C., Vignali C., 2000, in "X–ray Astronomy '999: Stellar Endpoints, AGN, and the Diffuse Background", Malaguti G., Palumbo G. & White N. eds. (astro-ph/0007118)
The BeppoSAX HELLAS survey: on the nature of hard X–ray selected sources

• Fiore F., Giommi P., Vignali C., Comastri A., Matt G., Perola G. C., La Franca F., Molendi S., Tamburelli F., Antonelli A., 2001, *M.N.R.A.S.*, submitted
The BeppoSAX High Energy Large Area Survey HELLAS – II: Number counts and X–ray spectral properties

• Fiore F., Comastri A., La Franca F., Vignali C., Matt G.,

Perola G. C., 2001, in "ESO workshop on deep fields" (astro-ph/0102041)
High Energy Large Area Surveys: from BeppoSAX to Chandra and XMM

• La Franca F., Fiore F., Vignali C., Comastri A., Pompilio F., 2001, in "The New Era of Wide Field Astronomy", Clowes R. G., Adamson A. J. & Bromage G. E. eds., ASP Conf. Series (astro-ph/0011008)
The evolution of AGN in the Hard X–rays from HELLAS

• La Franca F., Fiore F., Comastri A., Giommi P., Matt G., Molendi S., Perola S., Pompilio F., Vignali C., *M.N.R.A.S.*, in preparation
The BeppoSAX High Energy Large Area Survey – V. The nature of the X–ray source populations and its evolution

• Maiolino R., Salvati M., Antonelli A., Comastri A., Fiore F., Ghinassi F., Gilli R., La Franca F., Mannucci F., Risaliti G., Thompson D., Vignali C., 2000, *A.&A.* **355**, L47
Optically dim counterparts of hard X–ray selected AGNs

• Severgnini P., Maiolino R., Salvati M., Axon D., Cimatti A., Fiore F., Gilli R., La Franca F., Marconi A., Matt G., Risaliti G., Vignali C., 2000, *A.&A.* **360**, 457
Sub-mm and X–ray background: two unrelated phenomena ?

• Vignali C., Mignoli M., Comastri A., Maiolino R., Fiore F., 2000, *M.N.R.A.S.* **314**, L11
Optical, near-infrared and hard X–ray observations of SAXJ1353.9+1820: a red quasar

• Vignali C., Comastri A., Fiore F., 2000, in "Large scale structure in the X–ray Universe", Plionis M. & Georgantopoulos I. eds., p. 269
The HELLAS survey: broad band properties of hard X–ray selected sources

• Vignali C., Comastri A., Fiore F., La Franca F., 2000, *Mem. Soc. Astr. It.* , in press
The HELLAS Survey. Probing the existence of a dichotomy between optical and X–ray classification

• Vignali C., Comastri A., Fiore F., La Franca F., 2001, *A.&A.*, in press
The BeppoSAX High Energy Large Area Survey – IV. On the soft X–ray properties of the hard X–ray-selected HELLAS sources

SCENE It's a fine sunny day in the forest, and a rabbit is sitting outside his burrow, tippy-tapping on his typewriter.

Along comes a fox, out for a walk

FOX ''What are you working on ?''
RABBIT ''My thesis''
FOX ''Hmm... What's it about ?''
RABBIT ''Oh, I'm writing about how rabbits eat foxes''

(incredulous pause)

FOX ''That's ridiculous ! Any fool knows that rabbits don't eat foxes''
RABBIT ''Sure they do, and I can prove it. Come with me''

They both disappear into the rabbit's burrow.
After a few minutes, the rabbit returns, alone,
to his typewriter and resumes typing.
Soon, a wolf comes along
and stops to watch the hardworking rabbit.

WOLF ''What's that you're writing ? ''
RABBIT ''I'm doing a thesis on how rabbits eat wolves''

(loud guffaws)

WOLF ''You don't expect to get such rubbish published,

do you ?''

RABBIT ''No problem. Do you want to see why ?''

The rabbit and the wolf go into the burrow,
and again the rabbit returns by himself, after a few minutes,
and goes back by typing.

SCENE Inside the rabbit's burrow. In one corner, there is a pile of fox bones. In another corner, a pile of wolf bones. On the other side of the room a huge lion is belching and picking his teeth.

The End

MORAL It doesn't matter what you choose for a thesis subject.
It doesn't matter what you use for data.
What does matter is who you have for a thesis advisor.

Acknowledgments

Once a travel gets over it seems natural to remind of the beginnings. I remember the period when my "travel in the scientific world" begun four years ago, at first with my Laurea Degree and then with my PhD. I was enthusiastic, full of good ideas about my future works, spending the time by planning new discoveries and findings. The reality was really different from that: the work can be extremely tiring, boring sometimes, and the results not always of that kind you hoped. Nevertheless, I think that it's worth doing this experience, because it represents a a good way to learn something new day by day and about many fields of interest, not only yours; moreover, you grow your skill in investigating the nature of physical (and astrophysical) processes. In addition, it provides a splendid opportunity to meet people and to gain new friends (in the luckiest hypothesis).
Now I just can see the end of my PhD studies (within one month). In Italy it is common to say that once a door gets closed, another one gets opened. It's terribly true, and life can be considered a long journey ... The most important thing is therefore to have a goal, whatever you do and whenever you go.

I find extremely difficult to thank all the people who played a key role in my life during the three year of my PhD.
At first my family, in particular my mother. I think she knows nothing

about my work at the Astronomy Department, and truly I cannot remember whether sometimes (or even once only) I talked to her about my job. Confidentially, she accepts me without knowing what I do all day long in Bologna, and this is good for me: no questions, no answers, which is practically the opposite of my work (too many questions and too many answers to give).

Then my friends. In first position Roberto, I spent a considerable part of my life (at the University and within my PhD years) with him, for some years sharing the same apartment. Now he is away from here (in Canada), I hope his future with Katia (hello Katia) can be fully of great opportunities. Then all the other people (especially the friends) I met during the past years in Bologna. Alessio (Dante) and Barbara (now in Germany), Daniela (in Germany too), Barbara P., Ivan, Cristina, Luca, Michele, Roberto G., and many more ... and people I met during my research years, in particular Paola, a very good and kind friend.

Finally, the people of the "five o'clock coffee break": Marcella, Luca "the red", Charlie, Anna Lia, Piero, Luca "the black", Lorenzo, Marta, Matteo, Stefano, Francesca(s), ...

I cannot forget the other PhD students, with whom I shared many interesting seminars (??), school lessons (??) and some more ... In particular I want to thank Michele, who gave me (in the rare occasions we met) a very strong enthusiasm ..., and Emiliano: we spent a lot of week-ends in the institutes together ...

Then the people of my apartment, in particular Oscar and Emanuele, who are very good friends ... I hope we can meet again each other in the future with the same spirit...

Finally the professors and the other researchers, but in particular Dr. (sorry: Professor) A. Comastri, who "traced the main stream of the AGNs population synthesis models for the XRB" (known all over

the world) ... I just know what he will think when he'll read these acknowledgments ... Max, for his enthusiasm, Marco (who guided me towards the optical wavelengths), Paolo (who did the same, but in the field of radioastronomy) and Prof. G. Palumbo, a very good scientist, philosopher and talker.